

QUANTIFICATION AND MODELLING OF HETEROGENEITIES IN AQUIFERS

By

DEHOUEGNON PACOME AHOKPOSSI

Submitted in fulfilment of the requirements in respect of the Doctoral degree qualification "Philosophiae Doctor" at the Institute for Groundwater Studies, in the Faculty of Natural and Agricultural Sciences at the University of the Free State.

January 2017

Supervisor: Prof Abdon Atangana (PhD)

Co. Supervisor: Prof P. Danie Vermeulen (PhD)

DECLARATION

- (i) I, AHOKPOSSI DEHOUEGNON PACOME, declare that the Doctoral Degree research thesis or interrelated, publishable manuscripts / published articles, or coursework Doctoral Degree mini-thesis that I herewith submit for the Doctoral Degree qualification Philosophiae Doctor at the University of the Free State is my independent work and that I have not previously submitted it for a qualification at another institution of higher education.

- (ii) I, AHOKPOSSI DEHOUEGNON PACOME, hereby declare that I am aware that the copyright is vested in the University of the Free State.”

- (iii) I, AHOKPOSSI DEHOUEGNON PACOME, hereby declare that all royalties as regards intellectual property that was developed during the course of and/or in connection with the study at the University of the Free State will accrue to the University.

DEDICATION

This thesis is dedicated to all those who have built and shared knowledge for the protection of the natural resources in general, and water resources particularly.

This is the time of development of Africa. Let us not repeat the same mistakes like the most industrialised continents. Let us preserve the Nature.

We believe that the contributions of the present thesis will assist professionals and scientists in developing better approaches to reach such a goal.

ACKNOWLEDGEMENTS

I acknowledge the grace of God (Father, Son, and Holy Spirit) in my different life experiences, and for all the people I met.

I would like to express my deepest acknowledgment to:

- Prof Abdon Atangana, for the different supports, for showing me the way for the completion of the present thesis, for extending my knowledge in applied mathematics to earth sciences, and mainly for showing friendship. A French author, Victor Hugo said: « *Aux âmes bien nés la valeur n'attend point le nombre des années* ».
- The different stakeholders in the management and operation of the Mogalakwena platinum mine, and the Aqua Earth's team, especially the Managing Director Albertus Lombaard.

Special words of thanks to:

- My parents, Damassoh D. Catherine and Ahokpossi A. Marius, for continuously reminding me of completing the present thesis, and for the different supports.
- My spouse, Corine Gillette Toi, for her prayers, continuous supports and encouragement towards achieving our different projects.
- My lovely ones: Degnissou Fifa Benie, Eyram Marius, and Keli Emmanuella, for just being part of my life.

I would also like to acknowledge the assistance of all those who have contributed to the success of the present study but are not mentioned by names.

Abstract

The future of modelling of heterogeneity in aquifers is definitively in the designing of new in situ testing (hydraulic and mass transport) procedures with new corresponding mathematical models. New trends in mathematical differentiation offer opportunity to explore more flexible and practical mathematical model solutions. This applies to both analytical and numerical modelling. Only a sound understanding of rock structures can clearly pose the problem which will then be used to define hydraulic equations to be solved by mathematical models, and numerical software.

The most recent concept of differentiation based on the non-local and non-singular kernel called the generalized Mittag-Leffler function, was employed to reshape the model of fractured aquifer fractal flow. The solution was successfully applied to experimental data collected from four different constant discharge tests.

Additionally, a new analytical solution to the fractal flow in a dual media was proposed, where the media could be elastic; heterogeneous; and visco-elastic. The existing dual media fractal flow model was modified by replacing the local derivative with the non-local operator (operator with Mittag-Leffler kernel, and Mittag-Leffler-Power law kernel). The more accurate numerical scheme known as Upwind was used to numerically solve each model.

Heterogeneity in a typical South African crystalline rock aquifer was assessed. From this, a methodical level for quantifying and modelling heterogeneity in an aquifer was deduced. It was demonstrated how spatial heterogeneity in aquifers can be modelled based on the most commonly available tools and data in mining environment. The capability of selected numerical geohydrological softwares were assessed using spatial variability of hydraulic parameters (hydraulic conductivity and recharge). Geostatistical tools were specifically applied. Focus was also given to hydro-geochemical characterization by using bivariate scatter plots, Piper and Expanded Durov diagrams, and PHREEQC hydro-geochemical model as complimentary tools to analyse the groundwater chemistry data to describe different hydro-geochemical process which prevail in the monitored groundwater system.

Three manuscripts have been submitted out this thesis, in top tier journals of the Natural and Applied Sciences.

Key Words: Groundwater; heterogeneity; variability; fractal; Mittag-Leffler; numerical models; quantification; diffusion.

Opsomming

Die ontwikkeling van nuwe in situ toets (hidrouliese en massa vervoer) prosedures met nuwe ooreenstemmende wiskundige modelle is die toekoms van modellering van heterogeniteit in waterdraers. Nuwe tendense in die wiskundige differensiasies bied geleentheid om meer buigsaam, en praktiese wiskundige model oplossings te verken. Dit geld vir beide analitiese en numeriese modellering. Slegs 'n goeie begrip van die rots strukture kan die probleem duidelik stel wat dan gebruik word om die hidrouliese vergelykings te bepaal wat deur wiskundige modelle opgelos moet word.

Die mees onlangse konsep van differensiasie gebaseer op die nie-plaaslike en nie-singuliere kern wat bekend staan as die algemene Mittag-Leffler funksie, was gebruik om die model van gefrakteurde waterdraer fraktale vloei te hervorm. Die bestaan van 'n positiewe oplossing van die nuwe model was aangebied, en die uniekheid van die positiewe oplossing was gestig. Drie verskillende numeriese skemas was gebruik om die nuwe gefrakteurde fraktale model op te los. Die oplossing was daarna suksesvol toegepas op eksperimentele data wat van vier verskillende konstante vloei toetse versamel was. 'n Nuwe analitiese oplossing vir die fraktale vloei in 'n dubbele media sisteem was ook voorgestel, waar die media elasties; heterogeen; en visco-elasties kan wees. Die bestaande dubbele media fraktale vloei model was aangepas deur die vervanging van die plaaslike afgeleide met die nie-plaaslike operateur met krag. Twee nie-plaaslike operateurs was oorweeg - 'n operateur met Mittag-Leffler kern en Mittag-Leffler-Power wet kern. Vir elke model is 'n gedetailleerde studie van die bestaan en uniekheid van die sisteem oplossings met behulp van die vaste punt stelling aangebied. Die meer akkurate numeriese skema, bekend as windop, was gebruik om elke model numeries op te los.

Die heterogeniteit in 'n tipiese Suid-Afrikaanse kristallyne rots waterdraer was geassesseer. Uit hierdie was 'n metodiese vlak vir die kwantifisering en modellering van heterogeniteit in 'n waterdraer afgelei. Dit was gedemonstreer hoe ruimtelike heterogeniteit in waterdraers gemodelleer kan word op grond van die mees algemeen beskikbare gereedskap en data in Suid-Afrikaanse mynbou omgewings. Ruimtelike variasie van hidrouliese parameters is gebruik om heterogeniteit in die waterdraer in ag te neem. Geostatistiese gereedskap was gebruik om die geskatte hidrouliese geleiding en herlaai waardes te analiseer.

Contents

Abstract	4
Opsomming	5
1 Introduction	14
1.1 Research statement and objectives.....	16
1.1.1 Research statement	16
1.1.2 Research objectives.....	18
2 Theories and Literature Review	20
2.1 Spatial variability in rocks' hydraulic properties	20
2.2 Implication of rocks heterogeneities for spatial heterogeneity in the groundwater flow velocities.....	21
2.3 Implication for spatial heterogeneity in solutes transport.....	23
2.4 Accounting for spatial heterogeneity in groundwater studies	25
2.4.1 Spatial heterogeneity analytical modelling.....	27
2.4.2 Spatial heterogeneity numerical modelling	35
3 Modelling groundwater fractal flow with fractional differentiation via Mittag-Leffler law 41	
3.1 New Fractional differentiation with Mittag-Leffler Law.....	43
3.2 Existing of positive solution.....	45
3.3 The new fractal flow equation has a positive solution.	48
3.3.1 Application to the new fractal flow model	50
3.4 Numerical analysis with fractional integral	51
3.4.1 Numerical approximation of fractional integral	51
3.4.2 Application to new model	53
3.5 Numerical solution with fractional derivative	58
3.6 Conclusion.....	65
4 Modelling of fractal flow in dual media with power and generalized Mittag-Leffler laws.....	66
4.1 Fractional differentiation.....	68
4.2 Model of fractal flow in dual media accounting for elasticity	69
4.2.1 Existence of system solutions	69
4.3 Numerical Solution	73
4.4 Model of fractal flow in dual media accounting for visco-elasticity	78
4.4.1 Existence of system solutions	79

4.5	Numerical Solution with Mittag-Leffler law	84
4.6	Model of fractal flow in dual media with heterogeneity and visco-elasticity properties	89
4.7	Numerical simulation for different values of fractional order	94
4.8	Conclusion	99
5	General description of the case study area	101
5.1	Locality	101
5.2	Climate	101
5.3	Topography and surface water drainage	103
5.4	Geology.....	106
5.4.1	Regional Geology	107
5.4.2	Local Geology and mineralization	109
5.5	Geohydrology.....	116
5.5.1	Regional Geohydrology	116
5.5.2	Analysis of available GRIP II data base information on Boreholes in the catchment.....	117
6	Field characterization of the study area.....	121
6.1	Approach and Methodology for field characterisation	121
6.1.1	Methodology for Hydrocensus	121
6.1.2	Geophysical surveys and Drilling approaches	122
6.1.3	Setting of Hydraulic testing and interpretation tools	123
6.1.4	Groundwater Recharge estimation.....	126
6.2	Field characterisations results and interpretations.....	126
6.2.1	Hydrocensus in the catchment.....	126
6.2.2	Analysis of geophysical patterns (Magnetic and Electromagnetic)	133
6.2.3	Borehole drilling and geological characterization	136
6.2.4	Aquifer drainage, flow directions and gradients.....	143
6.2.5	Hydraulic tests results and interpretation	149
6.2.6	Hydro-geochemistry and groundwater quality.....	175
6.2.7	Groundwater recharge (Chloride Mass Balance Method) values	198
7	Conceptual and numerical geohydrological model of the Platreef	201
7.1	Objective of the Modelling	201
7.2	Conceptual geohydrological models.....	201
7.2.1	Soils and unsaturated zone	202

7.2.2	Hydro-stratigraphic units, types, and thicknesses.....	203
7.2.3	Aquifers domain and boundaries	205
7.2.4	Hydraulic Parameters	206
7.3	Numerical model	211
7.3.1	Software codes.....	211
7.3.2	Model area and boundaries conditions	213
7.3.3	Discretisation of the Model Area.....	216
7.3.4	Numerical Flow Model.....	222
7.3.5	Models Hydraulic properties.....	222
7.3.6	Calibrations of Steady state flow models, and model errors	226
7.3.7	Sensitivity analysis of the steady state models	247
7.3.8	<i>Transport numerical model</i>	249
7.4	Models Results and discussion.....	252
7.4.1	Cone of depression.....	252
7.4.2	Contaminants transport simulation.....	254
8	Conclusion	259
9	References	263
10	Appendices.....	274
10.1	Appendix A: Geophysical survey results.....	274
10.2	Appendix B: Summary of percussion drillings results.....	291
10.3	Appendix C: Recharge rates calculation	296
10.4	Appendix B: Drawdown fitting curves for hydraulic parameters from observation boreholes.....	304
10.4.1	Barker model.....	304
10.4.2	Logarithmic approximation of fractured fractal model	305
10.4.3	Fractured Fractal Flow solution with fractional differentiation via Mittag-Leffler law	306

List of Figures

Figure 1: Typical salt solute tracer breakthrough curve compared to water levels during natural gradient tracer test in the Karoo, South Africa (adapted from Modreck Gomo, 2011)..... 25

Figure 2: Characteristic fractal pressure transient behaviour in the abstraction borehole for a) $\delta < 1$ and b) $\delta > 1$ (from Acuna and Yortsos, 1995). 34

Figure 3: Numerical simulation contour plot of hydraulic head for $d = 1.2$: In (a) we chose $\theta = 0.25$, in (b) we chose $\theta = 0.75$, in (c), we chose, and in (d) we chose $\theta = 1.5$... 63

Figure 4: Numerical simulation contour plot of hydraulic head for $\theta = 0.25$: In (a) we chose $d = 1.80$, in (b) we chose $d = 1.1$, in (c) we chose $d = 2.3$, and in (d) we chose $d = 2.9$ 64

Figure 5: Numerical simulation of system solution with red the hydraulic head in a fracture system and blue in a matrix rock $\alpha = 0.5$ 95

Figure 6: Numerical simulation of hydraulic head in the fracture network for $\alpha = 0.5$.. 95

Figure 7: Numerical simulation of hydraulic head within the matrix rock for $\alpha = 0.5$ 96

Figure 8: Numerical simulation of system solution with red the hydraulic head in a fracture system and blue in a matrix rock $\alpha = 0.75$ 96

Figure 9: Numerical simulation of hydraulic head in the fracture network for $\alpha = 0.75$. 97

Figure 10: Numerical simulation of hydraulic head within the matrix rock for $\alpha = 0.75$ 97

Figure 11: Numerical simulation of system solution with red the quantity of water in a fracture system and blue in a matrix rock $\alpha = 1$ 98

Figure 12: Numerical simulation of hydraulic head in the fracture network for $\alpha = 1$ 98

Figure 13: Numerical simulation of hydraulic head within the matrix rock for $\alpha = 1$ 99

Figure 14: Monthly averages temperatures in the area101

Figure 15: Location of the investigation area102

Figure 16: Historical (05 years) average monthly recorded rainfall.....103

Figure 17: Average monthly evaporation103

Figure 18: Topography of the study area105

Figure 19: Geology in the catchment.....110

Figure 20: Lineaments frequency distributions.....113

Figure 21: Borehole depth frequency (Grip data)118

Figure 22: Depth to water levels frequency (Grip data)119

Figure 23: Distribution of GRIP data in the catchment120

Figure 24: Distribution of Borehole visited during hydrocensus in the catchment128

Figure 25: Distribution of combined hydrocensus and GRIP boreholes in the catchment129

Figure 26: Borehole depths frequency (Hydrocensus).....131

Figure 27: Depth to groundwater levels frequency (Hydrocensus).....131

Figure 28: Depth to first water strikes frequency (Hydrocensus).....132

Figure 29: Depth to first weathering bottom frequency (Hydrocensus)132

Figure 30: Position of geophysical traverses (red line, brown lineaments) with lineaments (blue: Dyke, black Fault,)134

Figure 31: Typical fault anomaly at the investigation area.....136

Figure 32: Typical Dyke anomaly at the investigation area.....136

Figure 33: Investigation boreholes locations and results138

Figure 34: Investigation borehole depths, water levels, and yields139

Figure 35: Blow yields frequency (Investigation boreholes drilling)141

Figure 36: Borehole video image of the fracture zone in selected boreholes143

Figure 37: Surface water elevation correlation to groundwater elevations145

Figure 38: Bayesian interpolated groundwater elevations and drainage146

Figure 39: Linear Kriging interpolated groundwater elevations and drainage compared to geological and structural lineaments147

Figure 40: Comparison of Bayesian (blue lines) to the Linear Kriging (orange lines) interpolated elevations.148

Figure 41: Evolution of depth to groundwater levels.....149

Figure 42: Borehole yields frequency (Slug test on investigation boreholes).....152

Figure 43: Correlation between measured blow yields (V Notch) and yields inferred from slug tests.....153

Figure 44: Spatial distribution of inferred conductivity values (Slug test on investigation boreholes)155

Figure 45: Constant Discharge tests setting for PC140, DPC7, DPC9158

Figure 46: Constant Discharge tests setting for DPC14, DPC15, DPC18, DPC26, DPC27159

Figure 47: Drawdown –Recovery of CDT in DPC27, DPC26, and DPC9162

Figure 48: Drawdown –Recovery of CDT in PC140, DPC18, DPC15, DPC14, and DPC17162

Figure 49: Comparison of modified equation with experimental data for DPC14170

Figure 50: Comparison of modified equation with experimental data for DPC15170

Figure 51: Comparison of modified equation with experimental data for DPC18171

Figure 52: Comparison of modified equation with experimental data for PPC140.....171

Figure 53: Drawdown curves recorded in observations boreholes during different CDT172

Figure 54: Expanded Durov diagram showing dominant water type in the catchment .177

Figure 55: Expanded Durov diagram showing dominant water type in the monitoring area (04 years)178

Figure 56: Piper diagram of samples representative of Non dominant type.....179

Figure 57: Piper diagram of samples representative of Bicarbonate Calcium magnesium type.180

Figure 58: Piper diagram of samples representative of Bicarbonate Sodium type.181

Figure 59: pH measured in the samples collected from borehole which linear hydro-geochemical trends on Piper diagram184

Figure 60: Scatter plot showing $(HCO_3^- + SO_4^{2-})$ against $(Ca^{2+} + Mg^{2+})$ concentrations measured during monitoring period.187

Figure 61: Scatter plot showing HCO_3^- against $(Ca^{2+}$ and $Mg^{2+})$ concentrations measured during monitoring period.189

Figure 62: Scatter plot showing Ca^{2+} against Mg^{2+} concentrations measured during monitoring period.190

Figure 63: Scatter plot showing Cl^{-} against Na^{+} concentrations measured during monitoring period.191

Figure 64: Scatter plot showing $(Mg^{2+} + Ca^{2+} - SO_4^{2-} - HCO_3^{-})$ against $(Cl^{-} - Na^{+})$ concentrations measured during monitoring period.192

Figure 65: Scatter plot of Dolomite SI against Calcite SI.....193

Figure 66: Scatter plot of pH against Dolomite and Calcite SI.....194

Figure 67: Scatter plot of Calcite SI against Mg^{2+} and Ca^{2+} 194

Figure 68: Scatter plot of Dolomite SI against Mg^{2+} and Ca^{2+} 195

Figure 69: Classification of historical groundwater quality samples data based on TDS WHO (2003).197

Figure 70: Classification of historical groundwater quality samples data based on Hardness Index (McGowan, 2000).197

Figure 71: Spatial distribution of the estimated recharge using Chloride Mass Balance method in the catchment.....200

Figure 72: Available Hydraulic conductivity frequency in the catchment.....207

Figure 73: Spatial distribution of available estimated Hydraulic conductivity in the catchment208

Figure 74: Frequency distribution of estimated recharge using Chloride Mass Balance method211

Figure 75: Numerical models boundary conditions215

Figure 76: 3D view of the aquifer geometry build from Finite Element Mesh in FEFLOW.218

Figure 77: 3D view of the aquifer geometry build from Finite Element Mesh in FEFLOW219

Figure 78: 3D view of the aquifer geometry and mesh build from Finite Element Mesh in SPRING221

Figure 79: Experimental (black) and linear model (blue) variogram of the available conductivity without dry boreholes.....224

Figure 80: Experimental and linear model variogram of the available conductivity with dry drilled boreholes224

Figure 81: Experimental and linear model variogram of the available recharge rates ..225

Figure 82: Locations of the boreholes used for the calibration of the steady state models.227

Figure 83: Observed groundwater elevations versus simulated elevations MODFLOW .228

Figure 84: Observed groundwater elevations versus simulated elevations FEFLOW229

Figure 85: Observed groundwater elevations versus simulated elevations SPRING230

Figure 86: Hydraulic conductivity values used for the calibration in MODFLOW231

Figure 87: Hydraulic conductivity values used for the calibration in FEFLOW.....232

Figure 88: Hydraulic conductivity values used for the calibration in SPRING233

Figure 89: Sensitivity of MODFLOW model to double calibrated K.....248

Figure 90: Sensitivity of FEFLOW model to double calibrated K248
Figure 91: Sensitivity of SPRING model to half calibrated K.....249
Figure 92: Cone of depression around active opencast mine in a typical fractured crystalline aquifer.253
Figure 93: Simulated contamination plume from existing tailings dam after 10 years. 256
Figure 94: Simulated contamination plume from potential tailings dam after 10 years with contact zone activated included257
Figure 95: Simulated contamination plume from potential tailings dam after 10 years with contact zone activated included258

List of table

Table 1: Information concerning quaternary catchment	104
Table 2: Details on the Lithology and stratigraphy in the catchment.....	114
Table 3: Statistics of borehole depths and groundwater levels from GRIP	118
Table 4: Statistics of borehole depths and groundwater levels (hydrocensus)	130
Table 5: Slug test results and estimated yields	150
Table 6: Hydraulic conductivity estimated from slug test	154
Table 7: Tested geological features and pumping tests time summary.....	156
Table 8: Constant discharge tests with observation details.....	157
Table 9: Summary on constant discharge tests results	160
Table 10: Typical groundwater head responses (drawdown) to CDT in the catchment.	164
Table 11: Summary of lithology of boreholes with Type1 drawdown behaviour	165
Table 12: Inferred aquifer hydraulic parameters from CDT (Pumping boreholes).....	168
Table 13: Inferred aquifer hydraulic parameters from abstraction boreholes during CDT using the proposed new fractured fractal flow solution.....	169
Table 14: Inferred aquifer hydraulic parameters from observations boreholes during CDT	174
Table 15: Statistics of the major ions in the plaatreef groundwater system during the monitoring period.	182
Table 16: Descriptive statistics of the metal concentration detected in the flooded underground mine ground water during the monitoring; also shown in the table is the SANS-241 (2015) and WHO (2011) drinking water quality guidelines.....	196
Table 17: Summary on the aquifers storativity values	210
Table 18: Inferred statics and stochastic parameters from spatial conductivity	223
Table 19: Inferred statics and stochastic parameters from spatial Recharges	225
Table 20: Calculated errors for the calibrated model in MODFLOW	235
Table 21: Calculated errors for the calibrated model in FEFLOW.....	239
Table 22: Calculated errors for the calibrated model in SPRING	243
Table 23 Summary on the input for transport simulation	250

1 Introduction

The development activities of human communities coupled with the climate variability have shown some fatal impacts on different constituents of the earth's landscape. This has been put in the agenda of many leaders around the world; the problem of management (rational use and protection) of the available natural resources. Water resources constitute one of these natural resources, and have an important socio-economic value. This is supported by the first and fourth Dublin-Rio principles, which infers that water should be treated as an economic good, especially in its competing uses for development; and as social good in its uses to sustain life and the environment. The highest priority arising for water uses in Africa (Domestic use, Growing cities, Energy, Agriculture, Industry) as published by the "African Ministers' Council on Water" (AMCOW) 2012, confirm the social, and economical value of water for Africa. Agriculture, Community supply, and Industry (and Mine) are the three major uses of water on the continent.

Unlike other natural resources, natural water is a continuous flux involving the atmosphere, the surface and the subsurface, but has to be considered as a finite and vulnerable resource. Subsequently, the management of water resources should be approached as such. The availability, and the development of freshwater is of big concern, especially in Africa where more than 300 million people live in water scarce environments, and still need to have access to freshwater and decent sanitation (UNEP, 1999).

Thanks to advantages such as its quality, availability, spread, vulnerability, durability, and processing (operating), groundwater has gained interests in many countries in recent decades. Groundwater becomes the main source for water supply in arid and semi-arid regions, where surface sources are rare. This is similar for urban and industrial regions where surface sources are highly polluted. Groundwater forms one of largest sources (after water in glaciers) of fresh water available for man. In Africa, groundwater accounts only for 15% of the continent's total renewable water resources (AMCOW, 2012). Still, it is used by more than 75% of the African population as its main source of drinking water. A net progress of development of groundwater infrastructure was noticed, over the development of other water related infrastructures (AMCOW, 2012). However, groundwater resources have to be developed responsibly (to be protected and efficiently used) to avoid the long term deterioration of its quality and quantity

(sustainability). Out of 06 major aquifer systems identified in Africa, based on their respective lithological units (Zektser and Everett, 2004), 05 are formed in consolidated hard, fractured rocks which may have dual porosity properties to a variable degree of extent. They are named continental sandstone, carbonate, sandstone-carbonate (variable), and basaltic and crystalline basement aquifers.

In South Africa, there is a need for greater and more efficient use of groundwater resources, in order to meet the demand in the central and western regions of the country. A large part of these regions is underlain by the so called Karoo Super group of geological formations. Karoo constitutes more than 50 % of the country's geological formations as a whole. These formations are characterised by low permeable sandstones, mudstone, shale and siltstone; with a variability of structures that deviate considerably from that of the standard media commonly considered in geohydrology (Vivier, 1995). Such variability in structures is also observed in the crystalline basement (Granitic Plutons, Greenstone and Late Proterozoic sediments) of the country. These complex structures yield some complex aquifers with unpredictable behaviour. Lesser degree of structural variability is observed in the unconsolidated aquifers which are present in South Africa (Kalahari, Atlantis, Langebaan and the Zululand/Mozambique aquifers).

Most published literatures on advanced aquifer characterization in South Africa are associated with mine development. This may be explained by the role of permeable features (discontinuities) in the formation of ore deposits, and their economic exploitation. The mining industry is the base rock upon which the economy of South Africa is built. South Africa is known as the world's largest producer (Mineral Commodity Summaries_2015) of chrome, manganese, platinum, vanadium and vermiculite; and the second largest producer of ilmenite, palladium, rutile and zirconium. The country is also known as the largest coal exporter (Mineral Commodity Summaries). Open pit mine is the techniques used to exploit shallow ore bodies. Some open pits are quite deep like the Bingham Canyon mine (1.2 km deep) of Salt Lake City, Utah, US. Groundwater (and surface water as well) control (dewatering) and protection (remediation if contamination occur) are part of the significant issues faced during the different phases (design, construction, operation, decommissioning) of a mining project. One of biggest sources of limitations to the different methods that have been developed and improved by groundwater specialists to address such issues, is the non-homogenous distribution of

the hydraulic properties of the rocks, and its effect on the flow and associated solute transport properties.

The geohydrology specialist is usually asked to use the modelling tools (analytical and numerical) to predict (quantify) impacts associated with mining activities (pit dewatering; wells field development; contamination plumes; decant rate and quality, etc.). Very often, the specialist is asked to identify and use the best methods to solve the problem, based on available data. When the specialist has the freedom to design and implement additional data collection phase, time and/or cost usually constrain (qualitatively and quantitatively) the collection of data, often leading to incorrect model conceptualization. When dealing with heterogeneity, specialists require considering the nature and the scale of the problem to be solved to define the appropriate method and the model to build, which should dictate the data required at the data collection phase.

1.1 Research statement and objectives

This PhD thesis aims to contribute to the overall efforts that have been developed and still under development, for efficient management of groundwater related issues.

1.1.1 Research statement

Sustainable and efficient management of groundwater resources can only be assured provided the main hydraulic and associated mass transport parameters that characterise their behaviour are well known and their spatial variability well understood. Due to the lack of efficient methods that can assist in determining the geometry of the voids in an aquifer, standard empirical models have been developed to study the influence of assumed geometries (porous, double porosity, etc...) on the behaviour of the aquifer through defined relational (hydraulic) parameters (Bear, 1972) such as hydraulic conductivity and specific storativity.

Various investigations and studies in different regions on earth have shown that the standard interpretations (or mathematical descriptions) of the physical behaviour of aquifers do not reflect observations of natural systems. Most of the methods developed and improved by groundwater specialists to describe aquifer behaviours are often found limited and fail to describe flow and mass transport processes in complex geological environment. The assumptions under the standard descriptions and mainly the non-consideration of the real structure (geometry) of the aquifers are mentioned as part of the reasons the conventional models deviate from the observations. This difficulty becomes more challenging particularly in fractured environments where even percolation

theory (Berkowitz and Balberg, 1993) and/or the parallel plate model (De Marsily, 1986) fail to simulate the observed flow. Faybishenko and Benson (2000) clearly referred to the characterization of fractured rocks as the most challenging current problem faced by geohydrologist. Many efforts have been developed in the investigation of heterogeneous aquifer flow systems. However, quantifying and modelling of heterogeneous aquifers still challenge a majority of geohydrologists over the world in their respective geohydrological investigations.

Furthermore, natural systems are known to be characterized by complex geometry and non-homogenous (heterogeneous) flow at all scales. The extent of such heterogeneity differs according to the geologic environments and is related to the lithological units as well as the type of porosity (fractures, vugs, inter-crystalline, inter-particle, etc. Porous aquifers (alluvial) are generally characterized by low (1 to 2 orders of greatness (Sudicky, 1986; Hess et al., 1992)) and intermediate up to 5 orders of greatness (Rehfeldt et al., 1992) heterogeneity. Fractured aquifers showed generally more than 5 orders of greatness (Shapiro and Hsieh, 1998) heterogeneity.

Although legislations, regulations, and guidelines in South Africa, provide guidance and content of geohydrological investigations, mainly for legal compliance purpose (EA, WUL, etc...), provisions are not adequately made on the investigations methodologies. For instance, the way of dealing with heterogeneity, and the degree at which it has to be accounted for in modelling is often skyped. In addition, the limitations of the existing analytical/mathematical tools in simulating observed data from complex aquifers do not encourage most of the geohydrologists in accounting for heterogeneity in groundwater studies. Consequently to this lack of guidance/provisions and appropriate mathematical solutions, many inconsistencies are noticed between the different approaches followed in different groundwater modelling studies. It is critical to consider a minimum level of heterogeneity (discontinuity) in the models of groundwater flow. Commonly available geohydrological data in mining environments for instance, allow for this minimum level of heterogeneity to be accounted. This is especially valid, when considering the current progress in mathematical models (new differentiation tools) together with current level of computers' capacities (model/software).

The present thesis intends to demonstrate how new differentiation approach allows for suitable mathematical formulation can be used to predict groundwater level responses to pumping test in heterogamous aquifers. It is proposed to show a typical case study of characterizing and conceptualising of a crystalline rock aquifer. It also proposed to

assess the conditions under which certain geohydrological numerical softwares could (or not) be applied in typical fractured and heterogeneous aquifers, considering most commonly available data.

1.1.2 Research objectives

The main objective of the study is to quantify (groundwater flow properties) heterogeneities in aquifers, to provide novel and suitable analytical (mathematical) models in such quantification, and to investigate some of the current geohydrological numerical software for the modelling of such heterogeneities in aquifers. The present thesis proposes a comprehensive approach to assist in quantifying and modelling heterogeneity in aquifers, based on geological, and aquifer hydraulics information. It specifically aims to:

- Develop new analytical (mathematical) models for fractal fractured flow, and for double porosity fractal flow respectively;
- Assess (Field characterization and data analysis, Conceptual and Numerical models) heterogeneity in a typical South African crystalline rocks (Bushveld Complex) aquifer. In the case study, we intend to focus on:
 - *Geological and geophysical characterisation* which englobe (a) the use of geological and geophysical information in the qualitative conceptualization of heterogeneity in fractured rocks, and their incorporation in quantitative models; and (b) the combining uses of publically available 1: 50 000 geological maps with drilling, and surface geophysical survey (magnetic, and electromagnetic) information;
 - *Geohydrological characterization and conceptualization* including (a) commonly available hydraulic testing (slug, step drawdown, and constant discharge) to assess the groundwater flow complexities at the intersections of fractures zones (discontinues features); and (b) use of a proposed new fractal flow model to infer fractal hydraulic parameters;
 - *Hydro-geochemical characterisation using* the application of (bivariate) scatter plots, trilinear diagnostic plots, and PHREEQC hydro-geochemical model as complimentary tools to describe different hydro-geochemical processes.
 - *Geohydrological numerical modelling* which focuses on assessing the capabilities of some (03) trending geohydrological numerical software, in capturing the salient phenomenological behaviour observed in in a typical

crystalline rock aquifer in a mining environment. This also includes investigating geo-statistical tools, and discrete fractures approach in modelling.

Prior to developing on such specific objectives, a background of the problem under investigation is given in the form of:

- A description of the theories on variability of rocks hydraulic properties, and the implication of such variability to heterogeneous aquifers; and
- A review of the existing methods for quantifying and modelling heterogeneity in aquifers;

2 Theories and Literature Review

2.1 Spatial variability in rocks' hydraulic properties

In the subsurface, the intensity of the movement (flux) of water through a specific cross section area is generally assumed to be proportional to the gradient of the hydraulic head, obeying Darcy's law (1856):

$$q(x) = \frac{\gamma k}{\mu} \frac{\partial h(x)}{\partial x_i} \quad (1)$$

Where $q(x)$ is a flux vector; where γ is the unit weight of water; k is the rock intrinsic permeability, μ is dynamic viscosity, $\frac{\partial h(x)}{\partial x_i}$ represent the components of a vector gradient operator with $i \in [1, \dots, d]$ being the number of spatial dimensions; and $h(x)$ is hydraulic head. The term $\frac{\gamma k}{\mu}$ of the equation is equal to the well-known scalar hydraulic conductivity K .

The natural world is known as disordered, non-uniform and heterogeneous. Geology is ubiquitously heterogeneous, exhibiting both discrete and continuous spatial variations (horizontal and vertical) on a multiplicity of scales (Neuman and Di Federico, 2003). The same can be said for the rock's properties through different regions in the world, even if some similarities are often noticed. Such heterogeneities in rocks properties are related to many factors such as sedimentation processes, tectonics, diagenesis, the formations of crystalline rock, stresses.

The variability of the rock intrinsic permeability k (and hence the permeability K) ranges from pore scale to kilometers, and differ from one region to another. The extent to which heterogeneities occur, differs according to the geologic environment and is related to the lithological units and the type of porosity (fractures, vugs, inter-crystalline, inter-particle, etc.). Porous aquifers (alluvial) are generally characterized by low (1 to 2 orders of greatness (Sudicky, 1986; Hess et al., 1992)) and intermediate up to 5 orders of greatness (Rehfeldt et al., 1992)) heterogeneity, whereas fractured aquifers generally shows high (more than 5 orders of greatness (Shapiro and Hsieh, 1998)) heterogeneity.

2.2 Implication of rocks heterogeneities for spatial heterogeneity in the groundwater flow velocities

The combination of the Darcy's law with the physical law of conservation (Lavoisier, 1789) has led to the saturated flow equation without density gradient as described by Bear (1979):

$$S_0(x, t) \partial_t \Phi = \nabla \cdot [K(x, t) \nabla \Phi] + f(x, t) \quad (2)$$

Where: S_0 is the specific storativity; ∇ is the gradient operator; K is the hydraulic conductivity tensor of the aquifer; Φ is the piezometric head in function of space x and time t ; $f(x, t)$ is the strength of any sources (sinks) with x and t the usual spatial and time coordinates; ∇ is the gradient operator; ∂_t is the time derivative.

$$\partial_t \Phi = z + \int_{p_0}^p \frac{1}{\varphi g} dp \quad (3)$$

With: p is the pressure, p_0 is the pressure at a suitably chosen reference plane z_0 ; φ is the density of the water; g is the acceleration of gravity.

The above flow equation (2) is a partial differential equation that is constrained by:

- the distribution of the relational parameters S_0 and K ;
- the geometry of the flow;
- the forcing factors;
- the boundary conditions; and
- the initial conditions.

As for any mathematical partial differential equation, the main difficulty here is that, the equation can be used to predict the distribution (time and space) and the evolution of the hydraulic head, only if these associated constraining parameters and auxiliary conditions are well known. To overcome the difficulties associated with the unknown constraining conditions in groundwater sciences, for each specific physical system (aquifer), "conceptual models" can be built by simplifying the constraining parameters. The reductions of mathematical models to conceptual models allow the development of either analytical or numerical solutions that describe a particular flow or transport phenomenon.

The aquifer hydraulic test is used in Geohydrology to derive the combined influences of the different factors controlling flow in an aquifer, based on its pressure distribution. It is a technique to test the medium hydraulic properties and to track scaling effects, since the perturbation induced by pumping grows with time and samples increasingly large volumes (Le Borgne et al, 2004). Conventional (standard) interpretation of the test consists of inferring the hydraulic properties of the system from its measured responses by fitting curves, based on known or assumed integer (absolute) flow geometry (integer : 1, 2, and 3 dimensional) in homogenous, isotropic, infinite, and continuous domains. The assumed geometry approach, such as the Theis (1935) radial model and the Miller (1962) linear model among others, results in forcing the test data into the assumptions of the idealized model.

Different models accounting for the flow in fractured rock aquifers were developed to consider for the uncertainty of geometry (Black, 1994) by assuming single fractures (Gringarten et al, 1974; Gringarten and Ramey 1974; Cinco-Ley et al., 1978) or dual porosity (Barenblatt et al, 1960; Warren and Root, 1964; Kazemi., 1969) systems with homogenous distribution of fractures. Such solutions have given satisfaction in characterizing reservoirs (aquifers and petroleum), but become problematic for many formations deviating from the underlying assumptions, especially in heterogeneous (multi-layered and/or highly fractured) systems. For instance, radial and uniform flow may be expected in a single uniform fracture of infinite extent, or within a dense network of interconnected fractures confined in a plan, but not in a system where fractures are poorly connected and dead end fractures prevail. The flow in heterogeneous (fractured) medium may have a fractional (non-integer) dimension that depends on the orientation, connectivity and variability of size (aperture) of the voids. Simultaneous determination of the hydraulic parameters and the flow dimension may be more appropriate for the description of the physical behaviour of the aquifer, than the conventional forcing approach (assuming geometry).

Darcy's description of the fluids' flow through subsurface material accounts for macroscopic flow, and relate the flux to the hydraulic conductivity in a direct manner under a fixed gradient. But underground fluids' flow occurs at pore scale as accounted by the Navier-Stokes' equations, and is not directly related to the rock's hydraulic properties, since the vector gradient of the hydraulic head varies spatially. The structure of the groundwater flow is not only controlled by the rock's hydraulic properties but also

on hydraulic connection between materials of similar property (spatial correlation). The issue of connectivity has first been emphasized by Matheron (1967), Marsily (1985) and Fogg (1986), and is well addressed in the well-known stochastic theory. Numerical and experimental studies (Tsang and Neretnieks, 1998, Tiedeman and Hsieh, 2004) have proved that groundwater flow in heterogeneous media is structured through independent connected channels.

In primary porosities (either consolidated or not), variation in aquifer's material grain sizes and internal architecture, are the most important factors that control the structure of the flow (hence the probable aquifer's heterogeneity). At macro scale, the poor contrast between the hydraulic properties of the minor scale sediments units that compose the macro hydro-stratigraphic unit, allows a trend of homogenous behaviour. However, as shown by numerical and experimental studies (Anderson, 1989; Scheibe and Yabusaki, 1998; and Zappa et al., 2006), the flow lines and specially the associated solute transport through such environments are often concentrated in most permeable and connected sediment subunits. This phenomenon is often cited among the reasons of the failure of the diffusive models to accurately represent the field observations. The preferential paths (or channels) require special attention when the physical behaviour of the aquifer needs to be understood and simulated or predicted through accurate models, particularly in contaminants studies and small scale assessments.

In secondary porosities (consolidated fractures rocks), the contrasts between the hydraulic properties of the different units constituting the aquifers display a wide range (up to 10) of orders, that involves a variety of possible heterogeneous flow structures. In this context, the flow net is mainly controlled by the combined effects of connections between fractured networks, the distribution of the length, the aperture size, and the density of the fractures. Even if strong evidence is still needed to clarify the sensitivity of the flow to each of these factors, works done by Bour and Davy (1997), Aupepin et al (2001), Darcel (2002), and Rivard and Delay (2004) show these dependences. When the distribution in the size of the fractures shows a low range of variability, at a specific critical density, the connectivity is independent of the scale. However, with a wide range in fractures size distribution, the scale of the system is of big concern.

2.3 Implication for spatial heterogeneity in solutes transport

The spatial (3 Dimensions) variation in rock permeability (hydraulic conductivity) involve contrasts in flow velocities at fine (pores and subunits up to 2 cm) scales, and between

regions of different hydraulic properties. These contrasts have huge impact on motion (transfer time) of the solute in the subsurface, which is dominated by molecular diffusion and the distribution of the flow velocities in the system. As shown in laboratory experiments (Stöhr et al., 2003), when the contrast in the flow velocity distribution is insignificant (homogenous or quasi-homogenous), the temporal variations in the mean displacement $\langle x \rangle$ (relating the position of the peak of the concentration) of the plume and the corresponding spreading σ^2 (variance of travel distance) of a given plume, show linear behaviours with respective slopes $\langle V \rangle = \frac{\partial \langle x \rangle}{\partial t}$ (mean flow velocity) and "2D" (coefficient of dispersion). Such linear relations are the basics principles behind the diffusive equation that is often used to describe temporal and spatial distribution of plume concentration and known as "Advection-Dispersion Equation":

$$\frac{\partial C}{\partial t} = \frac{1}{2} \frac{\partial \sigma^2}{\partial t} \frac{\partial^2 C}{\partial x_i^2} - \frac{\partial \langle x \rangle}{\partial t} \frac{\partial C}{\partial x_i} \quad (4)$$

In such a diffusive model (Advection-Dispersion Equation), the travel distance of the plume concentration is assumed to have a Gaussian distribution at late time as it is frequently assumed for diffusion equations. There is however no strong physical reason explaining the Gaussian distribution in natural subsurface systems.

In natural systems, with insignificant contrasts in the spatial distribution of flow magnitudes, such diffusive model may describe the plume concentration, but not in cases of significant contrasts as usually encountered in the geologic media. Both laboratory (Levy and Berkowitz (2003) and field experiments (Peaudecerf and Saut, 1978; Sudicky et al., 1983; and Roberts et al., 1986) have demonstrated that the temporal variation in the spreading of the plume in heterogeneous media is not linear, and is relatively considerable than usually observed in homogenous media. Such experiments showed that the coefficients of dispersion $D = \frac{1}{2} \frac{\partial \sigma^2}{\partial t}$ vary according to the scale of observation (travel distance) in heterogeneous systems. This phenomenon is known as non-Fickian behaviour (Nueman and Di Federico., 2003). It generally depicts an asymmetric spatial distribution of the plume's concentration around a well-defined peak at any given time, and is associated with specific structure of the underground fluxes.

The tracing of such spatial distribution of plumes requires a meticulous design of field instrumentations (observation points) based on an acceptable knowledge of the flow pattern in the targeted aquifer. Common evidences of non-Fickian solute dispersions are given by the traditional temporal monitoring of the plume concentration at single observation point known as “breakthrough curve” (Becker and Shapiro, 2003) and is characterized by a relatively quick peak of concentration followed a long recovering phase. As part of his research on typical alluvial aquifer behaviour, Modreck Gomo (2011) demonstrated some aspects of non-Fickian behaviour in the Karoo.

Models have been developed (Tsang and Neretnieks., 1998) to infer non-unique solute transport parameters that describe such behaviour at single point (Sanchez-Vila and Carrera, 2004), but they cannot be used to describe the specific flow structure that control such behaviour.

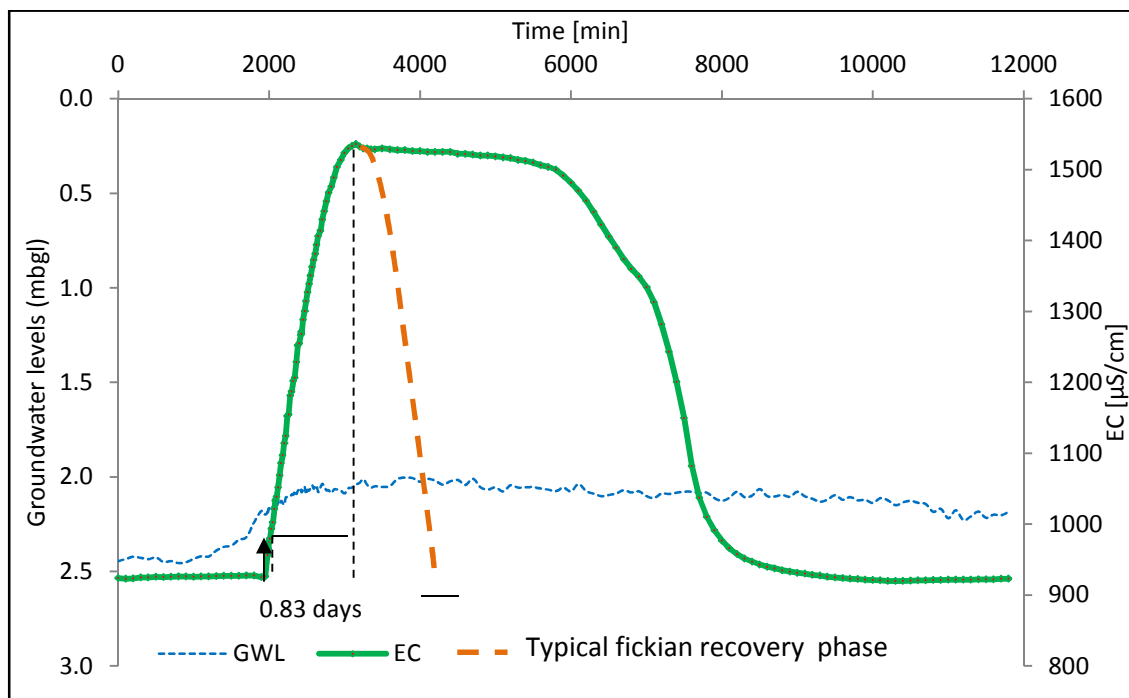


Figure 1: Typical salt solute tracer breakthrough curve compared to water levels during natural gradient tracer test in the Karoo, South Africa (adapted from Modreck Gomo, 2011)

2.4 Accounting for spatial heterogeneity in groundwater studies

The study of flow and transport processes in the subsurface involves the resolution of the governing hydraulic equations (using appropriate geometry, initial and boundary conditions of the system) and an acceptable description of the geology. The distribution of the geologic characteristics (properties) is the source of the challenging non-

homogenous conditions often faced by professionals and scientists, in different fields related to the earth subsurface. In groundwater sciences, the distribution of the hydraulic properties of the rocks, and its effect on the flow and associated solute transport properties are often in concerns. The focus here will not be, neither on the variety and classes of heterogeneity, the reasons of the geologic characteristics' variability, nor the different processes involved in flow and solute transport (dispersion, diffusion, sorption, precipitation, etc.) in the subsurface. It will rather be on available approaches and methods used to quantify heterogeneity, as well as model such processes.

Many approaches have been developed to deal with the occurrence of spatial heterogeneity in groundwater studies. Geological and geophysical methods used in groundwater exploration are based on the detection of underground global physical heterogeneities. These methods are helpful in locating anomalies which may be associated with water conducting layers and preferential path, to decide on well locations or discover springs.

The access to the subsurface for direct measurements of aquifers' properties (through aquifer pumping test) is limited to boreholes (percussion and core) and tunnels, which are not representative of the whole aquifer. This constrain makes it impossible to completely handle the variations in the organization of the flow and associated solute transport in the subsurface. Instead of completely accounting for such spatial variability, attempts have been made to use the limited direct measurements to come to models that could represent and predict the effect of underlying structures on the behaviour of the aquifers.

Hydraulic tests in boreholes have played a huge role in quantifying the subsurface flow, and they remain the most useful way to investigate the properties of the subsurface. During an aquifer hydraulic test, one or more known stresses (pumping or injection) are applied in a production borehole to the system being studied, and the responses of the system are measured in suitable placed observation boreholes.

The general mathematical model (Equation2) describing the flow of groundwater is a partial differential hydraulic equation in time and three-dimensional space governing the flow of groundwater in the saturated zone.

Although most mathematical models used in the world make use of analytical (simple) or numerical (complex) resources to solve the governing differential hydraulic equations; it is worthy to mention that the analytical element method (elaborate semi-analytical method), and the boundary integral method (combination of analytical and numerical methods), among others, can be used to solve such a governing differential equations. In the following review, we will however focus on the existing analytical and numerical means.

2.4.1 Spatial heterogeneity analytical modelling

Analytical models represent mathematically (Equation) exact solutions to the hydraulic equation for one/two dimensional flow problems by simplifying assumptions. Although they cannot handle spatial and temporal variability, analytical models are very useful tools, as they can be solved by hand or by simple computer programs (Flow Calculation, etc.). They provide rough approximations for many applications and they usually do not involve calibration to observed data. They can also suit most simple and low-complexity modelling studies.

2.4.1.1 The equivalent homogeneous properties (permeability and storativity) of an aquifer

Heterogeneities in groundwater flow structure were first handle by estimating “the equivalent homogenous properties” (Theis, 1935), or “equivalent uniform-properties stratum” (Morris Muskat, 1949). This was done by averaging local values (around wells) calculated with developed analytical solutions for either steady state (Thiem 1906), aquifers pumping (Theis, 1935), or injection tests. Inspired by work done by precursors (Cardwell and Parsons, 1945; Landau and Lifschitz, 1960) on the averaging of random variables, Matheron (1967) showed the usefulness of the geometric mean for the determination of an equivalent homogenous permeability from steady state tests for two-dimensional parallel flow. Meier et al (1999) demonstrated empirically that the geometric mean is the long-term average that a well test produces, in transient state tests.

Most of the present existing analytical solutions for the interpretation of field tests data are based on this concept. They are used to infer the transmissivity (assuming confining layers) of the aquifer. The calculated transmissivity is the product of the saturated thickness (D) of the aquifer and the equivalent hydraulic conductivity ($T = KD$) over the

thickness. If these solutions may represent the heterogeneity (by average) over the thickness (D), they fail to define the vertical distribution of conductivities over the thickness (D) and become problematic where saturated thickness varies like in unconfined layers (Neuman, 1973; Jacob, 1944).

2.4.1.2 Barker's Generalized Radial Flow model

The Generalized Radial Flow proposed by Barker (1988) model assumes a continuum in which drawdown evolves in flow dimension "n" ($n \in [1, 3]$ integer or not) during the transient test (pumping or injection). The continuum consists of a homogeneous and isotropic fractured system characterized by a hydraulic conductivity K and specific storage S_0 , in which the flow to the well is radial and n-dimensional. The dimensional flow here is seen as being dependent on the fracture connectivity rather than the aquifer dimensions and the fractional values of "n" describing the deviation (excess or lack) from perfect connections in integer values of n (Leveinen et al., 1998). The relationship between the cross-sectional area of flow and distance from the source is given by:

$$A(r) = b^{3-d} \frac{2\pi \frac{d}{2}}{\Gamma\left(\frac{d}{2}\right)} r^{d-1} \quad (5)$$

Where: $A(r)$ is the cross-sectional area of flow (unit area), r is the radial distance from the borehole (unit length), b is the extent of the flow zone (unit length), d is the flow dimension, and $\Gamma(\)$ is the gamma function (Davis, 1959). The gamma function has many alternatives definitions exist in the literature. This function is mainly defined as the integral $\Gamma(z) = \int_0^{\infty} x^{z-1} e^{-x} dx$ for all positive real part of the complex number z ($\text{Re}(z) > 0$).

The flow dimension d is related to the power-law relationship between flow area and radial distance from the borehole. The flow dimension is defined as the power of variation plus one, as follows:

$$n(r) = \frac{d \log A}{d \log r} + 1 \quad (6)$$

The relationship between cross-sectional area of flow and distance from the source leads to the following general flow governing equation:

$$s_0 \partial_t h(r, t) = \frac{K}{r^{d-1}} \partial_r \left[r^{d-1} \partial_r h(r, t) \right] \quad (7)$$

With: $h(r, t)$ the change in hydraulic head from $h(r, 0)$. Equation (7) is valid for a constant-rate condition and for specific initial and boundary conditions such as:

$$\left\{ \begin{array}{l} h(r, 0) = 0; \\ \lim_{r \rightarrow \infty} h(r, t) = 0; \\ Q = \frac{2\pi^{\frac{d}{2}}}{\Gamma\left(\frac{d}{2}\right)} r_w^{d-1} K b^{3-d} \partial_r h(r_w, t); \end{array} \right. \quad (8)$$

Equation (7) with the initial and boundary conditions described in Equation (8), represent a complete set of equations for which solutions exist (De Marsily, 1986; Yeh (1987); Kruseman and the De Ridder, 1991; Cloot and Botha, 2006; Atangana, 2010).

A generalized solution for this parabolic diffusive problem has been proposed by Barker (1988) by Laplace transform, using Theis (1935) assumptions. This solution called the generalized flow equation is expressed in term of drawdown (change of head from an initial hydraulic head) and is an inversion to a gamma function described as follow:

$$h(r, t) = \frac{Q r^{2-d}}{4\pi^{\frac{d}{2}} K b^{3-d}} \Gamma\left(\frac{d}{2} - 1, \frac{r^2 s_0}{4Kt}\right) \quad (9)$$

Where: Q is the discharge rate, b is the extent of the flow.

The baker solution provides estimates of Kb^{3-d} and s_0b^{3-d} and the hydraulic parameters K and S_0 can only be determined, if the parameter b is known. However, for non-integer values of n , b has no physical meaning.

By specifying an initial flow area $A(r_w)$ at the test zone, Roberts and Beauheim (2001), consider a constant b (9)

(9, as:

$$b = \left[\frac{A(r_w) \Gamma\left(\frac{d}{2}\right)}{r_w^{d-1} 2\pi^{\frac{d}{2}}} \right]^{\frac{1}{3-n}} \quad (10)$$

Based on this constant value of b , they gave an extension of equation as:

$$A(r) = A(r_w) \left(\frac{r}{r_w} \right)^{d-1} \quad (11)$$

The specific relationship between cross-sectional area of flow and distance from a specified source area proposed by Roberts and Beauheim (2001), extends the capability of the Baker solution to the diagnostic of boundary conditions (no flow and constant pressure) which are considered in the variation of the flow dimension in space. They demonstrated that the flow-dimension function $n(r)$ for a case with a no-flow boundary varies from a value of 2 to -1. The negative flow dimension means decreases in flow area due to the boundary.

The "flow dimension" as defined in the Barker (1988) solution, may be seen as a lumped parameter reflecting the effects of flow geometry and combination of hydraulic properties (K and S_0). As observed by Doe (1991), a constant flow-area system with varying hydraulic properties ($K(r)$ and $S_0(r)$) and homogeneous system with varying flow area ($n(r)$) may yield the similar hydraulic responses. The flow dimension may also be considered in function of the radius r as (Roberts and Beauheim. 2001):

$$n(r) = \frac{d \log\left(\frac{K}{A}\right)}{d \log(r)} + 1 \quad (12)$$

The concept of variable flow dimensions, introduced in the description of complex flow regimes is not limited by the assumption that all flow is radial until a boundary is encountered at some distance. This makes it easier to be applied to:

- complex flow geometries or variable properties or any combination of the two, by using simple transformation of $n(r)$;
- to transient flow-rate (constant-pressure) data as well as transient pressure data.;

The variable flow dimension approach allows the combined effects of unknown flow geometry and variable properties of the aquifer to be described in terms of a single parameter. These are significant advantages over more traditional approaches.

2.4.1.3 Fractal reservoir model (FRM)

As seen above, the Baker FR model introduced a lumped flow dimension parameter that account for the conductance, but may have only a qualitative character, since there is no physical meaning that can be associated with it. Using the physical theories on diffusion slow-down in disordered systems developed by O'Shaughnessy and Procaccia (1985) and Halvin and Ben-Avraham (1987); Chang and Yortsos (1990) proposed an analytical model that consider a fractal dimension "D" (geometry related) and a transport or hydraulic diffusion (Bernard et al., 2006) exponent θ which is not directly linked to the flow geometry but to the connectivity of the voids. The model is called fractal reservoir model (FR-Model) and apply for hydraulic responses of fractal characters in fractured networks created by natural processes like percolation and fracturing (Chang and Yortsos, 1990; Chang et al, 2011). In a fractal structure, parameters such as mass $M(r)$, or density $\varphi(r)$, decrease as by a power law (similar to Barker's varying flowing area) when an increasingly larger region is measured. For a fractal with mass fractal dimension "D" embedded in a Euclidean embedding dimension "d", the density $\varphi(r)$ function is given by:

$$\varphi(r) = \frac{M(r)}{A(r)} ; (D < d, d = \{1, 2, 3\}) \quad (13)$$

Where: $M(r) \propto ar^D$ is the mass or volume the fracture contained within the radius r and area $A(r) \propto ar^d$; and describes the relation between the density $\phi(r)$ and a considered radius r in a perfect fractal system with infinite size may be expressed as:

$$\phi(r) \propto r^{D-d} \quad (14)$$

But in a finite size system, for instance in fractured environments, this relation may not hold, even if the average over many origins is expected to give the same power law (Mandelbrot, 1983; Orbach, 1986; Feder., 1988).

In the case of impermeable fractured rock, the mass density at any given radius r corresponds to the macroscopic porosity (total void volume divided by the total volume) at that radius r . Unlike the Euclidean case where the porosity remains constant with respect to r , the macroscopic porosity $\phi(r)$ in a perfect fractal system therefore decreases in a power law manner with respect to r :

$$\phi(r) = \phi_0 \left(\frac{r}{r_0} \right)^{D-d} \quad (15)$$

Where: ϕ_0 is the macroscopic porosity at $r = r_0$ and r_0 is the smallest fracture block size above which the object is fractal (the lower cut-off scale). The porosity ϕ is linearly related to the specific storage as (Kruseman and the De Ridder, 1991):

$$S_0 = -\phi g \left(\frac{dV_T}{V_T d\sigma_e} + \phi \frac{dV_w}{V_w dp} \right) \quad (16)$$

Where: S_0 is the specific storage, as defined earlier; dV_T is the total volume of a given mass of material, $d\sigma_e$ is the change in effective stress, dp is a change in the water pressure, dV_w is the change in the volume of water of a given mass of water.

The change in the mass density with respect to "r" is used to describe the change in the ability of the mass to conduit fluid water flow through a fractured network (Conductivity K_f) with respect to r as follow (Sahimi and Yortsos., 1990):

$$K_f(r) = K_0 \left(\frac{r}{r_0} \right)^{D-d-\theta} \quad (17)$$

Where: θ is the hydraulic diffusion exponent and is related connectivity of the voids; K_0 is the macroscopic conductivity (for forced fluid flow) at $r=r_0$. The exponent θ rules the evolution of the main parameter (hydraulic diffusivity) that controls the fluid flow occurring in the fractal medium when the size of the latter increases.

The power law relationships between the changes in the macroscopic conductivity and specific storage, leads to a variation of hydraulic diffusion (K/S_0) with respect to a radial distance from a given pumping borehole. The general diffusion equation is as followed (Orbach, 1986):

$$r^2(t) = D(r)t \quad (18)$$

Where $D(r)$ is the length dependent diffusion constant (or coefficient); $\langle r^2(t) \rangle$ is the mean square distance that an ant moves in time t . Gefen et al (1973) showed that the mean square distance that an ant moves in time t along a fractal network could be mapped onto the diffusion problem in Euclidean space as:

$$r^2(t) \propto r^{2-d_w}, r \leq \xi_p \quad (19)$$

Where: d_w is the dimension of the random walk ($d_w = 2 + \theta$); ξ_p is an upper cutoff length which exists for percolating networks. Considering this mean square distance expression into the general diffusion equation, leads to the following scaling relationship that describes the diffusion slowdown in fractal networks (Halvin and Ben-Avraham, 1987):

$$r^2(t) \propto t^{\frac{2}{d_w}} \quad (20)$$

Note that when $d_w = 2$ ($\theta = 0$) equation (20) will be similar to the familiar normal diffusion equation $\langle r^2(t) \rangle \propto t$ in Euclidian space (1, 2, 3).

By inserting (16) and (17) in the general flow equation (7) leads to the generalized radial flow equation in a fractal network with a Euclidean dimension d and which is characterized by the four parameters: K_0 , S_0 , D and θ (O'Shaughnessy and Procaccia, 1985; Chang and Yortsos, 1990; Tanguy Le Borgne., 2004).

$$s_0 \partial_t h(r, t) = \frac{K}{r^{D-1}} \partial_r \left[r^{D-1-\theta} \partial_r h(r, t) \right] \quad (21)$$

Acuna and Yortsos (1990, 1995) used a simplification of the Green function approach at late time to propose a solution for the transient pressure responses in fractal networks:

$$P(r, t) = \frac{r^{(2+\theta)(1-\delta)}}{(2+\theta)\Gamma(\delta)} \Gamma\left(\delta-1, \frac{r^{2+\theta}}{(2+\theta)^2 t}\right) \quad (22)$$

Where: $P(r, t)$ is pressure drop at distance r and time t ; $\Gamma(x)$ is the Gamma function, and $\Gamma(x, y)$ is the incomplete Gamma function; $\delta = D/(2 + \theta)$ or $\delta = d_s/2$ with d_s the spectral dimension (Mandelbrot, 1983). Acuna and Yortsos (1995) approximated (22) to the first two terms of the series expansion for the drawdown response at the pumping borehole at short time as follow:

$$P(r, t) = \frac{\Gamma(\delta-1)r_w^{(2+\theta)(1-\delta)}}{(2+\theta)\Gamma(\delta)} + \frac{(2+\theta)^{1-2\delta}}{(1-\delta)\Gamma(\delta)} t^{1-\delta} \quad (23)$$

They showed that the plot of log of the derivative versus log of time gives a slope $s = 1 - \delta$, and the behaviour of (23) is controlled by δ . When $\delta < 1$, the fractal dimension $D < 2$ and the behaviour of flow is expected between linear and radial. When $\delta > 1$, the fractal dimension $D > 2$, and the flow behaviour is expected between radial and spherical. When $\delta = 1$, the traditional exponential integral solution arises.

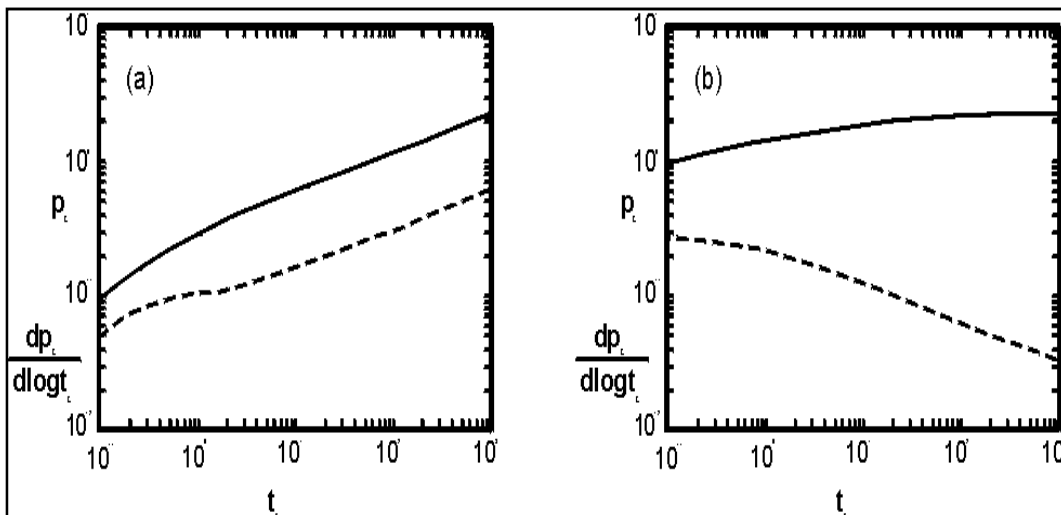


Figure 2: Characteristic fractal pressure transient behaviour in the abstraction borehole for a) $\delta < 1$ and b) $\delta > 1$ (from Acuna and Yortsos, 1995).

Bernard et al data inversion approach identifying fractal characteristics

Bernard et al (2006) developed an analytical logarithmic model (solution) to hydraulic interference tests in fractal media is developed in dimensional variables, which allows for a very rapid and unique fitting to data. The solution was developed by a logarithmic approximation of the well-known Cooper–Jacob expression (1946).

$$\Delta P(r, t) = \frac{Q\mu}{4\pi K_f e} \ln \left(\frac{2.25}{r^2} \frac{K_f}{\mu\phi_f C_f} t \right)$$

Where, Q is the constant pumping rate at the well; e the reservoir thickness; C_f is the fluid or composite compressibility; ϕ_f is the fracture porosity of the elementary volume (i.e., the ratio open fracture volume/total volume), K_f is the fracture permeability.

By considering the relation between space and time coordinates ($T \propto L^{2+\theta}$), the time-space coordinates relationship was derived from the expression of the scaling of the hydraulic diffusivity ($D_H = \frac{K_f}{\mu\phi_f C_f} \propto r^{-\theta}$) of dimension $[L^2 T^{-1}]$, in a fractal medium.

They expressed the analytical solution as follow:

$$K_f(t) = K_0 t^{-\alpha}, \alpha = \frac{d - D + \theta}{2 + \theta}, \phi_f(t) = \phi_0 t^{-\gamma}, \gamma = \frac{d - D}{2 + \theta}$$

$$\Delta P(r, t) = \frac{Q\mu}{4\pi K_0 e} t^\alpha \ln \left(\frac{2.25}{r^2} \frac{K_0}{\mu\phi_0 C_f} t^{1-\alpha+\gamma} \right) \quad (24)$$

Please note that this analytical solution is characterized by four parameters: K_0 , ϕ_0 , the fractal dimension D , and the hydraulic diffusion scaling exponent θ .

2.4.2 Spatial heterogeneity numerical modelling

Numerical models offer more precise ways to deal with heterogeneities in groundwater studies, since they permit to vary the constraining relational parameters in space and time, and adapt the auxiliary conditions of the conceptual model to the geometry of the system. The continuous differential terms in the governing groundwater flow equation is

replaced by finite quantities, resulting in multiples of algebraic equations that are solved by computational power of a computer by matrix arithmetic. The computer programme that contains algorithms to solve numerically the mathematical model is named the modelling code. To facilitate the data input, flow simulation and results output, most computer modelling codes run a graphical user interface (GUI), based on the Microsoft Windows system. Nowadays, most modelling codes also have a GUI for the pre- and post-processing of modelling data.

2.4.2.1 Calibrated (Inverse) numerical modelling

A common way that is used to account numerically for the variation of aquifers properties (mainly hydraulic), is to assign local (averaged) variables (mainly permeability or transmissivity) values estimated from wells test analyses, to the mesh hosting the respective wells. Since there are more meshes in the grid of the numerical model than estimated local values, the estimated variables are then interpolated (zoning, polynomial tern fitting, and hand-contouring, etc.) in space between adjacent wells. The generated (by interpolation) distribution of the hydraulics parameters generally fails to calculate observed heads and flow rates, and requires calibration (trial and error, automatic inverse procedures).

As mentioned for analytical modelling, the important point here is that the problem is solved inversely for the constraining relational parameters given specific observations and auxiliary conditions (initial and boundaries) of behaviour of the aquifer instead to be solved for the observations giving appropriate constraining parameters (Forward modelling). Thus, the fact that the inferring heterogeneity map satisfies a given observations (hydraulic head), does not mean they define the real parameter values and their distribution as well as their spatial correlation. An infinite number of inverse solutions may be inferred from such an approach. Even if techniques such zoning, regularity, algorithmic unicity have been developed to control the range of "inferred heterogeneities" (Marsily et al., 1992); the application of calibrated approaches remain problematic when dealing with heterogeneous features such as low permeability barriers, high permeability channels, and faults. This failure of the inverse inference approach is evident, primarily when the calibration is based on the head data alone. As a result, it is recommended to use both head and concentration data (e.g. environmental tracers or contaminants) in the calibration.

2.4.2.2 Continuous geostatistical methods

Dealing with spatial heterogeneities (low permeability barriers, high permeability channels, faults, etc.) in the subsurface requires devotion to the rock structure, facies and properties. Initially developed to treat problems that arises when applying conventional statistical to approximate changes in ore grade within a mine (Matheron, 1963, 1965), geostatistics tools have been introduced in geohydrological sciences by precursor such as Delhomme (1976, 1978, 1979), Freeze (1975), Gelhar (1976), and Dagan (1985, 1989), among others, to describe heterogeneities by using the concept of "regionalised variables". Geostatistic concepts consider that geological processes involved in the creation of the medium have imposed a "structure" (in a statistical sense) on the spatial distribution of the inhomogeneous parameters values. The structure is assumed to be represented by the spatial statistics for different lags (separations between two spatial locations) and is used as a tool to characterize the heterogeneity.

The first step of a geostatistical analysis is the deduction of this structure by calculating the spatial statistics from the available data. Three functions (covariance, correlation, and semi-variance) are usually used on lagged variables (aperture, porosity, permeability, etc.) in geostatistic analysis for this purpose, and are defined as:

$$C(h) = \frac{1}{N(h)} \sum_{i=1}^{N(h)} H(v_i)H(v_i + h) - (z_0 z_h) \quad (25)$$

$$z_0 = \frac{1}{N(h)} \sum_{i=1}^{N(h)} H(v_i) \quad (26)$$

$$z_h = \frac{1}{N(h)} \sum_{i=1}^{N(h)} H(v_i + h) \quad (27)$$

$$\rho(h) = \frac{C(h)}{\sqrt{\sigma_0 \sigma_h}}$$

$$\sigma_0 = \frac{1}{N(h)} \sum_{i=1}^{N(h)} [H(v_i) - z_0]^2 \quad (28)$$

$$\sigma_h = \frac{1}{N(h)} \sum_{i=1}^{N(h)} [H(v_i + h) - z_h]^2 \quad (29)$$

$$\gamma(h) = \frac{1}{2N(h)} \sum_{i=1}^{N(h)} [H(v_i + h) - H(v_i)]^2 \quad (30)$$

Considering v as the vector of horizontal spatial coordinates, $H(v)$ as the variable under consideration as a function of spatial location (porosity in this example) referred also as the “tail of lag vector”, h as the lag vector (directional distance) representing separation between two spatial locations $H(v + h)$ as the lagged version of variable under consideration referred also as the “head of lag vector”, and $N(h)$ as the number of pairs separated by lag h (plus or minus the lag tolerance).

The semi-variance is a measure of the degree of the spatial dependence between observations along a specific support (data points).

The variogram has two major components: (1) the range, which is proportional to the average size of heterogeneous bodies; and (2) the sill describing the magnitude of the changes of a given variable (e.g., in permeability) from one heterogeneous body to another.

The use of spatial statistics of measured values within a region to generate a heterogeneity map in the region, offers some advantages that help for a better description of continuous parameter fields, and therefore allows better numerical predictions than previous existing models. In comparison to the previous approaches (zoning, etc.), Chiles and Delfiner (1999) among others showed that geostatistic tools like Kriging and co-Kriging minimizes the variance of the estimation error, and can combine well-test results to additional measurements (specific capacity, electrical resistivity, and others) to generate better continuous heterogeneity (permeability) maps. These tools also allow, addressing the issue of “support”, which concerns the size of the domain on which a measurement is made. The “regionalize variables” approach has also been used in the constriction of inverse calibration procedure, for inferring spatial distribution of parameter values (Lavenue et al. 1995; Lavenue and Marsily 2001). Delhomme (1979), Lavenue et al (1995), and Zimmerman et al (1998), among others have used the Geostatistical approach and Monte-Carlo flow simulations

(conditional realizations) to study the sensitivity of flow and transport to the spatial heterogeneity of aquifers systems, and to perform resulting uncertainty analysis.

2.4.2.3 Stochastic Methods

The stochastic approach considers heterogeneous conductive and discontinuous objects or set of objects (flow units or facies) with different shapes and properties, embedded in continuous matrix (shale matrix, or other types of material structures). The shapes of the different objects are left to the decision of the modeller, but the sizes of the boxes and the positions of their centres are drawn randomly from a prescribed statistics that are estimated from available data, such as borehole logs, outcrop mapping, seismic surveys, etc. (Haldorsen and Damsleth, 1990). The properties (permeability, porosity, etc.) are then assigned to each facies (flow units) either by one specific set of parameters (direct relation), or by a random sampling of parameter values (distribution function, covariance). This approach deals with subsurface heterogeneity by focusing first on the geometries (shape, size, and position) of the conductive "objects", and the way such objects are hydraulically connected. The importance of the connectivity issue in the description of natural processes in the subsurface has been addressed by precursors (Matheron, 1967; and Marsily (1985) among others). The stochastic approach is very useful in handling the lack of connectivity and abrupt changes that happens in nature. This is the main advantage over the continuous Geostatistics tools which may only handle soft transitions in space. The usefulness of stochastic modelling in hydrogeology has been demonstrated by many authors (Marsily 1985; Cacas et al. 1990a, b; Billaux 1990; and Pozdniakov and Tsang 2004 among others). In the models developed by Marsily (1985), Cacas et al., (1990a, b), and Billaux (1990), the objects (flow units) were discrete fractured networks. These models used the concept of fracture connectivity (or percolation threshold) to describe the behaviour of fractures networks systems. However, the application of these Boolean tools requires issues such as the delineation and the characterization of the discontinuous facies, and the dynamic nature of flow channels to be addressed.

Surface (outcrops) and subsurface (Electromagnetic, radar and seismic tomography) data collected with available geological and geophysical tools tends to decrease as the scale of the heterogeneities goes down. Such data may provide information about densities and orientation, but fail to provide information about shapes and mainly fracture apertures in the real aquifer. Carlsson and Gidlund (1983) have shown that

fracture densities collected from surface outcrops are generally smaller than that collected boreholes (percussion and core). Correlation of such densities between boreholes is also difficult (Nueman, 2005). Attempts have been made to infer apparent fracture apertures from aquifer Hydraulics (or pneumatic) and tracer tests, but such apparent aperture may not be representative of potential highly variables apertures in the interior of each fracture (Lee et al., 2003; Konzuk and Kueper 2004). The stochastically generated facies (sand lenses, fractures, etc.) do not always occupy the exact positions of the observed ones (Lantuejoul 1997, a and b, 2002).

3 Modelling groundwater fractal flow with fractional differentiation via Mittag-Leffler law

Many solutions have been proposed and used to infer aquifer flow properties from pumping test (De Marsily, 1986; Yeh (1987); Kruseman and the De Ridder, 1991; Clout and Botha, 2006; Atangana, 2010). Some of them have been reviewed in previous sections (2.4.1.2 and 2.4.1.3), including the Barker generalised flow solution (Barker, 1998), and the Fractal flow solution model (Chang and Yortsos, 1990). The model of fractal flow has attracted attention of many researchers across the globe (O'Shaughnessy and Procaccia, 1985; Halvin and Ben-Avraham, 1987; Chang and Yortsos, 1990; Bernard et al., 2006). Acuna and Yortsos (1990, 1995) presented an analysis the model proposed by Chang with slight modifications. Many other researchers studied the last version and numerous research papers were published in some reputable journals of groundwater. Indeed these mathematical models are supposed to represent the physical problem observed in the real world problem but when comparing the observed facts to the mathematical equations there is no good agreement. To address this limitation, Sarah et al suggested a new model based on the fractional differentiation in 2015. In their work, the time derivative was replaced by the time fraction Caputo derivative. Although the model based on the fractional differentiation appears to be the most suitable one, there still some outstanding problems.

First the fractional derivative used in the last model is based on the power law $X^{-\alpha}$, which has a singularity at the origin. Thus the prediction around any given fractures will be unrealistic. Apart from this, it seems unrealistic to describe the fractal effect only by introducing r^{d-1} and called of the fractal dimension. One can find in the recent literature (Qiuming Cheng, 2016), fractal differentiation which has been employed in many other research problems to model fractal effect in some dynamical system. However, in the present work we will make use of the recently introduced a new approach of differentiation by Atangana and Baleanu (2016). The fractional differentiation based upon a non-singular and non-local Kernel known as the generalized Mittag-Leffler fraction was introduced in the literature to improve the limitations posed by the power law. In addition, the generalized Mittag-Leffler function induced the effect of memory, which is very important in groundwater flow studies. In essence, it is important for a drop of water to remember its trajectory with the fractures network.

One can notice that the medium via which this movement of water is taking place is very complex and request a very complex mathematical model that could take into account the: (a) viscosity, (b) elasticity, and (c) visco-elasticity. More importantly, experimental confirmation suggests that when a dissolved solid or a drop of water comes in contact with the matrix of a porous medium it may (a) pass through the medium with no apparent effect, (b) be absorbed by the porous matrix, and (c) react with the porous matrix. In case of the movement of dissolved solids, they encounter in porous flow are, for this reason, often classified as conservative, non-conservative, and reactive tracers. This behaviour implies that the quantity of dissolved solids in a porous medium depends not only on the flow pattern but also on the nature of the porous matrix and the solution. These situations (a), (b), and (c) can be characterized efficiently by the time-nonlocal differentiation than the local differentiation. Excellent literature regarding the advantages of using the concept of fractional calculus rather than the local calculus in groundwater flow problem can also be found in the following works (Benson et al., 2000; Cushman and Ginn, 2000; Wheatcraft and Tyler, 1998; Benson et al., 2001). The local calculus could be used only when we have a homogeneous system which is impossible to find in real world problem. We should recall that the concept of local differentiation was introduced to express the rate of change between two given points, however the dynamic system taking place between these two points are not included or taken into account while modelling real world problems. One can notice that the concept of fractional differentiation is based on the convolution concept, and has the ability to describe the dynamic between the two points. In this work, we shall put forward a concept of differentiation, which allows a physically correct generalization of movement of water as fractal flow. A more important fact is that researchers have established a clear relationship between the concept of fractal and fractional calculus (Tatom, 1975), and therefore it is more suitable to express the fractal behaviour observed in Groundwater with the concept of fractional calculus.

Thus in order to accurately replicate the observed facts into mathematical equation (21), we make use of the Atangana and Baleanu differentiation approach (2016) and the following equation is proposed,

$$s_0 {}^{ABC}D_t^\alpha h(r,t) = \frac{K}{r^{D-1}} \partial_r \left[r^{D-1-\theta} \partial_r h(r,t) \right] \quad (31)$$

$${}^{ABC}D_t^\alpha h(r,t) = \frac{AB(\alpha)}{1-\alpha} \int_0^t \partial_r \left[h(r,x) \right] E_\alpha \left[\frac{-\alpha}{1-\alpha} (t-x)^\alpha \right] dx \quad (32)$$

${}^{ABC}D_t^\alpha h(r,t)$ is considered here as a fading time memory. ABC has the same properties as in Caputo and Fabrizio (2015) case.

And d in (31) and (32) is still considered as fractal dimension. The initial conditions are the same as in previous studies in order to accommodate readers who are aware of this new finding. We present this new finding in the next section.

3.1 New Fractional differentiation with Mittag-Leffler Law

Definition1: Let f be a function $f \in H'(a,b)$, $b > a$, $\alpha \in [0,1]$ then, Atangana-Baleanu fractional derivative in Caputo sense is given as:

$${}^{ABC}D_t^\alpha \left[f(t) \right] = \frac{AB(\alpha)}{1-\alpha} \int_a^t f'(x) E_\alpha \left[-\frac{(t-x)^\alpha}{1-\alpha} \right] dx \quad (33)$$

Where: AB is a function with the following properties $AB(0) = AB(1) = 1$; $E_\alpha(t^\alpha)$ is the generalized Mittag-Leffler function defined as:

$$E_\alpha(t^\alpha) = \sum_{j=0}^{\infty} \frac{t^{\alpha j}}{j! \Gamma(\alpha j + 1)} \quad (34)$$

Definition2: Let f be a function $f \in H'(a,b)$, $b > a$, $\alpha \in [0,1]$ and not necessary differentiable then the Atangana-Baleanu fractional derivative in Riemann-Liouville sense is given as:

$${}^{ABR}D_t^\alpha (f(t)) = \frac{AB(A)}{1-\alpha} \frac{d}{dt} \int_0^t f(x) E_\alpha \left[\frac{-\alpha}{1-\alpha} (t-\tau)^\alpha \right] dx \quad (35)$$

Definition3: The fractional integral associate to the new fractional integral derivative with non-local Kernel is defined as:

$${}^{AB}I_t^\alpha = \{f(t)\} = \frac{1-\alpha}{AB(\alpha)} f(t) + \frac{\alpha}{AB(\alpha)\Gamma(\alpha)} \int_a^t f(y)(t-y)^{\alpha-1} dy \quad (36)$$

The authors noted that when $\alpha = 1$ they obtained the classical integral, while when $\alpha = 0$ they recover the function.

We present also some connection of the new derivatives with integral transform. In this work L will be denoted as Laplace transforms thus the Laplace transform of Atangana-Baleanu fractional derivative in Caputo sense is given as:

$$L\left({}^{ABR}D_t^\alpha (f(t))\right) = \frac{AB(\alpha) P^\alpha L(f(t))(P) - P^{\alpha-1} f(0)}{1-\alpha \left(P^\alpha + \frac{\alpha}{1-\alpha}\right)} \quad (37)$$

And the Laplace transform of Atangana-Baleanu fractional derivative in Riemann-Liouville sense is given as:

$$L\left({}^{ABR}D_t^\alpha (f(t))\right) = \frac{AB(\alpha) P^\alpha L(f(t))(P)}{1-\alpha \left(P^\alpha + \frac{\alpha}{1-\alpha}\right)} \quad (38)$$

Theorem1: Let $f \in H'(a, b)$, $b > a$, such that Atangana-Baleanu fractional derivative exists then the following relations are obtained:

$${}^{AB}I_t^\alpha \left\{ {}^{ABC}D_t^\alpha (f(t)) \right\} = f(t) - f(0)$$

$${}^{ABC}D_t^\alpha = \left[{}^{AB}I_t^\alpha f(t) \right] = f(t)$$

Also,

$${}^{AB}I_t^\alpha = \left[{}^{ABC}D_t^\alpha f(t) \right] = f(t)$$

$${}^{ABC}D_t^\alpha \left[{}^{AB}I_t^\alpha f(t) \right] = f(t)$$

The proof of these properties can be found in (Badr, 2016), and is not the focus of the present thesis.

3.2 Existing of positive solution

One of the most important facts in modelling is to show that the model suggested has a positive solution. The study of existence of positive solutions of a given nonlinear equation has attracted the attention of many researchers in the field of differential equations. The proof enables us to know whether or not the model is valid. In this subsection, we present the analysis of new model using the concept of fixed point theorem. To do this we present some preliminaries.

It is demonstrated in (Koca, 2015; Gomez-Aguilar et al., 2016) that if y is the solution of:

$${}^{ABC}D_t^\alpha y(t) = f(t, y(t)) \quad (39)$$

Then y is also solution of the following integral equation:

$$y(t) - y(0) = \frac{1-\alpha}{AB(\alpha)} f(t, y(t)) + \frac{\alpha}{AB(\alpha)\Gamma(\alpha)} \int_0^t (t-x)^{\alpha-1} f(x, y(x)) dx \quad (40)$$

Here we consider the following function:

$$f(r, t, h(r, t)) = \frac{K}{r^{d-1}} \partial_r \left[r^{d-1-\theta} \partial_r (r, t) \right] \quad (41)$$

We assume that we can find $M > 0$ Such that $\|f(r, t, h(r, t))\| < M$

According to the physical problem under study we can find a positive constant H such that $\forall (x, t) \in [a, b] * [0, T], |h(r, t)|$.

Lemma 1: The mapping $G: H_1 \rightarrow H_1$ defined as:

$$Th(r, t) = \frac{1-\alpha}{AB(\alpha)} f(r, t, h(r, t)) + \frac{\alpha}{AB(\alpha)\Gamma(\alpha)} \int_0^t (t-x)^{\alpha-1} f(r, x, h(r, x)) dx. \quad (42)$$

is completely continuous.

Lemma2: Let NCH_1 be bounded. Assume that there exists $l > 0$ such that,

$$|h(r, t_1) - h(r, t_2)| < l |t_1 - t_2| \forall h \in N,$$

Then, $\overline{T(N)}$ is compact.

Proof: Let $f = \max \left\{ \frac{1-\alpha}{AB(\alpha)} f(r, t, h(r, t)) \right\}$ for $0 \leq h \leq M$ for $h \in N$

The following inequality can be evaluated:

$$\begin{aligned} Th(r, t) &\leq \frac{1-\alpha}{AB(\alpha)} f(r, t, h(r, t)) + \frac{\alpha}{AB(\alpha)\Gamma(\alpha)} \\ &\int_0^t (t-x)^{\alpha-1} f(r, x, h(r, x)) dx \leq \frac{1-\alpha}{AB(\alpha)} M + \frac{\alpha M t^\alpha}{AB(\alpha)} < \infty \end{aligned} \quad (43)$$

Consider $h \in N, t_1 < t_2$. Then for any given $\varepsilon > 0$ if $|t_1 - t_2| < \Phi$ then

$$Th(r, t_2) - Th(r, t_1) \leq$$

$$\begin{aligned} &\frac{1-\alpha}{AB(\alpha)} f(r, t_2, h(r, t_2)) - f(r, t_1, h(r, t_1)) \\ &+ \frac{\alpha}{AB(\alpha)\Gamma(\alpha)} \int_0^{t_1} (t_1-x)^{\alpha-1} f(r, x, h(r, x)) dx \\ &- \frac{\alpha}{AB(\alpha)\Gamma(\alpha)} \int_0^{t_2} (t_2-x)^{\alpha-1} f(r, x, h(r, x)) dx \end{aligned}$$

We shall evaluate the above step by step:

$$\begin{aligned} &f(r, t_2, h(r, t_2)) - f(r, t_1, h(r, t_1)) = \\ &\frac{K}{r^{d-1}} \partial_r r^{d-1-\theta} \partial_r h(r, t_2) - \partial_r \left[r^{d-1-\theta} \partial_r h(r, t_1) \right] \leq \end{aligned}$$

$$\begin{aligned}
 & \frac{K}{r^{d-1}} \theta_1 r^{d-1-\theta} \partial_r h(r, t_2) - \partial_r h(r, t_1) \\
 & \leq K \theta_1 \theta_2 h(r, t_2) - h(r, t_1) b \leq K \theta_1 \theta_2 l |t_2 - t_1|
 \end{aligned} \tag{44}$$

We next evaluate:

$$\begin{aligned}
 & \int_0^{t_2} (t_2 - x)^{\alpha-1} f(r, x, h(r, x)) dx - \int_0^{t_1} (t_1 - x)^{\alpha-1} f(r, x, h(r, x)) dx \\
 & \leq \frac{\alpha}{AB(\alpha)\Gamma(\alpha)} \int_0^{t_2} (t_2 - x)^{\alpha-1} dx - \int_0^{t_1} (t_1 - x)^{\alpha-1} dx
 \end{aligned}$$

But:

$$\begin{aligned}
 & \int_0^{t_2} (t_2 - x)^{\alpha-1} dx - \int_0^{t_1} (t_1 - x)^{\alpha-1} dx \\
 & = \int_{t_1}^{t_2} (t_2 - x)^{\alpha-1} dx + \int_0^{t_1} (t_1 - x)^{\alpha-1} - (t_2 - x)^{\alpha-1} dx \\
 & = \frac{2}{\Gamma(\alpha+1)} (t_1 - t_2)^\alpha
 \end{aligned} \tag{45}$$

Chose:

$$\Phi = \frac{\varepsilon}{K \theta_1 \theta_2 l + \frac{2\alpha}{AB(\alpha)\Gamma(\alpha+1)}} \tag{46}$$

We obtain the requested result. Hence $T(N)$ is equi continuous and according to the well-known Anzela-Asule theorem $\overline{T(N)}$ is compact and continue.

Theorem 3: Let $T: [a_1, b_1] [a_2, b_2] \times [0, \infty) \rightarrow [0, \infty)$ be a continuous function and $T(r, t)$ for each $\epsilon \in [a, b]$. Let us suppose that there exists h_1 and h_2 satisfying

$$G(D)h_1 \leq f(r, x, h_1(r, x)), G(D)h_2 \geq f(r, x, h_2(r, x)), a < t < b$$

3.3 The new fractal flow equation has a positive solution.

We now present the analysis and conditions within which the solution is unique. We establish these conditions by considering the following:

$$\begin{aligned} & Th(r, t_2) - Th(r, t_1) \\ & \leq \frac{1-\alpha}{AB(\alpha)} f(r, t, h_2(r, t)) - f(r, t, h_1(r, t)) + \frac{\alpha}{AB(\alpha)\Gamma(\alpha)} \\ & \int_0^t (t-x)^{\alpha-1} f(r, x, h_2(r, x)) - f(r, x, h_1(r, x)) dx \\ & \leq \frac{1-\alpha}{AB(\alpha)} \delta h_2(r, t) - h_1(r, t) + \frac{\alpha}{AB(\alpha)\Gamma(\alpha+1)} \delta b^\alpha h_2 - h_1 \\ & \leq \left(\frac{1-\alpha}{AB(\alpha)} \delta + \frac{\alpha}{AB(\alpha)\Gamma(\alpha+1)} \right) h_2 - h_1 \leq K h_2 - h_1 \end{aligned} \quad (47)$$

Thus $K < 1$, then T is a contraction. This implies it has a fixed point, which is the positive solution of our equation. In this section we presented the derivation of a solution to our new model. The method used here is the mixture of integral transform with perturbation method. We first present the methodology of the used method for the general fractional differential equation based on the fractional derivative with Mittag-Leffler function.

Let "equation (48)" be a general non-linear partial differential equation with the new fractional derivative based on the Mittag-Leffler function.

$${}^{ABC}D_t^\alpha U(x, t) = LU(x, t) + NU(x, t) + f(x, t) \quad (48)$$

To solve this equation we apply the fractional integral transform on both side of the equation to obtain:

$$\begin{aligned}
 U(x, t) = & U(x, t) + \frac{1-\alpha}{AB(\alpha)} \{LU(x, t) + NU(x, t) + f(x, t)\} \\
 & \frac{\alpha}{AB(\alpha)\Gamma(\alpha)} \int_0^t (t-y)^{1-\alpha} \{LU(x, y) + NU(x, y) + f(x, y)\} dy
 \end{aligned} \tag{49}$$

The next stage is to assume that the solution of our equation to be in the following for

$$\begin{aligned}
 U_{n+1}(x, t) = & \frac{1-\alpha}{AB(\alpha)} \{LU_n(x, t) + NU_n(x, t) + f(x, t)\} \frac{\alpha}{AB(\alpha)\Gamma(\alpha)} \\
 & \int_0^t (t-y)^{1-\alpha} \{LU_n(x, y) + NU_n(x, y) + f(x, y)\} dy
 \end{aligned} \tag{50}$$

Where $U_0(x, t) = U(x, 0)$, L is a linear operator, N is a non-Linear operator $f(x, t)$ is a known function, and $U(x, 0)$ is the initial condition.

We shall now present the stability of the used method.

Theorem 4: Let us assume that the operator N Lipschitz, then the method is stable if:

$$\frac{1-\alpha}{AB(\alpha)} K_1 + \frac{\alpha T^\alpha}{AB(\alpha)\Gamma(\alpha+1)} K_2 < 1$$

Proof: Let $n, m \in \mathbb{N}$ and let us assume that the non-linear operator N is Lipschitz theorem.

$$\begin{aligned}
 U_{n+1} - U_{m+1} = & \frac{1-\alpha}{AB(\alpha)} \{L(U_n - U_m) + NU_n - NU_m\} + \\
 & \frac{\alpha}{AB(\alpha)\Gamma(\alpha)} \int_0^t (t-y)^{\alpha-1} \{L(U_n - U_m) + NU_n + NU_m\} dy
 \end{aligned}$$

Now, using the properties of norm, we obtain:

$$\begin{aligned}
 U_{n+1} - U_{m+1} &\leq \frac{1-\alpha}{AB(\alpha)} \{U_n - U_m K_1 + U_n - U_m K_2\} + \\
 &\frac{\alpha}{AB(\alpha)\Gamma(\alpha)} \{U_n - U_m K_1 + U_n - U_m K_2\} \int_0^t (t-y)^{\alpha-1} dy \leq \\
 &\left\{ \frac{1-\alpha}{AB(\alpha)} K_1 + K_2 + \frac{\alpha}{AB(\alpha)\Gamma(\alpha)} T^\alpha \right\} U_n - U_m
 \end{aligned} \tag{51}$$

Repeating (n,m) times this process, we obtain:

$$U_{n+1} - U_{m+1} \leq \left\{ \frac{1-\alpha}{AB(\alpha)} K_1 + K_2 + \frac{\alpha T^\alpha}{AB(\alpha)\Gamma(\alpha+1)} \right\}_1^2 U_{n-1} - U_{m-2} \tag{52}$$

However, choosing $m = n - 1$, we arrive at the following:

$$U_{n+1} - U_{m+1} \leq \left\{ \frac{1-\alpha}{AB(\alpha)} K_1 + K_2 + \frac{\alpha T^\alpha}{AB(\alpha)\Gamma(\alpha+1)} \right\}_1^n U(x,0) \tag{53}$$

If $n \rightarrow \infty$ the right hand side of equation (53) tends to zero this shows that the sequence is convergent since:

$$\frac{1-\alpha}{AB(\alpha)} K_1 + K_2 + \frac{\alpha T^\alpha}{AB(\alpha)\Gamma(\alpha+1)} < 1$$

3.3.1 Application to the new fractal flow model

Applying the Atangana-Baleanu fractional integral on both sides, we obtain:

$$\begin{aligned}
 S_0 [h(r,t) - h(r,0)] &= \frac{1-\alpha}{AB(\alpha)} \frac{K}{r^{D-1}} \partial_r [r^{D-1-\theta} \partial_r h(r,t)] + \\
 &\frac{\alpha}{AB(\alpha)\Gamma(\alpha)} \int_0^t (t-y)^{\alpha-1} \frac{K}{r^{D-1-\theta}} \partial_r [r^{D-1-\theta} \partial_r h(r,y)] dy
 \end{aligned} \tag{54}$$

Now, we consider the following recursive formula:

$$\begin{aligned}
 h_{n+1}(r, t) = & \frac{1-\alpha}{S_0 AB(\alpha)} \frac{K}{r^{D-1}} \partial_r \left[r^{D-1-\theta} \partial_r h_n(r, t) \right] + \\
 & \frac{\alpha}{S_0 AB(\alpha) \Gamma(\alpha)} \int_0^t (t-y)^{\alpha-1} \frac{K}{r^{D-1}} \partial_r \left[r^{D-1-\theta} \partial_r h_n(r, y) \right] dy
 \end{aligned} \tag{55}$$

3.4 Numerical analysis with fractional integral

In this section, we present the numerical solution of the new equation. We will present four different numerical schemes. The first is based on the Volterra version of our new equation given below as:

$$\begin{aligned}
 h(r, t) = & \frac{1-\alpha}{S_0 AB(\alpha)} \frac{K}{r^{D-1}} \partial_r \left[r^{D-1-\theta} \partial_r h(r, t) \right] + \\
 & \frac{\alpha}{S_0 AB(\alpha) \Gamma(\alpha)} \int_0^t (t-y)^{\alpha-1} \frac{K}{r^{D-1}} \partial_r \left[r^{D-1-\theta} \partial_r h(r, y) \right] dy
 \end{aligned} \tag{56}$$

The above equation will be solved numerically using a new numerical scheme. We present first the numerical scheme then use it for application.

3.4.1 Numerical approximation of fractional integral

In this section we suggest an approximation of fractional integral, let us consider a function f defined in a closed interval "I". By the definition of fractional integral we have the following:

$${}^{RL}I_t^\alpha f(t) = \frac{1}{\Gamma(\alpha)} \int_0^t (t-y)^{\alpha-1} f(y) dy,$$

For any given natural number $n > 1$, the above can be formulated as:

$$\begin{aligned}
 {}^{RL}I_t^\alpha f(t_n) &= \frac{1}{\Gamma(\alpha)} \int_0^{t_n} (t_n - y)^{\alpha-1} f(y) dy, \\
 &= \frac{1}{\Gamma(\alpha)} \sum_{k=0}^{n-1} \int_{t_k}^{t_{k+1}} (t_n - y)^{\alpha-1} \frac{f(t_{k+1}) + f(t_k)}{2} dy + \frac{1}{\Gamma(\alpha)} \sum_{k=0}^{n-1} (t_n - y)^{\alpha-1} (f(y) - f(t_{k+1})) dy, \\
 &= \frac{1}{\Gamma(\alpha)} \sum_{k=0}^{n-1} \frac{f(t_{k+1}) + f(t_k)}{2} \int_{t_k}^{t_{k+1}} (t_n - y)^{\alpha-1} dy + \frac{1}{\Gamma(\alpha)} \sum_{k=0}^{n-1} (t_n - y)^{\alpha-1} \frac{(f(y) - f(t_{k+1}))(y - t_{k+1})}{y - t_{k+1}} dy,
 \end{aligned} \tag{57}$$

We shall develop both component of the above equation; we start with the first component

$$\begin{aligned}
 &\frac{1}{\Gamma(\alpha)} \sum_{k=0}^n \frac{f(t_{k+1}) + f(t_k)}{2} \int_{t_k}^{t_{k+1}} (t_n - y)^{\alpha-1} dy \\
 &= \frac{(\Delta t)^\alpha}{\Gamma(\alpha + 1)} \sum_{k=0}^n \frac{f(t_{k+1}) + f(t_k)}{2} \left\{ (n - k)^\alpha - (n - k - 1)^\alpha \right\}, \\
 &\frac{1}{\Gamma(\alpha)} \sum_{k=0}^n \frac{f(t_{k+1}) + f(t_k)}{2} \int_{t_k}^{t_{k+1}} (t_n - y)^{\alpha-1} dy \\
 &= \frac{(\Delta t)^\alpha}{\Gamma(\alpha + 1)} \sum_{k=0}^n \frac{f(t_{k+1}) + f(t_k)}{2} \delta_{n,k}^\alpha,
 \end{aligned} \tag{58}$$

The second component, which is the remainder, could be evaluated as follows:

$$\begin{aligned}
 R_{n,k}^{\alpha}(t) &= \frac{1}{\Gamma(\alpha)} \sum_{k=0}^n \int_{t_k}^{t_{k+1}} \left\{ (t_n - y)^{\alpha-1} \frac{(f(y) - f(t_{k+1}))(y - t_{k+1})}{y - t_{k+1}} dy \right\}, \\
 &= \frac{1}{\Gamma(\alpha)} \sum_{k=0}^n \int_{t_k}^{t_{k+1}} (t_n - y)^{\alpha-1} f^{(\cdot)}(\lambda)(y - t_{k+1}) dy, \quad y \leq \lambda \leq t_n, \\
 &\leq \frac{\Delta t}{\Gamma(\alpha)} \sum_{k=0}^n \int_{t_k}^{t_{k+1}} (t_n - y)^{\alpha-1} f^{(\cdot)}(\lambda) dy, \quad y \leq \lambda \leq t_n, \\
 &\leq \frac{\Delta t}{\Gamma(\alpha)} \max_{0 \leq t \leq t_n} \{f^{(\cdot)}(t)\} \sum_{k=0}^n \int_{t_k}^{t_{k+1}} (t_n - y)^{\alpha-1} dy, \\
 &\leq \frac{(\Delta t)^{\alpha+1}}{\Gamma(\alpha+1)} \max_{0 \leq t \leq t_n} \{f^{(\cdot)}(t)\} \sum_{k=0}^n \left\{ (n-k)^{\alpha} - (n-k-1)^{\alpha} \right\},
 \end{aligned} \tag{59}$$

Theorem 1: Let f be defined in an open interval I , then the fractional integral of f can be approximated as:

$$\begin{aligned}
 {}^{RL}I_t^{\alpha} f(t_n) &= \frac{(\Delta t)^{\alpha}}{\Gamma(\alpha+1)} \sum_{k=0}^n \frac{f(t_{k+1}) + f(t_k)}{2} \left\{ (n-k)^{\alpha} - (n-k-1)^{\alpha} \right\} + R_{n,k}^{\alpha}(t), \\
 |R_{n,k}^{\alpha}(t)| &< \frac{(\Delta t)^{\alpha+1}}{\Gamma(\alpha+1)} \max_{0 \leq t \leq t_n} \{f^{(\cdot)}(t)\} \sum_{k=0}^n \left\{ (n-k)^{\alpha} - (n-k-1)^{\alpha} \right\}.
 \end{aligned} \tag{60}$$

3.4.2 Application to new model

This section is devoted to the derivation of a numerical solution of the new fractal flow model constructed with the concept of fractional differentiation based on the generalized Mittag-Leffler law. To do this, we first reformulate equation (3) as follows:

$$\begin{aligned}
 h(r,t) &= \frac{1-a}{S_0 AB(a)} \left\{ \frac{K(d-1-q)}{r^{1+q}} \partial_r h(r,t) + \frac{K}{r^q} \partial_{rr}^2 h(r,t) \right\}, \\
 &+ \frac{\alpha}{S_0 AB(\alpha) \Gamma(\alpha)} \int_0^t (t-y)^{\alpha-1} \left\{ \frac{K(d-1-\theta)}{r^{1+\theta}} \partial_r h(r,y) + \frac{K}{r^{\theta}} \partial_{rr}^2 h(r,y) \right\} dy,
 \end{aligned} \tag{61}$$

We now start the discretization of equation (32). We recall the first and second approximation for the local derivative. Here we shall employ three different numerical schemes for local derivative including implicit, explicit and Crank-Nicholson schemes.

Under the framework of implicit scheme, we have the following approximation:

$$\begin{aligned}\frac{\partial h(r,t)}{\partial t} &= \frac{h_i^{j+1} - h_i^j}{\Delta t}, \quad \frac{\partial h(r,t)}{\partial r} = \frac{h_{i+1}^{j+1} - h_{i-1}^{j+1}}{2\Delta x}, \\ \frac{\partial^2 h(r,t)}{\partial r^2} &= \frac{h_{i-1}^{j+1} - 2h_i^{j+1} + h_{i+1}^{j+1}}{(\Delta r)^2}.\end{aligned}\quad (62)$$

Using the above with the integral approximation suggested in section 3.1, equation (32) is reformulated as:

$$\begin{aligned}h_i^j &= \frac{1-\alpha}{S_0 AB(\alpha)} \left\{ \frac{K(d-\theta-1)}{r_i^{1+\theta}} \frac{h_{i+1}^{j+1} - h_{i-1}^{j+1}}{2\Delta r} + \frac{K}{r_i^\theta} \frac{h_{i-1}^{j+1} - 2h_i^{j+1} + h_{i+1}^{j+1}}{(\Delta r)^2} \right\} + \\ &\frac{(\Delta t)^{\alpha+1}}{S_0 AB(\alpha)\Gamma(\alpha)} \sum_{k=0}^j \left\{ \frac{K(d-\theta-1)}{r_i^{1+\theta}} \frac{h_{i+1}^{k+1} - h_{i-1}^{k+1}}{2\Delta r} + \frac{K}{r_i^\theta} \frac{h_{i-1}^{k+1} - 2h_i^{k+1} + h_{i+1}^{k+1}}{(\Delta r)^2} \right\} b_{n,k}^\alpha, \\ b_{n,k}^\alpha &= (n-k)^\alpha - (n-k-1)^\alpha.\end{aligned}\quad (63)$$

From the above when the index j is 0, we have

$$h_i^0 = \frac{1-\alpha}{S_0 AB(\alpha)} \left\{ \frac{K}{r_i^\theta} \frac{2h_i^1}{(\Delta r)^2} \right\} + \frac{(\Delta t)^{\alpha+1}}{S_0 AB(\alpha)\Gamma(\alpha)} \frac{K}{r_i^\theta} \frac{2h_i^1}{(\Delta r)^2}\quad (64)$$

For any $j > 0$, we let

$$\begin{aligned}
 a &= \frac{1-\alpha}{2\Delta r S_0 AB(\alpha)} K(d-\theta-1), b = \frac{(1-\alpha)K}{\Delta r S_0 AB(\alpha)}, \\
 c &= \frac{K(d-\theta-1)(\Delta t)^{\alpha+1}}{2\Delta r S_0 AB(\alpha)\Gamma(\alpha)}, e = \frac{K(\Delta t)^{\alpha+1}}{(\Delta r)^2 S_0 AB(\alpha)\Gamma(\alpha)}
 \end{aligned} \tag{65}$$

Then, the numerical solution of the new model using the implicit scheme is recursively represented as

$$\begin{aligned}
 h_i^j &= \left(\frac{-2b}{r_i^\theta} - \frac{2e}{r_i^\theta} b_{n,k}^\alpha \right) h_i^{j+1} + a \frac{h_{i+1}^{j+1} - h_{i-1}^{j+1}}{r_i^{1+\theta}} + b \frac{h_{i-1}^{j+1} + h_{i+1}^{j+1}}{r_i^\theta} + \\
 &\sum_{k=0}^{j-1} \left\{ c \frac{h_{i+1}^{k+1} - h_{i-1}^{k+1}}{r_i^{1+\theta}} + e \frac{h_{i-1}^{k+1} + h_{i+1}^{k+1}}{r_i^\theta} \right\} b_{j,k}^\alpha, \\
 b_{j,k}^\alpha &= (j-k)^\alpha - (j-k-1)^\alpha.
 \end{aligned} \tag{66}$$

Within the framework of explicit difference scheme, we have the following numerical approximation

$$\frac{\partial h(r,t)}{\partial t} = \frac{h_i^{j+1} - h_i^j}{\Delta t}, \frac{\partial h(r,t)}{\partial r} = \frac{h_{i+1}^j - h_i^j}{2\Delta x}, \frac{\partial^2 h(r,t)}{\partial r^2} = \frac{h_{i-1}^j - 2h_i^j + h_{i+1}^j}{(\Delta r)^2}. \tag{67}$$

Using the above with the integral approximation suggested in section 3.1, equation (32) is reformulated as:

$$\begin{aligned}
 h_i^{j+1} &= \frac{1-\alpha}{S_0 AB(\alpha)} \left\{ \frac{K(d-\theta-1)}{r_i^{1+\theta}} \frac{h_{i+1}^j - h_i^j}{2\Delta r} + \frac{K}{r_i^\theta} \frac{h_{i-1}^j - 2h_i^j + h_{i+1}^j}{(\Delta r)^2} \right\} + \\
 &\frac{(\Delta t)^{\alpha+1}}{S_0 AB(\alpha)\Gamma(\alpha)} \sum_{k=0}^j \left\{ \frac{K(d-\theta-1)}{r_i^{1+\theta}} \frac{h_{i+1}^k - h_i^k}{2\Delta r} + \frac{K}{r_i^\theta} \frac{h_{i-1}^k - 2h_i^k + h_{i+1}^k}{(\Delta r)^2} \right\} b_{j,k}^\alpha, \\
 b_{j,k}^\alpha &= (j-k)^\alpha - (j-k-1)^\alpha.
 \end{aligned} \tag{68}$$

For $j=0$, we have

$$h_i^1 = \frac{1-\alpha}{S_0 AB(\alpha)} \left\{ -\frac{K(d-\theta-1)}{r_i^{1+\theta}} \frac{h_i^0}{2\Delta r} - \frac{K}{r_i^\theta} \frac{2h_i^0}{(\Delta r)^2} \right\} \tag{69}$$

Also for an index greater than zero we have the following recursive formula

$$\begin{aligned}
 h_i^{j+1} &= h_i^j \left(-b_{n,j}^\alpha \frac{(\Delta t)^{\alpha+1}}{2r_i^{1+\theta}\Delta r S_0 AB(\alpha)\Gamma(\alpha)} - \frac{K(d-\theta-1)}{r_i^{1+\theta}} \frac{1-\alpha}{2\Delta r S_0 AB(\alpha)} - \frac{K}{(\Delta r)^2 r_i^\theta} \right) + \\
 &\frac{1-\alpha}{S_0 AB(\alpha)} \left\{ \frac{K(d-\theta-1)}{r_i^{1+\theta}} \frac{h_{i+1}^j}{2\Delta r} + \frac{K}{r_i^\theta} \frac{h_{i-1}^j + h_{i+1}^j}{(\Delta r)^2} \right\} + \\
 &\frac{(\Delta t)^{\alpha+1}}{S_0 AB(\alpha)\Gamma(\alpha)} \sum_{k=0}^{j-1} \left\{ \frac{K(d-\theta-1)}{r_i^{1+\theta}} \frac{h_{i+1}^k - h_i^k}{2\Delta r} + \frac{K}{r_i^\theta} \frac{h_{i-1}^k - 2h_i^k + h_{i+1}^k}{(\Delta r)^2} \right\} b_{j,k}^\alpha + \\
 &\left\{ \frac{K(d-\theta-1)}{r_i^{1+\theta}} \frac{h_{i+1}^j - h_i^j}{2\Delta r} + \frac{K}{r_i^\theta} \frac{h_{i-1}^j + h_{i+1}^j}{(\Delta r)^2} \right\} \frac{(\Delta t)^{\alpha+1}}{S_0 AB(\alpha)\Gamma(\alpha)}.
 \end{aligned} \tag{70}$$

The above formula can be used to obtain numerical simulations.

Using the Crank-Nicholson scheme, we have the following numerical approximations:

$$\begin{aligned}
 \frac{\partial h(r, t)}{\partial t} &= \frac{h_i^{j+1} - h_i^j}{\Delta t}, \\
 \frac{\partial h(r, t)}{\partial r} &= \frac{(h_{i+1}^{j+1} - h_{i-1}^{j+1}) + (h_{i+1}^j - h_{i-1}^j)}{2\Delta r}, \\
 \frac{\partial^2 h(r, t)}{\partial r^2} &= \frac{h_{i-1}^{j+1} - 2h_i^{j+1} + h_{i+1}^{j+1}}{(\Delta r)^2} + \frac{h_{i-1}^j - 2h_i^j + h_{i+1}^j}{(\Delta r)^2}, \quad (71) \\
 h(r, t) &= \frac{h_i^{j+1} + h_i^j}{2}
 \end{aligned}$$

The above approximations are replaced in equation:

$$\begin{aligned}
 \frac{h_i^{j+1} + h_i^j}{2} &= \frac{1 - \alpha}{S_0 AB(\alpha)} \left\{ \frac{K(d - \theta - 1) (h_{i+1}^{j+1} - h_{i-1}^{j+1}) + (h_{i+1}^j - h_{i-1}^j)}{r_i^{1+\theta} 2\Delta r} \right\} + \\
 &\quad \left\{ \frac{K}{r_i^\theta} \left[\frac{h_{i-1}^{j+1} - 2h_i^{j+1} + h_{i+1}^{j+1}}{(\Delta r)^2} + \frac{h_{i-1}^j - 2h_i^j + h_{i+1}^j}{(\Delta r)^2} \right] \right\} + \\
 \frac{(\Delta t)^{\alpha+1}}{S_0 AB(\alpha) \Gamma(\alpha)} \sum_{k=0}^j &\left\{ \frac{K(d - \theta - 1) \left[\frac{(h_{i+1}^{k+1} - h_{i-1}^{k+1}) + (h_{i+1}^k - h_{i-1}^k)}{2\Delta r} \right]}{r_i^{1+\theta}} \right\} \left\{ \frac{K}{r_i^\theta} \left[\frac{h_{i-1}^{k+1} - 2h_i^{k+1} + h_{i+1}^{k+1}}{(\Delta r)^2} + \frac{h_{i-1}^k - 2h_i^k + h_{i+1}^k}{(\Delta r)^2} \right] \right\} b_{j,k}^\alpha, \\
 b_{j,k}^\alpha &= (j - k)^\alpha - (j - k - 1)^\alpha. \quad (72)
 \end{aligned}$$

A recursive formula for any index greater than, zero is therefore given as:

$$\begin{aligned}
 & h_i^{j+1} \left\{ \frac{1}{2} + \frac{1-\alpha}{S_0 AB(\alpha)} \frac{2K}{(\Delta r)^2 r_i^\theta} + \frac{2(\Delta t)^{\alpha+1}}{(\Delta r)^2 S_0 AB(\alpha) \Gamma(\alpha)} \frac{K}{r_i^\theta} b_{j,j}^\alpha \right\} = \\
 & h_i^{j+1} \left\{ \frac{1}{2} + \frac{1-\alpha}{S_0 AB(\alpha)} \frac{2K}{(\Delta r)^2 r_i^\theta} + \frac{2(\Delta t)^{\alpha+1}}{(\Delta r)^2 S_0 AB(\alpha) \Gamma(\alpha)} \frac{K}{r_i^\theta} b_{j,j}^\alpha \right\} \\
 & + \frac{1-\alpha}{S_0 AB(\alpha)} \left\{ \frac{K(d-\theta-1) \left(\frac{h_{i+1}^{j+1} - h_{i-1}^{j+1}}{r_i^{1+\theta}} + \frac{h_{i+1}^{j+1} - h_{i-1}^{j+1}}{2\Delta r} \right)}{\right. \\
 & \left. + \frac{K}{r_i^\theta} \left[\frac{h_{i-1}^{j+1} + h_{i+1}^{j+1}}{(\Delta r)^2} + \frac{h_{i-1}^j + h_{i+1}^j}{(\Delta r)^2} \right] \right\} + \\
 & \frac{(\Delta t)^{\alpha+1}}{S_0 AB(\alpha) \Gamma(\alpha)} \sum_{k=0}^{j-1} \left\{ \frac{K(d-\theta-1) \left[\frac{(h_{i+1}^{k+1} - h_{i-1}^{k+1}) + (h_{i+1}^{k+1} - h_{i-1}^{k+1})}{r_i^{1+\theta}} \right]}{\right. \\
 & \left. + \frac{K}{r_i^\theta} \left[\frac{h_{i-1}^{k+1} - 2h_i^{k+1} + h_{i+1}^{k+1}}{(\Delta r)^2} + \frac{h_{i-1}^k - 2h_i^k + h_{i+1}^k}{(\Delta r)^2} \right] \right\} b_{j,k}^\alpha + \\
 & \frac{(\Delta t)^{\alpha+1}}{S_0 AB(\alpha) \Gamma(\alpha)} \left\{ \frac{K(d-\theta-1) \left[\frac{(h_{i+1}^{j+1} - h_{i-1}^{j+1}) + (h_{i+1}^{j+1} - h_{i-1}^{j+1})}{r_i^{1+\theta}} \right]}{\right. \\
 & \left. + \frac{K}{r_i^\theta} \left[\frac{h_{i-1}^{j+1} + h_{i+1}^{j+1}}{(\Delta r)^2} + \frac{h_{i-1}^j + h_{i+1}^j}{(\Delta r)^2} \right] \right\},
 \end{aligned}$$

$$b_{j,k}^\alpha = (j-k)^\alpha - (j-k-1)^\alpha.$$

(73)

3.5 Numerical solution with fractional derivative

In this section, we numerically solve the new partial fractional differential equation. We first present the numerical approximation of the fractional derivative based on the Mittag-Leffler function. The numerical approximation was suggested in the work with title "Solutions of Cattaneo-Hristov model of elastic heat diffusion with Caputo-Fabrizio and Atangana-Baleanu fractional derivatives" (Koca and Atangana, 2016). The following derivation was done,

$$\begin{aligned}
 {}_0^{ABC} D_t^\alpha \{f(t_j)\} &= \frac{AB(\alpha)}{1-\alpha} \int_0^{t_j} E_\alpha \left\{ -\frac{\alpha}{1-\alpha} (t_j - y)^\alpha \right\} \frac{df(y)}{dy} dy, \\
 &= \frac{AB(\alpha)}{1-\alpha} \sum_{k=0}^j \int_{t_k}^{t_{k+1}} E_\alpha \left\{ \frac{\alpha}{1-\alpha} (t_j - y)^\alpha \right\} \frac{f^{k+1} - f^k}{\Delta t} dy, \\
 &= \frac{AB(\alpha)}{1-\alpha} \sum_{k=0}^j \frac{f^{k+1} - f^k}{\Delta t} \int_{t_k}^{t_{k+1}} E_\alpha \left\{ -\frac{\alpha}{1-\alpha} (t_j - y)^\alpha \right\} dy, \\
 &= \frac{AB(\alpha)}{\alpha} \sum_{k=0}^j \frac{f^{k+1} - f^k}{\Delta t} \delta_{j,k}^\alpha, \\
 \delta_{j,k}^\alpha &= (t_j - t_{k+1}) E_\alpha \left\{ -\frac{\alpha}{1-\alpha} (t_j - t_{k+1}) \right\} - (t_j - t_k) E_\alpha \left\{ -\frac{\alpha}{1-\alpha} (t_j - t_k) \right\}
 \end{aligned} \tag{74}$$

Using the above discretization with the explicit numerical scheme the numerical solution of the fractal flow with the novel differentiation is provided by:

$$\begin{aligned}
 S_0 \frac{AB(\alpha)}{\alpha} \sum_{k=0}^j \frac{h_i^{k+1} - h_i^k}{\Delta t} \delta_{j,k}^\alpha \\
 = \frac{K(d - \theta - 1)}{r_i^{\theta+1}} \left\{ \frac{h_{i+1}^j - h_i^j}{2\Delta r} \right\} + \frac{K}{r_i^\theta} \left\{ \frac{h_{i-1}^j - 2h_i^j + h_{i+1}^j}{(\Delta r)^2} \right\}
 \end{aligned} \tag{75}$$

The above equation is reformulated as follows

$$\begin{aligned}
 h_i^{j+1} \frac{AB(\alpha)}{\alpha \Delta t} S_0 &= h_i^j \left\{ \frac{AB(\alpha)}{\alpha \Delta t} S_0 - \frac{K(d - \theta - 1)}{2r_i^{\theta+1} \Delta r} - \frac{2K}{r_i^\theta (\Delta r)^2} \right\} \\
 - S_0 \frac{AB(\alpha)}{\alpha} \sum_{k=0}^{j-1} \frac{h_i^{k+1} - h_i^k}{\Delta t} \delta_{j,k}^\alpha &+ \frac{K(d - \theta - 1)}{r_i^{\theta+1}} \left\{ \frac{h_{i+1}^j}{2\Delta r} \right\} + \frac{K}{r_i^\theta} \left\{ \frac{h_{i-1}^j + h_{i+1}^j}{(\Delta r)^2} \right\}
 \end{aligned} \tag{76}$$

When $j=0$, the recursive formula is given as:

$$h_i^1 \frac{AB(\alpha)}{\alpha \Delta t} S_0 = h_i^0 \left\{ \frac{AB(\alpha)}{\alpha \Delta t} S_0 - \frac{K(d-\theta-1)}{2r_i^{\theta+1} \Delta r} - \frac{2K}{r_i^\theta (\Delta r)^2} \right\} \quad (77)$$

Also the following inequality is observed

$$\left| \frac{h_i^1}{h_i^0} \right| = \left| \frac{\left\{ \frac{AB(\alpha)}{\alpha \Delta t} S_0 - \frac{K(d-\theta-1)}{2r_i^{\theta+1} \Delta r} - \frac{2K}{r_i^\theta (\Delta r)^2} \right\}}{\frac{AB(\alpha)}{\alpha \Delta t} S_0} \right| \leq 1$$

With the implicit numerical scheme the numerical solution of the fractal flow with the novel differentiation is provided by:

$$S_0 \frac{AB(\alpha)}{\alpha} \sum_{k=0}^j \frac{h_i^{k+1} - h_i^k}{\Delta t} \delta_{j,k}^\alpha = \frac{K(d-\theta-1)}{r_i^{\theta+1}} \left\{ \frac{h_{i+1}^{j+1} - h_i^{j+1}}{2\Delta r} \right\} + \frac{K}{r_i^\theta} \left\{ \frac{h_{i-1}^{j+1} - 2h_i^{j+1} + h_{i+1}^{j+1}}{(\Delta r)^2} \right\} \quad (78)$$

The above equation is reformulated as follows

$$h_i^{j+1} \left\{ \frac{AB(\alpha)}{\alpha \Delta t} S_0 + \frac{K(d-\theta-1)}{2r_i^{\theta+1} \Delta r} + \frac{2K}{r_i^\theta (\Delta r)^2} \right\} = h_i^j \left\{ \frac{AB(\alpha)}{\alpha \Delta t} S_0 \right\} - S_0 \frac{AB(\alpha)}{\alpha} \sum_{k=0}^{j-1} \frac{h_i^{k+1} - h_i^k}{\Delta t} \delta_{j,k}^\alpha + \frac{K(d-\theta-1)}{r_i^{\theta+1}} \left\{ \frac{h_{i+1}^{j+1}}{2\Delta r} \right\} + \frac{K}{r_i^\theta} \left\{ \frac{h_{i-1}^{j+1} + h_{i+1}^{j+1}}{(\Delta r)^2} \right\} \quad (79)$$

At $j = 0$, the recursive formula is given as:

$$h_i^0 \frac{AB(\alpha)}{\alpha \Delta t} S_0 = h_i^1 \left\{ \frac{AB(\alpha)}{\alpha \Delta t} S_0 + \frac{K(d-\theta-1)}{2r_i^{\theta+1} \Delta r} + \frac{2K}{r_i^\theta (\Delta r)^2} \right\} \quad (80)$$

Also the following inequality is observed

$$\left| \frac{h_i^1}{h_i^0} \right| = \left| \frac{\frac{AB(\alpha)}{\alpha \Delta t} S_0}{\frac{AB(\alpha)}{\alpha \Delta t} S_0 + \frac{K(d-\theta-1)}{2r_i^{\theta+1} \Delta r} + \frac{2K}{r_i^\theta (\Delta r)^2}} \right| \leq 1$$

With the Crank-Nicholson numerical scheme the numerical solution of the fractal flow with the novel differentiation is provided by:

$$S_0 \frac{AB(\alpha)}{\alpha} \sum_{k=0}^j \frac{h_i^{k+1} - h_i^k}{\Delta t} \delta_{j,k}^\alpha = \frac{K(d-\theta-1)}{r_i^{\theta+1}} \left\{ \frac{(h_{i+1}^{j+1} - h_{i-1}^{j+1}) + (h_{i+1}^j - h_{i-1}^j)}{2\Delta r} \right\} + \frac{K}{r_i^\theta} \left\{ \frac{h_{i-1}^{j+1} - 2h_i^{j+1} + h_{i+1}^{j+1}}{(\Delta r)^2} + \frac{h_{i-1}^j - 2h_i^j + h_{i+1}^j}{(\Delta r)^2} \right\} \quad (81)$$

The above equation is reformulated as follows

$$h_i^{j+1} \left\{ \frac{AB(\alpha)}{\alpha \Delta t} S_0 + \frac{2K}{r_i^\theta (\Delta r)^2} \right\} = h_i^j \left\{ \frac{AB(\alpha)}{\alpha \Delta t} S_0 - \frac{2K}{r_i^\theta (\Delta r)^2} \right\} - S_0 \frac{AB(\alpha)}{\alpha} \sum_{k=0}^{j-1} \frac{h_i^{k+1} - h_i^k}{\Delta t} \delta_{j,k}^\alpha + \frac{K(d-\theta-1)}{r_i^{\theta+1}} \left\{ \frac{h_{i+1}^{j+1} + h_{i-1}^{j+1}}{2\Delta r} + \frac{h_{i+1}^j + h_{i-1}^j}{2\Delta r} \right\} + \frac{K}{r_i^\theta} \left\{ \frac{h_{i-1}^j + h_{i+1}^j}{(\Delta r)^2} + \frac{h_{i+1}^j + h_{i-1}^j}{2\Delta r} \right\} \quad (82)$$

At $j = 0$, the recursive formula is given as:

$$h_i^0 \left\{ \frac{AB(\alpha)}{\alpha\Delta t} S_0 - \frac{2K}{r_i^\theta (\Delta r)^2} \right\} = h_i^1 \left\{ \frac{AB(\alpha)}{\alpha\Delta t} S_0 + \frac{2K}{r_i^\theta (\Delta r)^2} \right\} \quad (83)$$

Also the following inequality is observed

$$\left| \frac{h_i^1}{h_i^0} \right| = \left| \frac{\frac{AB(\alpha)}{\alpha\Delta t} S_0 - \frac{2K}{r_i^\theta (\Delta r)^2}}{\frac{AB(\alpha)}{\alpha\Delta t} S_0 + \frac{2K}{r_i^\theta (\Delta r)^2}} \right| \leq 1 \quad (84)$$

The numerical simulations of the modified equation are presented here. In these simulations, we chose the storativity S to be 0.03, the hydraulic conductivity K to be 5 m/day, the discharge rate Q to be 5 m³/day, the radius of the borehole to be $r_w=0.16$ m, the depth of the fracture aquifer to be 100 m. The numerical simulations are depicted in Figure 1 and 2 as function of time and space.

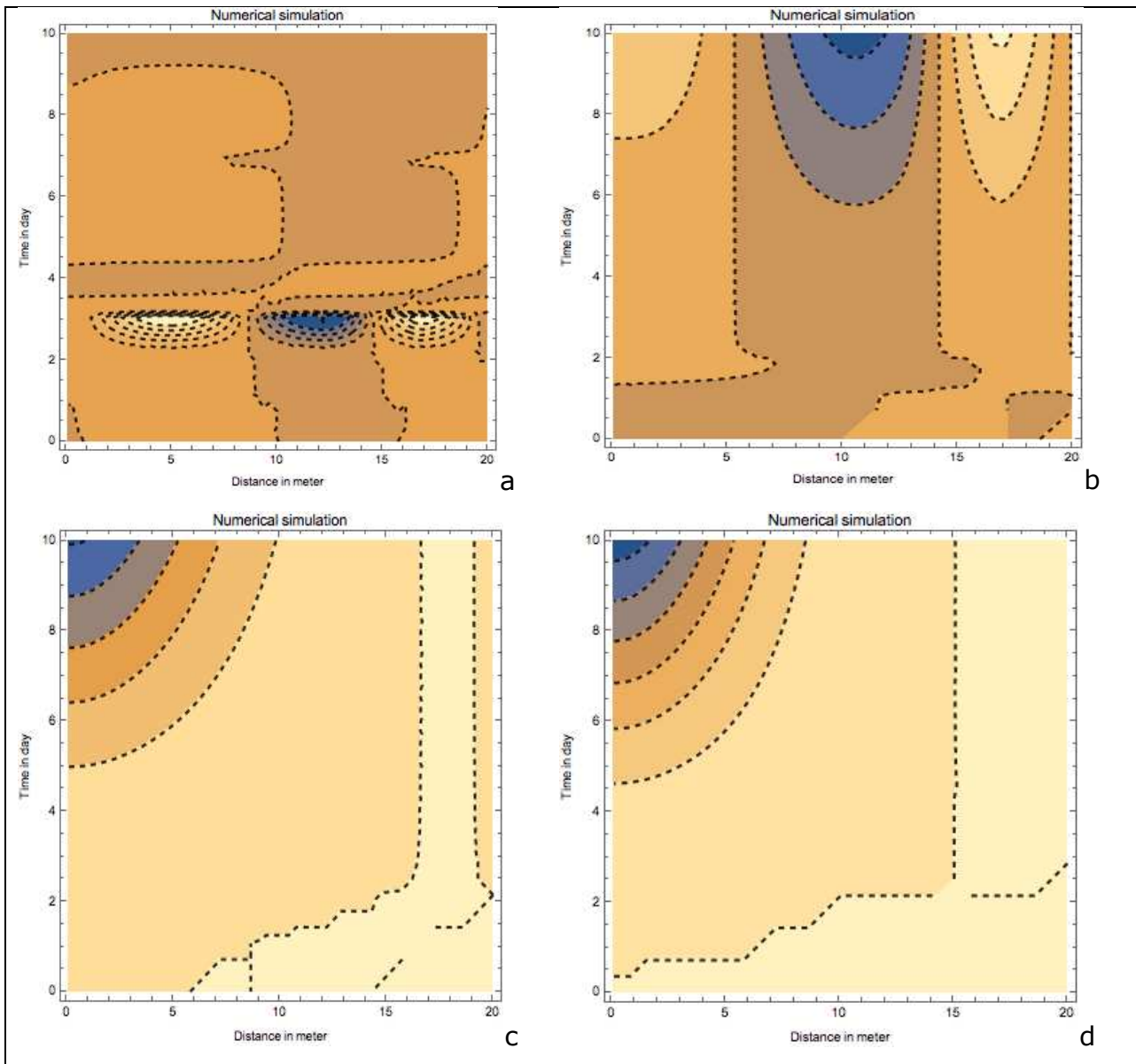


Figure 3: Numerical simulation contour plot of hydraulic head for $d = 1.2$: In (a) we chose $\theta = 0.25$, in (b) we chose $\theta = 0.75$, in (c), we chose, and in (d) we chose $\theta = 1.5$.

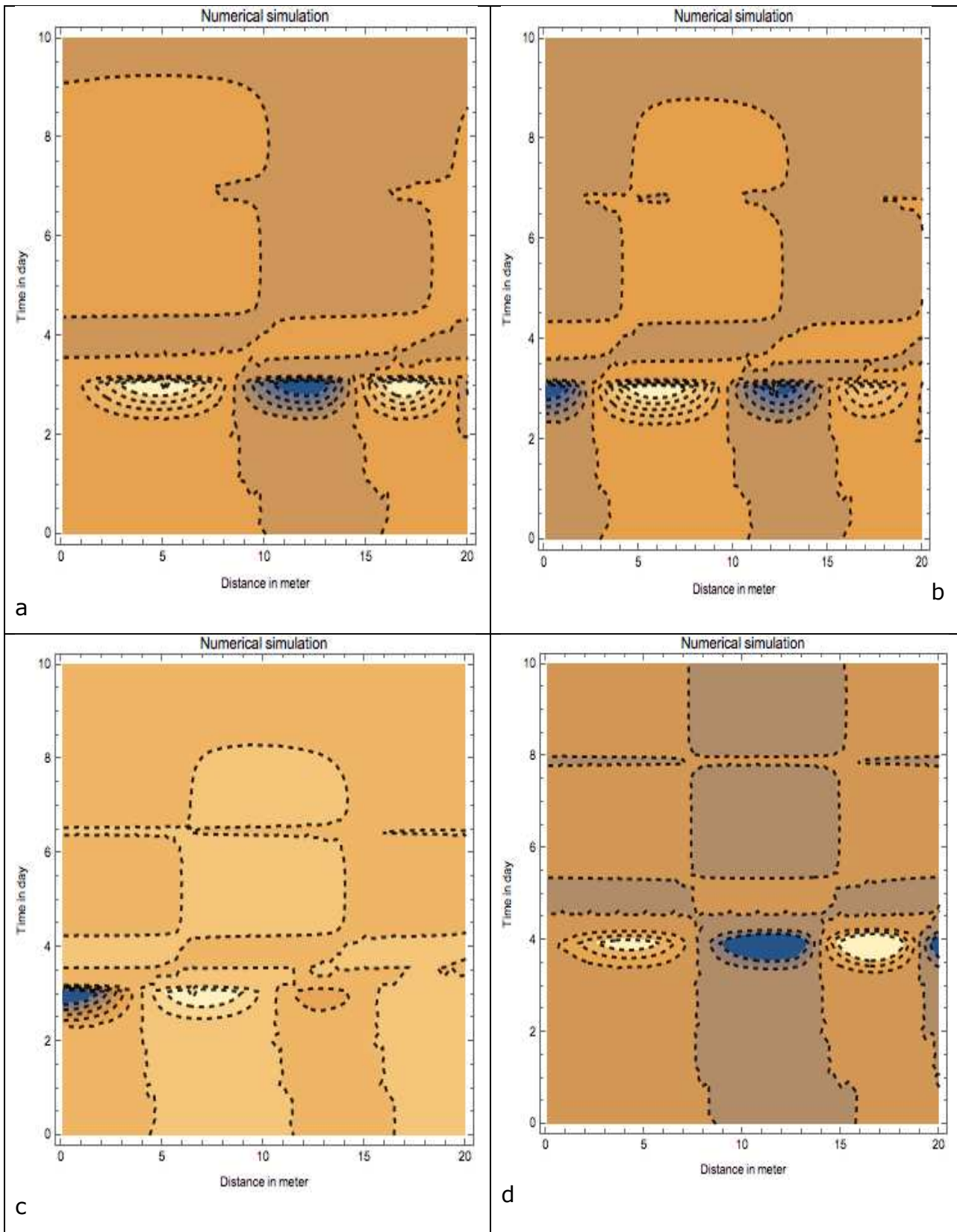


Figure 4: Numerical simulation contour plot of hydraulic head for $\theta = 0.25$: In (a) we chose $d = 1.80$, in (b) we chose $d = 1.1$, in (c) we chose $d = 2.3$, and in (d) we chose $d = 2.9$

3.6 Conclusion

The model of fractal flow is perhaps one of the most difficult physical problems within the field of Geohydrology due the following complexities: Fractal shapes are assumed to have a significant effect on pressure drop and turbulent intensity, owing to their edge self-similarity shape, which has been shown to enhance the mixing properties. A newly empirical work employing the so-called Koch snow flake fractal pattern as an orifice plate presented that the pressure drop after the fractal orifice of the aquifer is lesser than when the pressure drop measured all over the circular orifice with the same area. Therefore to model this complex system one will use the suitable concept of differentiation. To avoid the problem of differentiation posed by the fractional derivative based on the power law, a new concept was suggested recently using the concept of Mittag-Leffler law. The new fractional differentiation is more natural and more suitable to model real world problems due to the wider applicability of the generalized Mittag-Leffler function. In this work, we aimed to suggest a modified fractal flow model using the Atangana-Baleanu fractional derivative. The existence and the uniqueness of the solution were presented using the fixed-point theorem. We suggested three numerical schemes to derive the numerical solution of the modified model. To test the accuracy of the new model we compared field data from four different constant discharge tests with numerical solution simulations in a case study in Chapter 6.

4 Modelling of fractal flow in dual media with power and generalized Mittag-Leffler laws

Many simple analytical models of groundwater flowing within geological formations (aquifers) were developed for the interpretation of drawdown curves and have been proven to yield values that are easily comparable to each other (Theis, 1935; Cooper and Jacob, 1946). They provide quality criteria for the management of portion of the reservoir. Most are however based on the statement that a non-integer dimension prevails for flow, and flow takes place in a single homogenous/fractal medium. Originally introduced by Barenblatt et al (1960), and Warren and Root (1963), the concept of dual media assumes homogenized flow (and transport) in a fracture field and account for the relationships with the porous matrix (Barenblatt et al., 1960; Warren and Root, 1963). At the relatively large scale (greater than matrix block), the aquifer is mostly drained by connected fractures. Dershowitz and Miller (1995) demonstrated the concept on dual porosity fracture flow and transport, using fractured network models (de Swaan, 1976; Serra et al., 1983). Quintard and Whitaker (1998) applied the concept in the spatial averaging of the macroscopic behaviour of heterogeneous/fractured porous media. However, it is only in 2006 that Frederick et al, proposed a consistence tool for interpreting interference pumping tests based on the dual-medium approach. Considering the couple of equations at the Darcy scale describing flow in a dual medium as (Bourdet, 1984):

$$\begin{cases} S_{S_f} \frac{\partial h_f}{\partial t} = \nabla \cdot (k_f \cdot \nabla h_f) + \alpha(h_m - h_f) + q_f \\ S_{S_m} \frac{\partial h_m}{\partial t} = \alpha(h_m - h_f) \end{cases} \quad (85)$$

Where: h (in m) is the hydraulic head, k_f (in m/day) is the hydraulic conductivity (which is basically a tensor in multidimensional flow) of fracture continuum, S_s (in m^{-1}) is the specific storage capacity, α (in $m^{-1}day^{-1}$) the exchange rate coefficient between fractures and the matrix, and q_f (in m^3day^{-1}) a sink–source term from a pumping well that is located in the fracture continuum. The hydraulic conductivity within the matrix (k_m) is considered negligible compare to k_f and is dropped. The application of power

laws concept in space (fractal) on the hydrodynamic parameters of both the matrix and fractures is not new, and assumes that the parameters decrease with the lag distance r between the pumped well $(S_{S_{f_0}}, k_{f_0}, S_{S_{m_0}}, \alpha_0)$ and the observed ones. Many authors including Acuna and Yortsos, 1995; Delay and Porel 2004 have used this type of scaling laws (O'Shaughnessy and Procaccia, 1985) in interpreting interference pumping tests for single media (O'Shaughnessy and Procaccia, 1985; Leveinen, 2000). However, only few (Frederick and others in 1996 of its application to dual media have been recorded in literature, as the application involves 8 parameters as follow:

$$S_{S_f}(r) = S_{S_{f_0}} r^{-b}; k_f(r) = k_{f_0} r^{-a}; S_{S_m}(r) = S_{S_{m_0}} r^{-c}; \text{ and } \alpha(r) = \alpha_0 r^{-d} \quad (86)$$

Where a, b, c and d power-law exponents, and considered to be positive. The above model does not account for the heterogeneity, elasticity, visco-elasticity of the geological formation within which the flow is taken place. One may neglect to account for the heterogeneity, elasticity, and the visco-elasticity within the fractures into mathematical formulation. Nevertheless, the flow within the matrix rock will encounter natural obstacles and those need to be included into mathematical formulation to obtain better prediction. Therefore in order to include the physical properties into mathematical formulation the local classical operator of differentiation in this paper will be replaced with a non-local operator to be able to account for the heterogeneity, elasticity, and visco-elasticity of the geological formation within which the flow is taken place. The non-local operator can be the convolution of the power law and the unknown function to account for elasticity, or it could be a convolution of exponential decay law to account for heterogeneity, or could be replaced by a convolution of the generalized Mittag-Leffler function and the unknown function. A more complex model will be adjusted where the classical local time derivative will be replaced by a fractional differential operator with two orders. Before all, we shall present some useful information about the concept of fractional differentiation with power, exponential decay, Mittag-Leffler law and also the concept of fractional derivative with two orders. These three new concepts of fractional differentiation have been introduced and used in many research papers and have been proven to be very efficient mathematical tools for modelling real world problems.

4.1 Fractional differentiation

We present in this section some useful information about the new trend of fractional differentiation (Oldham et al., 1974; Atangana and Dumitru, 2016). However, we must first present the definition of existing fractional operator namely the Riemann-Liouville.

The Riemann-Liouville fractional integral of a non-differentiable function f is given as:

$${}^{\text{RL}}_0 D_x^\alpha (f(x)) = \frac{1}{\Gamma(1-\alpha)} \frac{d}{dx} \int_0^x (x-t)^{-\alpha} f(t) dt \quad (87)$$

The Caputo-Fabrizio derivative in Riemann-Liouville sense of non-differentiable function f is given as:

$${}^{\text{CF}}_0 D_x^\alpha (f(x)) = \frac{M(\alpha)}{(1-\alpha)} \frac{d}{dx} \int_0^x \exp\left[-\frac{\alpha}{1-\alpha}(x-t)\right] f(t) dt \quad (88)$$

The Atangana-Baleanu fractional derivative in Riemann-Liouville sense of a non-differentiable function f is given as:

$${}^{\text{ABR}}_0 D_x^\alpha (f(x)) = \frac{M(\alpha)}{(1-\alpha)} \frac{d}{dx} \int_0^x E_\alpha\left[-\frac{\alpha}{1-\alpha}(x-t)^\alpha\right] f(t) dt \quad (89)$$

The Riemann-Liouville fractional integral of a given continuous function f is given as:

$${}^{\text{RL}}_0 J_x^\alpha (f(x)) = \frac{1}{\Gamma(\alpha)} \int_0^x (x-t)^{\alpha-1} f(t) dt \quad (90)$$

The Caputo-Fabrizio fractional integral of a continuous function f is given as:

$${}^{\text{CF}}_0 J_x^\alpha (f(x)) = \frac{1-\alpha}{M(\alpha)} f(x) + \frac{\alpha}{M(\alpha)} \int_0^x f(t) dt \quad (91)$$

The Atangana-Baleanu fractional integral of a continuous function f is given as:

$${}^{\text{AB}}_0 J_x^\alpha (f(x)) = \frac{1-\alpha}{AB(\alpha)} f(x) + \frac{\alpha}{AB(\alpha)\Gamma(\alpha)} \int_0^x (x-t)^{\alpha-1} f(t) dt \quad (92)$$

The Atangana fractional derivative with two orders of a continuous function f is given as:

$${}^{\text{AR}}_0 D_x^{\alpha,\beta}(f(x)) = \frac{A(\alpha)}{1-\alpha} \frac{1}{\Gamma(1-\beta)} \frac{d}{dx} \int_0^x (x-t)^{-\beta} E_\alpha \left(-\frac{\alpha}{1-\alpha} (x-t)^{\alpha+\beta} \right) f(t) dt \quad (93)$$

The above nonlinear operators will be used in the following sections as mathematical tools to model the fractal flow within a dual media with inclusion of heterogeneity, elasticity, visco-elasticity and memory effect.

4.2 Model of fractal flow in dual media accounting for elasticity

In a dual media, water flows within the fracture network and also within the matrix soils. Within the matrix rock, it is without doubt that the media is non-viscous, homogeneous and but there is a memory effect. However the water flowing within the matrix rock flow within a geological formation that can have elastic property, this elasticity cannot be described with the time classical derivative but can efficiently be described with the non-local operator with a power law kernel known as Riemann-Liouville or Caputo fractional derivative. Thus in order to include into mathematical formula the effect of elasticity of the matrix rock, the time local derivative will be replaced by the Caputo fractional derivative to obtain:

$$\begin{cases} S_{S_f} \quad {}^c_0 D_t^\alpha (h_f(r,t)) = \nabla \cdot (k_f \cdot \nabla h_f(r,t)) + \eta (h_m(r,t) - h_f(r,t)) + q_f \\ S_{S_m} \quad {}^c_0 D_t^\alpha (h_m(r,t)) = \eta (h_m(r,t) - h_f(r,t)) \end{cases} \quad (94)$$

We shall first present the existence and uniqueness of the above system.

4.2.1 Existence of system solutions

The existence of a positive solution for a given fractional differential equation is a big concern for mathematician; because sometime some complex differential equations that cannot be solved analytically exist, but the proof of existence helps us know that there exists a solution under some conditions within a well-constructed Sobolev space. In this paper, we consider the following Sobolev space

$$H^1(0,T) = \{u \in L^2(a,b) / u' \in L^2(a,b)\}$$

We also consider the following Hilbert space where

$$H \in \left\{ u, v / \int_0^t (t-y)^\alpha v u dy < \infty \right\}.$$

To prove the existence of equation (10), we express the change of hydraulic head within the matrix soil in terms of the change of hydraulic head within the fracture. To achieve this we employ the Laplace transform in time to obtain:

$$\begin{aligned} S_{S_m} p^\alpha h_m(r, p) &= \eta (h_m(r, p) - h_f(r, p)) \\ (S_{S_m} p^\alpha - \eta) h_m(r, p) &= -\eta h_f(r, p), \\ h_m(r, p) &= \frac{-\eta h_f(r, p)}{S_{S_m} \left(p^\alpha - \frac{\eta}{S_{S_m}} \right)}, \end{aligned} \tag{95}$$

$$\begin{aligned} h_m(r, t) &= L^{-1} \left(\frac{-\eta h_f(r, p)}{S_{S_m} \left(p^\alpha - \frac{\eta}{S_{S_m}} \right)} \right), \\ h_m(r, t) &= -\frac{\eta}{S_{S_m}} \int_0^t h_f(r, y) E_\alpha \left(\frac{\eta}{S_{S_m}} (t-y) \right) dy. \end{aligned}$$

Equation (95) can now be replaced in system (94) to obtained

$$\begin{aligned} S_{S_f} {}^C D_t^\alpha (h_f(r, t)) &= \nabla \cdot (k_f \cdot \nabla h_f(r, t)) \\ &+ \eta \left(-\frac{\eta}{S_{S_m}} \int_0^t (r, y) E_\alpha \left(\frac{\eta}{S_{S_m}} (t-y) \right) dy - h_f(r, t) \right) + q_f \end{aligned}$$

Let

$${}^{\text{RL}}I_t^\alpha f(t) = \frac{1}{\Gamma(\alpha)} \int_0^t (t-\tau)^{\alpha-1} f(\tau) d\tau \quad (96)$$

We aim to prove that Γ possesses Lipschitz condition.

Let

$$K(r, t, h) = \nabla \cdot (k_f \cdot \nabla h_f(r, t)) - \frac{\eta^2}{S_{sm}} \int_0^t h_f(r, y) E_\alpha \left(\frac{\eta}{S_{sm}} (t-y) \right) dy \quad (97)$$

Let $h_1, h_2 \in H^1(0, T)$ then

$$\begin{aligned} & \left\| K(r, t, h_1) - K(r, t, h_2) \right\|_{H^1(0, T)} \leq \left\| \nabla \cdot (k_f \cdot \nabla h_f(r, t)) - \nabla \cdot (k_f \cdot \nabla h_2(r, t)) \right\| + \\ & \left\| \frac{\eta^2}{S_{sm}} \int_0^t \|h_1(r, y) - h_2(r, y)\| E_\alpha \left(\frac{\eta}{S_{sm}} (t-y) \right) dy \right\| \\ & \leq \theta_1 \theta_2 \|k_f\| \|h_1 - h_2\| + \left\| \frac{\eta^2}{S_{sm}} \right\| \|h_1 - h_2\|_{H^1(0, T)} M + \|\eta\| \|h_1 - h_2\| \\ & \leq \left(\theta_1 \theta_2 \|k_f\| + \left\| \frac{\eta^2}{S_{sm}} \right\| M + \|\eta\| \right) \|h_1 - h_2\|_{H^1(0, T)} \\ & \leq l \|h_1 - h_2\| \end{aligned} \quad (98)$$

With the definition of K , we define the following function

$$\Gamma h = \frac{1}{\Gamma(\alpha)} \int_0^t K(r, \tau, h) (t-\tau)^{\alpha-1} d\tau$$

Let h_1 and h_2 be elements of $H^1(0, T)$

$$\begin{aligned}
 \|\Gamma_1 h_1 - \Gamma_1 h_2\|_{H^1(0,T)} &= \left\| \frac{1}{\Gamma(\alpha)} \int_0^t (K(r, \tau, h_1) - K(r, \tau, h_2))(t - \tau)^{\alpha-1} d\tau \right\|_{H^1(0,T)} \\
 &\leq \frac{1}{\Gamma(\alpha)} \int_0^t \|K(r, \tau, h_1) - K(r, \tau, h_2)\| (t - \tau)^{\alpha-1} d\tau \\
 &\leq \frac{1}{\Gamma(\alpha)} \int_0^t l \|h_1 - h_2\| (t - \tau)^{\alpha-1} d\tau \\
 &\leq \frac{l}{\Gamma(\alpha)} \|h_1 - h_2\|_{H^1(0,T)} \frac{T^{\alpha-1}}{\alpha} \\
 &\leq \frac{lT^\alpha}{\Gamma(\alpha+1)} \|h_1 - h_2\|_{H^1(0,T)} \\
 &\leq \beta \|h_1 - h_2\|_{H^1(0,T)}
 \end{aligned} \tag{99}$$

Let us consider the following recursive formula

$$\begin{aligned}
 h_f^{n+1}(r, t) &= \Gamma_1 h_f^n = h_f(r, 0) + \frac{1}{\Gamma(\alpha)} \int_0^t K(h_f^n, r, \tau)(t - \tau)^{\alpha-1} d\tau \\
 \|\Gamma_1 h_f^n - \Gamma_1 h_f^{n-1}\|_{H^1(0,T)} &= \|h_f^{n+1} - h_f^n\|_{H^1(0,T)} \\
 &= \frac{1}{\Gamma(\alpha)} \left\| \int_0^t \{K(h_f^n, r, \tau) - K(h_f^{n-1}, r, \tau)\} (t - \tau)^{\alpha-1} d\tau \right\| \\
 &\leq \frac{l}{\Gamma(\alpha)} \|h_f^{n-1} - h_f^n\|_{H^1(0,T)} \frac{T^\alpha}{\alpha} = \frac{lT^\alpha}{\Gamma(\alpha+1)} \|h_f^{n-1} - h_f^n\|_{H^1(0,T)}
 \end{aligned} \tag{100}$$

Recursively on n , we obtain

$$\left\| \Gamma_1 h_f^n - \Gamma_1 h_f^{n-1} \right\| \leq \left(\frac{lT^\alpha}{\Gamma(\alpha+1)} \right)^n \left\| h_f^1(r, t) \right\| \quad (101)$$

We chose $\frac{lT^\alpha}{\Gamma(\alpha+1)}$ such $\frac{lT^\alpha}{\Gamma(\alpha+1)} < 1$ then for $n \rightarrow \infty$

$\left\| \Gamma_1 h_f^n - \Gamma_1 h_f^{n-1} \right\| \rightarrow 0$, thus $(h_f^n)_{n \in \mathbb{N}}$ to a Cauchy sequence in a Banach space

therefore converge toward h_f . Taking the limit on both sides, we obtain

$$\lim_{n \rightarrow \infty} h_f^{n+1} = \Gamma_1 h_f^n \Leftrightarrow h_f = \Gamma h_f$$

This shows that Γ has a solution and is unique

4.3 Numerical Solution

In this section, we argue the fact that the storativity coefficients within the aquifer follow the power decay law as suggested in the system of equation. Here we suggest that the storativity coefficient may follow the exponential law with an upper boundary. With this in mind, we present the numerical solution of the system of equation using the ‘‘Upwind’’ numerical scheme in space and the Crank-Nicholson in space. We first for each non-local operator present its numerical approximation for time derivative.

We present first the numerical approximation of Caputo fractional derivative in time. Let

$$t_{n+1} - t_n = \Delta t, u(t_n, x_i) = u_i^n$$

$$\begin{aligned}
 {}_0^c D_t^\alpha u(x_i, t_n) &= \frac{1}{\Gamma(1-\alpha)} \int_0^{t_n} \frac{\partial u(x_i, \tau)}{\partial t} (t_n - \tau)^{-\alpha} d\tau \\
 &= \frac{1}{\Gamma(1-\alpha)} \sum_{j=0}^n \int_{t_j}^{t_{j+1}} \frac{u_i^{j+1} - u_i^j}{\Delta t} (t_n - \tau)^{-\alpha} d\tau \\
 &= \frac{1}{\Gamma(1-\alpha)} \sum_{j=0}^n \frac{u_i^{j+1} - u_i^j}{\Delta t} \int_{t_j}^{t_{j+1}} (t_n - \tau)^{-\alpha} d\tau \\
 &= \frac{1}{\Gamma(1-\alpha)} \sum_{j=0}^n \frac{u_i^{j+1} - u_i^j}{\Delta t} \left(-\frac{Y^{-\alpha+1}}{1-\alpha} \Big|_{t_n-t_j}^{t_n-t_{j+1}} \right) \\
 &= \frac{1}{\Gamma(2-\alpha)} \sum_{j=0}^n \frac{u_i^{j+1} - u_i^j}{\Delta t} \left\{ ((n-j)\Delta t)^{1-\alpha} - ((n-j-1)\Delta t)^{1-\alpha} \right\} \\
 &= \frac{1}{\Gamma(2-\alpha)} \sum_{j=0}^n (u_i^{j+1} - u_i^j) \left\{ ((n-j)\Delta t)^{1-\alpha} - ((n-j-1)\Delta t)^{1-\alpha} \right\}
 \end{aligned} \tag{102}$$

We consider the second order upwind scheme for first order space derivate

$$u_x^- = \frac{3u_i^n - 4u_{i-1}^n + 3u_{i-2}^n}{2(\Delta x)}, \quad u_x^+ = \frac{-u_{i+2}^n - 4u_{i+1}^n + 3u_i^n}{2(\Delta x)} \tag{103}$$

This numerical scheme has been recognized as a powerful mathematical scheme with the ability to have less diffusive compared to the classical first order accurate scheme which is also recognized as a linear Upwind differencing scheme. However one can have the third order. With the third order Upwind numerical scheme, we have the following discretization:

$$u_x^- = \frac{2u_i^n + 3u_{i-1}^n - 6u_{i-2}^n + u_{i-3}^n}{6(\Delta x)}, \quad u_x^+ = \frac{-2u_{i+3}^n + 6u_{i+2}^n - 3u_{i+1}^n - 2u_i^n}{6(\Delta x)}$$

(104)

It is argued in the literature that this numerical scheme is less diffusive compared to the second-order scheme (Courant et al., 1952; Versteeg and Malalasekera, 1995). We shall note that, it is also known to introduce slight dispersive errors in the region where the gradient is elevated. Thus with second order upwind scheme, we have the following numerical formulas:

$$\begin{aligned} & \sum_{j=0}^n \frac{h_{f_i}^{j+1} - h_{f_i}^j}{(\Delta t)^\alpha \Gamma(2-\alpha)} \left\{ (n-j)^{1-\alpha} - (n-j-1)^{1-\alpha} \right\} S_{sf}(r_i) \\ &= \frac{k_f^{j+1} - k_f^j}{(\Delta r)} \bullet \frac{3h_{f_i}^n - 4h_{f(i-1)}^n + 3h_{f(i-2)}^n}{2(\Delta r)} + \\ & k_f^i \left\{ \frac{h_{f_1(i+1)}^{n+1} - 2h_{f_1(i)}^{n+1} + h_{f_1(i-1)}^{n+1}}{2(\Delta r)^2} + \frac{h_{f_1(i+1)}^n - 2h_{f_1(i)}^n + h_{f_1(i-1)}^n}{2(\Delta r)^2} \right\} \\ & + \eta \{ h_{m_i}^n - h_{f_i}^n \}, \end{aligned} \tag{105}$$

$$\sum_{j=0}^n \frac{h_{m_i}^{j+1} - h_{m_i}^j}{(\Delta t)^\alpha \Gamma(2-\alpha)} \left\{ (n-j)^{1-\alpha} - (n-j-1)^{1-\alpha} \right\} S_{sm}(r_i) = \eta (h_{m_i}^n - h_{f_i}^n)$$

if $\frac{k_f^{j+1} - k_f^j}{(\Delta r)} > 0$

And

$$\begin{aligned}
 & \sum_{j=0}^n \frac{h_{f_i}^{j+1} - h_{f_i}^j}{(\Delta t)^\alpha \Gamma(2-\alpha)} \left\{ (n-j)^{1-\alpha} - (n-j-1)^{1-\alpha} \right\} S_{sf}(r_i) \\
 &= \frac{k_f^{j+1} - k_f^j}{(\Delta r)} \bullet \frac{-h_{f(i+2)}^n - 4h_{f(i+1)}^n + 3h_{f_i}^n}{2(\Delta x)} + \\
 & k_f^i \left\{ \frac{h_{f_1(i+1)}^{n+1} - 2h_{f_1(i)}^{n+1} + h_{f_1(i-1)}^{n+1}}{2(\Delta r)^2} + \frac{h_{f_1(i+1)}^n - 2h_{f_1(i)}^n + h_{f_1(i-1)}^n}{2(\Delta r)^2} \right\} \\
 & + \eta \left\{ h_{m_i}^n - h_{f_i}^n \right\}, \\
 & \sum_{j=0}^n \frac{h_{m_i}^{j+1} - h_{m_i}^j}{(\Delta t)^\alpha \Gamma(2-\alpha)} \left\{ (n-j)^{1-\alpha} - (n-j-1)^{1-\alpha} \right\} S_{sm}(r_i) = \eta \left(h_{m_i}^n - h_{f_i}^n \right) \\
 & \text{if } \frac{k_f^{j+1} - k_f^j}{(\Delta r)} < 0
 \end{aligned}$$

(106)

Thus with the third order upwind numerical scheme, we obtain:

$$\begin{aligned}
 & \sum_{j=0}^n \frac{h_{f_i}^{j+1} - h_{f_i}^j}{(\Delta t)^\alpha \Gamma(2-\alpha)} \left\{ (n-j)^{1-\alpha} - (n-j-1)^{1-\alpha} \right\} S_{sf}(r_i) \\
 &= \frac{k_f^{j+1} - k_f^j}{(\Delta r)} \bullet \frac{2h_{f_i}^n + 3h_{f(i-1)}^n - 6h_{f(i-2)}^n + h_{f(i-3)}^n}{6(\Delta r)} + \\
 & k_f^i \left\{ \frac{h_{f_1(i+1)}^{n+1} - 2h_{f_1(i)}^{n+1} + h_{f_1(i-1)}^{n+1}}{2(\Delta r)^2} + \frac{h_{f_1(i+1)}^n - 2h_{f_1(i)}^n + h_{f_1(i-1)}^n}{2(\Delta r)^2} \right\} \\
 & + \eta \{ h_{mi}^n - h_{f_i}^n \}, \\
 & \sum_{j=0}^n \frac{h_{mi}^{j+1} - h_{mi}^j}{(\Delta t)^\alpha \Gamma(2-\alpha)} \left\{ (n-j)^{1-\alpha} - (n-j-1)^{1-\alpha} \right\} S_{sm}(r_i) = \eta (h_{mi}^n - h_{f_i}^n) \\
 & \text{if } \frac{k_f^{j+1} - k_f^j}{(\Delta r)} > 0
 \end{aligned}$$

(107)

And

$$\begin{aligned}
 & \sum_{j=0}^n \frac{h_{f_i}^{j+1} - h_{f_i}^j}{(\Delta t)^\alpha \Gamma(2-\alpha)} \left\{ (n-j)^{1-\alpha} - (n-j-1)^{1-\alpha} \right\} S_{sf}(r_i) \\
 &= \frac{k_f^{j+1} - k_f^j}{(\Delta r)} \bullet \frac{-2h_{f(i+3)}^n + 6h_{f(i+2)}^n - 3h_{f(i+1)}^n - 2h_{f_i}^n}{6(\Delta r)} + \\
 & k_f^i \left\{ \frac{h_{f_1(i+1)}^{n+1} - 2h_{f_1(i)}^{n+1} + h_{f_1(i-1)}^{n+1}}{2(\Delta r)^2} + \frac{h_{f_1(i+1)}^n - 2h_{f_1(i)}^n + h_{f_1(i-1)}^n}{2(\Delta r)^2} \right\} \\
 & + \eta \left\{ h_{m_i}^n - h_{f_i}^n \right\}, \\
 & \sum_{j=0}^n \frac{h_{m_i}^{j+1} - h_{m_i}^j}{(\Delta t)^\alpha \Gamma(2-\alpha)} \left\{ (n-j)^{1-\alpha} - (n-j-1)^{1-\alpha} \right\} S_{sm}(r_i) = \eta \left(h_{m_i}^n - h_{f_i}^n \right) \\
 & \text{if } \frac{k_f^{j+1} - k_f^j}{(\Delta r)} < 0
 \end{aligned} \tag{108}$$

4.4 Model of fractal flow in dual media accounting for visco-elasticity

In a dual media the water flows within the fracture network and also within the matrix rock as we said before. These matrix rocks possess different characteristics. In this section, we consider the matrix soil with the property of visco-elasticity. We shall note that a suitable or realistic representation of the subsurface may be achieved by putting together the mechanical properties of the elastic solids and that of the viscous fluids. In the resulting medium or material the stress depends both on the strain and the rate of strain together, as well as higher time derivatives of the strain. Such geological formation which combines solid-like and liquid-like behaviour is called visco-elastic. This section considers fractal dual flow simulation in a general heterogeneous inelastic geological formation within the framework of the theory of linear visco-elasticity. In this case, it is assumed that, groundwater flows within the matrix rock which has visco-elastic property. It is well documented that the real world observation cannot be described with the time classical derivative but can efficiently be described with the non-local operator with a Mittag-Leffler kernel known as Atangana-Baleanu fractional

derivative in Caputo and Riemann-Liouville sense. Thus in order to include into mathematical formula the effect of elasticity of the matrix rock, the time local derivative will be replaced by the Atangana-Baleanu fractional derivative to obtain:

$$\begin{cases} \mathcal{S}_{S_f} \quad {}_0^{ABC} D_t^\alpha (h_f(r,t)) = \nabla \cdot (k_f \cdot \nabla h_f(r,t)) + \eta (h_m(r,t) - h_f(r,t)) + q_f \\ \mathcal{S}_{S_m} \quad {}_0^{ABC} D_t^\alpha (h_m(r,t)) = \eta (h_m(r,t) - h_f(r,t)) \end{cases} \quad (109)$$

We shall first present the existence and uniqueness of the above system.

4.4.1 Existence of system solutions

In this section, the well-constructed Sobolev space is considered. In this paper, we consider the following Sobolev space

$$H^1(0,T) = \left\{ u \in L^2(a,b) / u' \in L^2(a,b) \right\}$$

We also consider the following Hilbert space where

$$H \in \left\{ u, v / \int_0^t E_\alpha \left[-\frac{\alpha}{1-\alpha} (t-y)^\alpha \right] v u dy < \infty \right\}. \quad (110)$$

To prove the existence of equation (109), we express the change of hydraulic head within the matrix soil in terms of the change of hydraulic head within the fracture as presented earlier in the case of power law. To achieve this we employ the Laplace transform in time to obtain:

$$\begin{aligned}
 \frac{S_{S_m}(r, \alpha) p^\alpha h_m(r, p)}{p^\alpha + \frac{\alpha}{1-\alpha}} &= \eta (h_m(r, p) - h_f(r, p)) \\
 \left(\frac{S_{S_m}(r, \alpha) p^\alpha}{p^\alpha + \frac{\alpha}{1-\alpha}} - \eta \right) h_m(r, p) &= -\eta h_f(r, p), \\
 h_m(r, p) &= \frac{-\eta h_f(r, p)}{\left(\frac{S_{S_m}(r, \alpha) p^\alpha}{p^\alpha + \frac{\alpha}{1-\alpha}} - \eta \right)}, \\
 h_m(r, t) &= L^{-1} \left(\frac{-\eta h_f(r, p)}{\left(\frac{S_{S_m}(r, \alpha) p^\alpha}{p^\alpha + \frac{\alpha}{1-\alpha}} - \eta \right)} \right), \\
 h_m(r, t) &= \frac{\eta}{\eta - S_{S_m}(r, \alpha)} \int_0^t h_f(r, y) E_\alpha \left(\frac{\alpha \eta}{(\eta - S_{S_m}(r, \alpha))(1-\alpha)} (t-y)^\alpha \right) dy + \\
 &\quad \frac{\eta \alpha}{(1-\alpha)(\eta - S_{S_m}(r, \alpha))} \int_0^t h_f(r, y) E_\alpha \left(\frac{\alpha \eta}{(\eta - S_{S_m}(r, \alpha))(1-\alpha)} (t-y) \right) dy.
 \end{aligned} \tag{111}$$

Equation (28) can now be replaced in system (26) to obtained

$$\begin{aligned}
 S_{S_f} {}_0^{ABC} D_t^\alpha (h_f(r, t)) &= \nabla \cdot (k_f \cdot \nabla h_f(r, t)) + \\
 \eta \left(\left[\frac{\eta}{\eta - S_{S_m}(r, \alpha)} \int_0^t h_f(r, y) E_\alpha \left(\frac{\alpha \eta}{(\eta - S_{S_m}(r, \alpha))(1-\alpha)} (t-y)^\alpha \right) dy + \right. \right. \\
 \left. \left[\frac{\eta \alpha}{(1-\alpha)(\eta - S_{S_m}(r, \alpha))} \int_0^t h_f(r, y) E_\alpha \left(\frac{\alpha \eta}{(\eta - S_{S_m}(r, \alpha))(1-\alpha)} (t-y) \right) dy \right] \right) &+ q_f \tag{112} \\
 -h_f(r, t) &
 \end{aligned}$$

Let us consider the following function

$$T_1 : H^1(0, T) \rightarrow H^1(0, T)$$

$$v \rightarrow T_1 v = {}_0^{AB}I_t^\alpha \left(\begin{array}{l} \nabla \cdot (k_f \cdot \nabla v(r, t)) \\ \left\{ \begin{array}{l} \frac{\eta}{\eta - S_{s_m}(r, \alpha)} \int_0^t h_f(r, y) E_\alpha \left(\frac{\alpha \eta}{(\eta - S_{s_m}(r, \alpha))(1 - \alpha)} (t - y)^\alpha \right) dy + \\ \frac{\eta \alpha}{(1 - \alpha)(\eta - S_{s_m}(r, \alpha))} \int_0^t h_f(r, y) E_\alpha \left(\frac{\alpha \eta}{(\eta - S_{s_m}(r, \alpha))(1 - \alpha)} (t - y) \right) dy \end{array} \right\} + q_f \\ -h_f(r, t) \end{array} \right) \quad (113)$$

The fractional integral used here is known as Atangana-Baleanu fractional integral and is given as:

$${}_0^{AB}I_t^\alpha f(t) = \frac{1 - \alpha}{AB(\alpha)} f(t) + \frac{\alpha}{AB(\alpha)\Gamma(\alpha)} \int_0^t (t - \tau)^{\alpha - 1} f(\tau) d\tau \quad (114)$$

We aim to prove that T_1 possesses Lipchitz condition.

Let us consider the following operator:

$$B(r, t, v) = \nabla \cdot (k_f \cdot \nabla v(r, t)) +$$

$$\eta \left(\begin{array}{l} \left\{ \begin{array}{l} \frac{\eta}{\eta - S_{s_m}(r, \alpha)} \int_0^t v(r, y) E_\alpha \left(\frac{\alpha \eta}{(\eta - S_{s_m}(r, \alpha))(1 - \alpha)} (t - y)^\alpha \right) dy + \\ \frac{\eta \alpha}{(1 - \alpha)(\eta - S_{s_m}(r, \alpha))} \int_0^t v(r, y) E_\alpha \left(\frac{\alpha \eta}{(\eta - S_{s_m}(r, \alpha))(1 - \alpha)} (t - y) \right) dy \end{array} \right\} \\ -v(r, t) \end{array} \right) \quad (115)$$

Let

$h_1, h_2 \in H^1(0, T)$ then:

$$\begin{aligned}
 & \left\| B(r, t, h_1) - B(r, t, h_2) \right\|_{H^1(0, T)} \leq \left\| \nabla \cdot (k_f \cdot \nabla h_1(r, t)) - \nabla \cdot (k_f \cdot \nabla h_2(r, t)) \right\| + \\
 & \left\| \frac{\eta}{\eta - S_{s_m}(r, \alpha)} \right\| \left\| \int_0^t \|h_1(r, y) - h_2(r, y)\| E_\alpha \left(\frac{\alpha \eta}{(\eta - S_{s_m}(r, \alpha))(1 - \alpha)} (t - y)^\alpha \right) dy + \right. \\
 & \left. \left\| \frac{\eta \alpha}{(\eta - S_{s_m}(r, \alpha))(1 - \alpha)} \right\| \left\| \int_0^t \|h_1(r, y) - h_2(r, y)\| E_\alpha \left(\frac{\alpha \eta}{(\eta - S_{s_m}(r, \alpha))(1 - \alpha)} (t - y) \right) dy \right\| \right. \\
 & \leq \theta_1 \theta_2 \|k_f\| \|h_1 - h_2\| + \left\| \frac{\eta M_2}{\eta - S_{s_m}(r, \alpha)} + \frac{\eta \alpha M_1}{(\eta - S_{s_m}(r, \alpha))(1 - \alpha)} \right\| \|h_1 - h_2\|_{H^1(0, T)} + \|\eta\| \|h_1 - h_2\| \\
 & \leq \left(\theta_1 \theta_2 \|k_f\| + \left\| \frac{\eta M_2}{\eta - S_{s_m}(r, \alpha)} + \frac{\eta \alpha M_1}{(\eta - S_{s_m}(r, \alpha))(1 - \alpha)} \right\| + \|\eta\| \right) \|h_1 - h_2\|_{H^1(0, T)} \\
 & \leq l_1 \|h_1 - h_2\|
 \end{aligned} \tag{116}$$

Using the definition of B presented previously, we consider the following operator

$$Ph = \frac{1 - \alpha}{AB(\alpha)} B(r, \tau, h) + \frac{\alpha}{AB(\alpha)\Gamma(\alpha)} \int_0^t K(r, \tau, h) (t - \tau)^{\alpha - 1} d\tau \tag{117}$$

Let h_1 and h_2 be elements of $H^1(0, T)$

$$\begin{aligned}
 \|Ph_1 - Ph_2\|_{H^1(0,T)} &= \left\| \frac{1-\alpha}{AB(\alpha)} \left\{ (B(r,\tau,h_1) - B(r,\tau,h_2)) \right\} + \right. \\
 &\quad \left. \frac{\alpha}{AB(\alpha)\Gamma(\alpha)} \int_0^t (B(r,\tau,h_1) - B(r,\tau,h_2))(t-\tau)^{\alpha-1} d\tau \right\|_{H^1(0,T)} \\
 &\leq \frac{1-\alpha}{AB(\alpha)} \left\| \left\{ (B(r,\tau,h_1) - B(r,\tau,h_2)) \right\} \right\|_{H^1(0,T)} + \\
 &\quad \frac{\alpha}{AB(\alpha)\Gamma(\alpha)} \int_0^t \|B(r,\tau,h_1) - B(r,\tau,h_2)\| (t-\tau)^{\alpha-1} d\tau \\
 &\leq \frac{(1-\alpha)l_1}{AB(\alpha)} + \frac{\alpha}{AB(\alpha)\Gamma^2(\alpha)} \int_0^t l_1 \|h_1 - h_2\| (t-\tau)^{\alpha-1} d\tau \\
 &\leq \left\{ \frac{(1-\alpha)l_1}{AB(\alpha)} + \frac{l_1 T^\alpha}{AB(\alpha)\Gamma(\alpha)} \right\} \|h_1 - h_2\|_{H^1(0,T)} \\
 &\leq \left\{ \frac{(1-\alpha)l_1}{AB(\alpha)} + \frac{l_1 T^\alpha}{AB(\alpha)\Gamma^2(\alpha)} \right\} \|h_1 - h_2\|_{H^1(0,T)} \\
 &\leq \beta_1 \|h_1 - h_2\|_{H^1(0,T)}
 \end{aligned} \tag{118}$$

In this section, the establishment of the existence of the system solutions will be achieved using the Picard integrative approach. Thus let us consider the following Volterra equation based on Atangana-Baleanu fractional integral.

$$h_f^{n+1}(r,t) = Ph_f^n = \frac{1-\alpha}{AB(\alpha)} B(h_f^n, r, \tau) + \frac{\alpha}{AB(\alpha)\Gamma(\alpha)} \int_0^t B(h_f^n, r, \tau) (t-\tau)^{\alpha-1} d\tau \tag{119}$$

Thus,

$$\begin{aligned}
 & \left\| Ph_f^n - Ph_f^{n-1} \right\|_{H^1(0,T)} = \left\| h_f^{n+1} - h_f^n \right\|_{H^1(0,T)} \\
 & = \frac{1-\alpha}{AB(\alpha)} \left(B(h_f^n, r, \tau) - B(h_f^{n-1}, r, \tau) \right) + \frac{\alpha}{AB(\alpha)\Gamma(\alpha)} \left\| \int_0^t \left\{ B(h_f^n, r, \tau) - B(h_f^{n-1}, r, \tau) \right\} (t-\tau)^{\alpha-1} d\tau \right\| \\
 & \leq \left\{ \frac{(1-\alpha)l_1}{AB(\alpha)} + \frac{l_1 T^\alpha}{AB(\alpha)\Gamma(\alpha)} \right\} \left\| h_f^{n-1} - h_f^n \right\|_{H^1(0,T)}
 \end{aligned} \tag{120}$$

Recursively on n , we obtain

$$\left\| Ph_f^n - Ph_f^{n-1} \right\| \leq \left\{ \frac{(1-\alpha)l_1}{AB(\alpha)} + \frac{l_1 T^\alpha}{AB(\alpha)\Gamma(\alpha)} \right\}^n \left\| h_f^1 \right\|_{H^1(0,T)} \tag{121}$$

The choice of l_1 such that, for a very large n

$$\left\{ \frac{(1-\alpha)l_1}{AB(\alpha)} + \frac{l_1 T^\alpha}{AB(\alpha)\Gamma(\alpha)} \right\}^n \rightarrow 0 \tag{122}$$

$\left\| Ph_f^n - Ph_f^{n-1} \right\| \rightarrow 0$, thus $(h_f^n)_{n \in \mathbb{N}}$ to a Cauchy sequence in a Banach space therefore converge toward h_f . Taking the limit on both sides, we obtain

$$\lim_{x \rightarrow \infty} h_f^{n+1} = Ph_f^n \Leftrightarrow h_f = Ph_f$$

This shows that B has a solution and is unique and the unique solution is the solution of equation (109).

4.5 Numerical Solution with Mittag-Leffler law

We present the numerical solution of the system of equation using the Upwind numerical scheme in space and the Crank-Nicholson in space. We present first the numerical approximation of the Atangana-Baleanu fractional derivative in Caputo sense. Let

$$t_{n+1} - t_n = \Delta t, u(t_n, x_i) = u_i^n,$$

Then the Atangana-Baleanu fractional derivative in Caputo sense is approximated as:

$$\begin{aligned}
 {}^{ABC}D_t^\alpha u(x_i, t_n) &= \frac{AB(\alpha)}{(1-\alpha)} \int_0^{t_n} \frac{\partial u(x_i, \tau)}{\partial t} E_\alpha \left\{ -\frac{\alpha}{1-\alpha} (t_n - \tau)^\alpha \right\} d\tau \\
 &= \frac{AB(\alpha)}{(1-\alpha)} \sum_{j=0}^n \int_{t_j}^{t_{j+1}} \frac{u_i^{j+1} - u_i^j}{\Delta t} E_\alpha \left\{ -\frac{\alpha}{1-\alpha} (t_n - \tau)^\alpha \right\} d\tau \\
 &= \frac{AB(\alpha)}{(1-\alpha)} \sum_{j=0}^n \frac{u_i^{j+1} - u_i^j}{\Delta t} \int_{t_j}^{t_{j+1}} E_\alpha \left\{ -\frac{\alpha}{1-\alpha} (t_n - \tau)^\alpha \right\} d\tau \\
 &= \frac{AB(\alpha)}{(1-\alpha)} \sum_{j=0}^n \frac{u_i^{j+1} - u_i^j}{\Delta t} \left\{ -(t_n - t_{j+1}) E_{\alpha,2} \left(-\frac{\alpha}{1-\alpha} (t_n - t_{j+1}) \right) + (t_n - t_j) E_{\alpha,2} \left(-\frac{\alpha}{1-\alpha} (t_n - t_j) \right) \right\} \\
 &= \frac{AB(\alpha)}{(1-\alpha)} \sum_{j=0}^n \frac{u_i^{j+1} - u_i^j}{\Delta t} \left\{ -\Delta t (n-j-1) E_{\alpha,2} \left(-\frac{\alpha \Delta t}{1-\alpha} (n-j-1) \right) + \Delta t (n-j) E_{\alpha,2} \left(-\frac{\alpha \Delta t}{1-\alpha} (n-j) \right) \right\} \\
 &= \frac{AB(\alpha)}{(1-\alpha)} \sum_{j=0}^n (u_i^{j+1} - u_i^j) \left\{ (n-j) E_{\alpha,2} \left(-\frac{\alpha \Delta t}{1-\alpha} (n-j) \right) - (n-j-1) E_{\alpha,2} \left(-\frac{\alpha \Delta t}{1-\alpha} (n-j-1) \right) \right\}
 \end{aligned} \tag{123}$$

Using the above numerical approximation and the Upwind second order in space, we obtain the below numerical formula.

$$\begin{aligned}
 & \frac{AB(\alpha)}{(1-\alpha)} \sum_{j=0}^n (h_{fi}^{j+1} - h_{fi}^j) \left\{ \begin{array}{l} (n-j)E_{\alpha,2} \left(-\frac{\alpha\Delta t}{1-\alpha} (n-j) \right) - \\ (n-j-1)E_{\alpha,2} \left(-\frac{\alpha\Delta t}{1-\alpha} (n-j-1) \right) \end{array} \right\} S_{sf}(r_i) \\
 &= \frac{k_f^{j+1} - k_f^j}{(\Delta r)} \bullet \frac{3h_{fi}^n - 4h_{f(i-1)}^n + 3h_{f(i-2)}^n}{2(\Delta r)} + \\
 & k_f^i \left\{ \frac{h_{f_1(i+1)}^{n+1} - 2h_{f_1(i)}^{n+1} + h_{f_1(i-1)}^{n+1}}{2(\Delta r)^2} + \frac{h_{f_1(i+1)}^n - 2h_{f_1(i)}^n + h_{f_1(i-1)}^n}{2(\Delta r)^2} \right\} \\
 & + \eta \{ h_{mi}^n - h_{fi}^n \}, \\
 & \frac{AB(\alpha)}{(1-\alpha)} \sum_{j=0}^n (h_{fi}^{j+1} - h_{fi}^j) \left\{ \begin{array}{l} (n-j)E_{\alpha,2} \left(-\frac{\alpha\Delta t}{1-\alpha} (n-j) \right) - \\ (n-j-1)E_{\alpha,2} \left(-\frac{\alpha\Delta t}{1-\alpha} (n-j-1) \right) \end{array} \right\} S_{Sm}(r_i) = \eta (h_{mi}^n - h_{fi}^n) \\
 & \text{if } \frac{k_f^{j+1} - k_f^j}{(\Delta r)} > 0
 \end{aligned} \tag{124}$$

And

$$\begin{aligned}
 & \frac{AB(\alpha)}{(1-\alpha)} \sum_{j=0}^n \left(h_{fi}^{j+1} - h_{fi}^j \right) \left\{ \begin{array}{l} (n-j)E_{\alpha,2} \left(-\frac{\alpha\Delta t}{1-\alpha} (n-j) \right) - \\ (n-j-1)E_{\alpha,2} \left(-\frac{\alpha\Delta t}{1-\alpha} (n-j-1) \right) \end{array} \right\} S_{sf}(r_i) \\
 &= \frac{k_f^{j+1} - k_f^j}{(\Delta r)} \bullet \frac{-h_{f(i+2)}^n - 4h_{f(i+1)}^n + 3h_{fi}^n}{2(\Delta r)} + \\
 & k_f^i \left\{ \frac{h_{f_1(i+1)}^{n+1} - 2h_{f_1(i)}^{n+1} + h_{f_1(i-1)}^{n+1}}{2(\Delta r)^2} + \frac{h_{f_1(i+1)}^n - 2h_{f_1(i)}^n + h_{f_1(i-1)}^n}{2(\Delta r)^2} \right\} \\
 & + \eta \{ h_{mi}^n - h_{fi}^n \}, \\
 & \frac{AB(\alpha)}{(1-\alpha)} \sum_{j=0}^n \left(h_{fi}^{j+1} - h_{fi}^j \right) \left\{ \begin{array}{l} (n-j)E_{\alpha,2} \left(-\frac{\alpha\Delta t}{1-\alpha} (n-j) \right) - \\ (n-j-1)E_{\alpha,2} \left(-\frac{\alpha\Delta t}{1-\alpha} (n-j-1) \right) \end{array} \right\} S_{S_m}(r_i) = \eta (h_{mi}^n - h_{fi}^n) \\
 & \text{if } \frac{k_f^{j+1} - k_f^j}{(\Delta r)} > 0
 \end{aligned} \tag{125}$$

Thus with the third order upwind numerical scheme, we obtain

$$\begin{aligned}
 & \frac{AB(\alpha)}{(1-\alpha)} \sum_{j=0}^n (h_{f_i}^{j+1} - h_{f_i}^j) \left\{ \begin{array}{l} (n-j)E_{\alpha,2} \left(-\frac{\alpha\Delta t}{1-\alpha} (n-j) \right) - \\ (n-j-1)E_{\alpha,2} \left(-\frac{\alpha\Delta t}{1-\alpha} (n-j-1) \right) \end{array} \right\} S_{sf}(r_i) \\
 &= \frac{k_f^{j+1} - k_f^j}{(\Delta r)} \bullet \frac{2h_{f_i}^n + 3h_{f_i(i-1)}^n - 6h_{f_i(i-2)}^n + h_{f_i(i-3)}^n}{6(\Delta r)} + \\
 & k_f^i \left\{ \frac{h_{f_i(i+1)}^{n+1} - 2h_{f_i(i)}^{n+1} + h_{f_i(i-1)}^{n+1}}{2(\Delta r)^2} + \frac{h_{f_i(i+1)}^n - 2h_{f_i(i)}^n + h_{f_i(i-1)}^n}{2(\Delta r)^2} \right\} \\
 & + \eta \{ h_{m_i}^n - h_{f_i}^n \}, \tag{126}
 \end{aligned}$$

$$\frac{AB(\alpha)}{(1-\alpha)} \sum_{j=0}^n (h_{f_i}^{j+1} - h_{f_i}^j) \left\{ \begin{array}{l} (n-j)E_{\alpha,2} \left(-\frac{\alpha\Delta t}{1-\alpha} (n-j) \right) - \\ (n-j-1)E_{\alpha,2} \left(-\frac{\alpha\Delta t}{1-\alpha} (n-j-1) \right) \end{array} \right\} S_{S_m}(r_i) = \eta (h_{m_i}^n - h_{f_i}^n)$$

$$\text{if } \frac{k_f^{j+1} - k_f^j}{(\Delta r)} > 0$$

And

$$\begin{aligned}
 & \frac{AB(\alpha)}{(1-\alpha)} \sum_{j=0}^n \left(h_{f_i}^{j+1} - h_{f_i}^j \right) \left\{ \begin{array}{l} (n-j)E_{\alpha,2} \left(-\frac{\alpha\Delta t}{1-\alpha} (n-j) \right) - \\ (n-j-1)E_{\alpha,2} \left(-\frac{\alpha\Delta t}{1-\alpha} (n-j-1) \right) \end{array} \right\} S_{sf}(r_i) \\
 &= \frac{k_f^{j+1} - k_f^j}{(\Delta r)} \bullet \frac{-2h_{f(i+3)}^n + 6h_{f(i+2)}^n - 3h_{f(i+1)}^n - 2h_{f_i}^n}{6(\Delta r)} + \\
 & k_f^i \left\{ \frac{h_{f_1(i+1)}^{n+1} - 2h_{f_1(i)}^{n+1} + h_{f_1(i-1)}^{n+1}}{2(\Delta r)^2} + \frac{h_{f_1(i+1)}^n - 2h_{f_1(i)}^n + h_{f_1(i-1)}^n}{2(\Delta r)^2} \right\} \\
 & + \eta \{ h_{m_i}^n - h_{f_i}^n \}, \\
 & \frac{AB(\alpha)}{(1-\alpha)} \sum_{j=0}^n \left(h_{f_i}^{j+1} - h_{f_i}^j \right) \left\{ \begin{array}{l} (n-j)E_{\alpha,2} \left(-\frac{\alpha\Delta t}{1-\alpha} (n-j) \right) - \\ (n-j-1)E_{\alpha,2} \left(-\frac{\alpha\Delta t}{1-\alpha} (n-j-1) \right) \end{array} \right\} S_{S_m}(r_i) = \eta (h_{m_i}^n - h_{f_i}^n) \\
 & \text{if } \frac{k_f^{j+1} - k_f^j}{(\Delta r)} > 0
 \end{aligned} \tag{127}$$

4.6 Model of fractal flow in dual media with heterogeneity and visco-elasticity properties

In this section, we consider the model with a more complex non-local operator. The considered operator here is a convolution of power-Mittag-Leffler with the unknown function. This non-local operator was recently proposed by Atangana on his paper with title "Derivative with two fractional orders: A new avenue of investigation toward revolution in fractional calculus" (Atangana, 2016). Therefore using the new established non-local fractional operator suggested by Atangana, the modified model is given as follows:

$$\left\{ \begin{array}{l} S_{S_f} \quad {}^AC_0 D_t^\alpha (h_f(r,t)) = \nabla \cdot (k_f \cdot \nabla h_f(r,t)) + \eta (h_m(r,t) - h_f(r,t)) + q_f \\ S_{S_m} \quad {}^AC_0 D_t^\alpha (h_m(r,t)) = \eta (h_m(r,t) - h_f(r,t)) \end{array} \right. \tag{128}$$

The discussion regarding the analysis of existence and uniqueness of exact solution will not be presented in this section. Rather, the model will be solved numerically. To do this we present first the numerical approximation of the Atangana fractional derivative with two orders.

$$\begin{aligned}
 {}_0^A C D_t^{\alpha, \beta}(f(x, t)) &= \frac{A(\beta)}{1-\beta} \frac{1}{\Gamma(1-\alpha)} \int_0^t \partial_t f(x, y) (t-y)^{-\alpha} E_\beta \left(-\frac{\beta}{1-\beta} (t-y)^{\alpha+\beta} \right) dy, \\
 &= \frac{A(\beta)}{1-\beta} \frac{1}{\Gamma(1-\alpha)} \int_0^t \frac{f(x, y+\Delta y) - f(x, y)}{\Delta t} (t-y)^{-\alpha} E_\beta \left(-\frac{\beta}{1-\beta} (t-y)^{\alpha+\beta} \right) dy, \\
 &= \frac{A(\beta)}{1-\beta} \frac{1}{\Gamma(1-\alpha)} \sum_{j=0}^n \int_{t_j}^{t_{j+1}} \frac{f_i^{j+1} - f_i^j}{\Delta t} (t_n - y)^{-\alpha} E_\beta \left(-\frac{\beta}{1-\beta} (t_n - y)^{\alpha+\beta} \right) dy, \\
 &= \frac{A(\beta)}{1-\beta} \frac{1}{\Gamma(1-\alpha)} \sum_{j=0}^n \left(\frac{f_i^{j+1} - f_i^j}{\Delta t} \right) \int_{t_j}^{t_{j+1}} (t_n - y)^{-\alpha} E_\beta \left(-\frac{\beta}{1-\beta} (t_n - y)^{\alpha+\beta} \right) dy
 \end{aligned} \tag{129}$$

In the above expression, the integral is given as follows:

$$\begin{aligned}
 \int_{t_j}^{t_{j+1}} (t_n - y)^{-\alpha} E_\beta \left(-\frac{\beta}{1-\beta} (t_n - y)^{\alpha+\beta} \right) dy &= (t_n - t_{j+1})^{1-\alpha} E_{\beta, 2-\alpha} \left(-\frac{\beta}{1-\beta} (t_n - t_{j+1})^{\beta+\alpha} \right) + \\
 & (t_n - t_j)^{1-\alpha} E_{\beta, 2-\alpha} \left(-\frac{\beta}{1-\beta} (t_n - t_j)^{\beta+\alpha} \right)
 \end{aligned} \tag{130}$$

Replacing (130) in (129) we obtain the following numerical approximation

$${}_0^A C D_t^{\alpha, \beta} f(x_i, t_n) = \frac{A(\beta)}{(1-\beta)\Gamma(1-\alpha)} \sum_{j=1}^n \left(\frac{f_i^{j+1} - f_i^j}{\Delta t} \right) \left[\begin{aligned} & \left((t_n - t_{j+1})^{1-\alpha} E_{\beta, 2-\alpha} \left(-\frac{\beta}{1-\beta} (t_n - t_{j+1})^{\beta+\alpha} \right) \right) + \\ & \left((t_n - t_j)^{1-\alpha} E_{\beta, 2-\alpha} \left(-\frac{\beta}{1-\beta} (t_n - t_j)^{\beta+\alpha} \right) \right) \end{aligned} \right] \tag{131}$$

Coupling the Upwind for second order with the above the numerical solution of equation (129) is given as:

$$\begin{aligned}
 & \frac{A(\beta)}{(1-\beta)\Gamma(1-\alpha)} \sum_{j=1}^n \left(\frac{h_{fi}^{j+1} - h_{fi}^j}{\Delta t} \right) \left\{ \begin{array}{l} (t_n - t_{j+1})^{1-\alpha} E_{\beta,2-\alpha} \left(-\frac{\beta}{1-\beta} (t_n - t_{j+1})^{\beta+\alpha} \right) \\ (t_n - t_j)^{1-\alpha} E_{\beta,2-\alpha} \left(-\frac{\beta}{1-\beta} (t_n - t_j)^{\beta+\alpha} \right) \end{array} \right\} S_{Sf}(r_i) \\
 &= \frac{k_f^{i+1} - k_f^i}{\Delta r} \frac{3h_{f(i)}^n - 4h_{f(i-1)}^n + 3h_{f(i-2)}^n}{2(\Delta r)} + k_f^i \left\{ \frac{h_{f(i+1)}^{n+1} - 2h_{fi}^{n+1} + h_{f(i-1)}^{n+1}}{2(\Delta r)^2} + \frac{h_{f(i+1)}^n - 2h_{fi}^n + h_{f(i-1)}^n}{2(\Delta r)^2} \right\} \\
 &+ \eta (h_{fi}^n - h_{mi}^n), \\
 & \frac{A(\beta)}{(1-\beta)\Gamma(1-\alpha)} \sum_{j=1}^n \left(\frac{h_{mi}^{j+1} - h_{mi}^j}{\Delta t} \right) \left\{ \begin{array}{l} (t_n - t_{j+1})^{1-\alpha} E_{\beta,2-\alpha} \left(-\frac{\beta}{1-\beta} (t_n - t_{j+1})^{\beta+\alpha} \right) \\ (t_n - t_j)^{1-\alpha} E_{\beta,2-\alpha} \left(-\frac{\beta}{1-\beta} (t_n - t_j)^{\beta+\alpha} \right) \end{array} \right\} S_{Sm}(r_i) \\
 &= \eta (h_{fi}^n - h_{mi}^n) \\
 & \text{if } \frac{k_f^{i+1} - k_f^i}{\Delta r} > 0
 \end{aligned} \tag{132}$$

Otherwise we have the following

$$\begin{aligned}
 & \frac{A(\beta)}{(1-\beta)\Gamma(1-\alpha)} \sum_{j=1}^n \left(\frac{h_{fi}^{j+1} - h_{fi}^j}{\Delta t} \right) \left\{ \begin{array}{l} (t_n - t_{j+1})^{1-\alpha} E_{\beta, 2-\alpha} \left(-\frac{\beta}{1-\beta} (t_n - t_{j+1})^{\beta+\alpha} \right) + \\ (t_n - t_j)^{1-\alpha} E_{\beta, 2-\alpha} \left(-\frac{\beta}{1-\beta} (t_n - t_j)^{\beta+\alpha} \right) \end{array} \right\} S_{Sf}(r_i) \\
 = & \frac{k_f^{i+1} - k_f^i}{\Delta r} \frac{-h_{f(i+2)}^n - 4h_{f(i+1)}^n + 3h_{f(i)}^n}{2(\Delta r)} + \\
 & k_f^i \left\{ \frac{h_{f(i+1)}^{n+1} - 2h_{fi}^{n+1} + h_{f(i-1)}^{n+1}}{2(\Delta r)^2} + \frac{h_{f(i+1)}^n - 2h_{fi}^n + h_{f(i-1)}^n}{2(\Delta r)^2} \right\} + \\
 & \eta(h_{fi}^n - h_{mi}^n), \\
 & \frac{A(\beta)}{(1-\beta)\Gamma(1-\alpha)} \sum_{j=1}^n \left(\frac{h_{mi}^{j+1} - h_{mi}^j}{\Delta t} \right) \left\{ \begin{array}{l} (t_n - t_{j+1})^{1-\alpha} E_{\beta, 2-\alpha} \left(-\frac{\beta}{1-\beta} (t_n - t_{j+1})^{\beta+\alpha} \right) + \\ (t_n - t_j)^{1-\alpha} E_{\beta, 2-\alpha} \left(-\frac{\beta}{1-\beta} (t_n - t_j)^{\beta+\alpha} \right) \end{array} \right\} S_{Sm}(r_i) \\
 = & \eta(h_{fi}^n - h_{mi}^n) \\
 \text{if } & \frac{k_f^{i+1} - k_f^i}{\Delta r} < 0
 \end{aligned} \tag{133}$$

Coupling the derived numerical approximation with the Upwind for third order then the numerical solution of equation (129) is given as:

$$\begin{aligned}
 & \frac{A(\beta)}{(1-\beta)\Gamma(1-\alpha)} \sum_{j=1}^n \left(\frac{h_{fi}^{j+1} - h_{fi}^j}{\Delta t} \right) \left\{ \begin{array}{l} (t_n - t_{j+1})^{1-\alpha} E_{\beta,2-\alpha} \left(-\frac{\beta}{1-\beta} (t_n - t_{j+1})^{\beta+\alpha} \right) + \\ (t_n - t_j)^{1-\alpha} E_{\beta,2-\alpha} \left(-\frac{\beta}{1-\beta} (t_n - t_j)^{\beta+\alpha} \right) \end{array} \right\} S_{sf}(r_i) \\
 = & \\
 & \frac{k_f^{i+1} - k_f^i}{\Delta r} \frac{2h_{f(i)}^n + 6h_{f(i-1)}^n - 6h_{f(i-2)}^n + 6h_{f(i-3)}^n}{6(\Delta r)} + \\
 & k_f^i \left\{ \frac{h_{f(i+1)}^{n+1} - 2h_{fi}^{n+1} + h_{f(i-1)}^{n+1}}{2(\Delta r)^2} + \frac{h_{f(i+1)}^n - 2h_{fi}^n + h_{f(i-1)}^n}{2(\Delta r)^2} \right\} + \\
 & \eta(h_{fi}^n - h_{mi}^n), \\
 & \frac{A(\beta)}{(1-\beta)\Gamma(1-\alpha)} \sum_{j=1}^n \left(\frac{h_{mi}^{j+1} - h_{mi}^j}{\Delta t} \right) \left\{ \begin{array}{l} (t_n - t_{j+1})^{1-\alpha} E_{\beta,2-\alpha} \left(-\frac{\beta}{1-\beta} (t_n - t_{j+1})^{\beta+\alpha} \right) + \\ (t_n - t_j)^{1-\alpha} E_{\beta,2-\alpha} \left(-\frac{\beta}{1-\beta} (t_n - t_j)^{\beta+\alpha} \right) \end{array} \right\} S_{sm}(r_i) \\
 = & \eta(h_{fi}^n - h_{mi}^n) \\
 \text{if } & \frac{k_f^{i+1} - k_f^i}{\Delta r} > 0
 \end{aligned} \tag{134}$$

Otherwise we have the following:

$$\begin{aligned}
 & \frac{A(\beta)}{(1-\beta)\Gamma(1-\alpha)} \sum_{j=1}^n \left(\frac{h_{fi}^{j+1} - h_{fi}^j}{\Delta t} \right) \left\{ \begin{array}{l} (t_n - t_{j+1})^{1-\alpha} E_{\beta, 2-\alpha} \left(-\frac{\beta}{1-\beta} (t_n - t_{j+1})^{\beta+\alpha} \right) + \\ (t_n - t_j)^{1-\alpha} E_{\beta, 2-\alpha} \left(-\frac{\beta}{1-\beta} (t_n - t_j)^{\beta+\alpha} \right) \end{array} \right\} \mathcal{S}_{Sf}(r_i) \\
 = & \frac{k_f^{i+1} - k_f^i - h_{f(i+3)}^n + 6h_{f(i+2)}^n - 3h_{f(i+1)}^n - 2h_{f(i)}^n}{\Delta r} + \\
 & k_f^i \left\{ \frac{h_{f(i+1)}^{n+1} - 2h_{fi}^{n+1} + h_{f(i-1)}^{n+1}}{2(\Delta r)^2} + \frac{h_{f(i+1)}^n - 2h_{fi}^n + h_{f(i-1)}^n}{2(\Delta r)^2} \right\} + \\
 & \eta(h_{fi}^n - h_{mi}^n), \\
 & \frac{A(\beta)}{(1-\beta)\Gamma(1-\alpha)} \sum_{j=1}^n \left(\frac{h_{mi}^{j+1} - h_{mi}^j}{\Delta t} \right) \left\{ \begin{array}{l} (t_n - t_{j+1})^{1-\alpha} E_{\beta, 2-\alpha} \left(-\frac{\beta}{1-\beta} (t_n - t_{j+1})^{\beta+\alpha} \right) + \\ (t_n - t_j)^{1-\alpha} E_{\beta, 2-\alpha} \left(-\frac{\beta}{1-\beta} (t_n - t_j)^{\beta+\alpha} \right) \end{array} \right\} \mathcal{S}_{Sm}(r_i) \\
 = & \eta(h_{fi}^n - h_{mi}^n) \\
 \text{if } & \frac{k_f^{i+1} - k_f^i}{\Delta r} < 0
 \end{aligned} \tag{135}$$

4.7 Numerical simulation for different values of fractional order

In this section, the numerical simulations of the modified groundwater fractal flow in dual media are presented for different values of fractional order. We consider the contour plot of the solutions to see the solution in space and time for a given value of alpha and beta. The aquifer parameters used here are theoretical not measured from the field however; this section is designed to show readers more scenarios that can be described using the concept of fractional differentiation. In these simulations, we will not only consider the aquifer parameters in power decay law form, we will suggest other form and see the effect. The numerical simulations are depicted in Figure 1 to Figure 9.

The numerical graphics show some interesting real world observations. The numerical simulations are generated based on the non-local operator with Mittag-Leffler kernel.

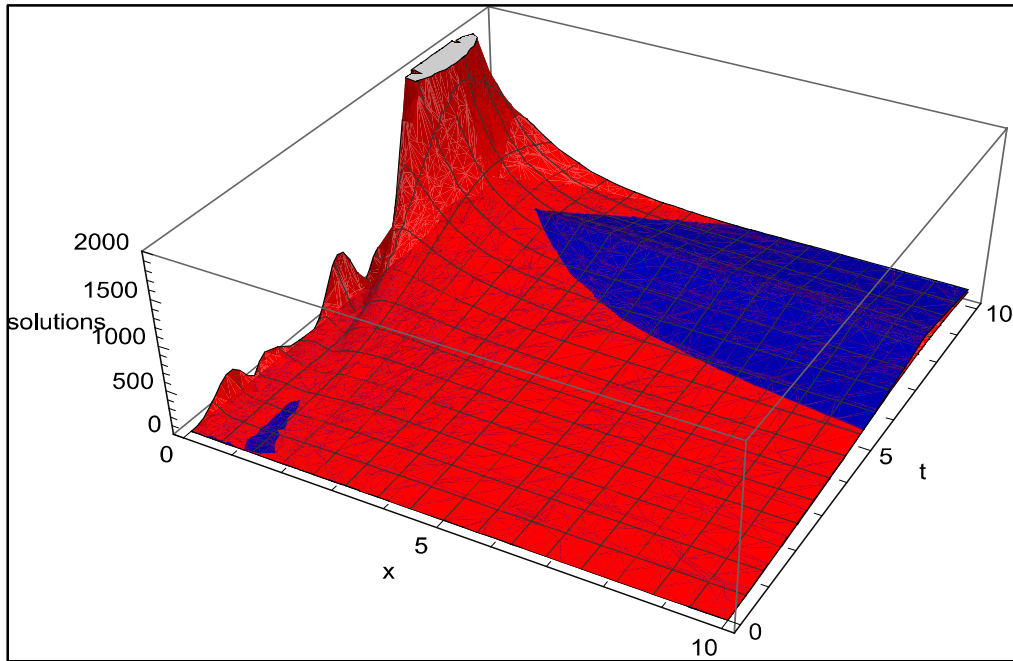


Figure 5: Numerical simulation of system solution with red the hydraulic head in a fracture system and blue in a matrix rock $\alpha = 0.5$

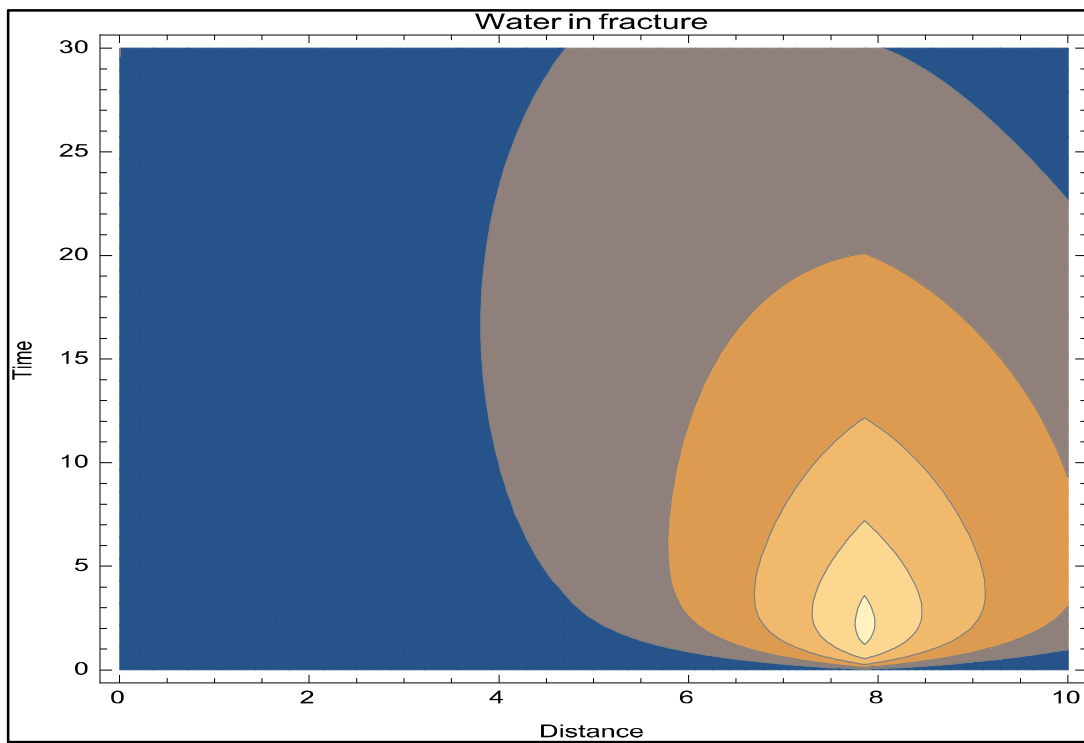


Figure 6: Numerical simulation of hydraulic head in the fracture network for $\alpha = 0.5$

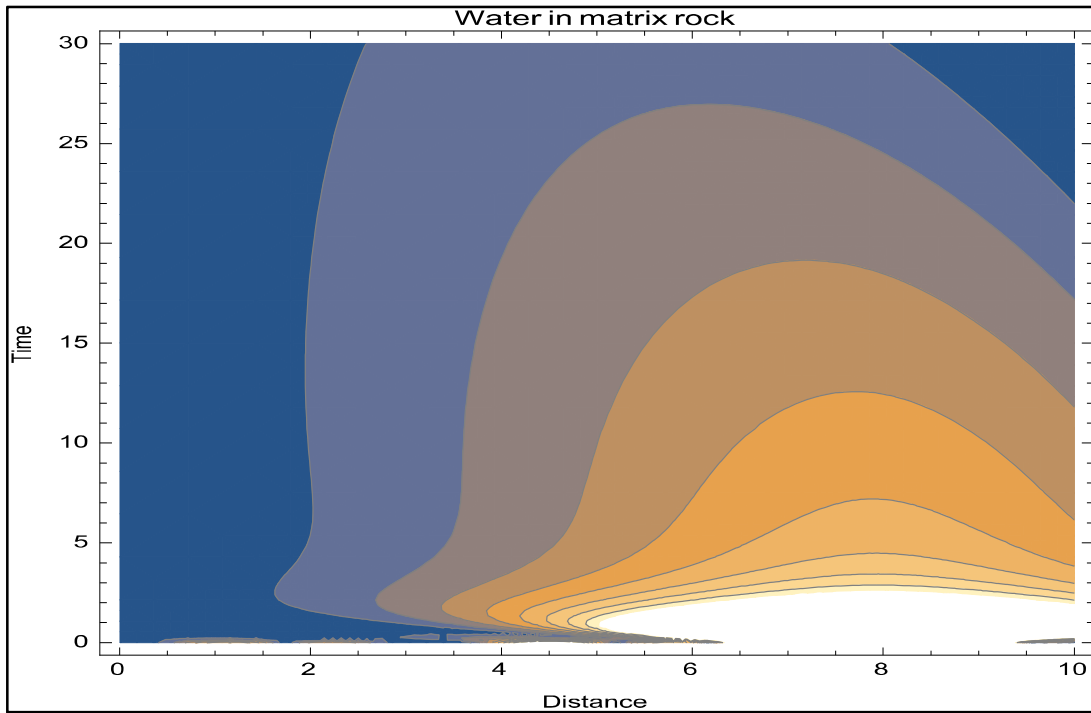


Figure 7: Numerical simulation of hydraulic head within the matrix rock for $\alpha = 0.5$

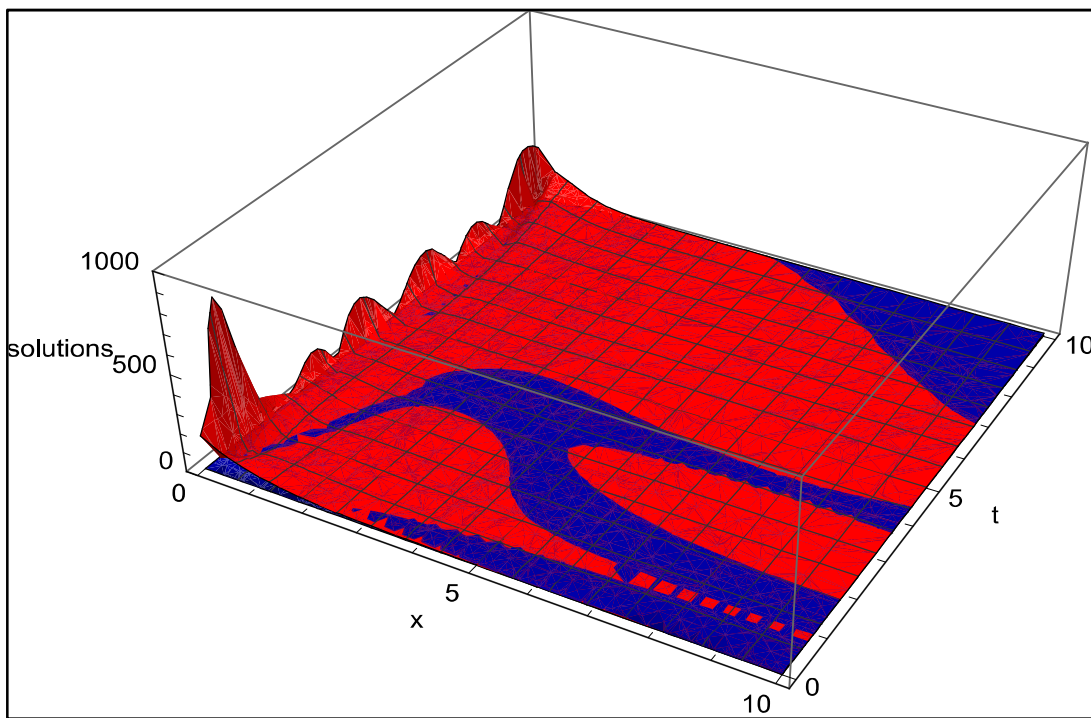


Figure 8: Numerical simulation of system solution with red the hydraulic head in a fracture system and blue in a matrix rock $\alpha = 0.75$

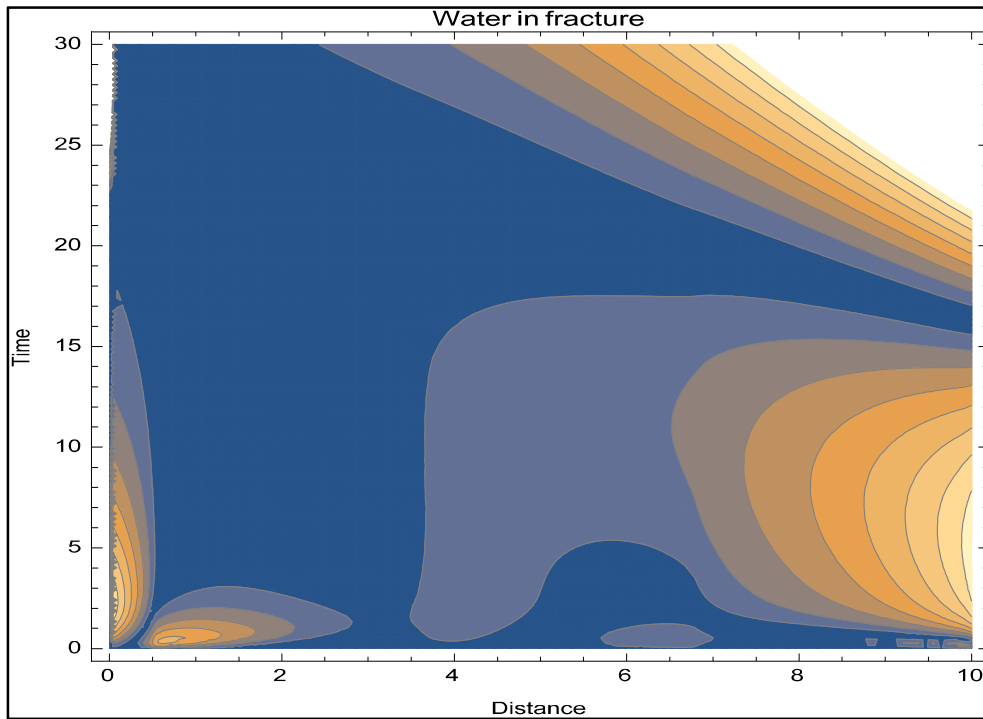


Figure 9: Numerical simulation of hydraulic head in the fracture network for $\alpha = 0.75$

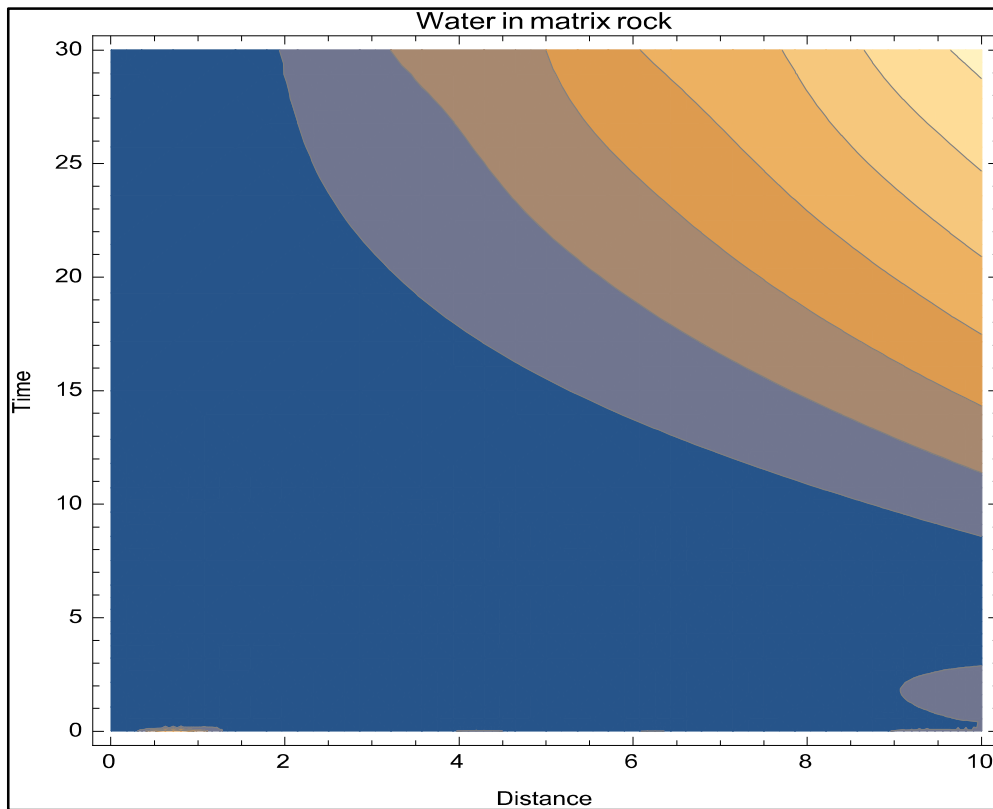


Figure 10: Numerical simulation of hydraulic head within the matrix rock for $\alpha = 0.75$

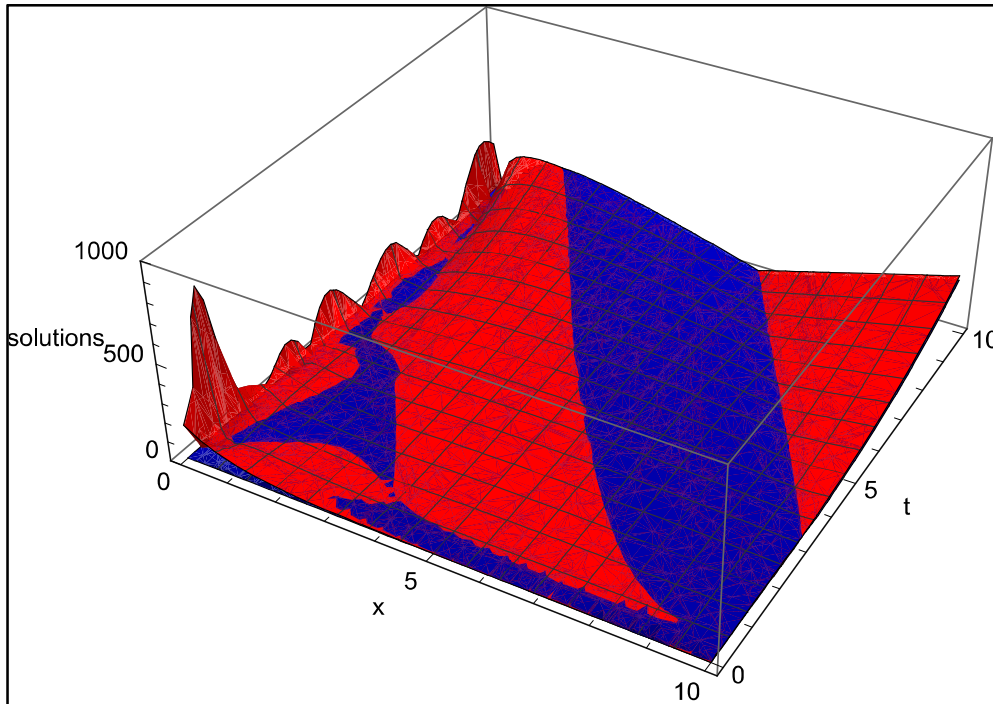


Figure 11: Numerical simulation of system solution with red the quantity of water in a fracture system and blue in a matrix rock $\alpha = 1$

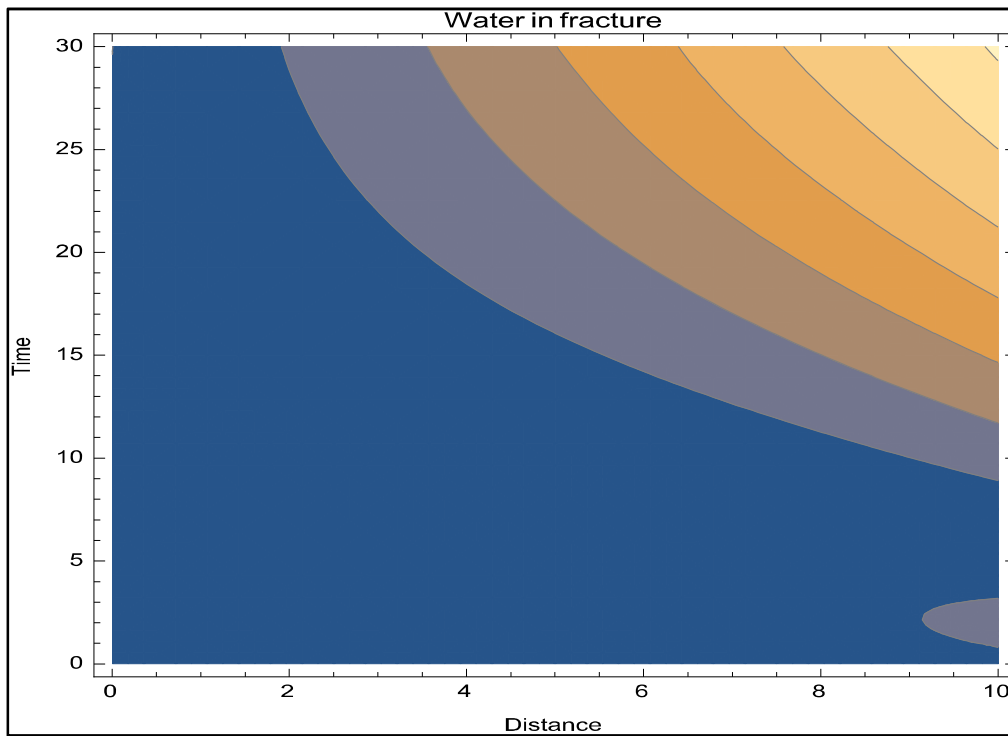


Figure 12: Numerical simulation of hydraulic head in the fracture network for $\alpha = 1$

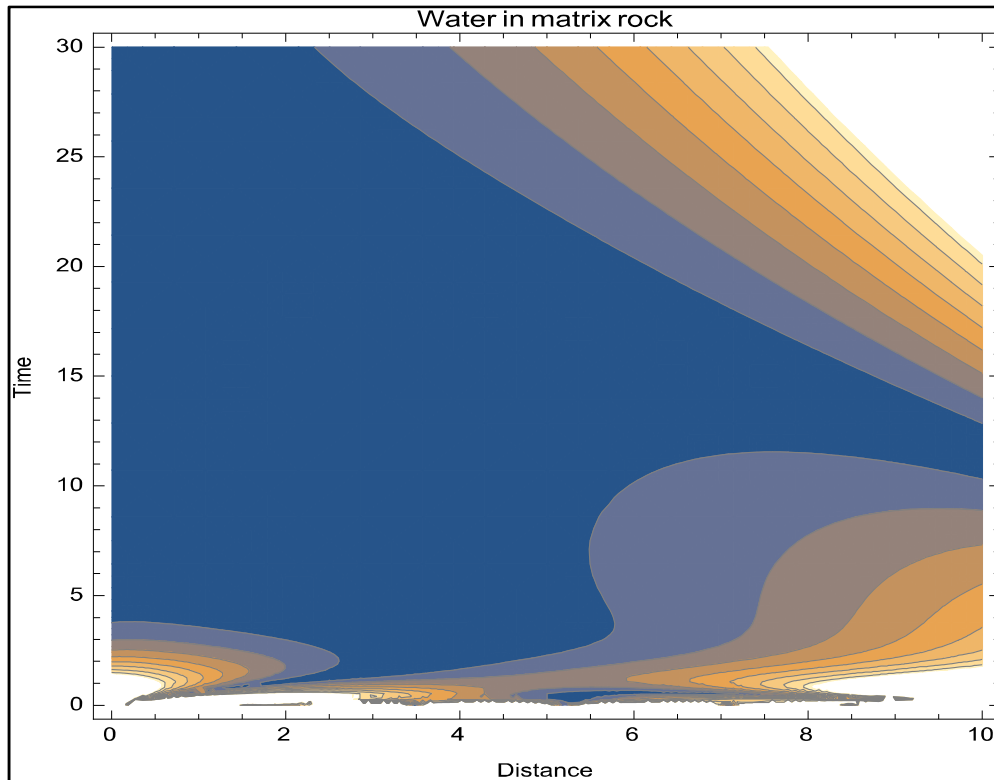


Figure 13: Numerical simulation of hydraulic head within the matrix rock for $\alpha = 1$

It is important to notice that, the numerical simulation of hydraulic head of water within the matrix rock and fracture network depend on the fractional order. When the fractional order is one that is we are dealing with the classical model the hydraulic change within the fracture network and matrix rock are homogeneous which is correct because the classical derivative is unable to portray a non-homogeneous scenario. The numerical simulation when the fractional order is less than 1 show new features that could not have been pointed out with the classical differentiation. In figure 1, 2, 3, 4, 5, and 6 we can see the flow within a visco-elastic media. More importantly we observe that when using the fractional differentiation, the total amount of water within the matrix rock is less than in the fracture network. In addition, one can observe that the water within the matrix rock is moving toward the fracture and this scenario is always observed in the real world problem.

4.8 Conclusion

The flow of groundwater within a given geological formation has been a focus of many researchers in the last decades due to the importance of the groundwater which is in many countries a source of fresh water on one hand. On the other hand, this water is estimated to constitute about 30.1% (Igor Shiklomanov, 1993) of the world's fresh

water supply, which is about 0.61% of the entire world's water, including oceans and permanent ice. One of the top challenges is the geological formation via which this water is moving. To monitor the flow of these water, one need to construct a mathematical equation that accounts for some parameters and properties of these aquifers. The fractal flow model in dual media is perhaps one of the most complex groundwater flow model as it accounts for the flow within the fractured network and also the flow within the matrix rock. One can easily conclude that the flow within fractures does not require more complex mathematical formulas as the medium is considered to be homogeneous, non-elastic and non-viscoelastic. Nevertheless the flow within the matrix rock needs to be modelled with care as the matrix rock may be heterogeneous, elastic or visco-elastic. The mathematical tools used to construct the partial differential equation (85) cannot account for heterogeneous, elastic or visco-elastic properties, therefore a suitable operator with differentiation need to be used. Thus, to include the observed facts into mathematical formula, we have modified the model by replacing the local derivative with the non-local operator with power, Mittag-Leffler law and finally we combined both laws to obtain power-Mittag-Leffler law. The modified models were analysed numerically using the Upwind for second and third order approximation in space. Some numerical simulations are presented to see the effect of power, Mittag-Leffler and Mittag-Leffler-Power laws.

5 General description of the case study area

5.1 Locality

The study area is located north-west of Mokopane town (approximately 30km) within Mogalakwena Municipal Area, which forms part of the Waterberg District Municipality of the Limpopo Province (Figure 15). The area covers the entire quaternary catchment A61G.

5.2 Climate

The study area is close to the tropic of Capricorn, and therefore there is plenty of sunshine, long summer afternoons and dry days. The summer months (October to March) averaging 27°C (Figure 14). It is a sunny season of chilly, early mornings, warm dry afternoons, and cools to cold nights.

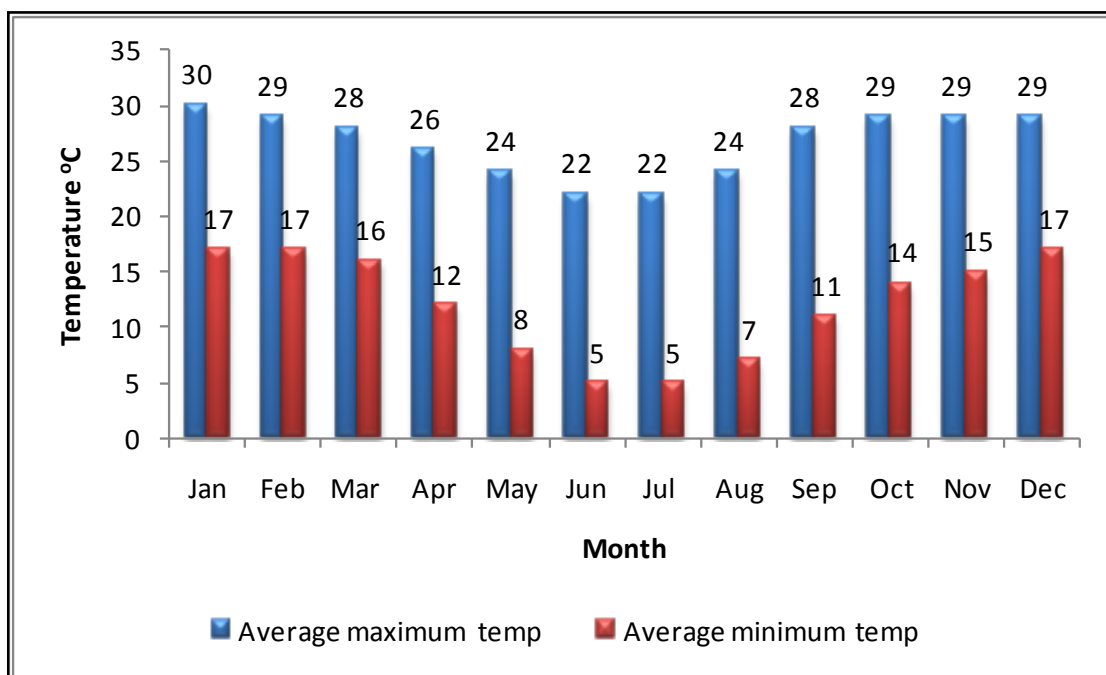


Figure 14: Monthly averages temperatures in the area

The area normally receives up to 860mm of rain per year. Most rainfall occurs during summer in the form of afternoon thunderstorms. It receives its lowest rainfall (0-3mm) in July/August/September and its highest rainfall in November as shown in Figure 16.

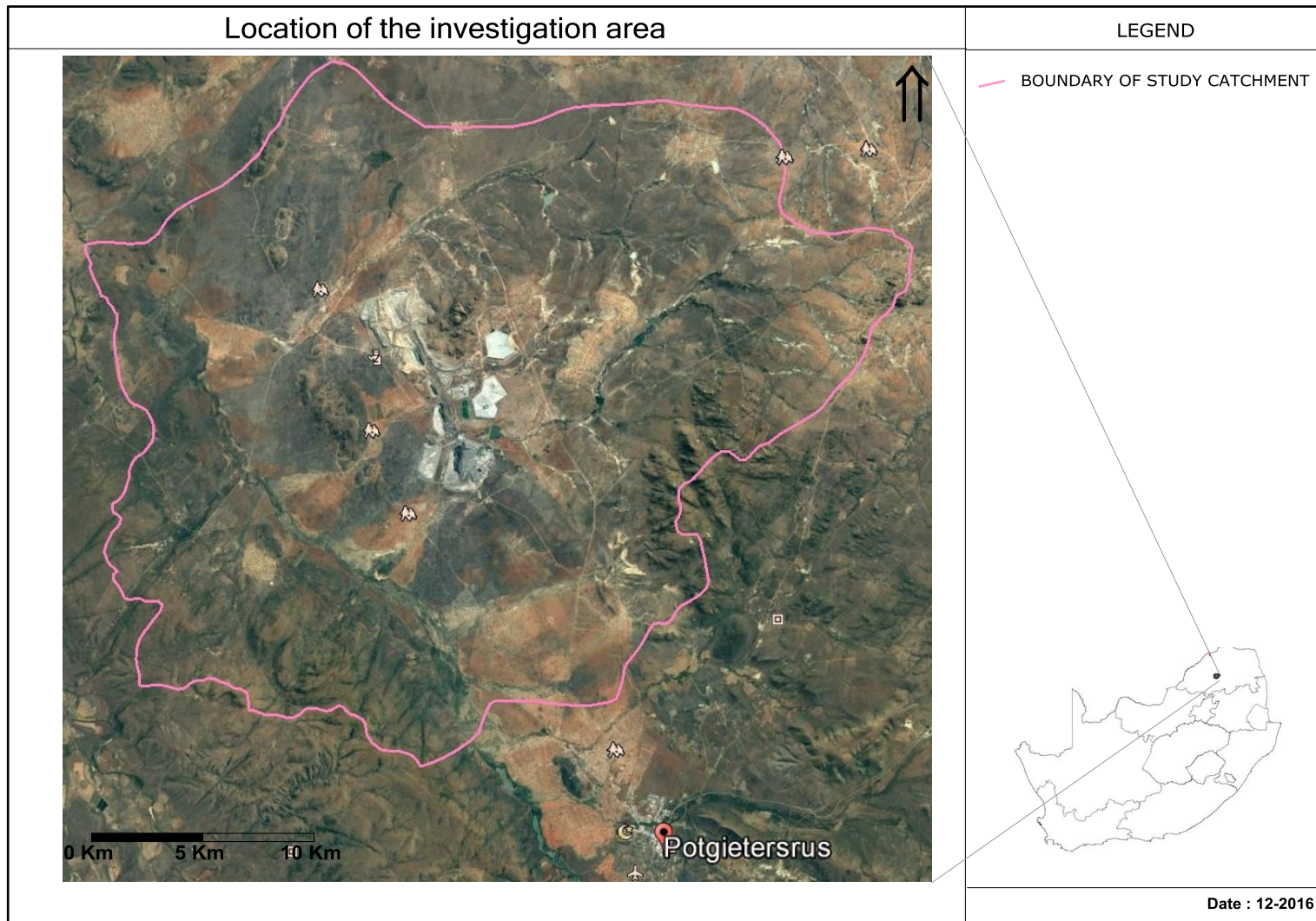


Figure 15: Location of the investigation area

The mean annual Class A pan evaporation is approximately 2155 mm, with the average monthly evaporation shown in Figure 17.

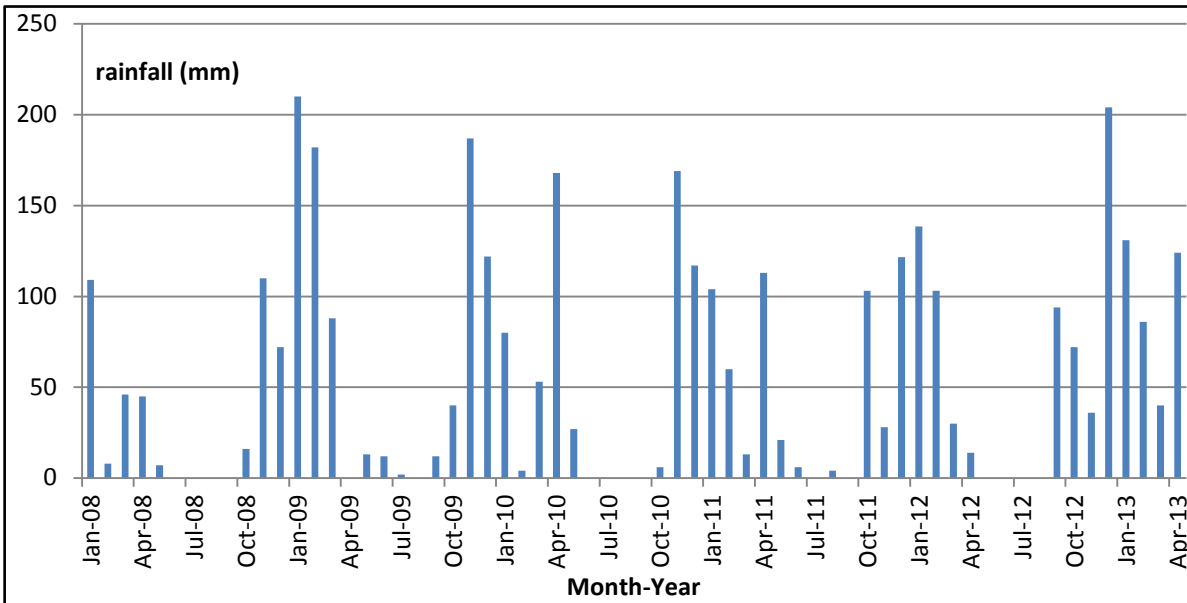


Figure 16: Historical (05 years) average monthly recorded rainfall

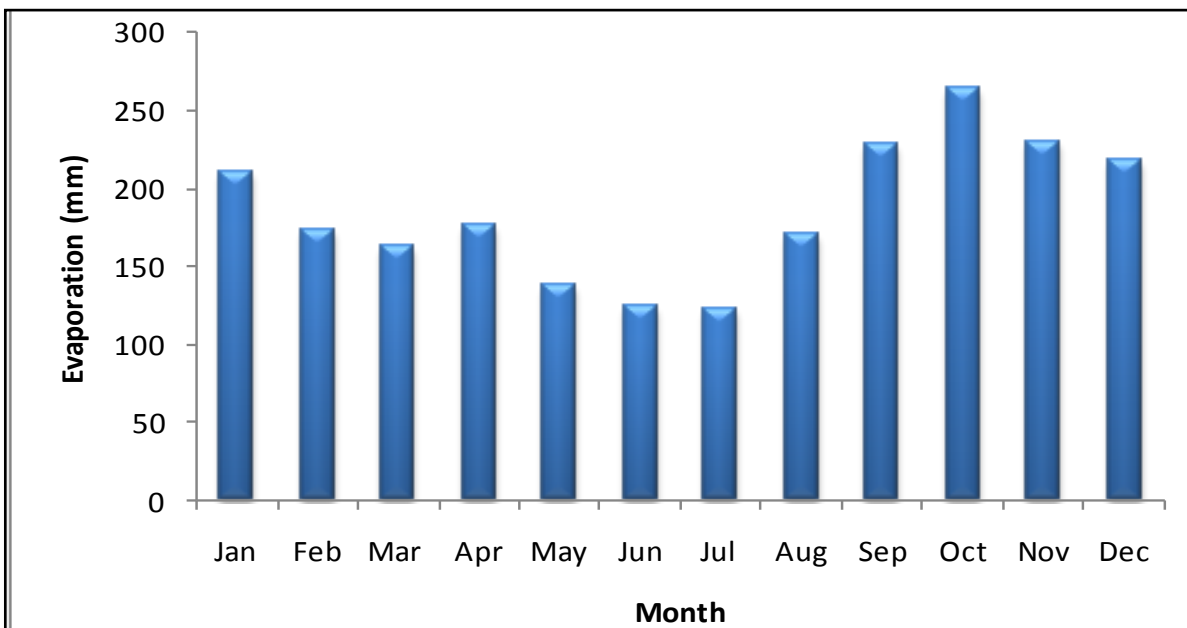


Figure 17: Average monthly evaporation

5.3 Topography and surface water drainage

Digital information from 1:50 000 topographical maps (2328DD – Limburg, 2329CC, 2428BB –Tintype), were used together with Shuttle Radar Topography Mission (SRTM) 90 for the demarcation of the catchments and for the description drainage of the area. Pits volumes were used to incorporate natural topography disturbance in the pits area, where available.

The quaternary catchment A61G falls in the Limpopo Water Management Area (Figure 18). The catchment is primarily drained by the Mogalakwena River. The Mogalakwena River runs SE-NW, draining in a north westerly direction along the base of the key topographical feature of Waterberg Mountains. The catchment elevations range from 948.773 to 1804.773 mamsl (SRTM 90) and are generally higher than 1000 mamsl (except along the Mogalakwena River). The catchment is situated on the African erosion surface as described by Partridge and Maud (1987). The pristine topography and drainage have been disturbed locally by mining activities (tailings and return water dams, pits, rivers diversion, rocks dumps, buildings, etc.).

Table 1: Information concerning quaternary catchment

Primary Catchment	Tertiary Catchment	Quaternary Catchment	Area	Mean Annual Runoff
			(KM ²)	(mm/a)
A	A61	A61G	926.648	17.3

The Mogalkwena River is feed fed from the eastern watershed by 03 tributaries (affluent). These streams are highly seasonal and only occur after larger rainfall events. The main tributaries of Mogalkwena River are: (a) Mohlosane river Sand, (b) Groot Sandsloot River, and The Thwathwe/Wit river which flows NE-SW into the Mogalakwena River.

In the catchment, the runoff is highly seasonal and variable, with intermittent flow in many of the tributaries. Only a small number of river courses are perennial and most rivers sustain flow only during the wet season (December to April) or following intense rainfall events.

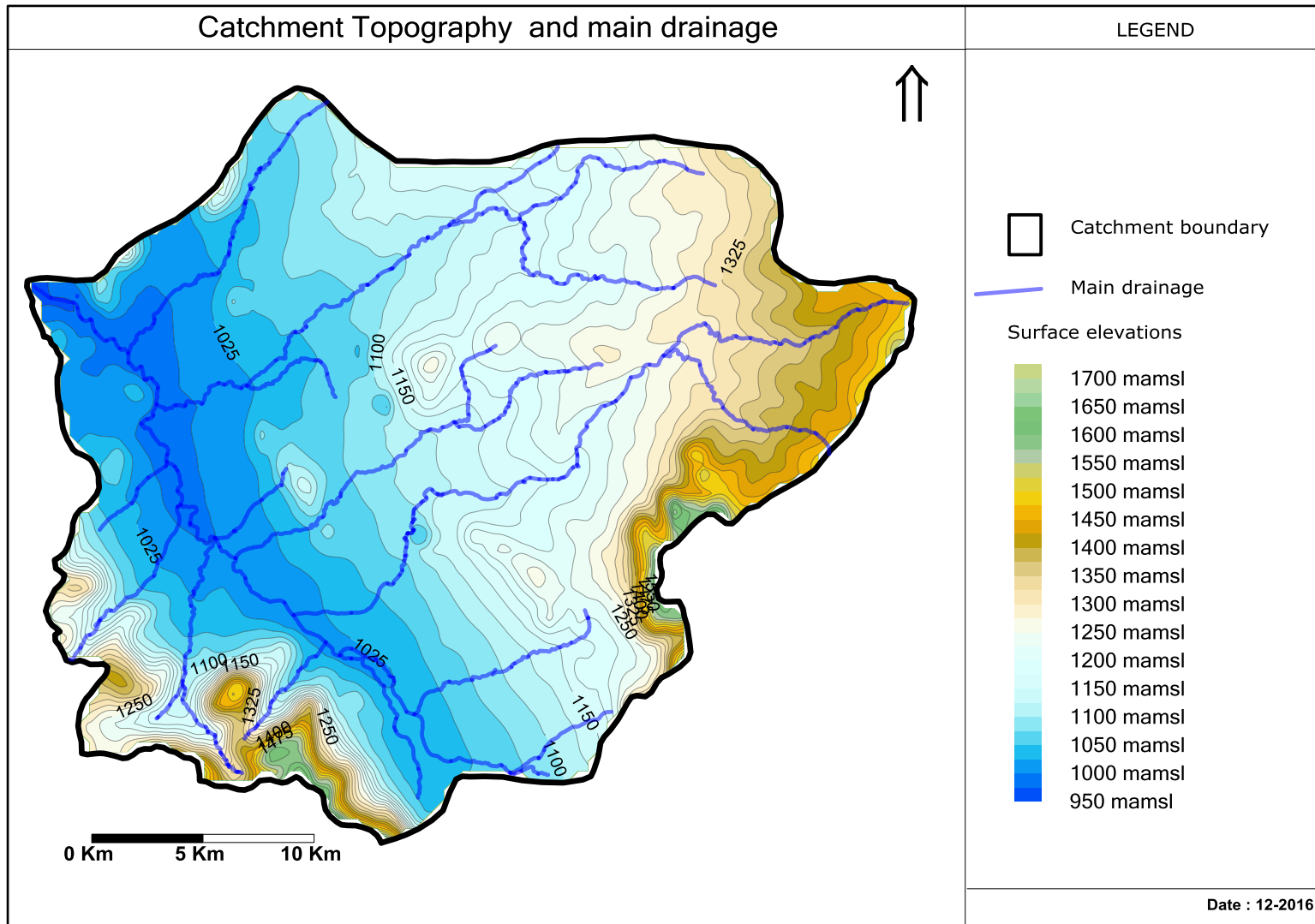


Figure 18: Topography of the study area

The Mohlosane River flows NE-SW into the Mogalakwena river. It flows between 02 (Vaalkop and Blinkwater) tailings dams, and between 02 open platinum mining pits (North and Zwartfontein). The total area drained by Mohlosane River is approximated to 57 km². The highest point in the drained area is approximately 1290 mamsl, where the watercourse slope is more than 2 %, and the lowest point (confluence with Mogalakwena River) is approximately 1003 mamsl with a slope less than 1 %. The bedrock of the sub catchment is granite which outcrops at the highest and lowest points.

The Groot Sandsloot River flows westerly south of the Vaalkop tailings dam, between Zwartfontein and Sandsloot pits, and is deviated to follow the western side of a mining pits (Sandsloot) where it flows NE-SW to its confluence with the Mogalakwena Rivers. The highest point in the sub-catchment that is drained by Groot Sandsloot River is approximately 1191 mamsl, where the watercourse slope is more than 7 %, and the lowest point (confluence with Mogalakwena River) is approximately 1017 mamsl with a slope less than 4 %. The bedrock of the sub catchment is granite which outcrops at the highest and lowest points.

The gentle relief results in relatively slow flowing rivers which accumulate alluvial deposits on their floodplains particularly along the Sand River. All of these rivers flow towards the Limpopo River in the north and eventually reach the Indian Ocean in Mozambique.

5.4 Geology

The main objective of the present geological characterization is to generate a better understanding/description of the rock structure, facies and properties in a geologically realistic manner in the study area. This description will be used in the development of any approach of following sections related to characterizing and modelling the heterogenous fractures aquifers in a typical crystalline rocks basement. Hydrogeological information related to this challenge in groundwater flow systems (drainage, flow regime, flow dynamic, aquifers compartments delineations) include:

- Preferential flow delineations and the spatial variations in their characteristics
- Functions of Dykes, lineaments (geological and structural) in the groundwater systems
- Vertical aquifer parameters variability
- Recharge zones delineations

Digital information from the Council for Geoscience in the form of 1:250 000 vector data for: 2328 Pietersburg, 2438 Nylstroom geological maps, were used to delineate the local and regional geology of the project area.

5.4.1 Regional Geology

The regional geology of the study area consists of the Northern part of Kaapvaal Craton, and the Southern Marginal and Central Zones of the Limpopo Mobile Belt in the Limpopo basin. The Limpopo basin covers part of Zimbabwe, South Africa, Botswana, and Mozambique. Chinoda G et al (2009) gave some outlines of the geology of Limpopo in the riparian nations.

The regional geology of the study area consists of the Northern part of Kaapvaal Craton, and the Southern Marginal and Central Zones of the Limpopo Mobile Belt (Figure) in the Limpopo basin. The Limpopo basin covers part of Zimbabwe, South Africa, Botswana, and Mozambique, and its simplified geology is showed in Figure shows. Chinoda G et al (2009) gave some outlines of the geology of Limpopo in the riparian nations.

Regarded as an area of typical Archean high grade deformation, (Blenkinsop and Rollinson, 1992; Van Reenen et al., 1992), the Limpopo Mobile Belt (LMB) is a quasi E-W elongated low lying belt of granulite facies rocks situated between the greenschist - amphibolite rocks of the Zimbabwe craton to the north and the low-grade metamorphism granitoid-greenstone terrane of the Kaapvaal craton to the south. The belt overlaps eastern Botswana, southern Zimbabwe and the northern part of the Northern Province in South Africa. LMB is subdivided in three main crustal zones, namely the Northern Marginal Zone (NMZ), the Central Zone (CZ) and the Southern Marginal Zone (SMZ), which lie parallel to one another in an ENE direction. The boundaries of these 3 zones are defined by major tectonic breaks in form of shear zones (Stuart and Zengeni, 1987; Mkweli et al., 1995), and the peripheral shear zones are:

- The North Limpopo Thrust Zone separates the Zimbabwe craton and the NMZ.
- The Hout River Shear Zone (HRSZ) forms the boundary between the Kaapvaal Craton and the higher grade metamorphism rocks of the Southern Marginal Zone. It is developed over a width of up to 4 km in places (Anhaeusser, 1992). EW striking, steeply northward-dipping thrusts and reverse faults, as well as several

NE-SW striking strike-slip faults were found to be characteristic structures of the HRSZ (Roering et al., 1992).

- Occurring to the south of LMB, the Kaapvaal craton is broadly divided into the southern, central and northern zones (De Wit and Roering, 1990):
 - The central Kaapvaal craton (near Johannesburg), consists of the Barberton-type granite-greenstone terrane, overlain by the Witwatersrand Basin. The Witwatersrand Supergroup is overlain by the bimodal volcanic and clastic sediments of Ventersdorp Supergroup (Armstrong et. al., 1990).
 - The southern Kaapvaal craton comprises the Ancient Gneiss Complex and the Barberton granite-greenstone terrane separated by fault zones of tectonic amalgamation.
 - The northern Kaapvaal craton comprises the Murchison, Pietersburg and Sutherland greenstone belts and surrounding granitoids, associated with thrustings and intrusions of different types (McCourt and Van Reenen, 1992; and Vearncombe, 1991). The Bushveld Intrusive is a typical intrusion in the Kaapvaal Craton.

The Bushveld Complex represents the largest intrusive body in the world, and is well-known for its large proportion of the world's platinum and palladium resources. Five main limbs of the intrusion had been identified on a regional basis: (a) Far Western Limb, (b) Western Limb, (c) South Eastern Limb, (d) Eastern Limb, and the (e) Western Limb. The complex has been divided into three principal units: (a) the Rustenburg Layered Suite which emplaced during the mafic phase, and (b) the Raseop Granophyre Suite and (c) the Lebowa Granite Suite of the (SACS, 1980) which both emplaced during the acid phase. Typical stratigraphic succession in the Bushveld Complex (apart from the Far Western Limb) comprises from the base upwards: (a) the Marginal, (b) Lower, (c) Critical, (d) Main and (e) Upper Zones. Three main occurrences of Platinum Group Elements (Pt, Pd, Ru, Rh, Os and Ir), can be located within the region: (a) the Merensky Reef, (b) UG-2 chromitite and (c) Platreef. The term 'Reef' refers to the economically (profitable metal mining) important zone contained largely within a medium to coarse grained plagioclase-pyroxenite. These main occurrences of PGE are associated to at least three large interlinked chambers, with separate feeder pipes. A feeder pipe close to Potgietersrus resulted in the Potgietersrus Limb, with which the Platreef is associated. The covering area of the Potgietersrus Limb is approximated to 2000 km² and consists of a north striking trough-shaped body.

5.4.2 Local Geology and mineralization

The local geology is associated with the geology of northern Kaapvaal Craton, in the northern Bushveld complex intrusion area, North West of Pietersburg and Sutherland greenstone belts. M. J. de Wit (1990), McCourt and Van Reenen (1992), and Vearncombe (1991) outlines the main geological features, deformation and events in the area.

The local geology is characterised in the North East by Biotite Gneiss (Archean) of the Goudplaats-Hout River Gneiss Suit (Brandl G, 1986), of different types: Leucocratic, strongly migmatized; greyish, weakly migmatized; or minor leucogneiss and dark grey. J.P. van Wyk (1976, 1977) estimated the Dip of this Gneiss in the study area of about 35° and in the NNW direction. The Biotite Gneiss is bounded in Far East by the pink, medium to coarse-grained, hornblende-biotite Granite of the Lunsklip of the Mashashane Suit.

In the South East part of the study area, the granites of Mashashane Suit, lay and extends to east, outside the boundary of the catchment. These granites are found in the form of: reddish, fine- to coarse-grained biotite Granite (Uitloop); pink, medium- to coarse-grained, hornblende-biotite Granite (Lunsklip); or grey to pink, medium- to coarse-grained, adamellitic/granodioritic biotite granite (Turflop).

The geology of Central and West part of catchment consists mainly of the sequences (formations) of the Platreef (Northern limb of the Bushveld Complex intrusion).

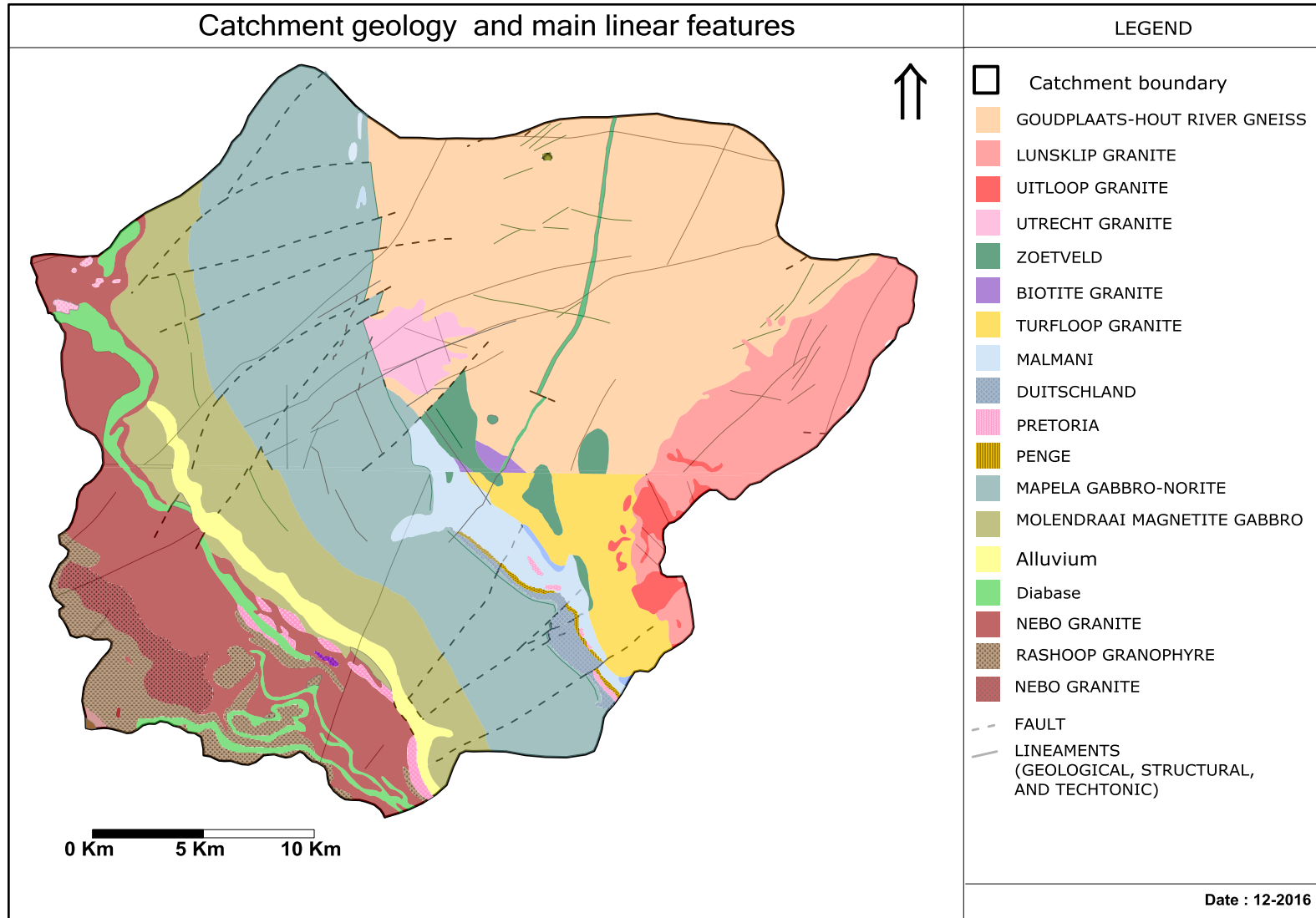


Figure 19: Geology in the catchment

5.4.2.1 The Platreef

Several authors (Viljoen and Schürmann 1998; White, 1994; Harris and Chaumba, 2001; Byea and Bell, 2001; Manyeruke et al., 2005) described the geology of the Platreef.

The Platreef has an economic (well mineralised) strike length approximated between 35km and 40km and is generally developed between norites and gabbronorites north of Mokopane (Viljoen and Schürmann, 1998; Manyeruke et al., 2005). The Platreef varies in thickness, with a maximum thickness of 400 m occurring in the south, thinning to less than 50m in the north (Manyeruke et al., 2005). Its thickness at Sandsloot ranges from 70 to 200 m (Byea and Bell, 2001). At the farm Townlands, the Platreef consists of three packages of medium grained gabbronorite and, feldspathic pyroxenite, separated by hornfels interlayers, with a total thickness of approximately 150 m (Manyeruke et al., 2005).

Rocks in these zones include cordierite spinel hornfels, clino-pyroxenites, calcsilicates and graphite-bearing serpentinites, include serpentinitised peridotites and pyroxenites. These rocks have all been serpentinitized to varying degrees. The most abundant rock type in the heterogeneous zones is the hornfels which is thought to have originated from pyritic black shales, dolomitic and pelitic floor rocks. Between Tweefontein and Sandsloot farms, a dolomite formation (of the Transvaal Super Group) known locally as the "dolomite tongue" thins the Platreef.

The interaction of the pyroxenite of the Platreef with different sedimentary sequences has resulted in a highly complex suite of rock types. This complexity in the Platreef mineralisation is partly due to the transgressive relationship of the Northern Limb Bushveld with the Transvaal Super Group and Archaean granites as it progresses northwards. This transgressive is also known to be at the origin of different degrees of metasomatism and assimilation of the floor rocks.

The contact between Platreef and the overlaying Main Zone gabbro Norites is fairly uniform in general, with local (in places) irregularities which are mainly associated with interlayered norites and pyroxenites. Von Gruenewaldt et al., (1989), and White (1994), among others, do not accept that the Platreef is at the base of the Main Zone, but rather a part of the Upper Critical Zone (UCZ).

The Platreef overlays more than 1600 m thick Lower Zone (LZ) which is predominantly developed in the South of Mokope town, and as small satellite unit in the study area. The Lower Zone consists of at least 37 different cyclic units of pyroxenites and harzburgites, with chromitite layers (Hulbert and Von Gruenewaldt 1985; 1986) of the Lower Zone. LZ of the North Limb distinguishes itself from the LZ of the other limbs (Western and Eastern) of the Bushveld Complex, by (a) a higher Mg ($(\text{Mg}/(\text{Mg}+\text{Fe}))$) values in olivine and orthopyroxene, (b) the presence of chromitites with higher Cr_2O_3 , (c) and a sulphide horizon with PGE occurs in the Volspruit Subzone.

Authors (Wagner, 1929; White 1994) correlate the Platreef to the Merensky reef (of the Western and Eastern Limbs), partly based on the presence of sulphide mineralisation associated with coarse-grained (pegmatoidal) pyroxenites in both cases. McDonald et al (2005) have demonstrated this theory may be incorrect and they have shown that the Platreef is formed from a different magma than that which generated the Upper Critical Zone in the eastern and western lobes of the complex.

The Main Zone is capped by cyclic units of magnetite, magnetite gabbro, gabbro, anorthosite and olivines diorites of the Upper Zone, which thickness is approximated to 1400 m (McDonald et al., 2005). The Main Zone of the Northern Limb is thinner than in the eastern and western limbs, and reaches a thickness of 2200 m.

5.4.2.2 Structures and Lineaments

The above geological sequences have been disturbed at different degree by several sets of lineaments (Faults, Dykes (Dolerite, Diabase)), with NE dominant striking trends.

Several set of quasi parallel NE striking faults disturbed the sequence's Northern Limb of the Bushveld Complex, and part of the Biotite Gneiss (East of the Plat reef). A series of NNW striking faults, are also evident in the region. The faults geometry is pre-Bushveld (Byea and Bell, 2001). The Platreef is disturbed by a steeply dipping set of NS striking faults.

A number of extensive (up to 30 km long) structural lineaments run NE and ENE across the catchment. Less extensive (< 3 km) NNW structural lineaments occur also. The Biotite Gneiss and the Granites of Mashashane Suit are intruded by a several sets of striking Diabase/Dolerite Dyke, with a predominance of NE striking trends.

Such structures and lineaments may have alternated and deformed at different degrees to the adjacent rock types. For instance, a major oblique-sinistral fault was reported by Byea and Bell (2001) to have displaced the ore body to the south-east by approximately 400 m, causing alteration and deformation in the rocks at the open pit at Sandsloot.

The patterns of such structures (faults and lineaments) are of importance, primarily at the crossing with the Plaatreef, as they may constitute preferential paths for groundwater flow into the associated open pits, and for contamination migration from associated waste facilities.

The geometry and functions of such lineaments in the groundwater drainage system have been poorly investigated and documented.

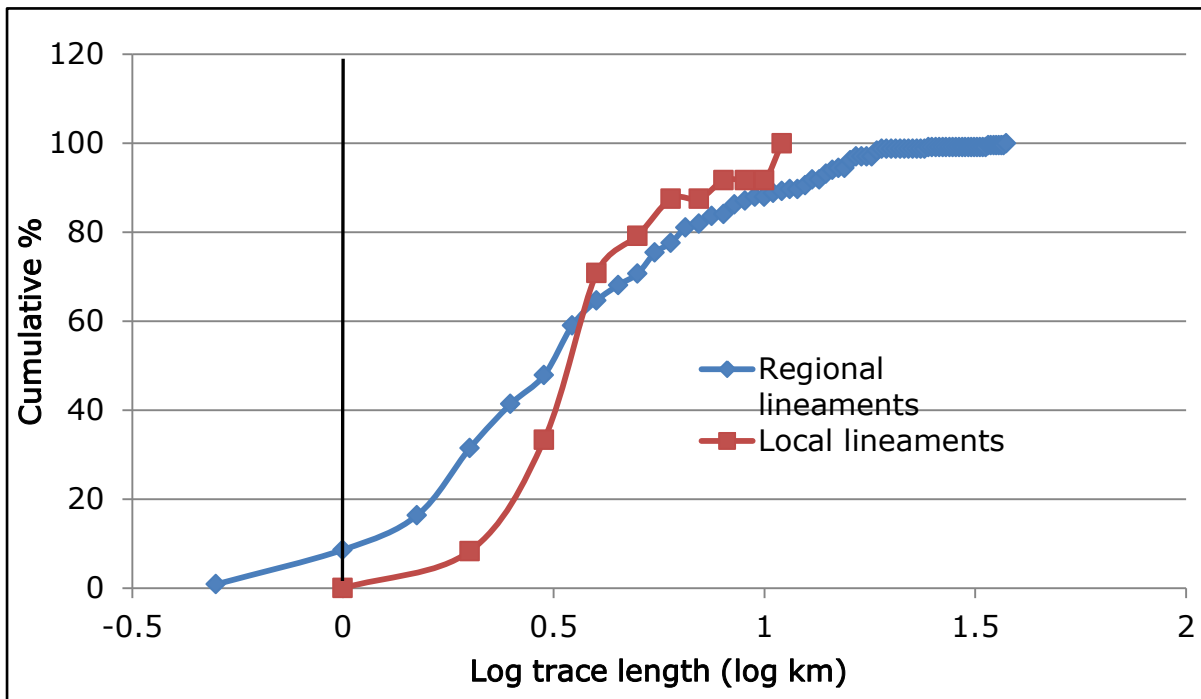


Figure 20: Lineaments frequency distributions

Table 2: Details on the Lithology and stratigraphy in the catchment

LithoStratigraphy	Description	Parent 1	Parent 2
MAKGABENG	Fine- to medium- grained cross-bedded sandstone, slightly feldspathic at the base	MATLABAS	WATERBERG
RASHOOP GRANOPHYRE	Quartz-feldspar porphyry, granophyre	-	BUSHVELD COMPLEX
MOLENDRAAI MAGNETITE GABBRO	Magnetite gabbro with magnetite layers	RUSTENBURG LAYERED SUIT	
MAPELA GABBRO-NORITE	Gabbro, norite	RUSTENBURG LAYERED SUIT	
UTRECHT GRANITE	Pink, fine-grained, granodioritic biotite granite	-	
GOUDPLAATS-HOUT RIVER GNEISS SUIT	Leucocratic, strongly migmatized biotite gneiss and greyish, weakly migmatized biotite gneiss; minor leucogneiss and dark grey biotite gneiss	-	
ZOETVELD SUB SUIT	Pyroxenite, harzburgite, chromitite	RUSTENBURG LAYERED SUIT	
NEBO GRANITE	Coarse-grained granite	LEBOWA GRANITE	
	Sandy soil		-
PRETORIA GROUP	Quartzite, shale and andesitic-basaltic lava	TRANSVAAL SUPER GROUP	TRANSVAAL SUPER GROUP
DUITSCHLAND	Dolomite/limestone (+ chert), shale,	CHUNIESPOORT	

LithoStratigraphy	Description	Parent 1	Parent 2
FORMATION	subordinate quartzite, conglomerate and diamictite	GROUP	
SCHRIKKLOOF	Fine-grained, flow-banded, porphyritic and spherulitic felsite	ROOIBERG	
PENGE FORMATION	Iron-formation	CHUNIESPOORT GROUP	
BLACK REEF FORMATION	Quartzite, subordinate conglomerate and shale	TRANSVAAL SUPER GROUP	
MALMANI SUBGROUP	Dolomite, subordinate chert, minor carbonaceous shale, limestone and quartzite	CHUNIESPOORT GROUP	-
MATLALA GRANITE	Fine-grained grey to pink biotite granite, coarse-grained and in places porphyritic		-
UITLOOP GRANITE	Reddish, fine- to coarse-grained biotite granite	MASHASHANE SUIT	-
LUNSKLIP GRANITE	Pink, medium- to coarse-grained, hornblende-biotite granite	MASHASHANE SUIT	-
TURFLOOP GRANITE	Grey to pink, medium- to coarse-grained, adamellitic/granodioritic biotite granite	-	-

5.5 Geohydrology

5.5.1 Regional Geohydrology

The regional geohydrology corresponds to the “classical” model of a basement aquifer as described by Gustafson and Krásný (1994), Chilton and Foster (1995), and Martin Holland (2011):

- Alluvial aquifers: These aquifers develop along rivers (valley trains), sand rivers or drainage lines. The extent (width and depth.) of such aquifers is limited and typically varies according to the topography and climate. Alluvial material overlies or replaces the weathered overburden and creates a distinct intergranular aquifer type. Orpen (1986) estimated the thickness of alluvium deposits in the region (along Sand River) to be not more than 8 to 15 m. In the absence of a continuous impermeable clay layer, the alluvial and weathered-fractured aquifers are expected to be in hydraulic continuity (Nel, 2000).
- Shallow weathered or aquifers: The East of the region is characterized by a number of batholiths, forming distinct inselbergs interpreted as residual hills which became exhumed in successive stages of stripping of the weathering cover of the African erosion surface. The thickness of the regolith in the Limpopo Plateau generally extends between 15 and 50 metres below surface, and usually has a high porosity and a low permeability due to clay-rich material (Acworth, 1987). When saturated, the regolith constitutes the reservoir of the aquifer. The porosity of the weathered profile generally decreases with depth, along with clay content, until fresh rock is reached. Based on 2D electrical resistivity depth imaging, Timmerman et al (1983) indicated weathering depths ranging between 20 and 40 m, in the region (South west of Makhado). Geohydrological investigations conducted by Du Toit (1986) suggested the weathering depths between 9 and 36 m may be expected around Polokwane, and there is some correlation between yield and weathering depth. However, higher yields ($> 3 \text{ l/s}$) are more often associated with the fractured fissure layer irrespective of the thickness of the overlying weathered layer. Martin Holland (2011) found weathering depths between 1 and 62 mbgl with an average of 45 mbgl.
- Deeper fractured aquifers in non-weathered hard bedrock (fresh basement): These type of aquifers are permeable only locally where deep tectonic fractures are present. Based on studies conducted at the east of the region (Dziembowski, 1976; and Jolly,

1986), the fractured fresh rock aquifers in the Dendron/Mogwadi area, may extend to depths greater than 120 m, with blow yields that exceeding 40 ℓ/s .

A survey conducted by Vegter (2003a) on the Polokwane/Pietersburg Plateau groundwater region found that 52% of boreholes drilled were successful (yield > 0.1 ℓ/s), based on data from the National Groundwater Database. Holland (2011) found that 61% of boreholes drilled were successful (yield > 0.1 ℓ/s), based on data the Limpopo GRIP programme. Furthermore, 35% of the successful boreholes from the in the Limpopo GRIP programme yielded more than 3 ℓ/s , suggesting generally good yielding (yield > 1 ℓ/s) borehole according to Clark (1985).

Geohydrological investigations conducted by Martin Holland (2011) in the basement-weathered-fractured rock aquifers of Archaean age crystalline lithologies suggested that the regional water table was between 0.6 mbgl and 83 mbgl, with a mean of 17 mbgl and 90% of recorded depths to groundwater levels below 30 mbgl. Martin's work was based on drilling data collected from the Limpopo GRIP dataset. Recorded borehole depths in the region range from 7 mbgl to 250 mbgl, with 60% of boreholes drilled to depths between 50 and 80 mbgl. Water strikes during drilling in the region were recorded at depths ranging from 1 mbgl to 87 mbgl, with 60% of successful boreholes encountering water before a depth of 40 mbgl in the region. Furthermore, inferred aquifer transmissivity values from pumping tests data of the Limpopo GRIP (Martin Holland, 2011) suggests 70% of the transmissivities lie between 04 m^2/d and 40 m^2/d , with an arithmetic mean of 38 m^2/d .

Based on the chloride method (CMB) which was adjusted to account for factors such as depth to groundwater, land cover, variation of MAP and slope, the Groundwater Assessment Projected II (GRA II, 2006) conducted by the Department of Water Affairs (DWA), groundwater recharge was approximated to 2% (702 million m^3/a) of mean annual precipitation (MAP) in the Limpopo WMA. Martin Holland (2011) estimated recharge rate values between 0.4 to 4.6 % of MAP by applying chloride method to data from Limpopo GRIP programme. His study showed that active recharge zones may be occurring in higher lying areas associated with the main surface water drainage divides.

5.5.2 Analysis of available GRIP II data base information on Boreholes in the catchment
The borehole depths follow a normal distribution (Figure 21) for the study area with 70% of boreholes drilled to depths between 40 and 80 mbgl, indicating the tendency to drill to fixed depths regardless of the hydrogeological conditions encountered.

Table 3: Statistics of borehole depths and groundwater levels from GRIP

	Unit	Count	Min	Mean	Max
Borehole Depth	mbgl	241	16.11	63.28	180.9
Depth to Ground Water level	mbgl	259	0.73	11.17	41.34

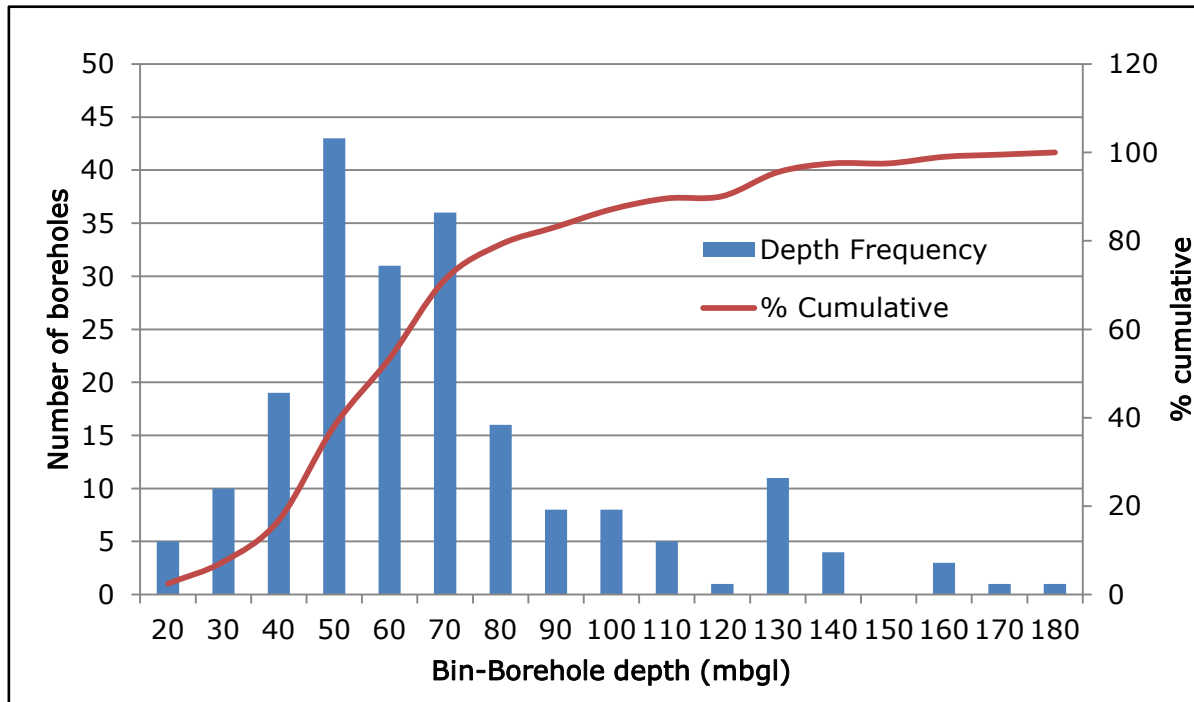


Figure 21: Borehole depth frequency (Grip data)

Recorded depths to groundwater levels follow approximately a log-normal distribution (Figure 22), with the highest frequency (modes) between 5 and 10 mbgl, and 95% of groundwater levels are shallower than 20 mbgl.

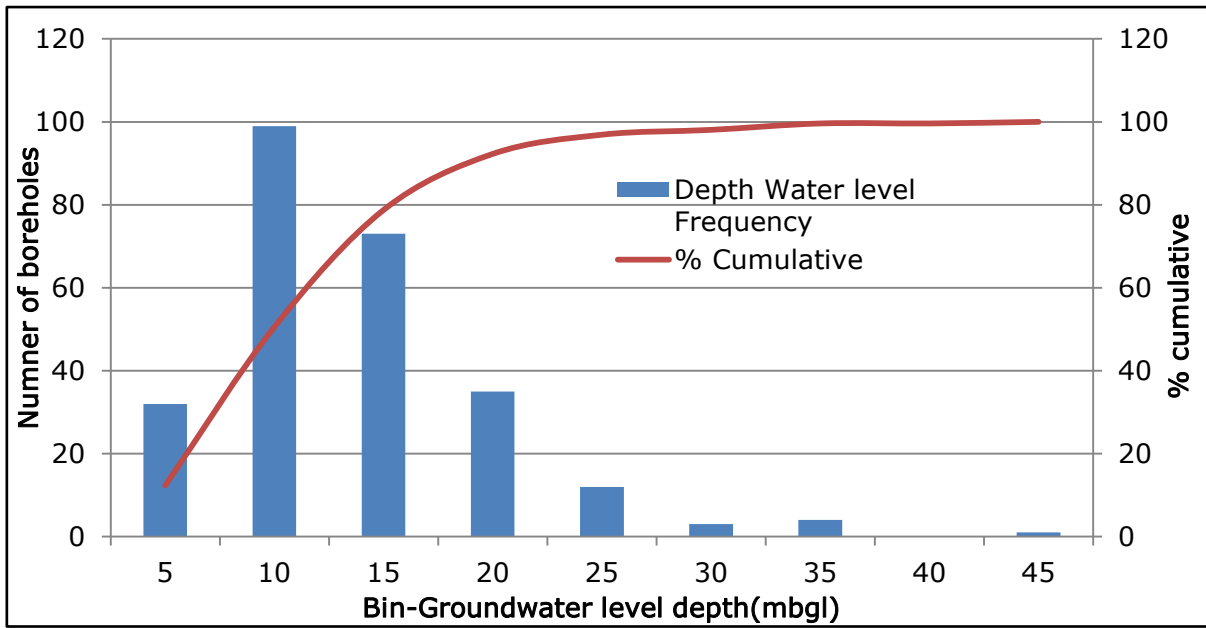


Figure 22: Depth to water levels frequency (Grip data)

No data on borehole log (water strikes, blow yield, weathering depths) were collected for processing, from the GRIP Limpopo data, at the time of the dissertation.

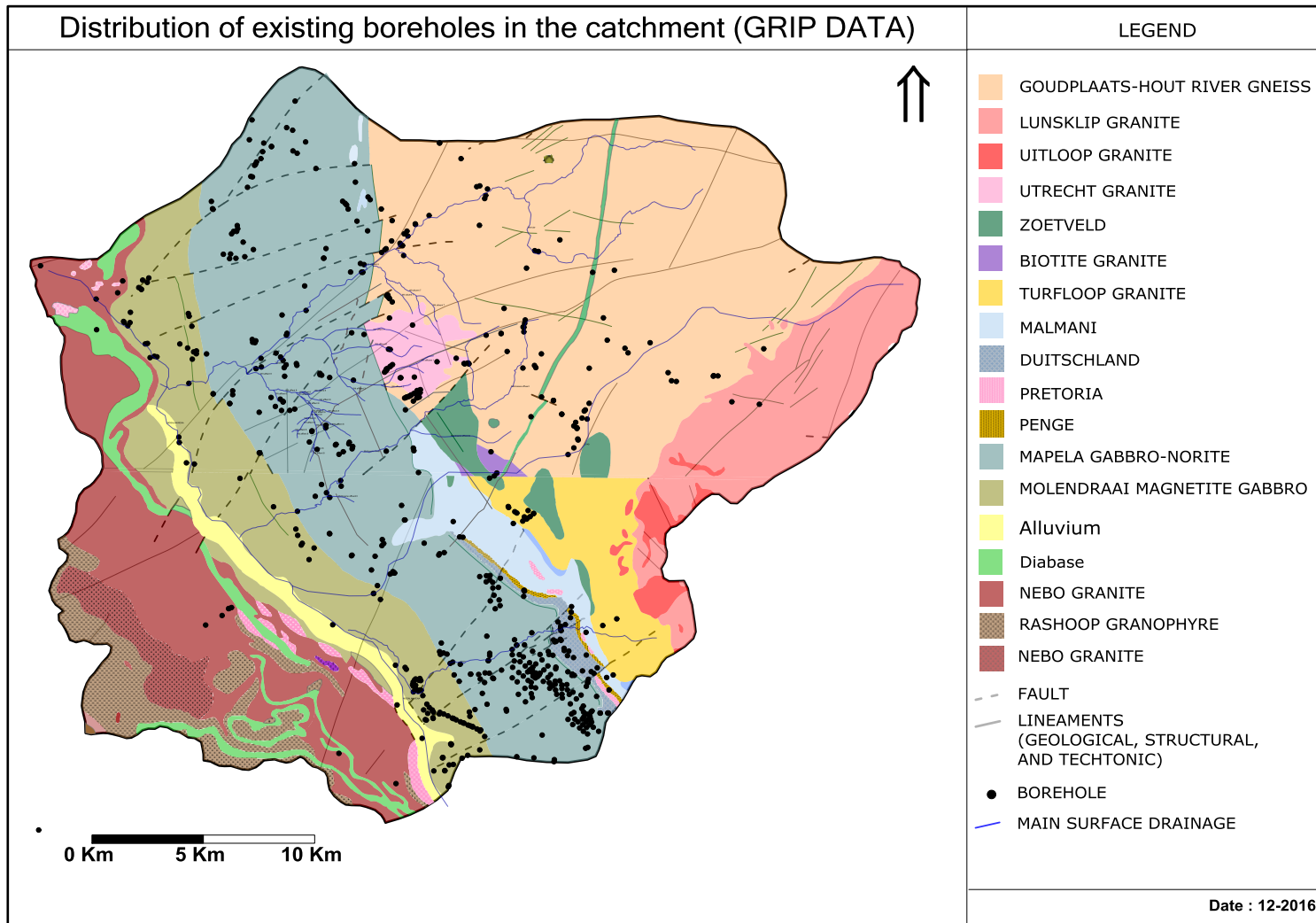


Figure 23: Distribution of GRIP data in the catchment

6 Field characterization of the study area

Several geohydrological field investigations (phases) were conducted from September 2013 to October 2014, within the quaternary catchment of interest. This was conducted as part long term mining pit dewatering, and water resource protection and waste management programmes for an operating open cast platinum mine within the catchment. The author of the thesis successfully managed the different phases of the investigations. The author found that the amount and the detail of data collected can be used to enhance the geohydrological conceptual model of the catchment, by accounting for and quantifying spatial heterogeneity in the aquifer associated with the Platreef. The investigations included routine water monitoring, hydrocensus, geophysical, borehole drilling, and aquifer testing.

6.1 Approach and Methodology for field characterisation

6.1.1 Methodology for Hydrocensus

A hydrocensus was carried out in March 2014 as part of a water resource protection and waste management program for a Mine in the quaternary catchment.

The coordinates of each identified site (boreholes and significant surface water use point), were recorded on a handheld Garmin GPS. Water level measurements were recorded, where possible, using a Solinst TLC (Temperature, water level and conductivity) meter.

Grab water samples were collected from the identified boreholes, using a "single-check valve weighed poly" nylon bailer (1.6" OD, 36" Length) and a labelled rope. Water samples were collected in standard 01 litre plastic sample bottles, and were stored in a cooler box. At each sampling point, the sampler wears latex examination gloves, and new sterilised nylon bailer is used. The bailer was lowered to the possible sample depth, and as the bailer is lowered; the valve located at the bottom opens, allowing water to flow through the sampler. When reaching the possible sampling depth, the bailer is raised using the support cable. The weight of water and upward movement of the bailer keeps the ball valve closed. The bottom ball valve keeps the water in the bailer. Once at the surface, the bailer is emptied by opening the valve with a sample release device, allowing the water to drain slowly through the sample release device into the sample container.

Surface water samples were collected from surface water streams. Samples were taken in the middle of the bankfull, using the lotic systems. Hydrocensus was carried out during the rainy season, when the majority of the rivers and streams were filled with water.

A total of 142 groundwater samples were collected from community boreholes and submitted to the Capricorn Veterenary Laboratory (Cap Vet Lab) for analysis.

6.1.2 Geophysical surveys and Drilling approaches

6.1.2.1 Geophysical investigation approach

Digital information from the Council for Geoscience in the form of 1:250 000 vector data for: 2328 Pietersburg, 2438 Nylstroom geological maps, of aeromagnetic map, with other were used to plan the geophysical survey. Additional geological information collected during previous study in the mine was used to refine the planning of the site geophysical survey. The information included a local geological map indicating structures such as faults which are not indicated on the 1:250 000 geological maps or on the aeromagnetic data.

The main objective of the geophysical investigation is to identify drilling targets for boreholes that will be used for further geological and hydrogeological characterisation for a long term pit dewatering project. A total of 41 geophysical traverses were selected around the active open cast mine. The locations of the traverses have been dictated by the above described objectives, and others constraints related to safety, and site accessibility.

ENVIMAG instrument (combination of mag and VLF) and a EM-34 electromagnetic instrument were used with observations on surface and in pit, to identify drilling targets and further characterise geological structures in the mine area.

The geophysical survey lines were chosen perpendicular to lineaments and prioritised based on site access. The geophysical traverses were set out in the following manner:

- Lines were set out perpendicular or close to the possible structures as indicated on the geological map;
- Lines were marked with a default station spacing of 10 m and 5 m in areas where the possible structure could be intersected;
- GPS coordinates were taken at the start and end of each line; and

6.1.2.2 Drilling technic

Drilling was conducted using an air percussion drill rig (900 cfm compressor), on specific targets identified during the geophysical surveys as well as other geological units and features.

The drilled boreholes were generally constructed as follows:

- Confirmation of the coordinates which includes surface elevation, using handheld Garmin GPS.
- Safety setting (Site clearance on pre-determined site to check for underlying cables and or pipes; Site barricading, and HSE (Toolbox talk, etc.);
- Drill and solid casing (177mm OD steel) installation through weathered into solid, hard rock formation;
- Continued drilling to indicate depth. Thereafter, a gravel pack is inserted to the top; and where necessary, a bentonite or cement seal is inserted above intersected fractures; and
- Installation of a concrete block, head-works and a lockable cap.

Drill cuts were sampled at 1m intervals during drilling, for lithological logging. Depth to water strikes and corresponding measured blow yields were recorded. Blow yields were measured using a 90 ° "V" Notch. At the end of drilling, and after stabilisation of water levels in the borehole, the static water level was measured using Solinst dip meters and level loggers. For more information about procedures followed during borehole drilling, the reader is referred to the SANS 10299-2:2003 and the Department of Water Affairs (DWA) minimum standards and guidelines for groundwater resource development

6.1.3 Setting of Hydraulic testing and interpretation tools

Generally, the hydraulic response of an aquifer to pumping (or any pressure disturbance) is measured and analysed with the objective to (a) characterize an aquifer, (b) quantify its hydraulic properties, and/or (c) determine the efficiency and sustainable yield from the tested borehole. The type and duration of a pumping test depends on the planned usage of the borehole. In South Africa, SANS 10299-4:2003 provides the requirements for the pumping test of a water borehole in order to obtain information about its possible long-term use and management. Typical tests include a slug test, a multiple discharge test (step-drawdown test), a constant discharge test (CDT) and a recovery test.

As a minimum, a slug test was conducted on all relatively low yielding boreholes. This was followed by four 1 hour step tests, a 24 hour constant discharge test, and recording of recovery measurements for the relatively high yielding boreholes.

In order to effectively analyse the various features of the borehole, the following data were collected during pumping tests:

- the time and date of the test;
- the water level drawdown;
- the rate of discharge;
- the static water level;
- the depth of the borehole;
- the distance to observation boreholes (when necessary);
- the depth of pump suction;
- the depth at which water was struck (if available);
- the diameter of the borehole;

For quality control and assurance, water level measurements were taken with a dip meter (Solinst) and an automatic data logger (Solinst), simultaneously. The data logger was set to automatically record water levels every minute and at a constant accuracy of $\pm 5\text{mm}$. The automated recording of water levels allows simultaneous measurements of drawdown in multiple boreholes. It also allows observations to be made regarding the smaller variation in drawdown, which would not have been the case, if only hand measurements were used.

6.1.3.1 Slug test

Slug test is proposed as a minimum requirement for the determination of the yield of the boreholes present on site. It also serves as the first estimate of the hydraulic conductivity values on relatively low yielding boreholes. The test is useful for a first approximation of the yield of the borehole (Van Tonder et al., 2001).

A slug test involves the sudden addition, removal, or displacement of a known volume of water and the subsequent measurements of changes in water level in the well, as equilibrium conditions return. Slug tests are conducted by displacing water. Water displacement was done instantaneously by manually lowering a slug into the borehole underneath the water level. Two slugs (closed PVC pipes filled with concrete) of different volumes (0.28 m^3 , 0.35 m^3) were used. Prior to the application of the slug, depth to water level was measured in each borehole, and is used as static water level. No pre-test water level stabilisation was assessed. The water level recording continued until at

least 85 % of the initial water level measurement was obtained. The time required for a slug test to be completed is a function of the volume of the slug, the hydraulic conductivity of the formation, and the type of well completion (Environmental Protection Agency, 1994).

The responses of the water levels in tested boreholes were used to predict borehole yields by correlating the recession time and the yield of borehole (Vivier et al, 1995). Following this, the Bouwer and Rice method was used to determine hydraulic conductivity values.

6.1.3.2 Pumping tests

Considering the limited budget of the project, the specific objectives of the study, site safety and accessibility, only the 10 boreholes could be pump tested.

A pump test rig equipped with borehole submersible pumps (3-Phase, 5.5kw and 7.5kw), which can yield up to 12m³/hour at 70m head, and a generator 150kva was used. The pumping rates were kept constant using a variable speed driver and an ultrasonic flow meter. For quality assurance purposes, the flow rate was measured using a 200L drums and a stop watch. The design of the pump test is presented with test results and interpretations. (Section 6.2.5).

6.1.3.3 Step test

The step drawdown test is a single-well test and it is performed to determine the optimum yield at which a borehole can be subjected to CDT. Groundwater was pumped from the borehole sequentially at least two higher pumping rates over prescribed periods of time. During each step a steady state drawdown was observed prior to increasing the pumping rate for the next step.

6.1.3.4 Constant Discharge test

Based on results from the step tests, boreholes were chosen to be pumped constantly for 24 hours. Responses to abstraction were recorded for abstraction and observation boreholes (starting from the closest one, toward the distant ones) as well. The outlet pipe was at 100m down gradient to pumping borehole. Each CDT was followed by a recovery phase where residual drawdown was recorded up to at least 90% of recovery at least. The same pump test rig used for step tests was used for CDT.

6.1.3.5 Recovery test

Data from recovery test is used to determine the aquifer parameters and to determine how rapidly the water level recovers. This is required for the design and management of mine pit dewatering and slope depressurization.

6.1.3.6 Data Interpretation

The response (drawdown/recovery) of the aquifer during the hydraulic tests were analysed with different methods provided in the program "Flow Calculation" (FC) developed and compiled by the Institute of Groundwater Studies (IGS). These methods include: Diagnostic plots (Log-Log; Semi-Log); Nueman, Hantoch, and Barker. It has to be pointed out that; these methods were used based on the diagnostic form water level drawdown in response to constant discharge tests. The results from these interpretations will serve for comparison purpose.

In addition to these existing methods, the two proposed new analytical (mathematical) models for fractal fractures flow and fractal double porosity flow respectively, were also applied to the data to infer fractal hydraulic parameters of the tested aquifers.

For better confidence in the estimate of the aquifer flow parameters, we also used a 3D numerical model calibration. Using numerical tools, hydraulic parameters which can more adequately simulate the observed heads, were assessed. The section on Numerical Modelling gives better insight to the approaches used in the numerical modelling.

6.1.4 Groundwater Recharge estimation

Groundwater recharge (R) for the area was also calculated using the chloride method (Bredenkamp et al., 1995; Eddie van Wyk, 2001) method and assuming there is no other source of chloride than the rainfall. It is expressed as a percentage of the Mean Annual Precipitation (MAP). The method is based on the following equation:

$$R = \frac{\text{Chloride concentration in rainfall (mg/l)}}{\text{Cl concentration in ground water}} \times 100 \quad (136)$$

6.2 Field characterisations results and interpretations

6.2.1 Hydrocensus in the catchment

Hydrocensus was conducted in the catchment, aiming to:

- Locate and identify all groundwater users and uses;
- Locate and log boreholes, and measure groundwater levels for inclusion into the groundwater conceptual flow model;

- Sampling and analysis of groundwater quality for the establishment of water types.

During the hydrocensus survey and review of available borehole information, a total of approximately 232 boreholes were identified, of which 197 were sampled, 54 water levels measured, and 40 boreholes logs recorded. The positions of the borehole that have been identified during hydrocensus are indicated in Figure 24, and a short summary is provided in Table 4.

In the present section we will present aspects of the results of the hydrocensus that are most relevant to groundwater flow characterisation in the catchment. The presentation of the water quality results and discussions on the spatial variability of the water quality types in the catchment are included in section (6.6) dedicated to the Hydro-geochemistry.

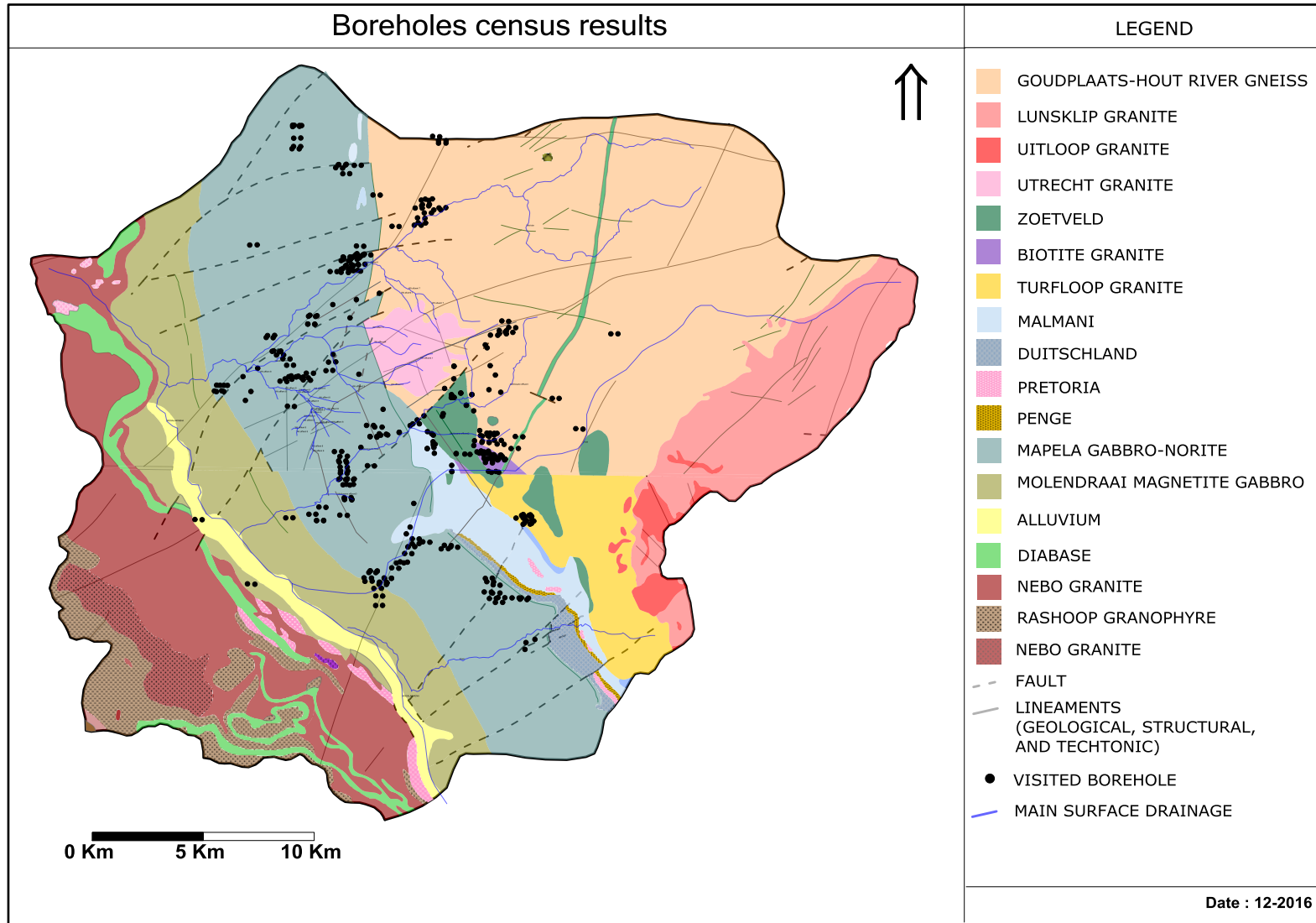


Figure 24: Distribution of Borehole visited during hydrocensus in the catchment

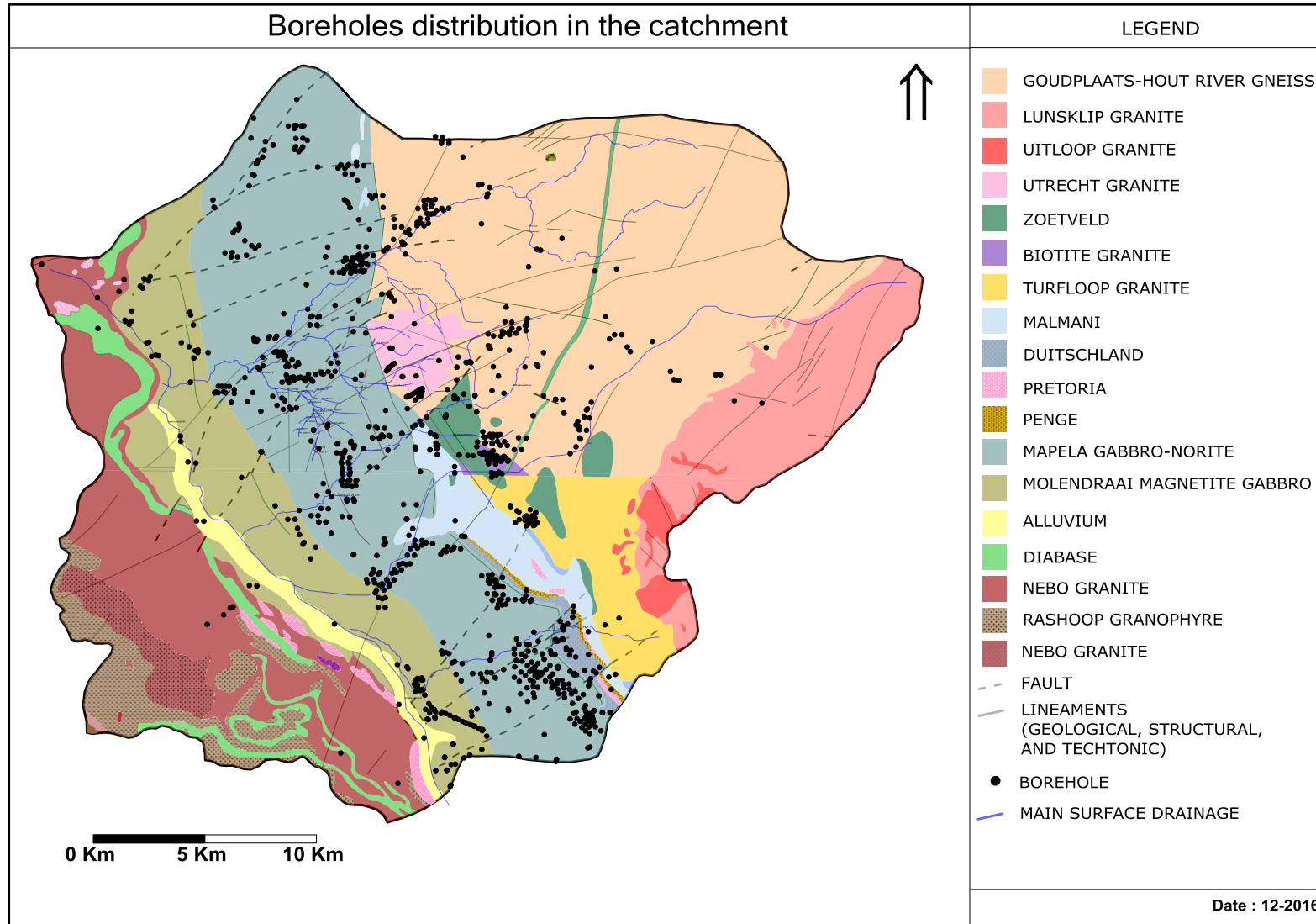


Figure 25: Distribution of combined hydrocensus and GRIP boreholes in the catchment

6.2.1.1 Boreholes uses, accessibility and management/maintenance

The reduced number of measured water levels is mainly due to limited access into the majority of community boreholes, as the majority of them were equipped with pump (submersible or hand pump) and often covered with concrete against thieves. Few (11) boreholes accessible for water levels measurement in the community, are the one not equipped due pump being stolen or are recently drilled boreholes. This also shows that community boreholes are not regularly monitored by individual/private owners, and raises the issue of the responsibility of local communities in groundwater management at catchment level.

The remaining (45) water levels recorded during hydrocensus were measured from monitoring boreholes of platinum mine located within the catchment. The mine is also sourcing groundwater from 03 well fields (PPL, Commandodrift, Blinkwater) of 31 boreholes in total, within the catchment. Access to these well field boreholes was not possible during hydrocensus.

In the catchment, the groundwater is found to be mainly used for domestic and agricultural (Irrigation and cattle farming), and mining purposes.

6.2.1.2 Boreholes depths, and depths to water levels

The analysis of the Hydrocensus data with other collected borehole information from private mine, confirm the normal distribution (Figure 26) of borehole depth within the catchment. 68% of boreholes depths vary between 30 and 80 mbgl. The slight change in the borehole depth distribution, when compare to the GRIP data, is probably associated to data collected from the mine monitoring network, where boreholes' depths tend to be fixed to 30mbgl.

Table 4: Statistics of borehole depths and groundwater levels (hydrocensus)

		Count	Min	Mean	Max
Borehole Depth	mbgl	58	2.45	49.47	150
Depth to Groundwater level	mbgl	81	0.1	9.75	30.28

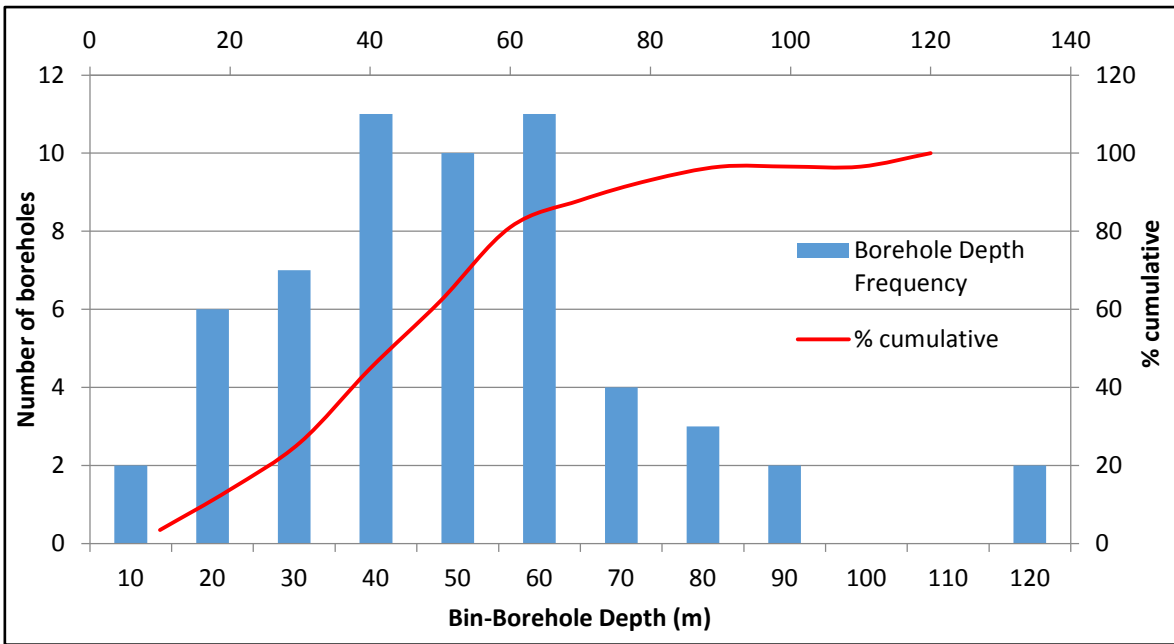


Figure 26: Borehole depths frequency (Hydrocensus)

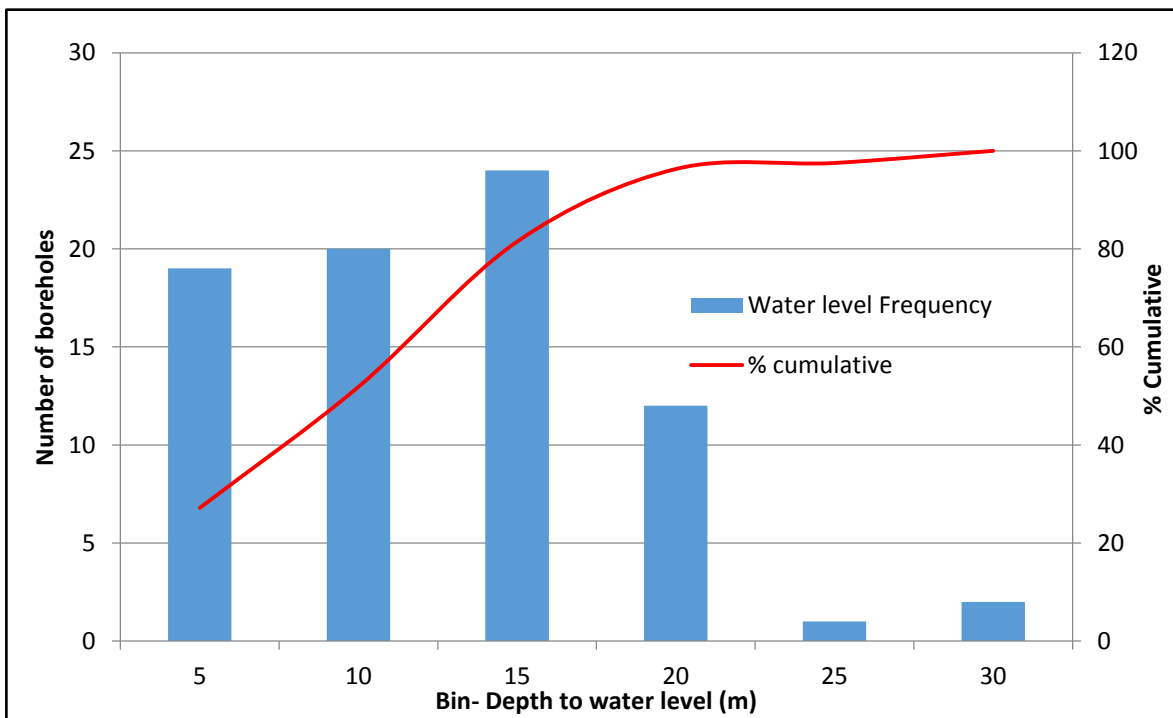


Figure 27: Depth to groundwater levels frequency (Hydrocensus)

As per the GRIP data, the recorded depths to groundwater levels during hydrocensus and review of available borehole information show an approximately log-normal distribution (Figure 27), with the highest frequency (modes) between 5 and 15 mbgl, and more than 95% of groundwater levels shallower than 20 mbgl.

6.2.1.3 Water strikes and weathering/fracture zones thicknesses

The analysis of the 45 existing boreholes in the catchment that contain information on water strike depths, it was found that the depths to first water strike when drilling, are normally distributed. 85% of boreholes encountered water before a depth of 25 m in the catchment. This might explain the generally shallower (approximately 50mbgl) drilling depths in the catchment.

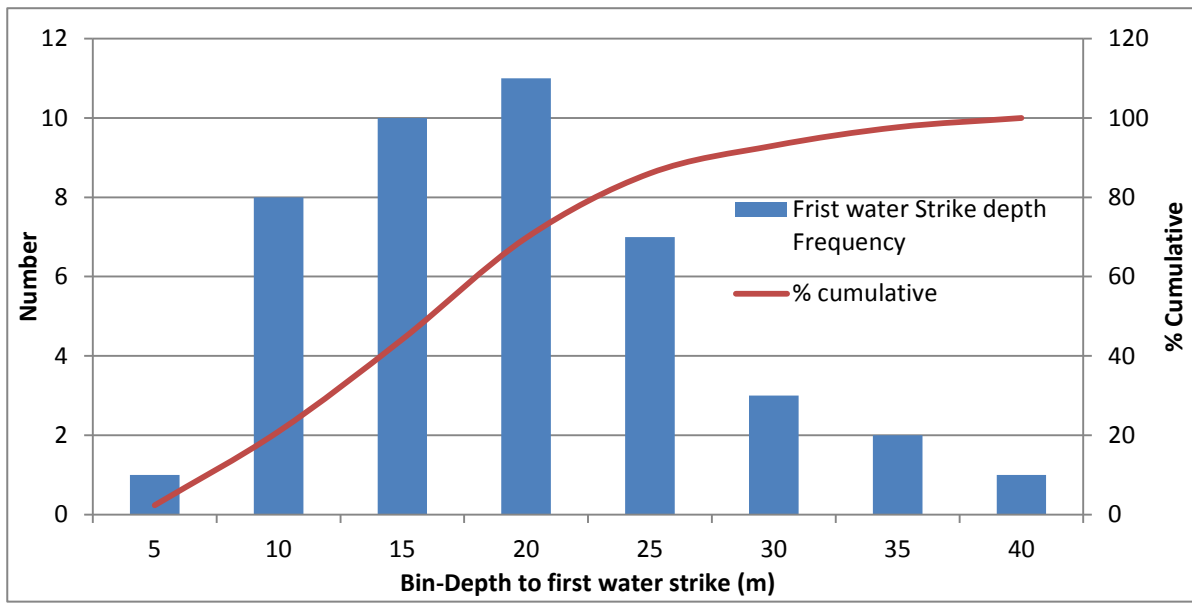


Figure 28: Depth to first water strikes frequency (Hydrocensus)

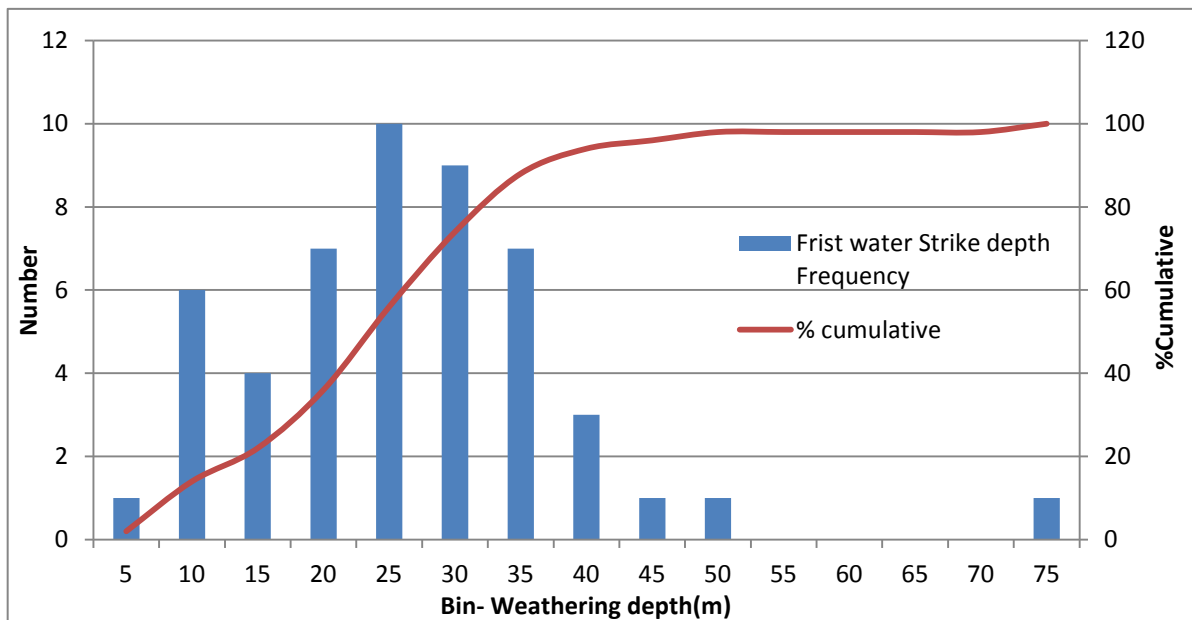


Figure 29: Depth to first weathering bottom frequency (Hydrocensus)

As, it is difficult to distinguish the depths of weathering from fracturing from the geological logs (especially from percussion drilling), a proxy for the depth to bottom of

weathering/fracturing zone (to fresh bedrock) was estimated by combining (weathering and fractures) dataset from 50 boreholes of the catchment.

The mean depth of weathering/fracturing is 24.5 mbgl in the catchment, and 88% of the boreholes with depth of weathering/fracturing shallower than 35 mbgl. This typical distribution of the weathering contrasts to the general average depth of weathering/fracturing of 45 mbgl in the Limpopo Plateau as found by Martin Holland (2011).

6.2.2 Analysis of geophysical patterns (Magnetic and Electromagnetic)

In total 14.111 kilometres of geophysical survey lines (41 traverses) were run. The locations and directions of the geophysical traverses are illustrated in Figure 30, where targeted structures are described by local names. The full detail on the geophysical survey can be found in Appendix A.

- Focus was given to the following targets:
- Structures cutting through the mine pit (the Plaatreef);
- Structures located at some distance Less than 02 away from the pits; and
- Structures located towards the north western corner of the Blinkwater tailings dam.

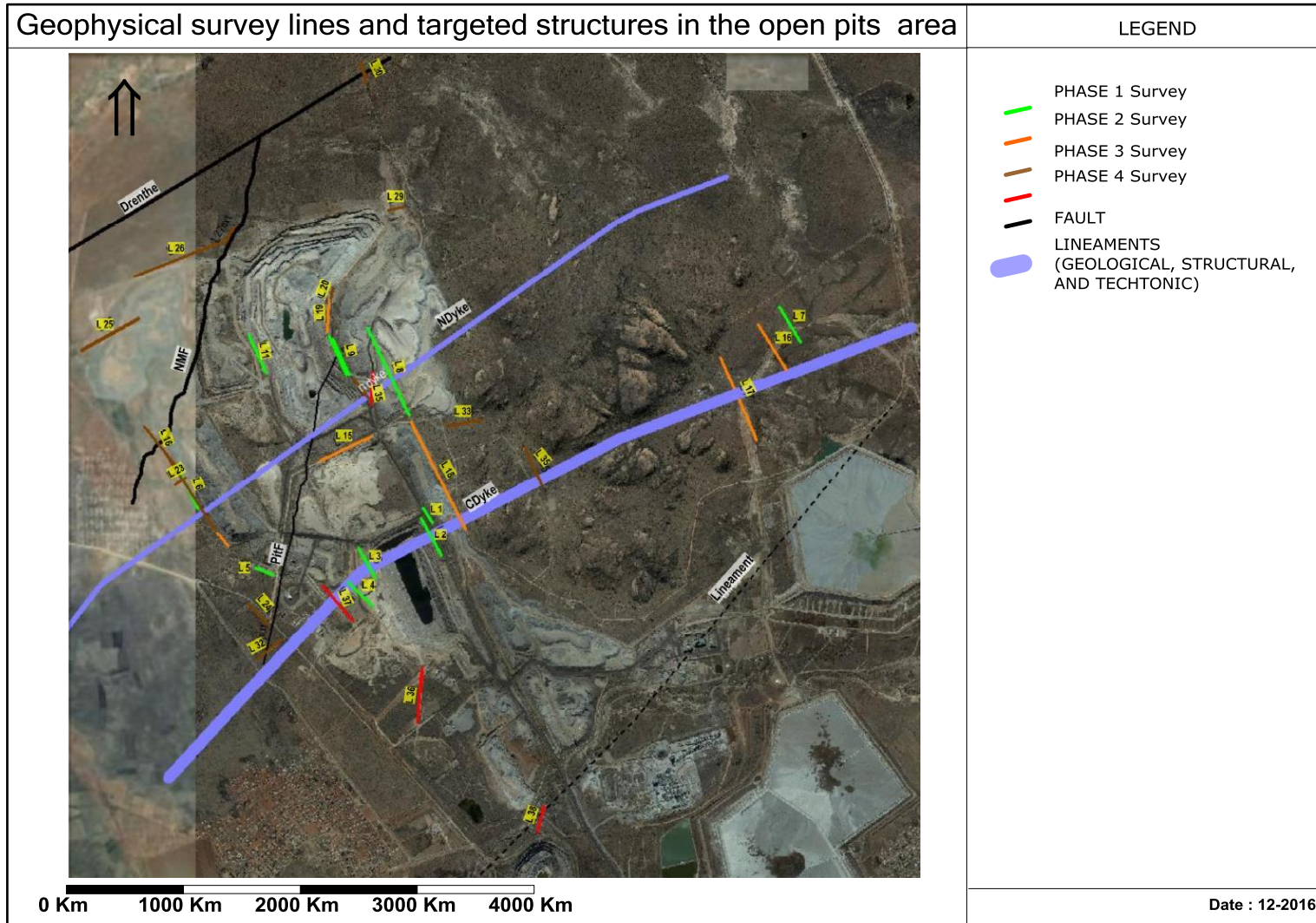


Figure 30: Position of geophysical traverses (red line, brown lineaments) with lineaments (blue: Dyke, black Fault,)

These structures are known to be associated with high yielding fractures intersected by existing strong boreholes, and they included:

- Aeromagnetic and landsat lineaments;
- Dolerite dykes;
- Geological faults; and
- Geological contact zones.

Specific targets included:

- The contact between the dykes (Please put numbers!) and both the hanging wall (gabbro-norites), and footwall (granite);
- The contact zones between the Dykes and Faults; and
- The contacts between lineaments in general.

Both magnetic and aeromagnetic methods were found to be appropriate to detect linear structures and weathering in the typical geology consisting of Gabbro-Norite, Granite and Gneiss.

6.2.2.1 NM Fault and Pit Fault:

Faults in the investigation area, are depicted easily by the typical sinusoidal magnetic and electro-magnetic curves. The anomaly developed when approaching fault, repeat itself after the fault position. A typical anomaly associated Faults in the investigation is presented in Figure 31.

6.2.2.2 Dykes

The narrow shape anomalies showed by the geophysical results on dykes, suggests that the wide of the dyke structures in the investigated are ranges between 40 m and 80 m. A typical anomaly on dykes in the area is showed in Figure 32. The investigated Dykes were found shallow (top is less than 10 mbgl) or outcropping (C Dyke). The Dip of the Dykes are between 10° and 15° in NW-SE direction, but almost vertical;

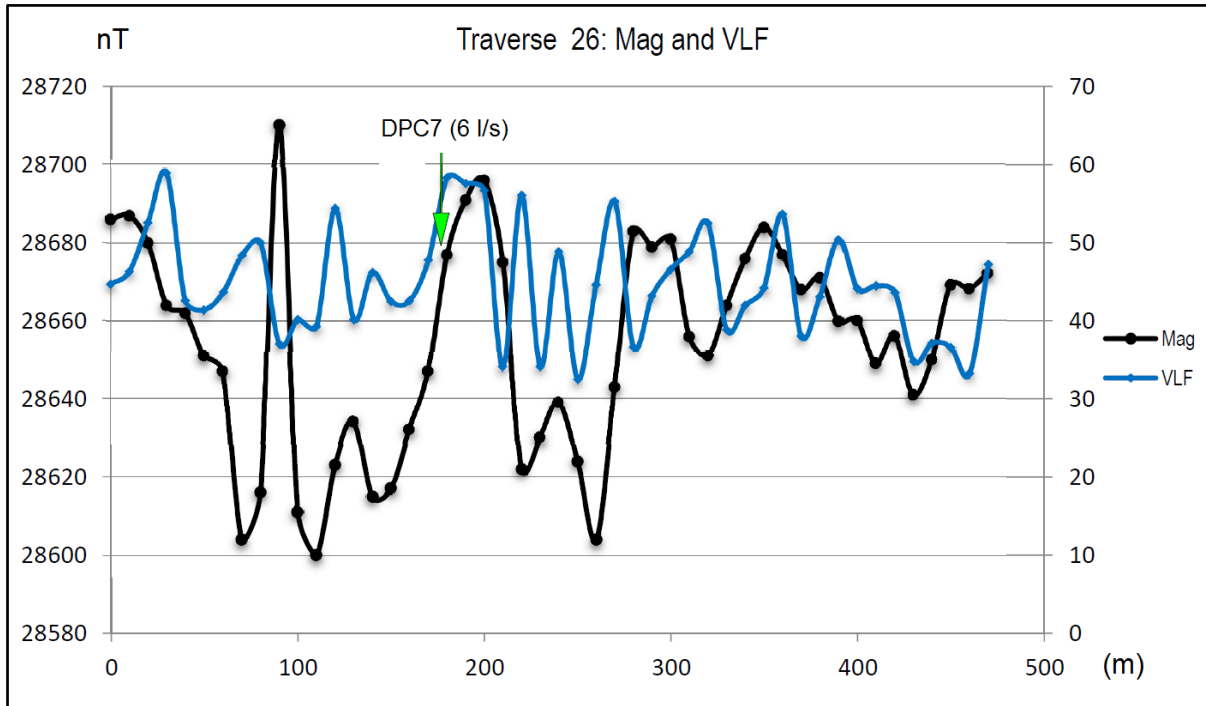


Figure 31: Typical fault anomaly at the investigation area

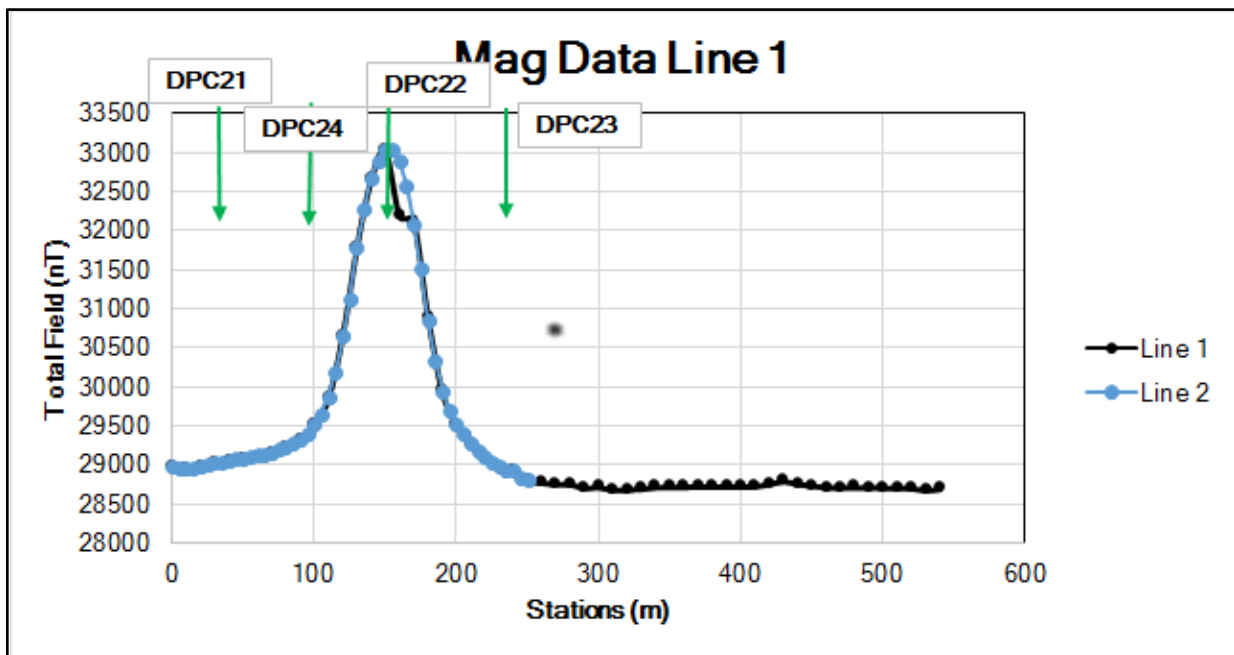


Figure 32: Typical Dyke anomaly at the investigation area

6.2.3 Borehole drilling and geological characterization

Based on the geophysical survey results, drilling were focused on major geological units and linear structures that were identified from existing information and geophysical surveys. Specific geological character of interest included:

- Geometry (Width, Dip, etc.) of Dykes that intersect existing and potential open pits;
- The weathering, fractures occurrence (distributions), and groundwater yielding capacity of the Hanging (Gabbro-Norite) and Foot wall (Gneiss and Granite).

As the investigations were conducted around open pits, drilling locations were also constrained by site accessibility and safety conditions. And drilling results are supposed to reflect active mining impacts (Cone of depression, etc...) on surrounding groundwater system.

In total 46 boreholes, were drilled in the hanging and foot walls of a platinum ore body. Drilling was conducted from October 2013 to October 2014.

Borehole geological logs were analysed to identify and describe the lithology per each meter of the drilled depth. Summary of the drilling result is presented in Figure 33 shows the location of the boreholes drilled in the fractured igneous aquifer associated with the Plaatreef. A summary table of the drilling results is given in appendix B.

CCTV inspection was conducted on selective boreholes to infer the thickness of main fractures/weathering zone.

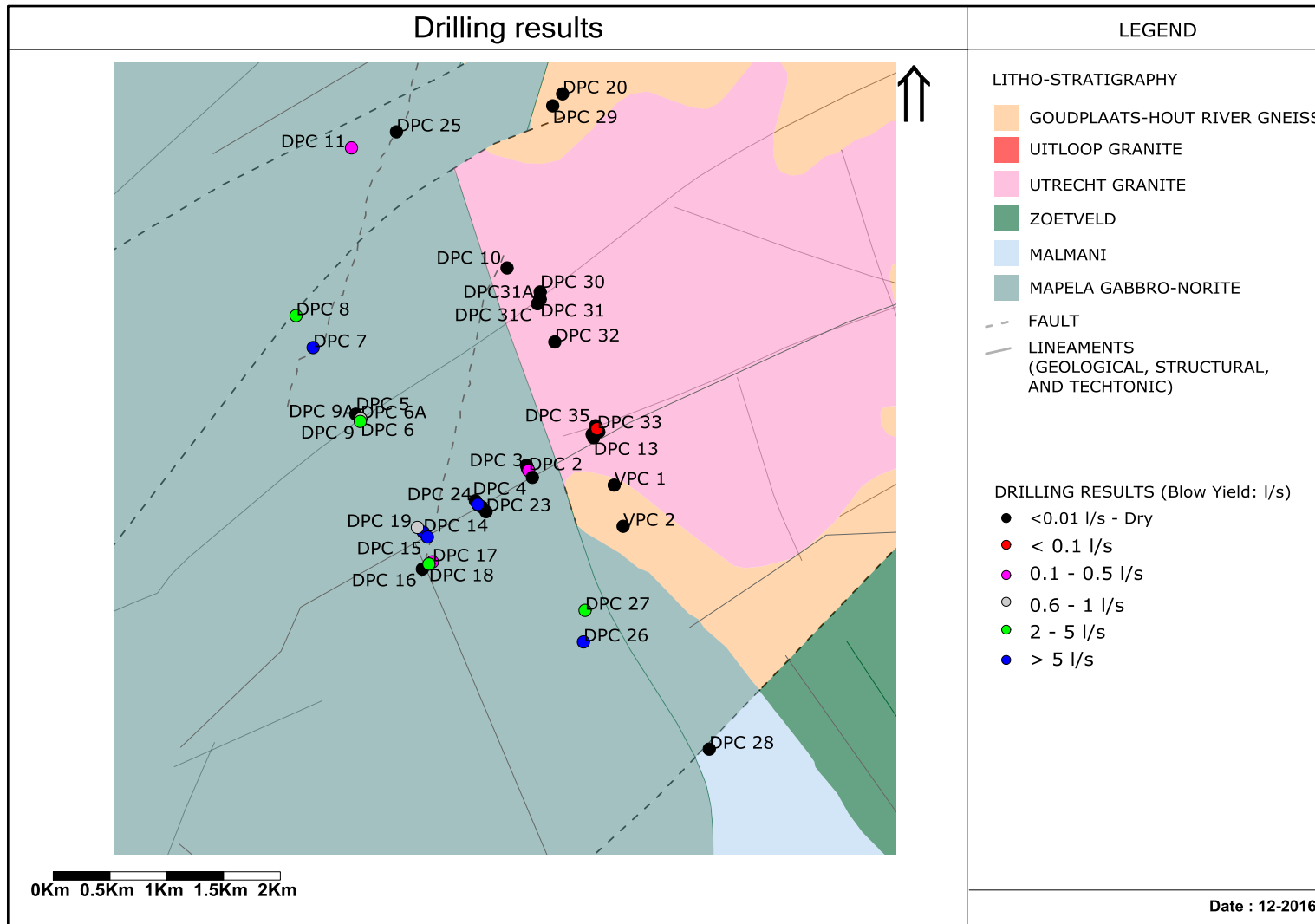


Figure 33: Investigation boreholes locations and results

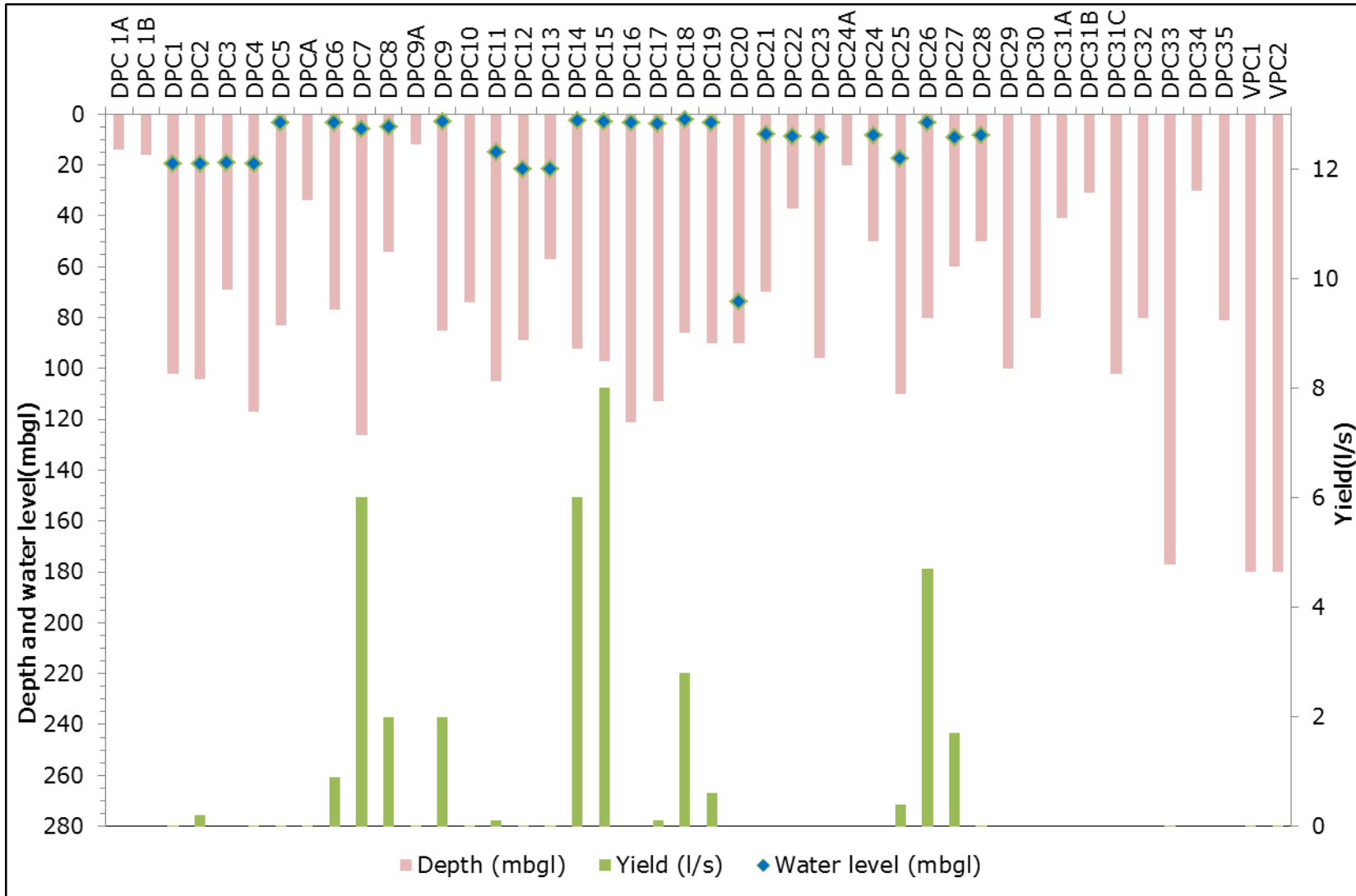


Figure 34: Investigation borehole depths, water levels, and yields

Drilling results confirmed the general low yielding aquifer of the igneous rocks (Gabbro-Norite, Granite, Pyroxinite, Gneiss, etc....) environment within which valuable PGE deposits occurred in the northern limb of the Bushveld complex.

6.2.3.1 Water strikes, blow yield, and water bearing features

44% of boreholes proved to be dry. 90% of the water strikes were achieved at depths less than 50 mbgl. The yields intercepted at depth are negligible ranging below 0.1 l/s blow yields (Figure 35). Only 9% of boreholes proved to have their blow yields of more than 4 l/s whereas 28% of boreholes proved to have their blow yields below 0.1 l/s; Among the 24 drilled boreholes that returned blow yield, only 08 (DPC7, DPC8, DPC9, DPC14, DPC15, DPC18, DPC26, and DPC27) proved to have their blow yields of more than 1 l/s.

The Gabbro-Norite formation was found to have a higher yielding capacity potential than the other formations (Granite and Gneiss) which form the footwall of the pits. Out of 15 drilling attempts in the granite, only 02 (DPC12 and DPC13) showed low yields with groundwater seepage recorded. These results from the drilling attempts in the Granite may also be related to the close proximity of drilling localities to the pits in the Gneiss and Granite.

Groundwater was found to flow not so much in the dyke, but along the contact zone in the baking zone. The main water bearing features are fractures and weathering associated with geological faults and mainly the SW-NE oriented ones.

The variation in the measured blow yield values as well as the number of dry boreholes recorded, confirm the non-continuous flow character of the aquifer, and the high degree of heterogeneity that control groundwater hydrology and associated solute transport in investigated area. Such discontinuities in the groundwater flow pattern should be taken into account for groundwater management and for predictions of the pit dewatering.

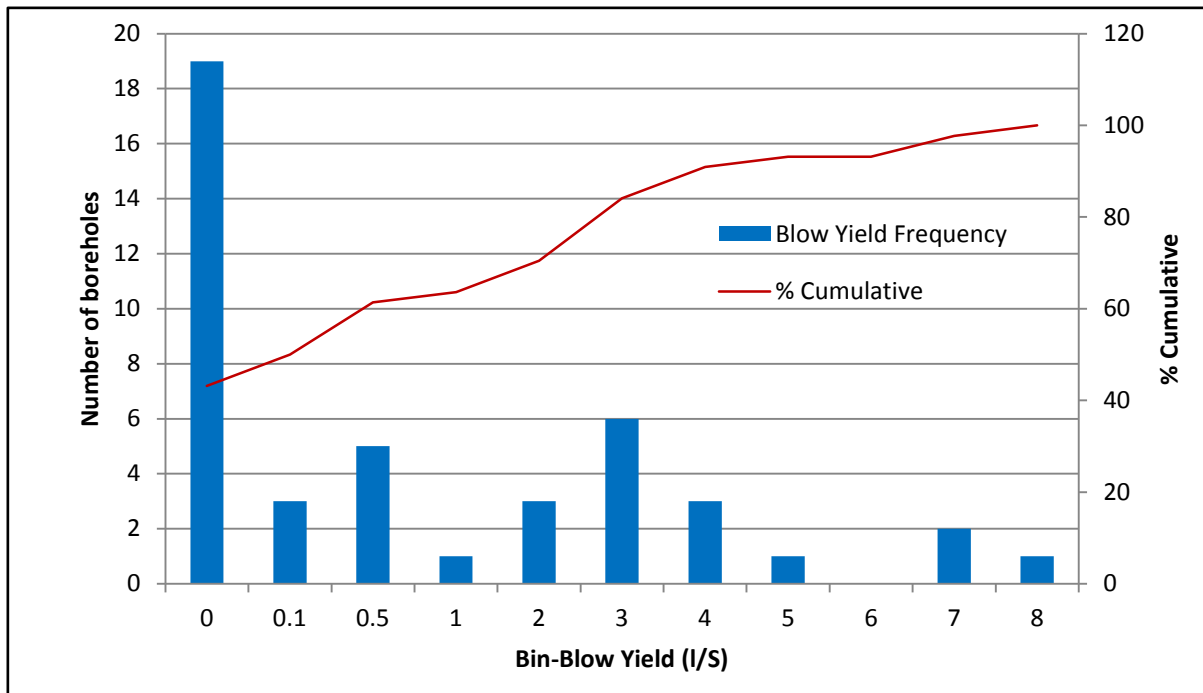


Figure 35: Blow yields frequency (Investigation boreholes drilling)

Dykes

Drilling took place on the targeted dykes, aiming to intercept the dykes in the middle, on the edges at various depths, as well as further away from the dykes, nearing the edge of the baked ones. One wide dyke and one thinner dyke were investigated. The drillings revealed that although some water strikes were encountered in the dykes, very limited water strikes were encountered on the edges of the dykes. Both dykes located between two open pits (North and Central) were found to be very tight and fresh and would probably act as a competent barrier in terms of groundwater flow.

Water strikes were recorded at depths between 5 mbgl and 50 mbgl, with a highest frequency at around 25 mbgl.

Although fractures were intersected in all the boreholes, no water strike was intersected during drilling of boreholes (DPC12; DPC13; DPC30, DPC31A, DPC31B and DPC31C) at contact between the footwall (Granite and Gneiss) and the targeted dykes.

In the hanging wall however, water strikes were recorded, with the highest frequencies at depths between 20 and 25 mbgl. Except for DPC6 (drilled through the dyke), all the remaining boreholes associated with Dykes that showed water strikes were drilled at side (baking zone contact zone) of the Dykes. These boreholes (DPC9, DPC12, DPC13, DPC24, DPC22,) indicated water strikes with blow yields of between 0.1 and 2 l/s.

Recorded blow yields are relatively low and vary between 0.1 l/s up to 8 l/s with an average of 2.21 l/s.

Intersection point of Dyke and Fault were found to form potential high yielding borehole position, as revealed by the drilling of DPC14, DPC15, and DPC18 which appears to be part of the highest yielding in boreholes in the investigated area. In deed these are located at positions close or on the dykes, but associated with faulting.

Dip of the Dykes

Based on the result from the drilling investigation on the main lineaments (striking SW-NE) that cross the Plaatreef, it appears that Dykes are shallow and outcrop at places. Up 120 mgbl, the investigated Dykes are sub-vertical.

Faults and lineaments

Some of the boreholes that were drilled along faults and lineaments (other than Dyke) indicated blow yields of between 2.0 to 8.0 l/s in the hanging wall. 50 % of these boreholes (DPC7, DPC8, DPC14 and DPC15) were drilled on faults (Not my Fault, and Pit Fault) and returned the highest blow yields (between 6.0 – 8.0 l/s).

In the Foot wall, none of the faults that were targeted during the drilling investigation, indicated water strike. However two existing monitoring boreholes (PPC140; RPC25) located on faults in the Foot wall proved to yield up 7 l/s. PPC 140 was drilled at the contact zone between the gneiss and the granite and in the Drenthe Fault, whereas RPC25 was drilled in fault zone at the contact zone between the gneiss and the Pyroxenite.

The rest of the boreholes associated with faults, indicated blow yields of between 0.1 to 2 l/s which are deemed as low yielding boreholes.

Weathering

None of the borehole drilling attempts in the weathered gneiss formation and that was not targeting any linear feature (DPC20, DPC29) yielded water strikes.

In the hanging 02 drilling attempts (DPC26 and DPC27) that were not found to be associated to any recognised lineaments, intersected fracture yields of ranging between 4.7 l/s and 1.7 l/s at depths between 12 and 30 mbgl.



	DPAC7 estimated thickness of about of fractured zone 280 mm
	DPAC15 estimated thickness of about 305 mm

Figure 36: Borehole video image of the fracture zone in selected boreholes

6.2.4 Aquifer drainage, flow directions and gradients

The depth to water levels collected from boreholes during the hydrocensus (including monitoring borehole) conducted in March 2014, were combined with some of the Grip water levels data collected in the same month (March) to calculate groundwater level elevations.

The observed water level elevations (Grip database, Monitoring, and hydrocensus) in the catchment show a very strong correlation coefficient of 98% with the corresponding surface elevations. This suggests that water levels at observation points mimic the surface topography. This may also be valid across the study area to a large extent.

In such a situation the Bayesian Interpolation method may be used to generate water levels elevations at others points of the study area where water elevations were not measured. Bayesian interpolation method determines the correlation that exist between the topography and observed water level elevations and use it to generate water level elevations at non observations points. However, the method may fail to consider abrupt variations in the surface topography, low aquifer recharge, groundwater abstraction and

artificial aquifer recharge, if the measured groundwater level elevations are not well distributed throughout the study area. This also valid for groundwater level elevations along valley bottoms and lower lying areas where groundwater levels are closer to the surface. These limitations lead to over and under estimations of the water level elevations when using the Bayesian Interpolation method.

We compare in Figure 37 the groundwater elevations contour plots of the Bayesian interpolation to the one of a linear kriging (slope: 1, anisotropy: 1). According to both groundwater digital elevations models, the general groundwater flow directions in the quaternary catchment is E-W and W-E toward the Mogalakwena River. However as expected, unlike the linear kriging which is controlled by the hydraulic head gradient between observation points, the Bayesian interpolated groundwater elevations (drainage) mimic the topography. The Bayesian interpolated groundwater elevations show some differences in groundwater flow directions along the Mogalakwena affluents/tributaries (Groot-Sandsloot River, Mohlosane River, and Wit River), and suggesting that groundwater flow into these tributaries. The water flows in these tributaries are known to be seasonal (in response to rainfall) and does not show any physical proof of receiving groundwater flow. The linear kriging of observed groundwater elevations (including observations along tributaries of Mogalakwena River) however, show very limited links between groundwater flow direction and such tributaries. The segments along such tributaries, where kriged observed groundwater elevations suggests some interaction with surface water flow, coincides with lineaments (dykes and faults) locations. This makes it difficult to confirm, the real function of such tributaries in groundwater drainage in the catchment. In the north eastern part of the study area for instance, Wit River seems to receive groundwater flow from SSE and NNE.

The generated groundwater elevations contours (Bayesian and Linear Kriging) reflect also some perturbations in the natural groundwater drainage, as results of dewatering effects (Open pits, Wells field). The shape of these cones of depressions curved along lineaments (faults and dykes were present.) suggesting the preferential paths (or barrier) associated with such lineaments.

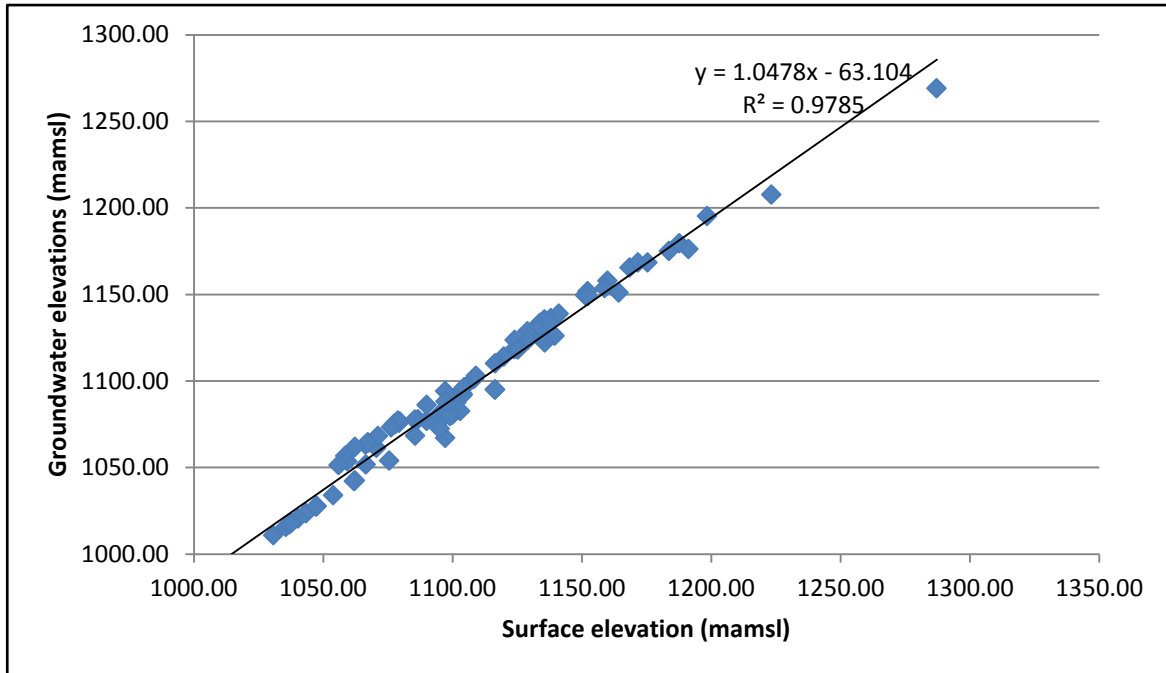


Figure 37: Surface water elevation correlation to groundwater elevations

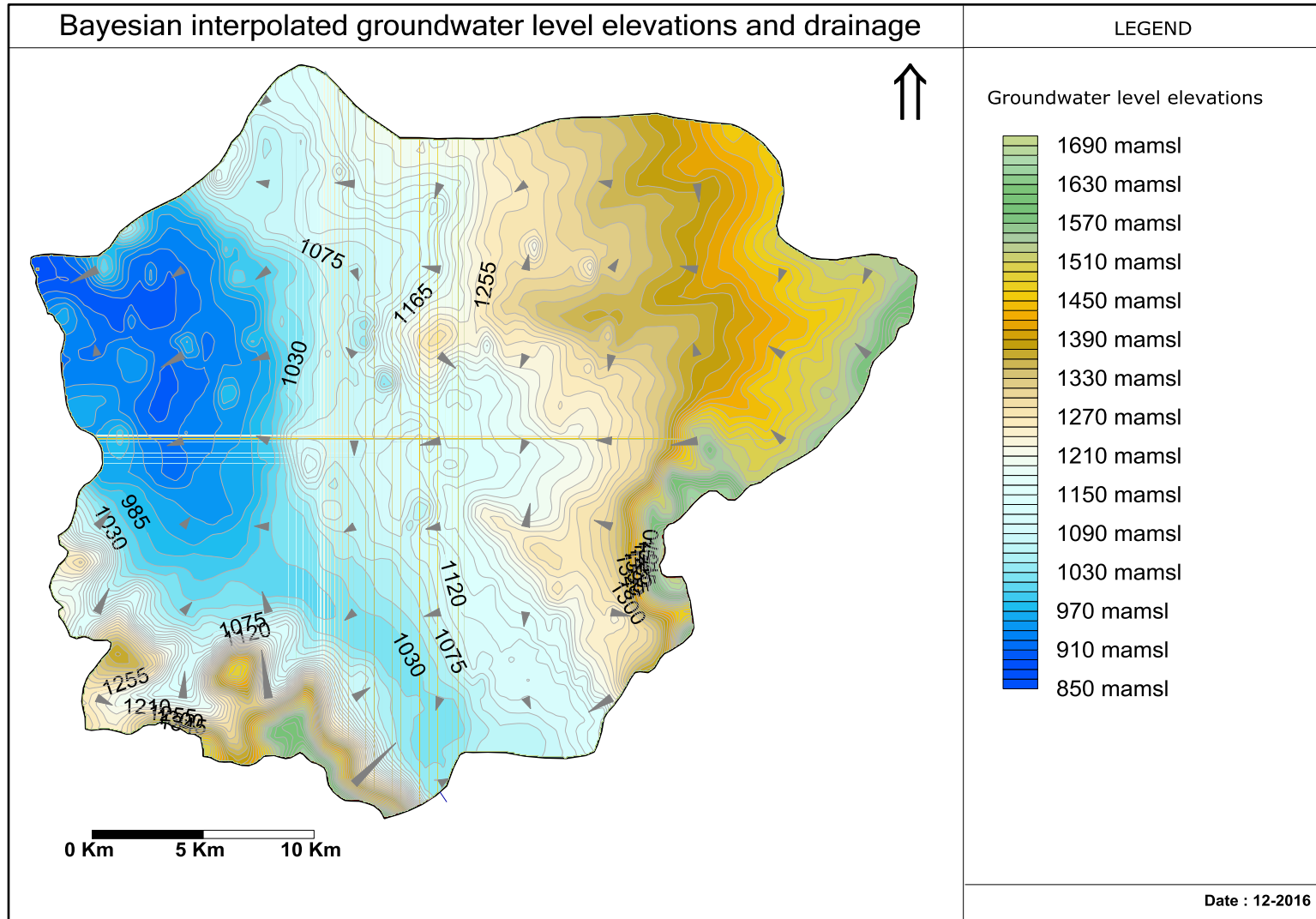


Figure 38: Bayesian interpolated groundwater elevations and drainage

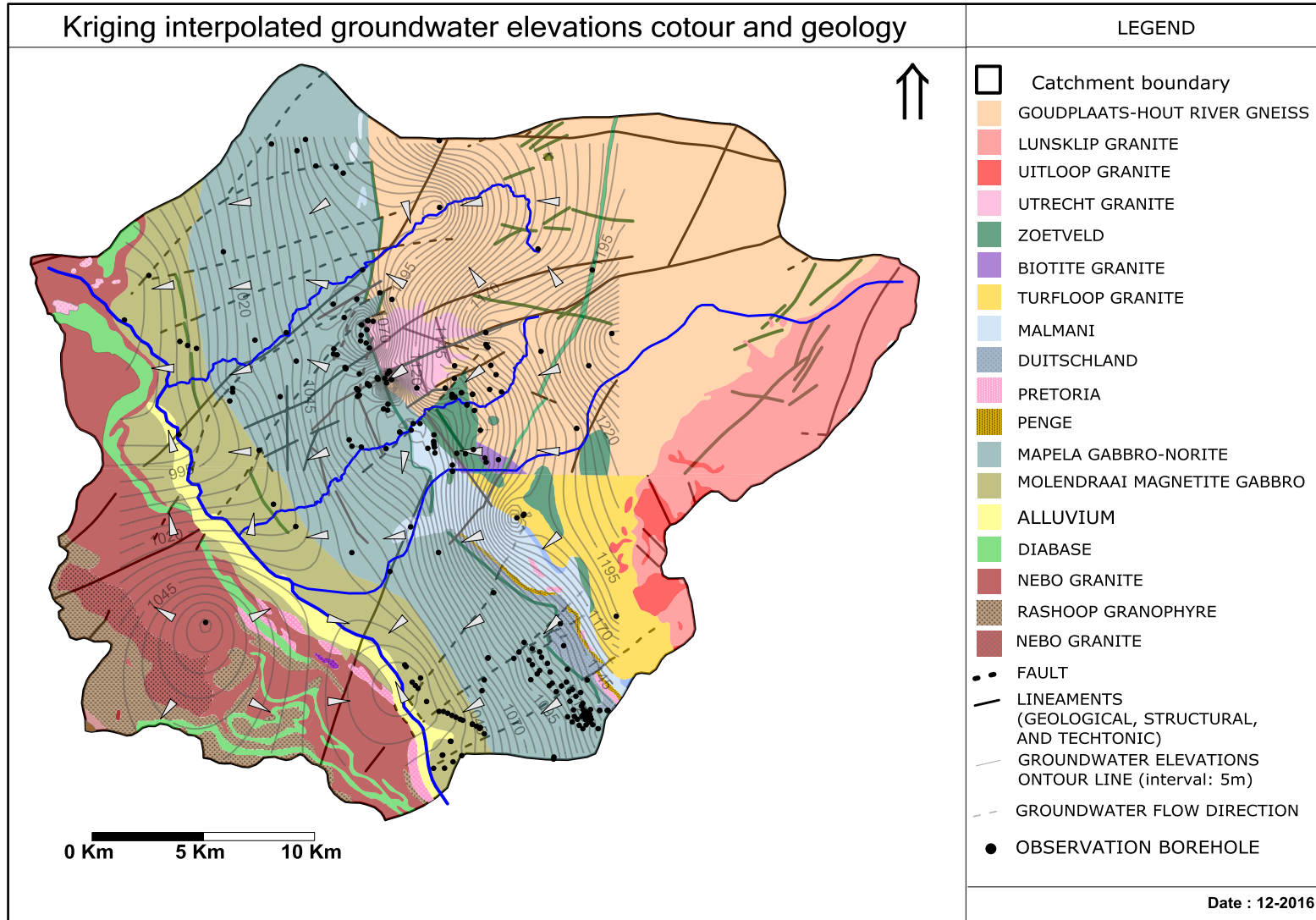


Figure 39: Linear Kriging interpolated groundwater elevations and drainage compared to geological and structural lineaments

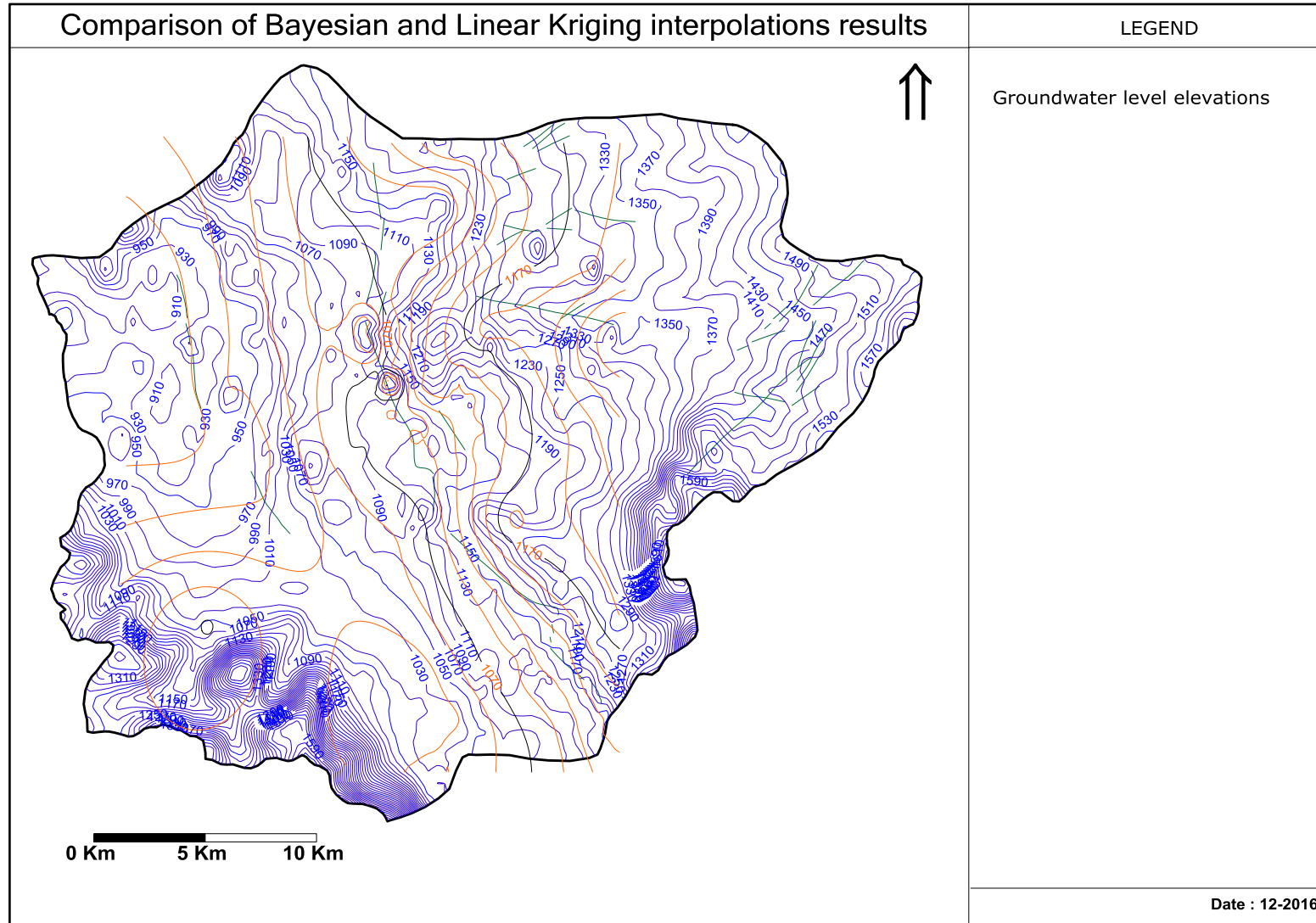


Figure 40: Comparison of Bayesian (blue lines) to the Linear Kriging (orange lines) interpolated elevations.

Groundwater gradient under steady state flow (in absence of any stress) seems continue ranging between 0.015 and 0.02. But at induced cones of depression, steep groundwater heads surface are developed, with gradient ranging between 0.04 and 0.06 around the pit and around 0.03 for wellfields.

6.2.4.1 Dynamic of the groundwater elevations

Significant groundwater levels fluctuations are occurring, probably in response to the recharge and discharge cycles that occur during the wet and dry seasons. An overall groundwater level rising is observed during the considered monitoring period (4years) in boreholes located close to tailing dam suggesting artificial groundwater recharge, in form of water infiltration from the tailing dams.

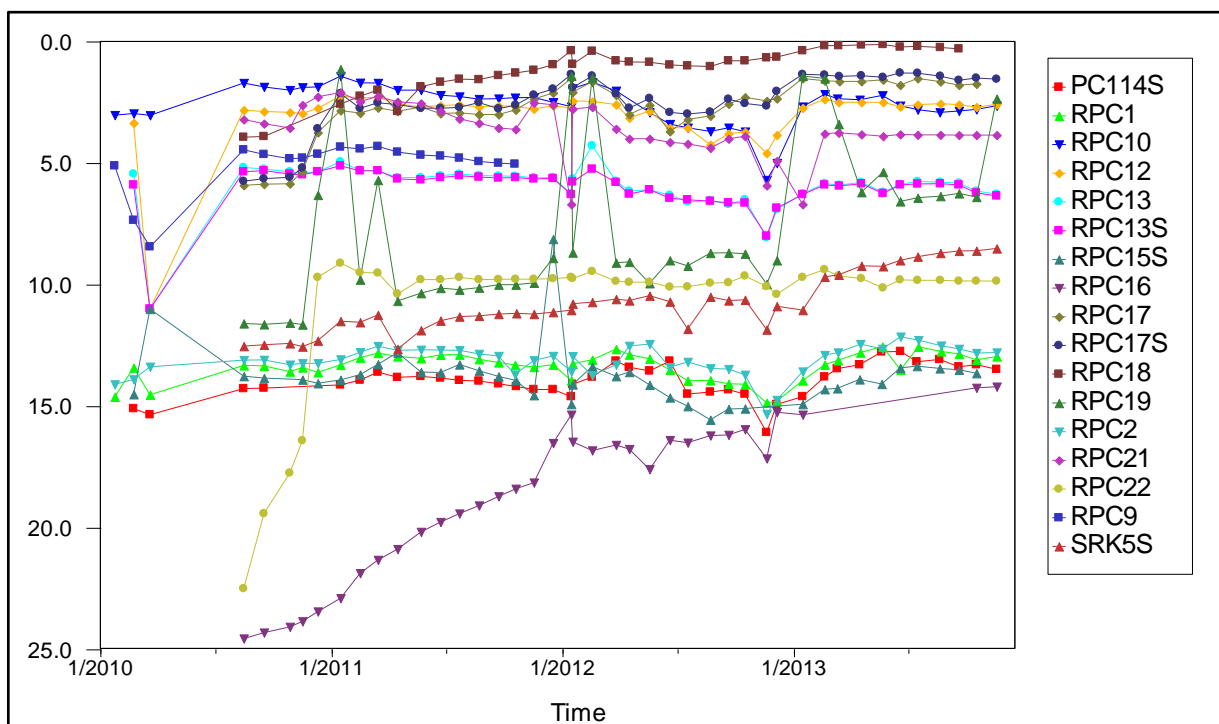


Figure 41: Evolution of depth to groundwater levels

6.2.5 Hydraulic tests results and interpretation

The aquifer tests conducted in the present detailed groundwater investigation; aim to characterize collect/confirm in-situ hydraulic properties for site conceptualization, and for numerical modelling. They have been conducted in the typical crystalline Bushveld Complex as part of planning and design of long term open pits dewatering. The spatial (horizontal/2D) variability of the hydraulic properties of the aquifer and the assessment of the functions of the lineaments are also of importance and have been considered for a more representative groundwater numerical model.

As results of very low hydraulic conductivity (mainly igneous formation) and the relatively high degree of heterogeneity, groundwater flow rate is not expected to be continuous, and is mainly constrain to fractures and weathering associated with geological lineaments (dykes, and mainly faults).

6.2.5.1 Slug testing

24 slug tests were conducted successfully between November 2013 and August 2014. The results were used to determine borehole yields and horizontal K values of the materials in the immediate vicinity of the tested boreholes.

Borehole Yields from slug testing

Table 5 presents a summary of the slug test results and estimated yields. The frequency distribution of the calculated yields and spatial (horizontal) distribution of the hydraulic conductivities are shown in Figure 42 and Figure 44 respectively.

Table 5: Slug test results and estimated yields

Borehole Number	Borehole Depth	S.W.L	Water Rise	Water Drop/ Recovery	% of Recovery	Recovery	Estimated Yields
	(m)	(mbgl)	(m)	(m)	%	(sec)	(l/s)
DPC1	102	19.40	0.38	0.38	100	3600	0.02
DPC3	69	19.07	0.72	0.72	100	420	0.13
DPC4	117	19.55	0.36	0.36	100	3060	0.04
DPC5	83	3.3	0.32	0.32	100	5340	0.03
DPC6	66	3.18	0.25	0.25	100	480	0.13
DPC9	85	2.95	0.13	0.13	100	600	0.22
DPC11	105	14.91	0.23	0.23	100	6180	0.01
DPC12	89	21.60	0.42	0.42	100	2400	0.09
DPC13	83	21.50	0.4	0.40	100	3240	0.07
DPC14	92	2.56	0.11	0.112	100	120	0.22

Borehole Number	Borehole Depth	S.W.L	Water Rise	Water Drop/ Recovery	% of Recovery	Recovery	Estimated Yields
DPC15	97	2.97	0.10	0.10	100	60	0.7
DPC16	121	3.32	0.37	0.21	56.76	1140	0.07
DPC17	113	3.59	0.40	0.533	133.25	20340	<<0.01
DPC18	86	2.03	0.34	0.23	67.65	840	0.07
DPC19	90	3.17	0.21	0.08	37.14	660	0.13
DPC20	90	73.78	0.34	0.07	20.59	57120	<<0.01
DPC21	70	7.99	0.21	0.18	85.24	7680	0.01
DPC22	37	8.95	0.21	0.18	83.33	4260	0.02
DPC23	96	9.00	0.19	0.13	66.84	14520	0.02
DPC24	50	8.28	0.33	0.16	48.79	54240	0.01
DPC25	110	17.45	0.16	0.12	72.5	9540	0.04
DPC26	80	3.27	0.10	0.02	20.00	60	0.13
DPC27	60	9.32	0.19	0.11	58.95	600	0.09
DPC28	50	8.47	0.18	0.13	73.33	21780	0.01

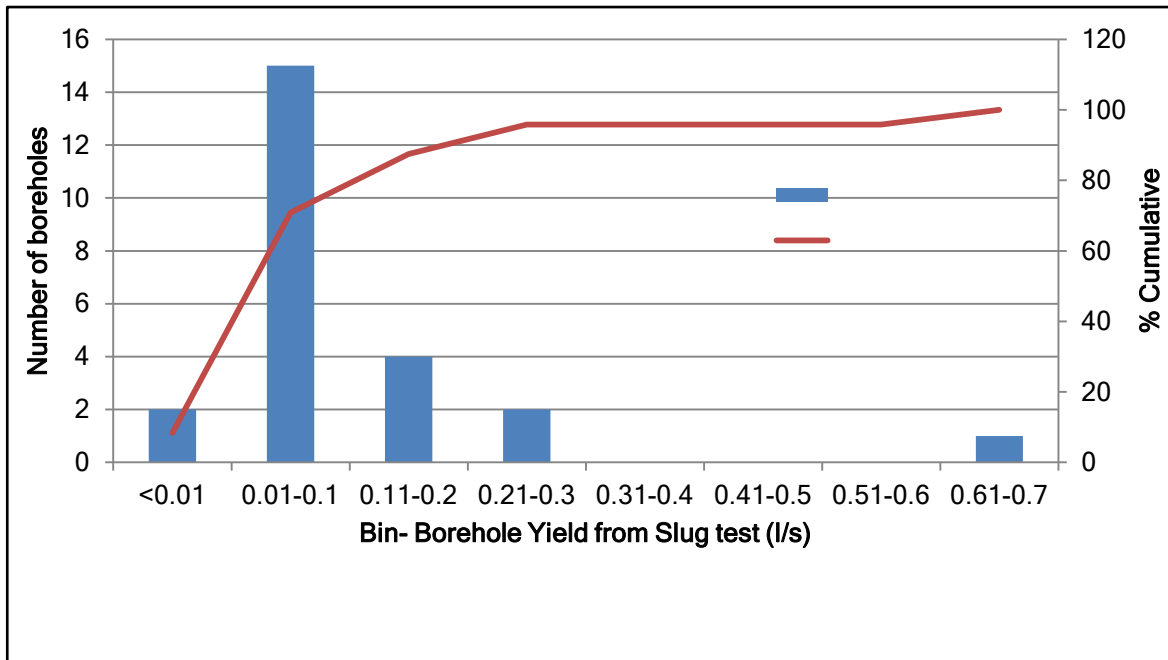


Figure 42: Borehole yields frequency (Slug test on investigation boreholes)

The estimated yields from the slug tests were found generally lower by an order of magnitude compared to the ones estimated from the blow yields, but a correlation of 96.37 % was found between their values, confirming the findings from the slug tests. The inferred boreholes yields ranged below 0.01 l/s to 0.7 l/s (Figure 42). 70% of the inferred borehole yields are less than 0.1 l/s and only 5% (DPC9, DPC14, and DPC15) of the yields are found above 0.2 l/s. The Gabbro-Norite formation was confirmed to have a higher yielding capacity potential than the other formations (Granite and Gneiss) which form the footwall of the pits.

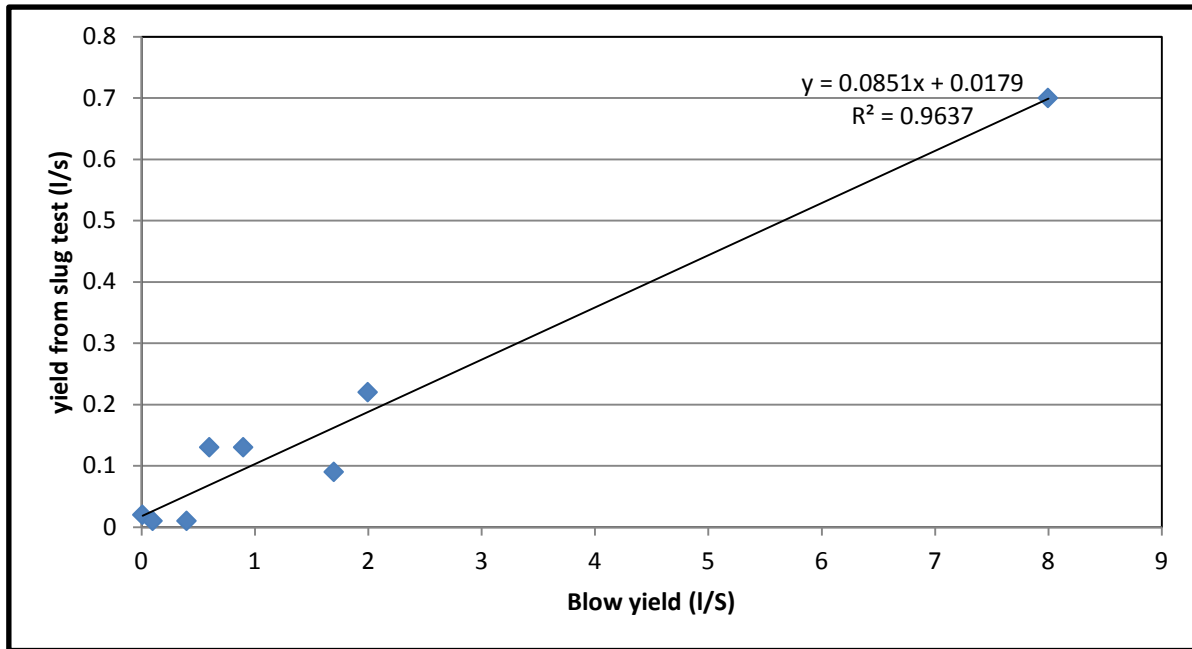


Figure 43: Correlation between measured blow yields (V Notch) and yields inferred from slug tests

Hydraulic conductivity from slug testing

The estimate of K-value using Bouwer and Rice method (1976) is highly dependent and sensitive to the thickness of the part of the aquifer in which flow occurs due to the slug input (van Tonder and Vermeulen, 2002). In fractured crystalline rock aquifers, such thickness depends on the number and the thickness of fractures and weathering zones intersected by the tested boreholes.

Typical fractures zone thickness estimated from borehole logs and CCTV logging in the area (Figure 36), was used with borehole logs information of the tested boreholes to estimate the respective thickness open to flow. Estimated hydraulic conductivities are summarised in Table 6

Table 6: Hydraulic conductivity estimated from slug test

	Borehole Depth	S.W.L	Water depth	Estimated Open to flow thickness	Estimated K values
	(m)	(mbgl)	(m)	(m)	(m/day)
DPC1	102	19.41	82.60	0.1	2.21
DPC3	69	19.07	49.93	0.1	23
DPC4	117	19.55	97.45	0.1	2.45
DPC5	83	3.39	79.62	0.1	3.14
DPC6	66	3.18	62.82	0.3	19.9
DPC9	85	2.95	82.05	0.2	47.2
DPC11	105	14.91	90.09	0.2	1.45
DPC12	89	21.6	67.4	0.1	12.9
DPC13	83	21.5	61.50	0.1	10.9
DPC14	92	2.56	89.44	0.3	49.2
DPC16	121	3.32	117.68	0.1	11.36
DPC17	113	3.59	109.41	0.1	0.54
DPC18	86	2.03	83.97	0.3	26.98
DPC19	90	3.17	86.83	0.2	24.4
DPC21	70	7.99	62.01	0.1	0.94
DPC22	37	8.95	28.05	0.09	2.6
DPC23	96	9	87.00	0.09	1.71
DPC24	50	8.28	41.72	0.09	0.95
DPC25	110	17.45	92.55	0.3	4.12
DPC26	80	3.27	76.73	0.2	6.74
DPC27	60	9.32	50.68	0.1	17.9
DPC28	50	8.47	41.53	0.09	0.77

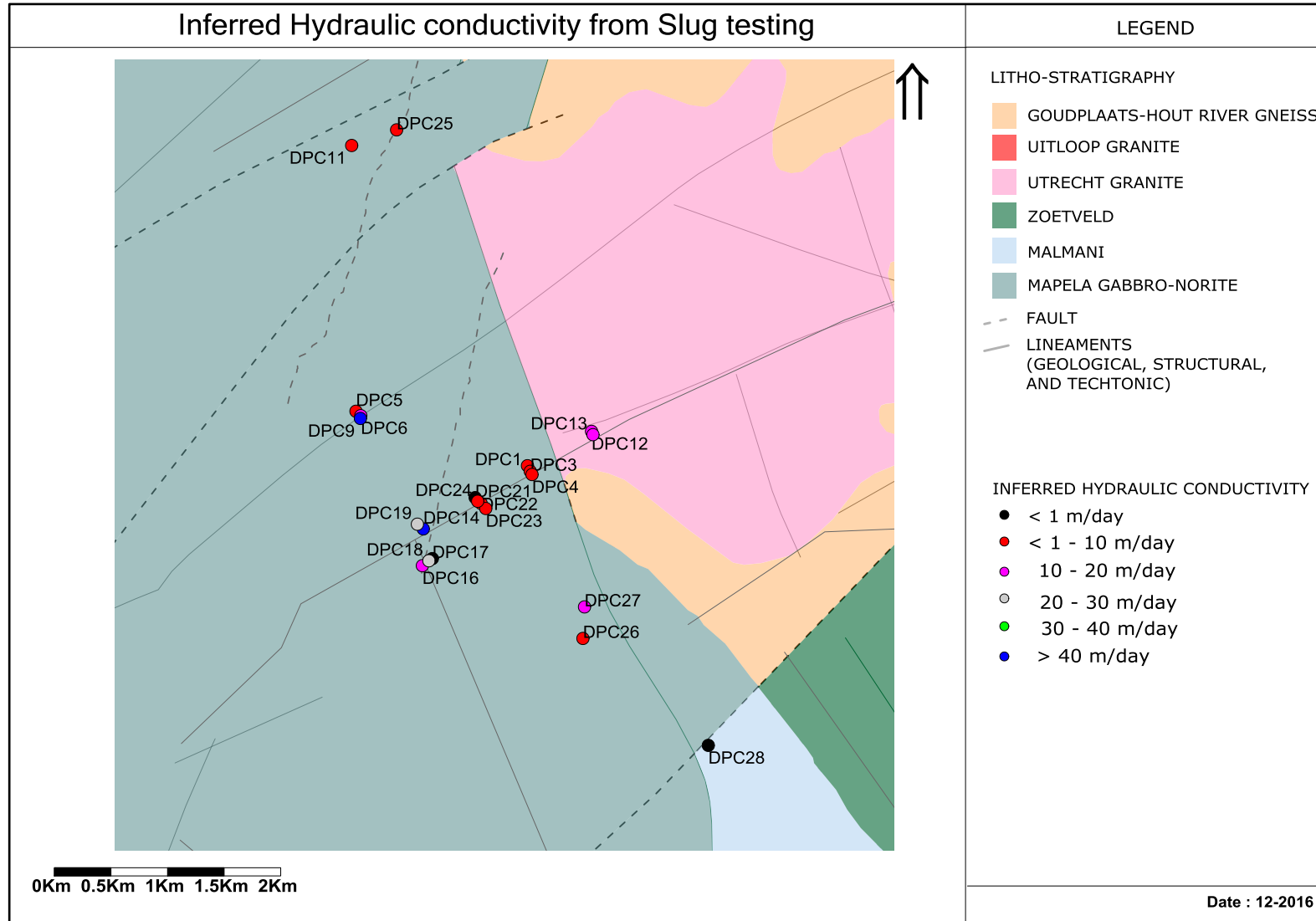


Figure 44: Spatial distribution of inferred conductivity values (Slug test on investigation boreholes)

6.2.5.2 Pumping tests results

Prior to Constant discharge test, Step tests were conducted on selected 08 relatively highest yielding boreholes. This was mainly to set up the respective CDT pumping rate for 24 hours. Up to 04 observations were chosen to

Table 7 provides summary of the time and number of borehole used, Table 8 provides a summary of the pumping time, observation borehole distances, and Table 9 provides a summary of the results. The time-drawdown plots of the CDT are provided in Figure 47 and Figure 48.

Table 7: Tested geological features and pumping tests time summary

Borehole Number	Geological features	Step test	CDT	Recovery		Number of Observations
		min		Step test	CDT	number
		min	min			
DPC 15	Fault area, at the intersection with a dolerite dyke	4*15	1440	35	180	3
DPC 26	Weathering within 70m away from a lineament	1*15	1440	10	80	3
DPC 14	Fault area, within 60 m away from a dolerite dyke	4*60	1440	40	240	3
DPC 9	Contact between the dyke and the hosting Rock (Baking zone)	3*15	1440	10	30	3
DPC 18	Fault area	4*15	1442	90	90	18
DPC 7	Fault area	3*15	1440	20	40	4
DPC 27	Weathering	3*15	1440	30	90	4
PPC 140	Fault area	4*15	1440	90	226	4

Table 8: Constant discharge tests with observation details

Pumping BH Name	Borehole Depth	S.W.L	Pump depth	Level logger depth	Observation boreholes with distance away from pumping borehole							
	(m)	(mbgl)	(mbgl)	(m)	OBS1	(m)	OBS2	(m)	OBS3	(m)	OBS4	(m)
DPC7	126	5.96	62	64	P126	180	DPC8	318	DPC5	688	DPC9	762
DPC9	85	2.95	52	80	DPC6	24	DPC5	74	P125	671.5	-	-
DPC14	92	2.56	52	85	DPC15	56	DPC22	551	-	-	-	-
DPC15	97	2.97	52	90	DPC19	127	DPC14	56	DPC18	235.7	-	-
DPC18	86	2.03	62	80	DPC17	35.5	DPC16	71	DPC15	235.7	-	-
DPC26	80	3.27	52	75	DPC27	276	P124	196	P118	1168	-	-
DPC27	60	9.32	62	55	DPC26	276	P124	302	P118	1409	DPC18	1419
PC140	40	20.80	38	40	P139	1118	P141	1119	DPC7	2712	DPC25	709

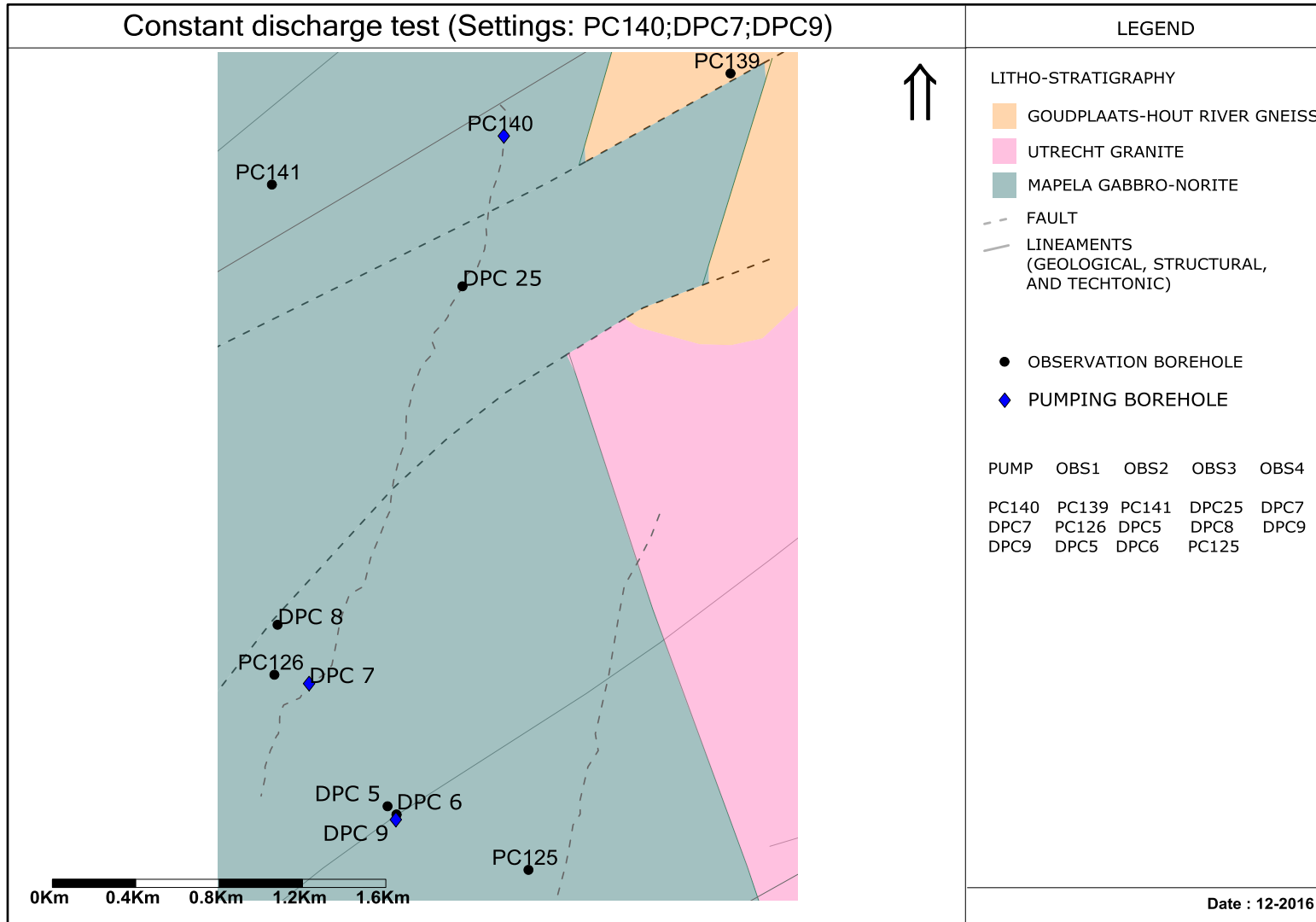


Figure 45: Constant Discharge tests setting for PC140, DPC7, DPC9

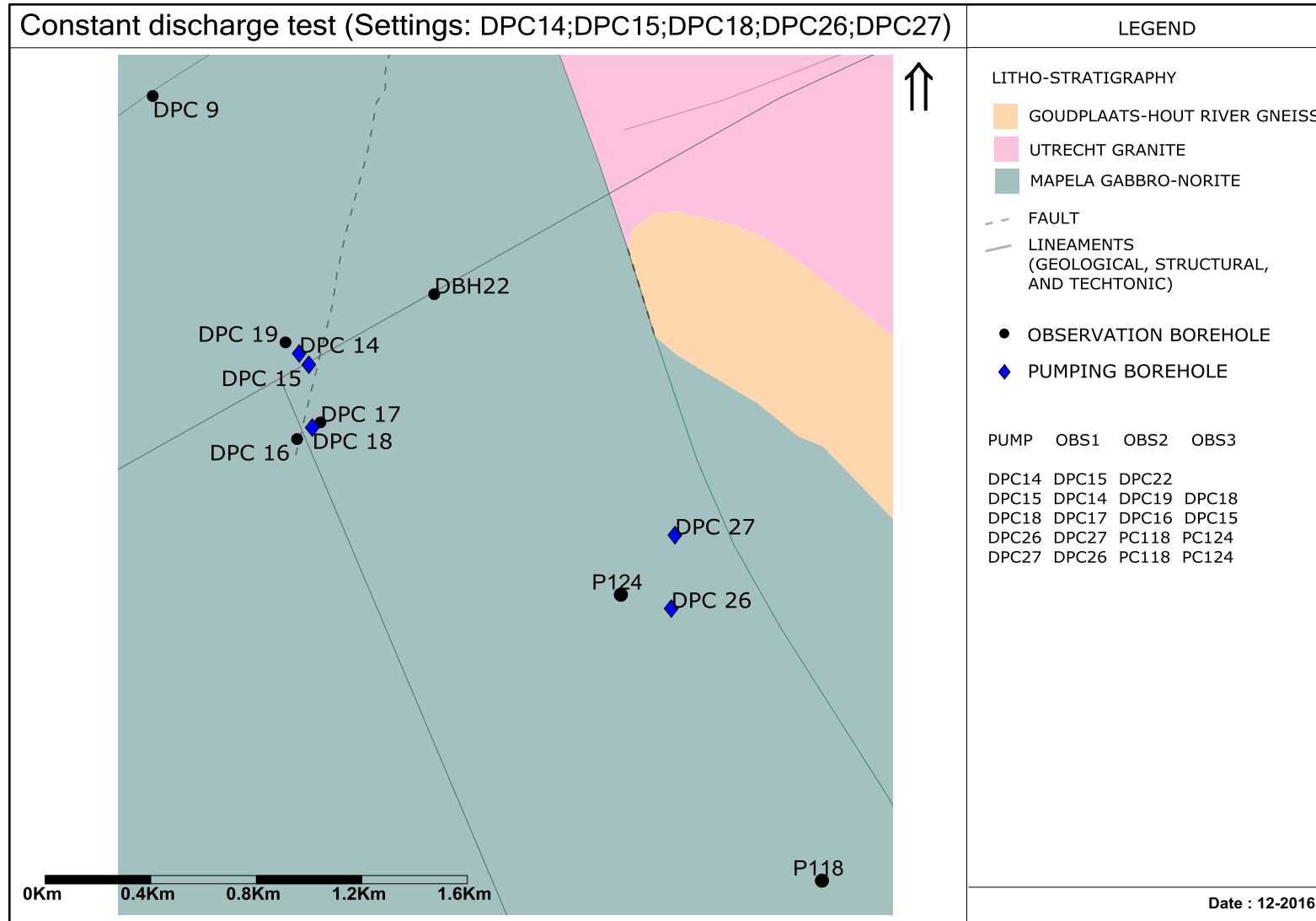


Figure 46: Constant Discharge tests setting for DPC14, DPC15, DPC18, DPC26, DPC27

Table 9: Summary on constant discharge tests results

Pumping Borehole Name	Pumping Rate	Pumping borehole			Drawdown in observation boreholes							
		Drawdown	Residual Drawdown	Recovery Time	OBS1	(m)	OBS2	(m)	OBS3	(m)	OBS4	(m)
	(l/s)	(m)	(m)	(min)								
DPC7	12.20	7.27	0.86	270	PC126	0.00	DPC8	0.14	DPC5	0.02	DPC9	0.01
DPC9	2.80	19.52	0.55	30	DPC6	1.05	DPC5	0.37	PC125	0.01	-	-
DPC14	8.70	12.34	0.46	282	DPC15	1.38	DPC22	0.01	-	-	-	-
DPC15	9.60	4.15	0.39	229	DPC19	0.04	DPC14	1.18	DPC18	0.00	-	-
DPC18	1.10	4.42	0.01	19	DPC17	1.20	DPC16	0.09	DPC15	0.00	-	-
DPC26	5.30	28.60	1.22	98	DPC27	0.01	PC124	0.01	PC118	0.01	-	-
DPC27	1.90	36.15	2.27	158	DPC26	0.01	PC124	0.01	PC118	0.01	DPC18	0.05
PC140	5.04	6.54	1.30	235	PC139	0.29	PC141	0.04	DPC7	0.00	DPC25	0.00

At the end of the pumping test, the final drawdown in DPC26, DPC27, and DPC9 were between 18 m and 33 m. Whereas in the boreholes associated with faults (DPC7, DPC14, DPC15, DPC18 and PC140) final drawdowns were between 4.50 m and 12.30 m despite them being pumped at higher rates (>5ls), suggesting higher transmissivities. The observed drawdown differed considerably from observed boreholes to the other.

An interesting feature from the observed responses is that; although DPC18 and DPC15 appear to be associated to the same Fault line and distant of only 235 m from each other, these boreholes seem not to be connected to the fractures network. This suggests that the Dyke intersected by DPC15 may form a boundary across which there is a limited groundwater flow.

Visual inspection of observed drawdowns showed that the tested (pumped and observed) boreholes can be grouped three groups, mainly:

- Group1: 32 % of the tested boreholes fall into this group and showed consistent and regular drawdown behaviours (DPC7, DPC14, DPC15, DPC18, PC140, DPC6, and DPC17) during pumping tests;
- Group2: 27% of tested boreholes show consistent but irregular drawdown behaviours (DPC5, DPC8, DPC9, DPC26, DPC27, and PC139) during pumping tests;
- Group3: 41% of the tested boreholes, show limited (or no) drawdown response (PC118, PC124, PC126, PC125, PC141, DPC16, DPC19, DPC22, and DPC25) during pumping tests.

The Group3 (limited (or no) drawdown response) suggests that the boreholes that are members of this group do not intersect the same fractures that the respective pumping boreholes was sourcing the groundwater from during the pumping tests. This limited (or no) drawdown response may also have been accentuated by the distances of the observations from the corresponding pumping boreholes, and the duration (24 hours) of the CDT. In crystalline aquifers such as the one associated Bushveld Complex, the characters (hydraulic parameters) can generally not be reliably assessed using short-term (less than 12 hours) tests. The heterogeneous and discontinuous nature of crystalline basement aquifers requires generally long term testing (from 24 hours up to 10 days) preferably with a comprehensive monitoring network to characterize and quantify hydraulic parameters.

Borehole member of Group 2 showed irregular drawdown behaviours as results poor fractures connectivity.

Group1 boreholes showed drawdown behaviours that are similar to drawdowns describe by classical analytical of Theis (1935), for a confined porous (homogenous and isotropic) aquifer. However, it will not be accurate to interpret the CDT results with such model without prior assessment of the flow character, and boundary conditions.

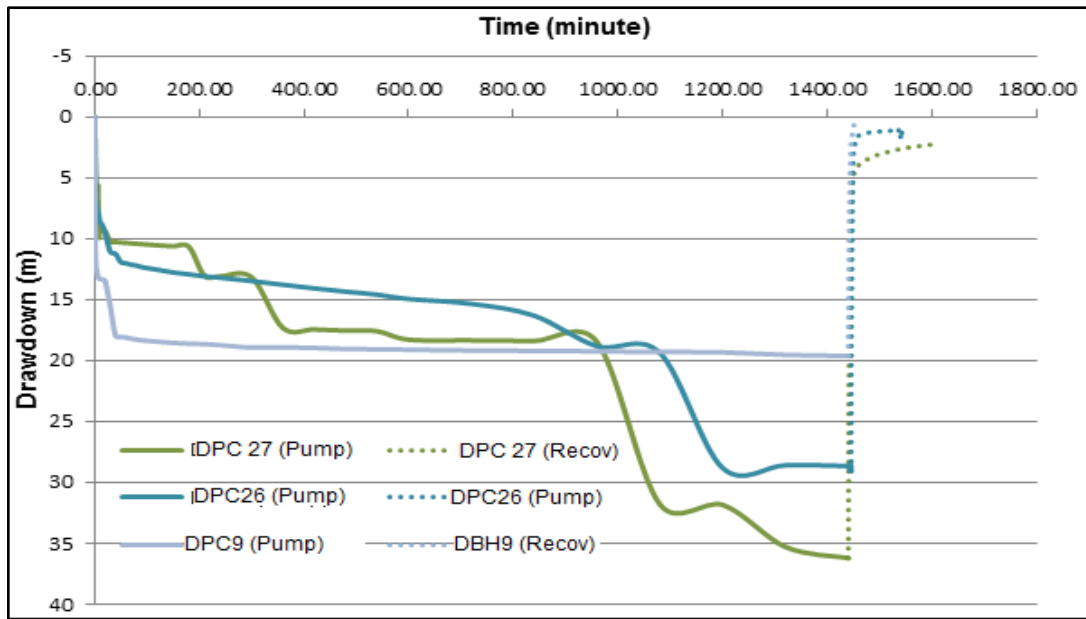


Figure 47: Drawdown -Recovery of CDT in DPC27, DPC26, and DPC9

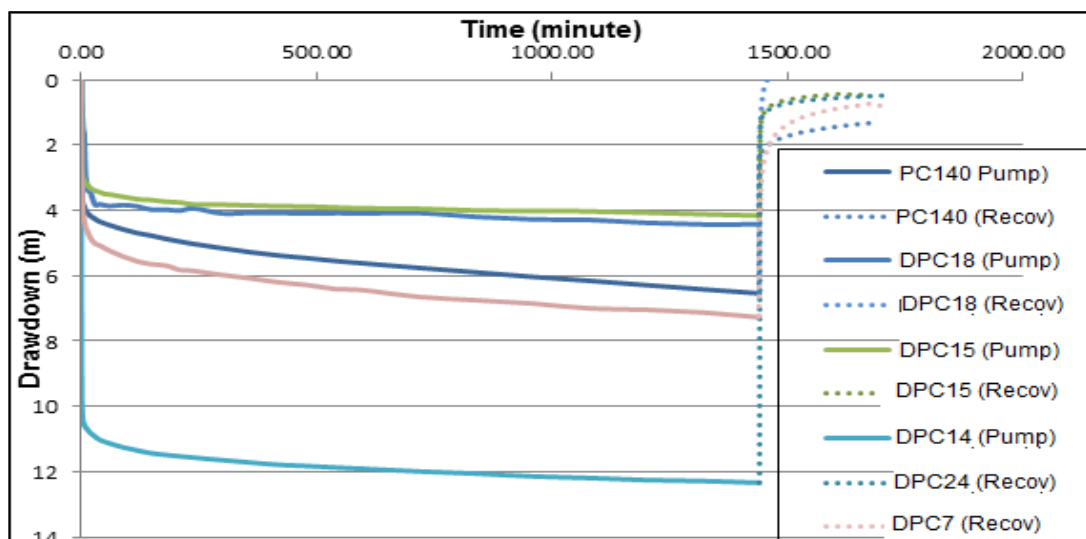


Figure 48: Drawdown -Recovery of CDT in PC140, DPC18, DPC15, DPC14, and DPC17

6.2.5.3 Aquifer flow characterisation and determination of boundary conditions

In order to identify the flow regime/characters of the aquifer, and determine which model can be used to best interpret the data, the observed drawdown with its logarithmic derivatives was plotted as a function of time in logarithmic scale. These plots were then visually compared to a set of typical diagnostic plots (Renard et al., 2009).

Typical drawdown behaviours identified in the study catchment are presented can be grouped in 3 main types

Type 1_Double porosity or unconfined aquifer – approximate S-type

This type of drawdown behaviour is common in the crystalline basement aquifers within the Limpopo region (Holland, 2011), and is confirmed to be the dominant from the pumped tested aquifers in the present study. The drawdown shows an inflection point at intermediate times and a dip (double porosity) in the derivative. Such typical drawdown (and derivative) response to constant rate discharge, is well described by Neuman (1974), Moench (1984), Barker (1988), and Moench, (1997) among many others.

The first part of the (early time, before stabilisation of the drawdown, is associated with groundwater flow coming from only fractures (or the saturated zone of an unconfined aquifer) intersected by pumping well. Water level responses of all pumped boreholes showed linear fractures flows behaviour after well borehole storage, on log-log plot at early time.

Then the drawdown stabilised, as a delayed flux is provided by another part of the aquifer. Neuman (1974) and Moench (1997) showed that the provided delayed flux can be in form of delayed recharge from the overlying, less permeable part in an unconfined aquifer. Moench (1984) and Barker (1988) demonstrated that drainage from matrix blocks in fractured aquifers can also result in drawdown stabilisation at intermediate time. Considering the geology/lithology from the drilling logs (Table 11) of the boreholes that show such a response to CDT, we can conclude that the observed stabilisation of the drawdown at intermediate time is probably due to associated quasi saturated top weathered/regolith layer, which is providing a delayed flux.

Table 10: Typical groundwater head responses (drawdown) to CDT in the catchment

Borehole name	Description	Applicable analytical model
DPC26, DPC18, DPC7 DPC27;	Type1: Double porosity or unconfined porous aquifer– approximate S-type	Warren & Root (1963) Moench (1984) Neuman (1972, 1974).
DPC14, DPC15	Type2: General radial flow model—non-integer flow dimension $n > 2$	Barker (1988); Bernard et al (2006)
PC140	Type 3: Single fracture or general radial flow (GRF) model – non-integer flow dimension $n < 2$ Steepening of drawdown Response	Barker (1988)
DPC9	Type1-1:Fracture dewatering Stepwise drawdown	

Table 11: Summary of lithology of boreholes with Type1 drawdown behaviour

ID	Simplified Geology/ Lithology	Weathering thickness
		(m)
DPC7	Soil and Clay up 5mbgl, weathered to fractured Norite overlaying Solide fresh Norite	25
DPC18	Soil up 1mbgl, weathered Granite/Norite overlaying fresh Solide Norite with seldom fractures	10
DPC26	Soil up 2mbgl, weathered Norite overlaying fresh Solide Norite with seldom fractures	10

At late time, the flow system tends toward a typical infinite acting radial flow (IRF) asymptote, if no boundary condition is encountered. In the case of IRF, the semi-log plot shows the characteristic parallel straight line segment at early and late pumping times. When a no-flow boundary is encountered, a doubling of the value of the derivative is observed (Van Tonder et al., 2002). The observed Type 2 behaviour from DPC7, DPC18, and DPC26 showed some different types of boundary conditions ranging from single no flow (DPC18), to closed boundary (DPC26). Such boundary conditions were confirmed by the late time behaviour from the plots of the recovery data (time/ (derivative of time) versus residual drawdown plots, as well as late time behaviour of the semi-log plots. DPC27 showed the probable existence of "two no flow boundaries" on the log-log plot. Drawdown response from DPC7 (located in a fault area) reached one on flow boundary, which is probably the contact between the fracturing/weathering of the faults zone and the fresh host rock. The logarithm derivative of drawdown suggests good fracture networks for DPC7 and limited fracture networks for DPC18, DPC26, and DPC27

Type1-1Fracture dewatering - Stepwise drawdown

This model behaves as the double porosity model, with frequent dewatering of discrete fracture systems at intermediate and late times. Once these fractures are dewatered, a clear increase in drawdown and decrease in transmissivity becomes apparent. The drawdown response from DPC9, showed such frequent fractures dewatering patent. DPC9 intersected limited fractures of the contact zone between a thin dyke and Norite. Two no flow boundaries were also identified from the semi-log plots of DPC9.

Type2: General radial flow model—non-integer flow dimension larger than 2

The General Radial Flow model assumes a continuum in which drawdown evolves in radial (spherical) flow with dimension n ($n \in [2, 3]$ integer or not) during the transient test (pumping or injection). The spatial distribution of flow through the fractures towards the well is assumed to depend entirely on the properties of the fracture network (fracture density and connectivity) as described by Barker (1988) and Black (1994).

Water level responses of DPC14, DPC15, which are located in fault area, indicated radial flow at intermediate and late time on the semi-log plot. The logarithm derivative of drawdown in pumped boreholes suggested good fracture networks for DPC14, DPC15. These are common behaviours of igneous fractured rock aquifers in South Africa, especially along lineaments with high transmissivity values like the faults the Bushveld Complex. DPC15 did not show any boundary effects; whilst a clear no flow boundary condition was depicted on the drawdown response of DPC14. The dyke that intersects the fault, in which DPC14 was drilled, is probably the physical boundary that affects the induced flow toward DPC14

Type 3: Single fracture or general radial flow (GRF) model –Response non-integer flow dimension less than 2

This model considers well connected fracture segments which control the flow linearly (flow dimension $n \in [1, 2]$ integer or not) toward the well, with very limited contribution of the host rock, especially at early time. Such linear flow is common in the crystalline rock of the study area, especially along the extensive near vertical dykes, lineaments, faults and shear zones (Stettler et al., 1989; and Petzer, 2009).

At intermediate times water is supplied by the fracture and matrix (highly weathered igneous rock). Drawdown response from P140 was found to mimic such linear fractures flow pattern, and intersect fracturing associated with intrusive pyroxenite, and fault zone respectively. PC140 indicated radial flow at intermediate and late time on the semi-log plot, with the effect of one no flow boundary. The logarithm derivative of drawdown suggested good fracture networks for PC140. PC140 indicated the effect of one no flow boundary, at late time on the log-log plot.

6.2.5.4 Determination of aquifer hydraulic parameters from pumping tests

Based on the typical identified drawdown behaviours and flow characters, most appropriate analytical model were chosen for fitting of observation, and the calculation

of the corresponding hydraulic parameters. As groundwater is known to flow mainly in the fractures toward the wells, and the geology consists mainly of igneous (crystalline) rock type, the analytical logarithmic model for radial flow with cylindrical symmetry in a fractured fractal medium (Bernard et al., 2006) was also used on all pump test data to infer the mass fractal dimension (exponent) of the fracture network (D) and the "transport" exponent (θ). An effective borehole radius of 5m instead of the real radius of 0.0825m was used for the abstraction borehole, to account for the negative pseudo skin.

The hydraulic parameters (T , K , S , S_y) obtained from the pumping tests analysis by fitting of curve according identified existing models are summarised in Table 12.

Table 12: Inferred aquifer hydraulic parameters from CDT (Pumping boreholes)

BH Name	Recovery vs. Rise W/L	Nueman			Hantush		Barker			Bernard et al			
	T	T	S _y	S	T	S	K _f	S _f	n	K ₀	S	D	θ
	m ² /d	m ² /d	-	-	m ² /d	-	m/d	1/m		m/d			
DPC7	132	140	0.127	8.24*10 ⁻³	148	2.35*10 ⁻⁴	107	2.95*10 ⁻⁴	1.32	92	--	1.88	0.8
DPC9	10.1	14	0.001	1.16*10 ⁻³	17	2.35*10 ⁻³	65	2.35*10 ⁻³	1.25	51	--	1.55	0.8
DPC14	220.8	130	0.12	1.2*10 ⁻⁵	183	1.2*10 ⁻⁷	140	2*10 ⁻⁷	1.30	139	--	1.8	0.21
DPC15	340	356	0.42	1.1*10 ⁻⁵	355	2.4*10 ⁻⁷	151	2.3*10 ⁻⁵	1.33	138	--	1.85	0.38
DPC18	14.50.00	26	0.01	1*10 ⁻⁵	34	3.82*10 ⁻⁷	24	1.3*10 ⁻⁶	1.20	14		1.85	0.70
DPC26	52.2	23	0.011	13.01*10 ⁻³	20	3.16*10 ⁻⁴	23	2.1*10 ⁻⁶	1.76	17	--	1.85	0.67
DPC27	13.1	6	0.008	1.6*10 ⁻⁴	5.5	5.5*10 ⁻⁴	17	1.48*10 ⁻⁴	1.88	23	--	1.9	0.36
P140	131	63	0.017	8.31*10 ⁻³	81.8	7.48*10 ⁻⁴	84	1.17*10 ⁻⁵	1.14	80	--	1.84	0.51

For the abstraction boreholes, K_0 varies between 14 and 139 m/day. K_f is in general higher than K_0 ranging from 17 to 151 m/day. The diffusion scaling exponent θ varies between 0.21 and 0.18. The mass fractal dimension D is found between 1.555 and 1.9, whereas the fractional dimension n varies between 1.14 and 1.88.

Application of Fractal Flow solution with fractional differentiation via Mittag-Leffler law

In this section, the Fractured Fractal Flow solution with fractional differentiation via Mittag-Leffler law is used on experimental data obtained from the constant discharge tests. Figure 49 to Figure 52 represent the comparison of the modified fractured fractal flow equation (new fractional differentiation based on the generalized Mittag-Leffler law) and the experimental data (blue diamonds), from real field measurement from abstraction boreholes. The inferred aquifer hydraulic parameters from the pumping boreholes using Fractured Fractal Flow solution with fractional differentiation via Mittag-Leffler law are presented in Table 13. These values appear to compare well with the values calculated from Barker the Approximated Logarithmic analytical solutions for fractal flow.

Table 13: Inferred aquifer hydraulic parameters from abstraction boreholes during CDT using the proposed new fractured fractal flow solution

BH Name	New modified fractured fractal flow model				Barker fracture flow		
	K_f	S	D	θ	K_f	S_f	n
	m/d				m/d	1/m	
DPC7	97	3.15×10^{-5}	1.72	0.78	107	2.95×10^{-4}	1.32
DPC9	53	1.80×10^{-5}	1.69	0.55	65	2.35×10^{-3}	1.25
DPC14	159	7.19×10^{-3}	1.82	0.82	140	2×10^{-7}	1.30
DPC15	155	5.28×10^{-3}	1.88	0.77	151	2.3×10^{-5}	1.33
DPC18	27	3.80×10^{-5}	1.82	0.61	24	1.3×10^{-6}	1.20
DPC26	19	4.25×10^{-5}	1.79	0.31	23	2.1×10^{-6}	1.76
DPC27	18	3.45×10^{-5}	1.69	0.38	17	1.48×10^{-4}	1.88
P140	75	1.19×10^{-5}	1.88	0.62	84	1.17×10^{-5}	1.14

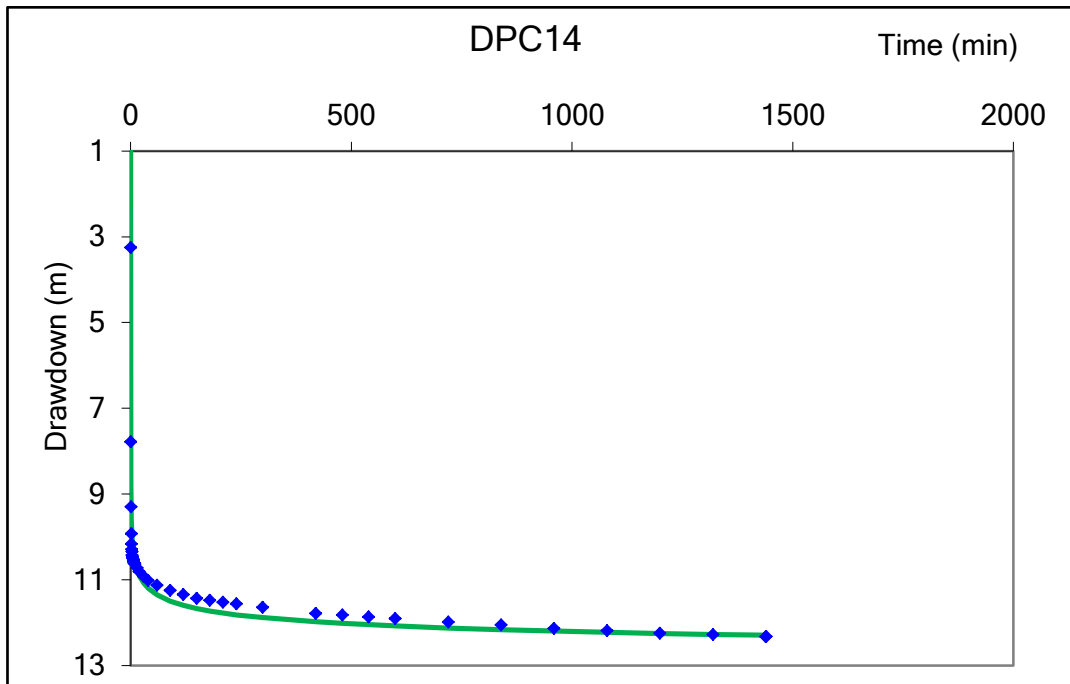


Figure 49: Comparison of modified equation with experimental data for DPC14

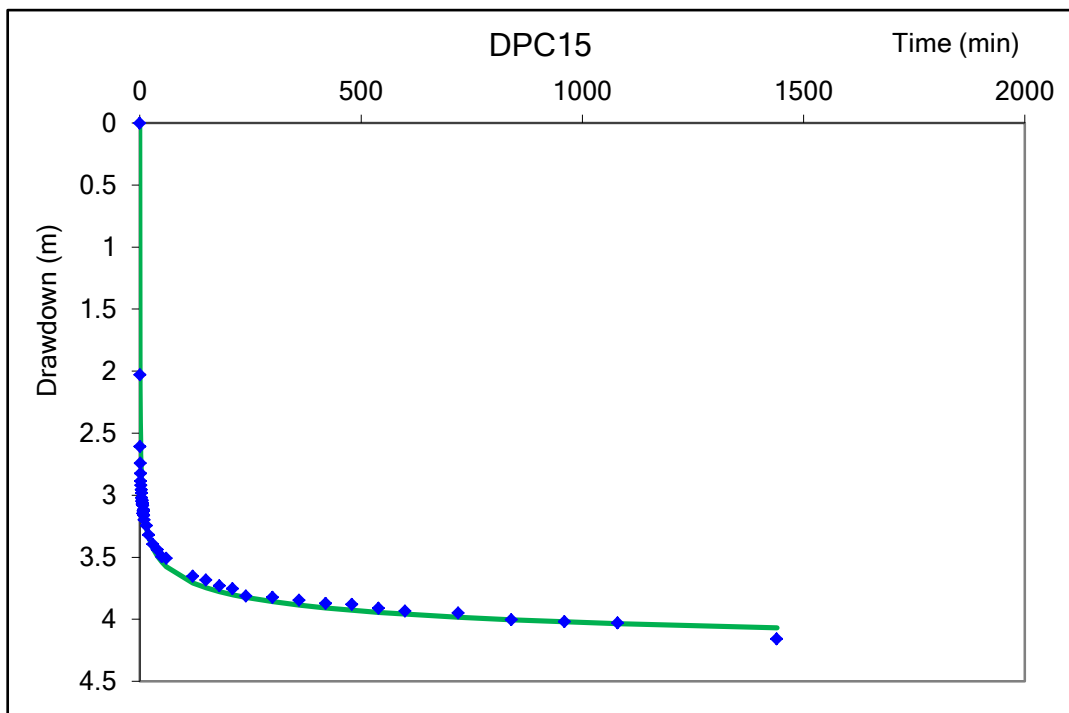


Figure 50: Comparison of modified equation with experimental data for DPC15

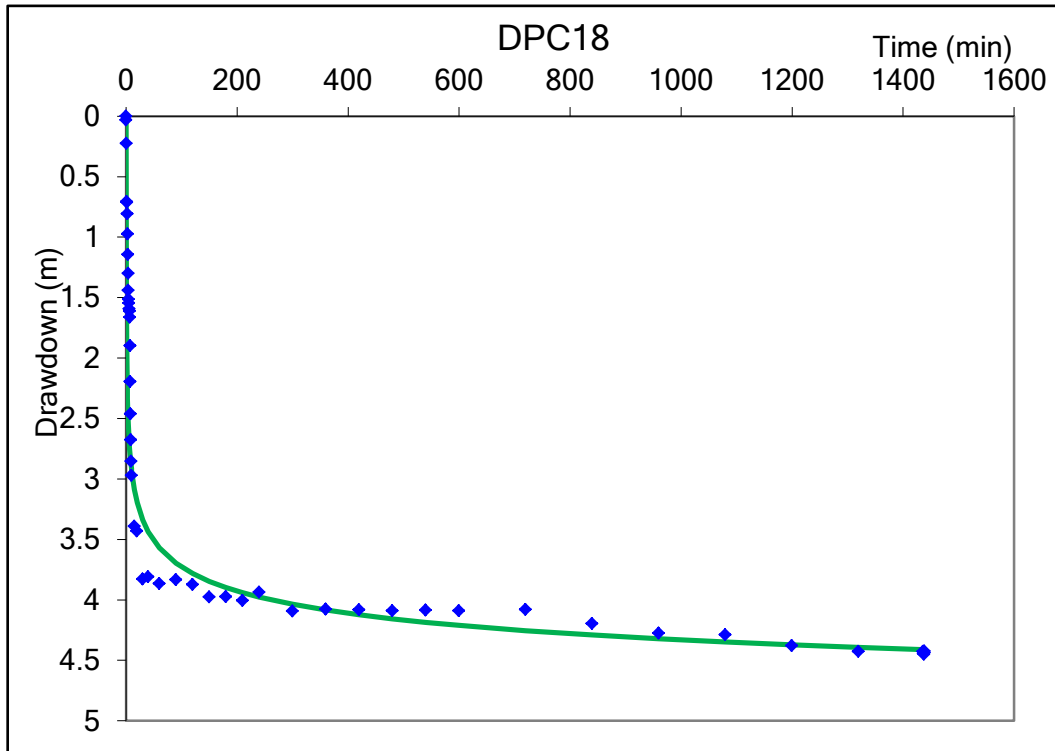


Figure 51: Comparison of modified equation with experimental data for DPC18

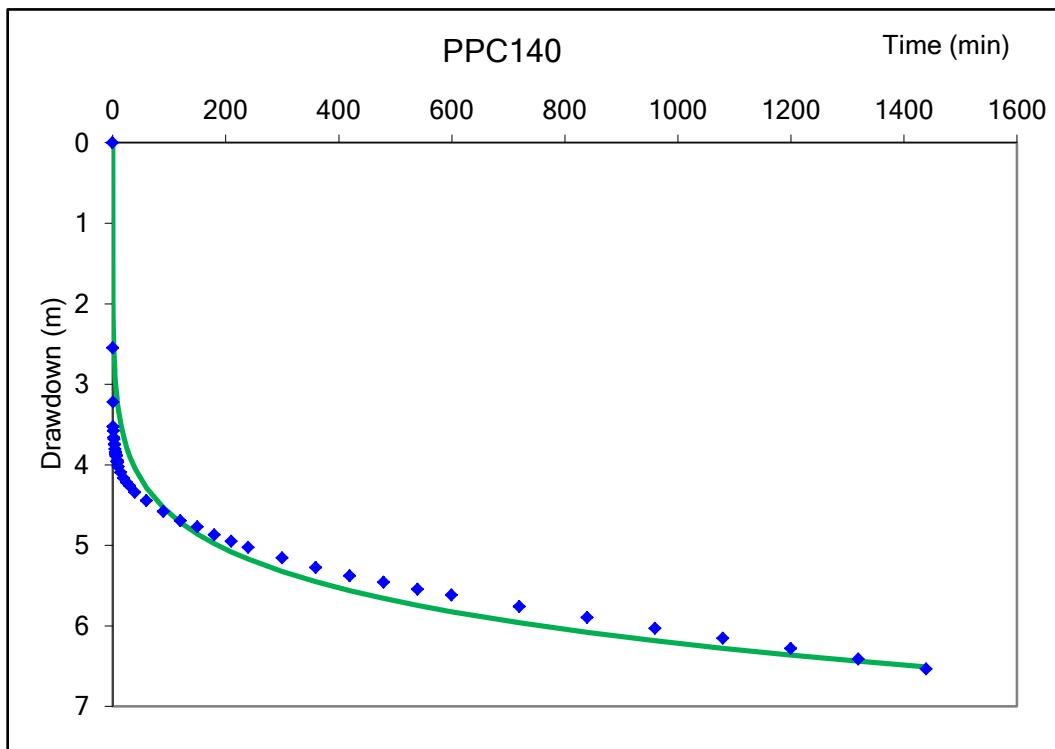


Figure 52: Comparison of modified equation with experimental data for PPC140

Applicability of fractal analytical model solutions on drawdowns in observations boreholes

The confidence level of the determined hydraulic parameters generally increases if observation boreholes are present. The representative values of the hydraulic parameters were obtained from the aquifer test analysis using also observation boreholes where possible. Only CDT that allowed measurement of significant drawdown in observations boreholes, and that show fractal behaviour in abstraction borehole, will be considered in this sub section.

One can remark that all considered observations boreholes respond with a head draw-down (Figure 53) developing more rapidly than linearly with "ln (time)". This type of behaviour is a characteristic of fractured rocks with fractal behaviour. We attract the attention on the facts that these drawdown curves are from 04 different pumping tests, and described as "A pump B obs" meaning Borehole A was pumped and borehole B observed.

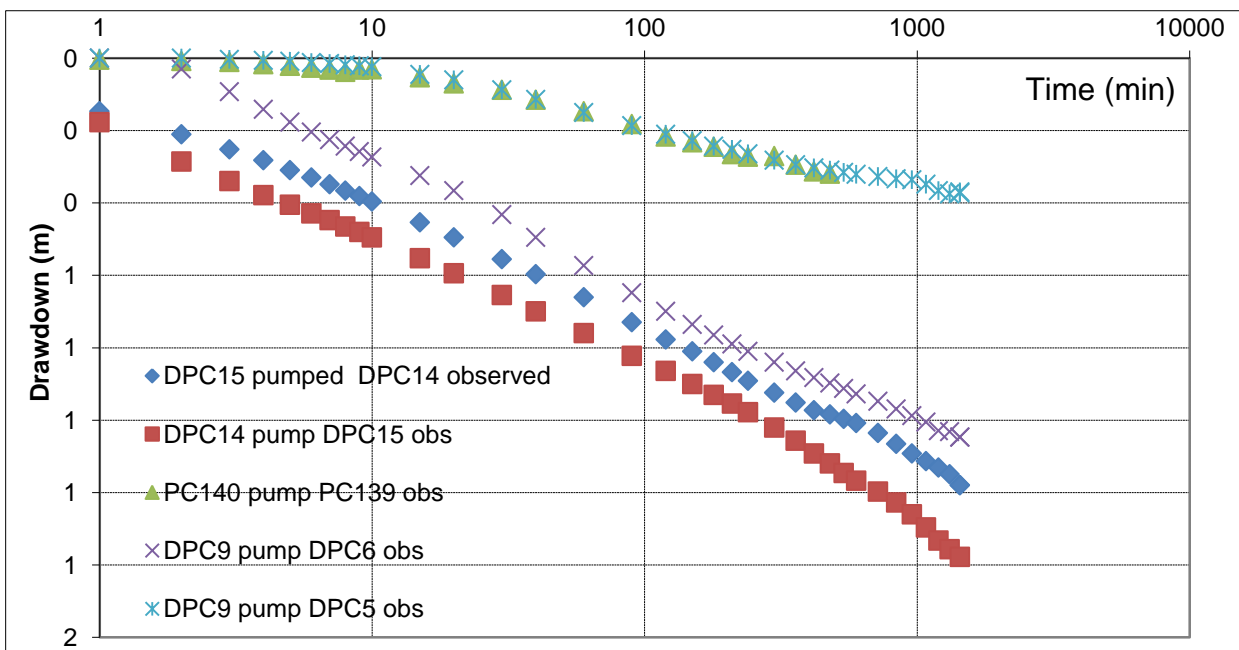


Figure 53: Drawdown curves recorded in observations boreholes during different CDT

Observation boreholes DPC14, DPC15 exhibits the response of a high-connected borehole with a progressive increase (monotonous) in the pressure drawdown. DPC6 shows the response of non-monotonous and connected is intermediately) to DPC 9 (lag distance of 24 m) with the slight delay in response time (after 2mn). DPC14 and DPC6 show however a transition phase between 240 and 720 minutes, where their respective

curve is inflected before the behaviour becomes that of a classical fractal medium at late time.

On the other hand, the drawdown response in boreholes DPC5 and PC 139 suggest low-connectivity to their respective corresponding abstraction boreholes DPC 9 (lag distance: 74 m) and PC 140 ((lag distance: 1118 m). This is reflected by the delayed response and a subsequent very rapid increase in the draw-down, before the transition and the classical fractal medium behaviour at late time. The classical fractal medium behaviour is not clearly reflected by these curves at late time because of the relatively shorter duration (1440 minutes) of the CDT. As demonstrated by Acuna and Yortsos (1995) for numerical exercises on synthetic fractal media, this behaviour is interpreted as a transition from a typically 3D flow at early times to a 2D one at long times. At early times, the problem is basically 3D, since the stress induced by pumping does not affect evenly the aquifer thickness and the effect of fluctuations of the groundwater flow along the vertical direction is significant. At long times, after sufficient propagation of the stress the flow fluctuations along the vertical direction becomes negligible as compared to horizontal ones; and the problem becomes 2D.

To infer the hydraulic parameters from the drawdown data of observations boreholes, only the GRF-model (Barker, 1988), the log approximated fractured fractal flow model (Bernard et al, 2006); and the new Modified fractured fractal flow model (developed above) were used and the results are in compared tables Table 14 . Fitting curves can be found in appendix D. The results are in general within the same range from one analytical model to the others for the observations. The difference, if any is by 01 order magnitude at most.

For the observation boreholes, K_f from the different methods varies between 69 and 179 m/day. The diffusion scaling exponent θ varies between 0.35 and 0.85. The mass fractal dimension D is found between 1.69 and 1.9 whereas the fractional dimension n varies between 1.84 and 1.95. We attract the attention to the fact that fracture storage (S_f) estimated from the observation boreholes are significantly lower than the one estimated from abstraction boreholes.

Table 14: Inferred aquifer hydraulic parameters from observations boreholes during CDT

BH Name	Pumping borehole and distance		Barker			Bernard et al				Modified fractured fractal flow			
	Pump	Distance	K _f	S _f	n	K _f	S _f	D	θ	K _f	S _f	D	θ
		m	m/d			m/d		m/d					
DPC5	DPC9	74	70	3.45 *10 ⁻⁵	1.86	81	-	1.81	0.53	75	3.25 *10 ⁻⁶	1.72	0.41
DPC6	DPC9	24	82	2.25 *10 ⁻⁵	1.84	91	-	1.79	0.40	69	3.15 *10 ⁻⁵	1.69	0.35
DPC14	DPC15	56	172	1.49 *10 ⁻⁵	1.80	160	-	1.77	0.75	135	1.80 *10 ⁻⁴	1.92	0.70
DPC15	DPC14	56	98	2.89 *10 ⁻⁵	1.95	110	-	1.90	0.85	120	1.19 *10 ⁻⁴	1.87	0.75
PC140	PC139	1118	108	1.20 *10 ⁻⁵	1.94	120	-	1.88	0.55	93	7.19 *10 ⁻⁷	1.78	0.62

6.2.6 Hydro-geochemistry and groundwater quality

The acid mine drainage (AMD) and associated impact on groundwater resources is well known to be one of the most serious environmental concern associated with mining (Bell et al., 2001; Vermeulen and Usher, 2009). In South Africa, the acid mine drainage (AMD) issues are mostly investigated in the gold and coal mining industries. Very few works were conducted to investigate the AMD potential of mining of Magmatic Sulphide Deposits in Bushveld Complex rocks for instance. The Platreef (Northern limb oredeposit in the BC) is well known for its feldspathic pyroxenite-norite hosting one of the world class magnetic-type nickel, copper and platinum ground element (Kinnaird et al., 2005). Since mid to late 1920's (Buchanan, 1988), the Platreef has become a site of platinum prospecting and mining.

During AMD a number of hydro-geochemical processes can occur. Among hydrogeochemical processes that can occur during AMD are: acid neutralization/buffering, chemical precipitation, attenuation or dissolution of metals (Blowes and Ptacek, 1994). A sound hydro-geochemical conceptual model based on the site geology, hydrogeology, and mineralogy, is necessary for investigating the groundwater quality characteristics. One also needs to assess (test) the validity of each hypothetically conceived hydro-geochemical reaction based on measured data. This is done for main hydro-geochemical types occurring in the catchment.

The present study aims at investigating the hydro-geochemical characteristics in the catchment and how they relate to the overall groundwater quality. The study makes use of a diagnostic approach, including: the application of (bivariate) scatter plots, and other diagnostic plots (Piper and Expanded Durov diagrams) as complimentary tools to analyze the groundwater chemistry data collected across a quaternary catchment. It specifically uses groundwater monitoring data from an open cast platinum mine to describe different hydro-geochemical processes which prevail in the monitored groundwater system. The monitoring period extends over four years (2011–2014).

6.2.6.1 Hydro-geochemical types associated with the Platreef

04 different hydro-geochemical types were identified from the analyzed chemical data. This was based on where they plotted on the Expanded Durov (ED) diagram (Burdon and Malzoum, 1958). The corresponding hydro-geochemical facies on the Piper diagram (Walton, 1970; and Piper, 1944) are discussed upon.

Non-dominants Ions (Anions or Cations) hydro-geochemical type

45.30% of the analyzed samples indicate that dissolution or mixing processes (falling under Field 5 of the ED diagram) are mainly occurring in the groundwater system, with non-dominants ions (Anions or Cations). The Piper Diagram plot confirms that no specific cation-anion pair exceeds 50% of the total dissolved elements. Furthermore, 03% of the samples show (Figure 56) water of static regimes with combined concentrations of Sulfate, Chloride, magnesium and exceeding 50% of their respective total mEq/L.

When there is no dominant Anions or Cations in the groundwater system; literature (Freeze and Cherry, 1979; Fetter, 1988) suggests that one should investigate rather multiple minerals dissolution or mixing of two chemically distinct ground-water bodies as source of hydro-chemical type. This can be dissolution of the evolved Magnesium Bicarbonate water by freshly recharge water. Moreover, it could also be a missing of such water by distinctive water type, for instance like contaminated water.

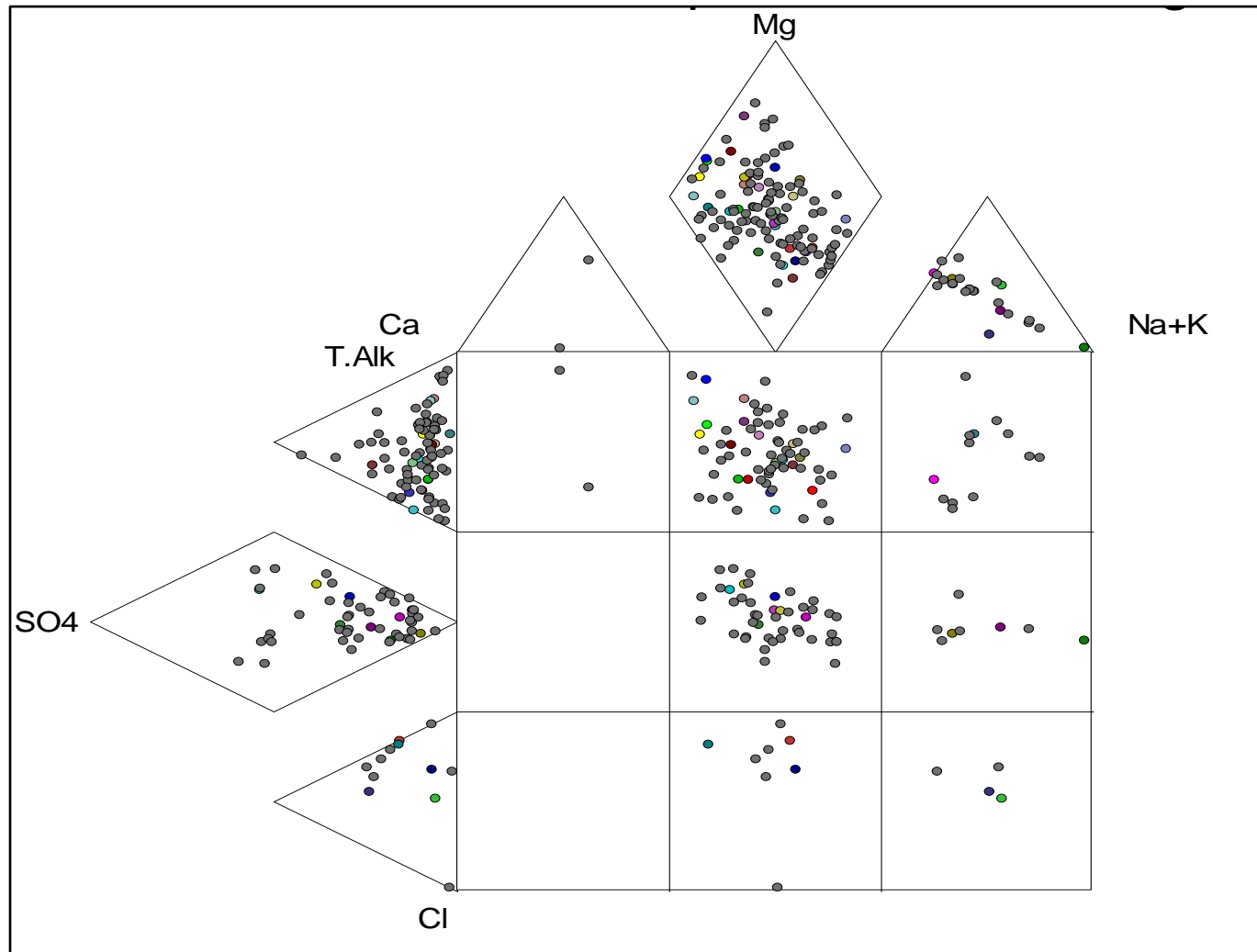


Figure 54: Expanded Durov diagram showing dominant water type in the catchment

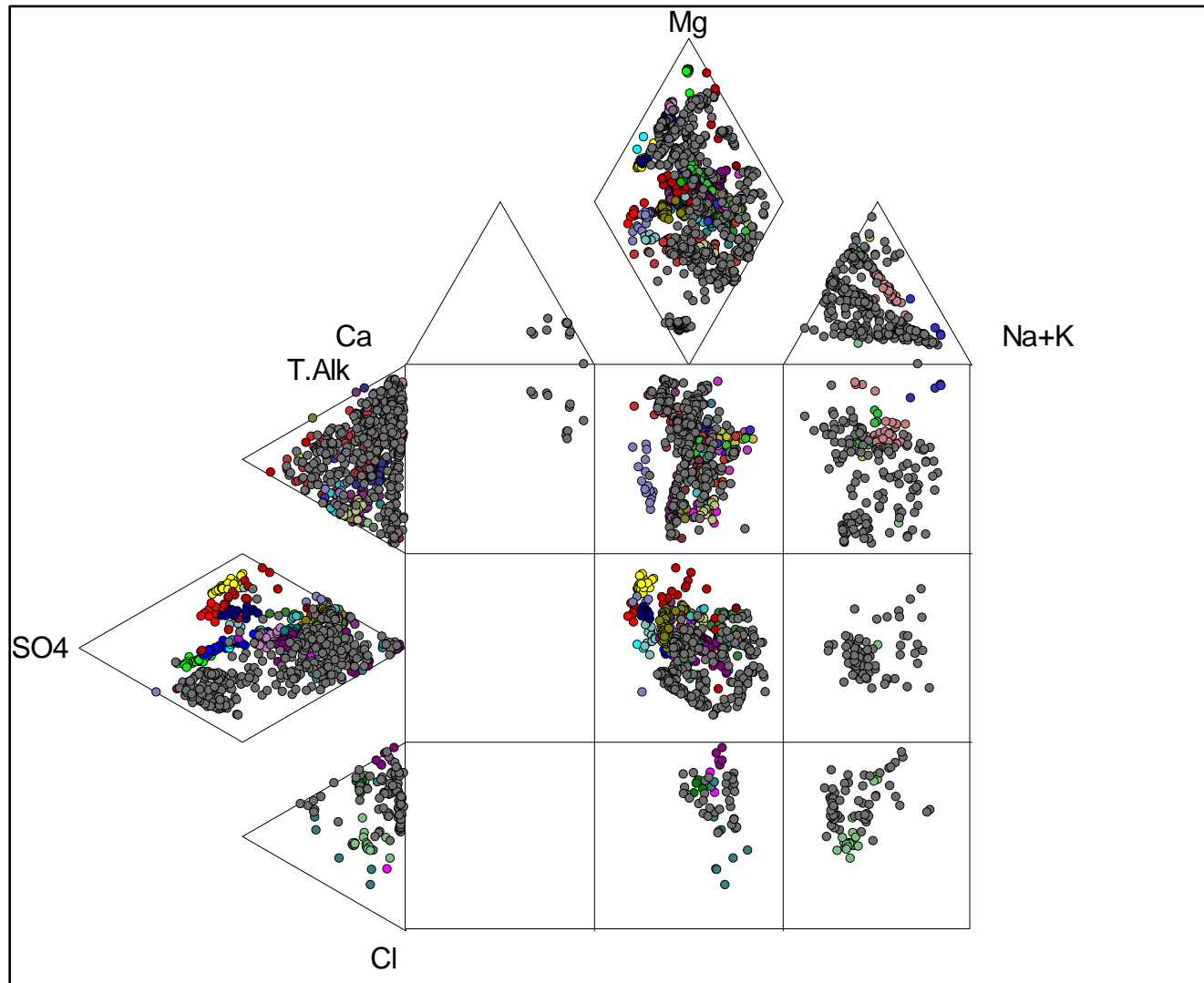


Figure 55: Expanded Durov diagram showing dominant water type in the monitoring area (04 years)

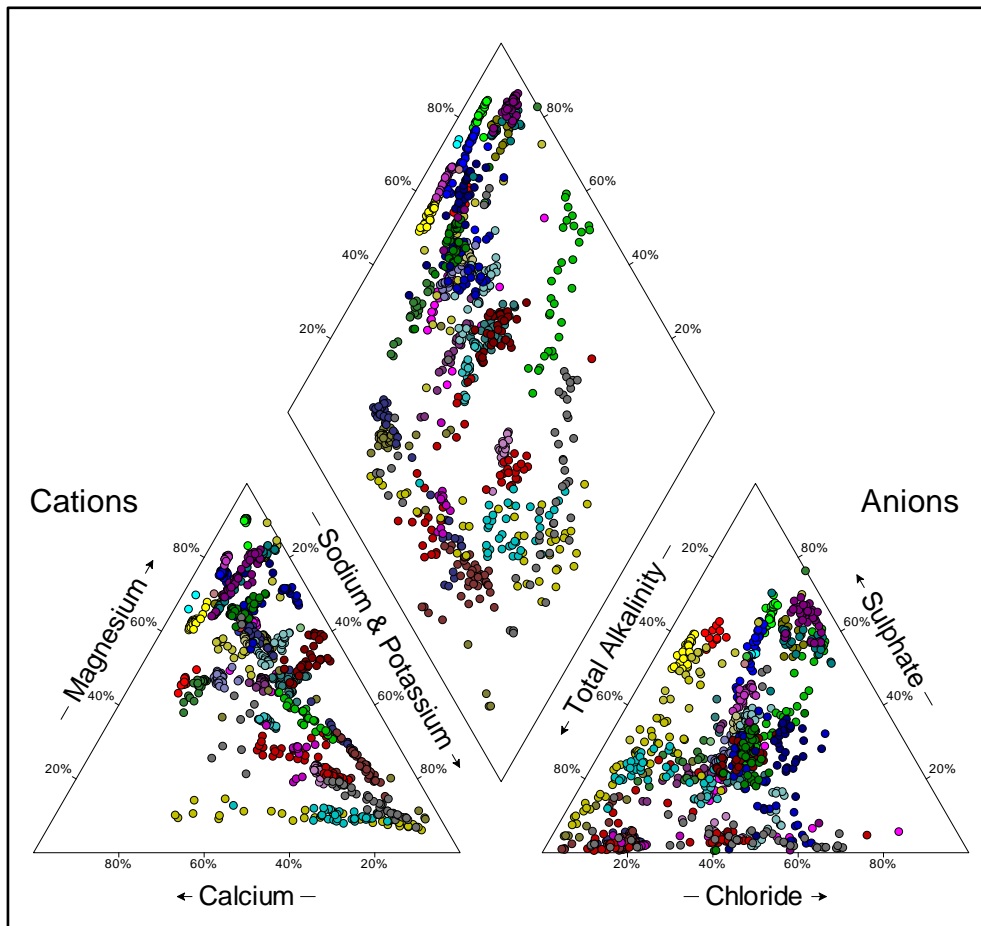


Figure 56: Piper diagram of samples representative of Non dominant type

Bicarbonate Magnesium Calcium hydro-geochemical type

34.38% of the samples fall in Field2 of the E.D diagram, and are classified as Bicarbonate Magnesium (HCO_3^- and Mg^{2+}). This suggests water associated with Dolomite (of Transvaal Super Group) or Mafic Igneous Rocks (Biotite Gneiss and granite, Diabase/Dolerite Dyke, Magnetite gabbro) of the Bushveld Complex, depending on the location of the sampled boreholes. Such samples show (Figure 57) some primary hardness (plot on the left side of Piper Diagram Diamond), and so suggest recently recharge water. The combined concentration of calcium, magnesium and bicarbonate exceed 50% of their respective total mEq/L.

Martin Holland (2011) suggested that the dominant $\text{Mg}-\text{HCO}_3^-$ in the Limpopo Plateau may be explained by the abundance of ferromagnesian minerals present within the rocks of the area.

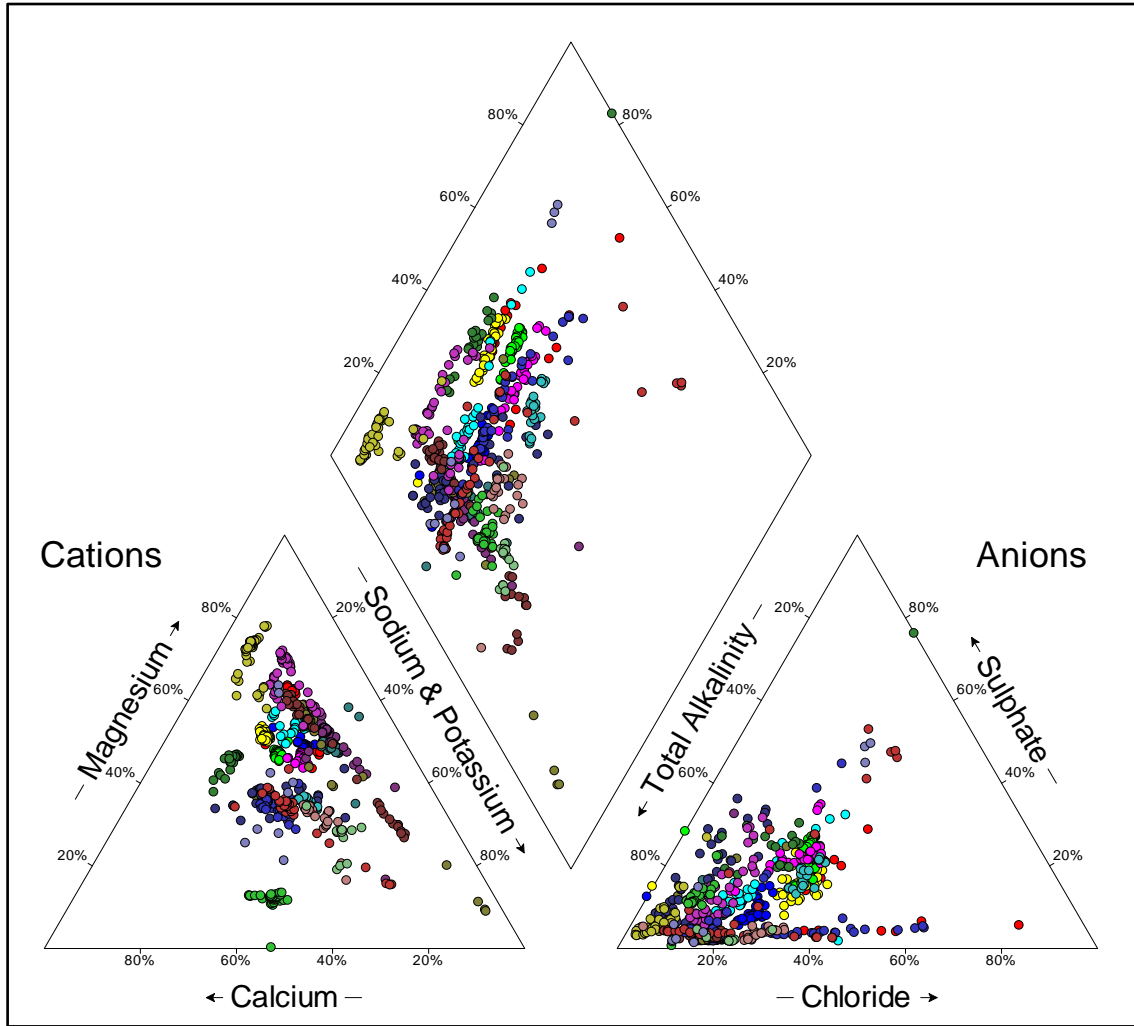


Figure 57: Piper diagram of samples representative of Bicarbonate Calcium magnesium type.

Bicarbonate Sodium (HCO_3^- and Na^+) hydro-geochemical type

Bicarbonate Sodium (HCO_3^- and Na^+) hydro-geochemical type appears to characterize 14.06% of the analyzed samples. This corresponds to the Field3 on Expanded Durov diagram which suggests that ions exchange processes are taking place within the groundwater system. A study conducted in the Limpopo Plateau (Martin Holland, 2001) indicated that $Na^+ - HCO_3^-$ hydro-geo-chemical type as one of the dominant in the Plateau. Martin Holland suggested that the direct infiltration of $Ca^{2+} - HCO_3^-$ which dominated rainwater, may have evolved to a $Na^+ - HCO_3^-$ facies due to the replacement of calcium by sodium through cation exchange in the aquifer matrix. Alternatively it could be due to the weathering of albite to kaolinite in the crystalline rocks, releasing sodium and bicarbonate.

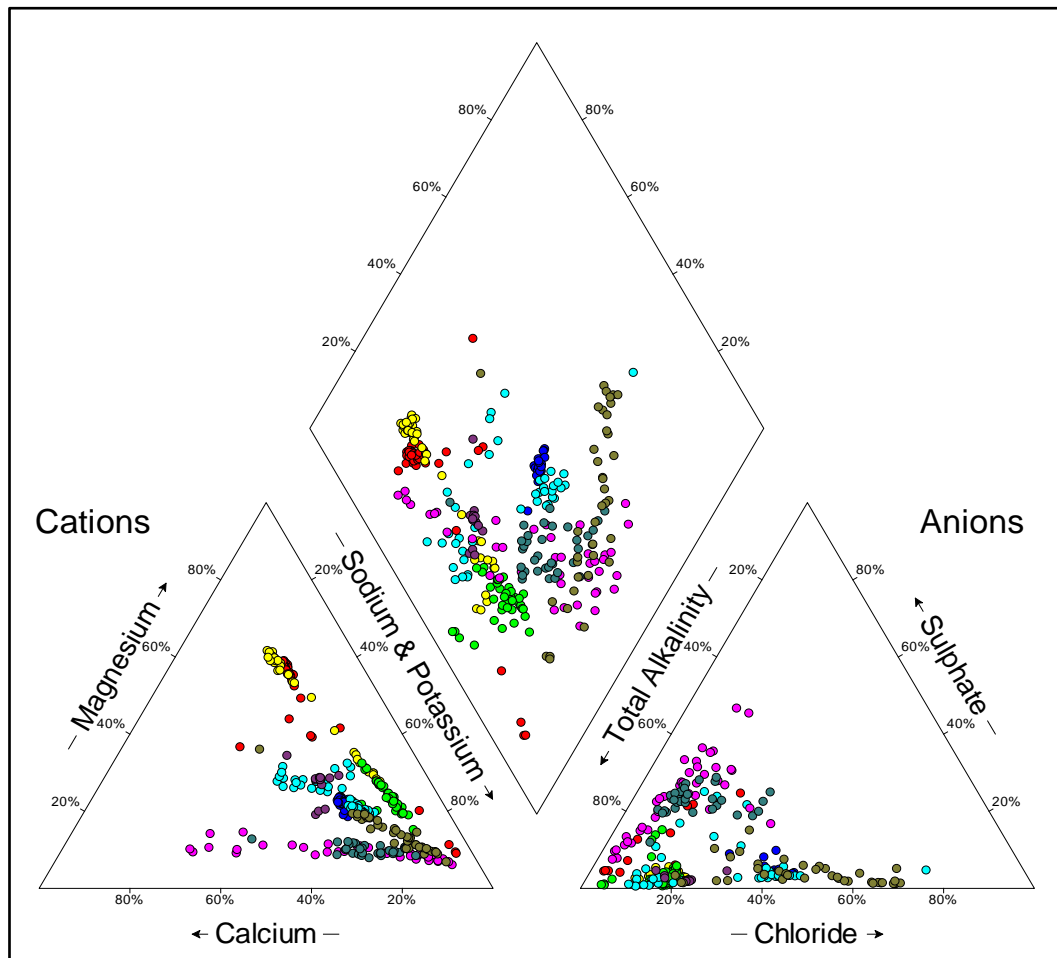


Figure 58: Piper diagram of samples representative of Bicarbonate Sodium type.

Minor hydro-geochemical types

The remaining of the samples (<6.5%) are Minor hydro-chemical types that plot as Sulfate-Sodium (SO_4^{2-} and Na^+), Chloride (Cl^-), Chloride-Sodium (Cl^- and Na^+), and Chloride-Calcium (Cl^- and Ca^{2+}) minor hydro-chemical types. Minor hydro-chemical groundwater types are probably a reflection of the mixing, and chemical evolution processes that occur as the groundwater evolves to the main Ca^{2+} - SO_4^{2-} main hydro-chemical type.

6.2.6.2 Major ions in the Plaatreef groundwater system

The descriptive statistics of the major ions detected in the Plaatreef's groundwater system during the monitoring period are summarized in Table 15. Major ions concentration in the groundwater, were detected in the following order $HCO_3^- > SO_4^{2-} > Cl^- > Na^+ > Mg^{2+} > Ca^{2+} > NO_3^- > K^+ > F^-$.

Furthermore, the pH measured in the groundwater samples during the monitoring period range from 5.6 to 9.27 (Figure 59). Since samples considered values of pH less than 9.7; alkalinity (Alk) is assumed to be solely due to carbonate alkalinity (i.e., $\text{Alk} = [\text{HCO}_3^- \text{ total}] + 2[\text{CO}_3^- \text{ total}]$).

Table 15: Statistics of the major ions in the plaatreef groundwater system during the monitoring period.

	Number	Minimum	Maximum	Arithmetic Mean	Standard Deviation	SANS-241 (2015)	WHO (2011)
Ca^{2+}	1920	0.83	289.4	69.18	1.25	a	a
Mg^{2+}	1920	0.01	511	103.67	2.23	a	a
Na^+	1920	5.84	738.8	109	2.35	200	a
K^+	1920	0.023	61.9	5.18	0.13	a	a
HCO_3^-	1920	15.8	824	316.8	3.3	a	a
Cl^-	1920	0.54	1561.7	181.87	4.74	300	a
SO_4^{2-}	1920	0.66	1640.239	217.82	7.49	250	a
F^-	1920	0.01	2	0.29	0.006	1.5	1.5
NO_3^-	1920	0.06	167	8.27	0.43	11	50

a: No established guideline value

6.2.6.3 Hydro-geochemical processes within the monitoring area

The focus here is on the hydro-geochemical reactions and processes that result from the dominant water quality types associated with the Plaatreef and the subsequent to mining activities.

Knowing that the majority (90%) of the boreholes from which groundwater have been sampled, are less than 70m deep; and considering the local topography and drainage, we assume the sampled aquifer system is directly recharge by the rainwater. This is confirmed by the Trilinear/Piper Diagram showing the maximum of the samples is from freshly recharge type. Furthermore rain water quality in the region is known to be

mostly of Calcium Bicarbonate type (Martin Holland., 2011), but how does rainwater (general) evolve to the different main hydro-geochemical types that occur in the catchment?

There is no doubt that a same hydro-chemical groundwater type can result from various rock-mineral and water reaction processes. One needs to develop a sound hydro-geochemical conceptual model based on the site geology, hydrogeology, and mineralogy. One also needs to assess (test) the validity of each hypothetically conceived reaction based on measured chemical data. This is done for main hydro-geochemical types occurring in the catchment.

We are not interested in determining information on the kinematic rate (speed) with which acid generation or neutralization will proceed. We are however interested in relating through thermodynamic chemical reactions, the observed dominant water type to the most probable rock-mineral and water reactions.

Over the period of monitoring, hydro-geochemical processes occurred in the sampled groundwater system. This was confirmed by the linear trends observed on the Piper Diagram Plots (Figure 56, Figure 57, and Figure 58). More than 60% of the sampling points (boreholes) show this linear correlation trend. One can therefore use such linear dependence to infer the chemical reaction/processes which result in the main hydro-geochemical types. To add, most of the boreholes showing these trends are located down gradient of waste rock dumps, tailing and dirty water dams, and have shown a constant rising trends in water levels during monitoring period (Figure 41).

Bicarbonate appears to be the most abundant ion (anion) in the hydro-geochemistry of the Platreef. Carbonate minerals are ubiquitous in our environment. Rainwater itself is a source for bicarbonate ions. Silicate weathering can also constitute a source of Bicarbonate. Microbial mediated processes (CH_4 production or consumption) are potential sources of bicarbonate. Furthermore, bicarbonate can also be generated from reaction of CO_2 with water. Moreover, CO_2 is present in rain from equilibrium with the atmosphere. CO_2 dissolved in water may form carbonic acid; and since groundwater moves through the aquifer, the carbonic acid will also dissociate to form bicarbonate and hydrogen ions, depending on the buffering capacity of the groundwater. One also has to bear in mind that, the alkalinity and acidity of groundwater might be influenced by other

constituents (organic acids, phosphates, etc.). Bicarbonate (HCO_3^-) is a function of pH and salinity. Its content in the groundwater will change as function of pH (Figure 59).

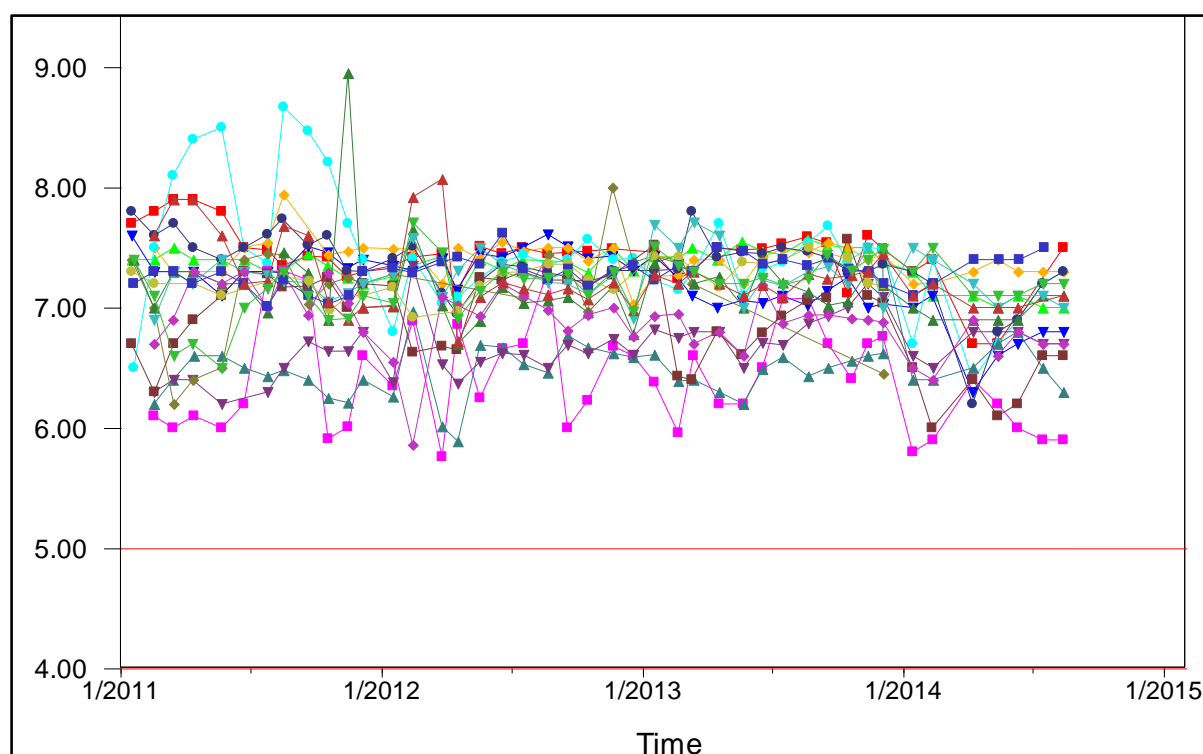


Figure 59: pH measured in the samples collected from borehole which linear hydro-geochemical trends on Piper diagram

Acid mine drainage in the Platreef

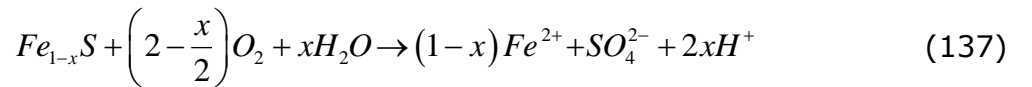
Misinterpretation of work done by precursors (Foose et al., 1995) has led to perceive the Platinum group-element-rich deposit as a low generator of acidic and (or) metal enriched drainage. This is due to their trend of low sulphide abundances. The platinum mineralogy (Platreef) is characterized by prolific base metal sulphides which occurred in the following order of decreasing abundance: pyrrhotite, pentlandite, chalcopyrite and minor pyrite (Foose et al., 1995; Kinnaird, 2005; K. L. Lishman., 2009). Following pyrite, pyrrhotite is the next most abundant iron sulphide in nature.

Based on an Acid Base Accounting investigation, K. L. Lishman (2009) demonstrated that some of the rocks to be mined and tailings material to be generated (from beneficiation) at the Platreef, included low risk as well as high risk acid generating material. From the investigation, Lishman established that some rocks (including Pegmatitic Gabbro-Norite, Melanorite, Norite Cycles and Feldspathic Pyroxenite) and tailings samples contained more than 0.3% sulphide-sulphur and classified them as high risk acid producing potential. Soregaroli and Lawrence (1998) demonstrated that rock

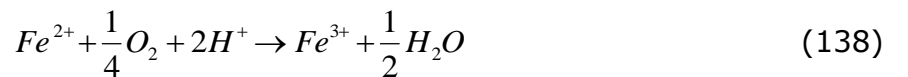
material with at least 0.3% sulphide-sulphur content may generate acid, if exposed to the atmosphere (oxidation) for extended periods of time. Open and exposed (to atmosphere) fractures in the Marginal Zone Norite and Hornfels of the footwall of the Platreef, and the associated xenoliths in the Platreef, are likely to allow the oxidation of the base metal sulphides, provided it is exposed for longtime.

Pyrrhotite oxidation

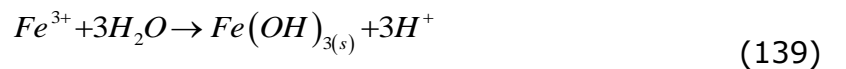
Sulphate (SO_4^{2-}) appeared to constitute the second most abundant ion (anion) in the investigated area, and is known to be high oxidation state of sulfur. The overall series of reactions that lead to acid production from pyrrhotite oxidation is described by the reaction presented from equation (137) to equation (140) (Benner et al, 2000; Blowes et al, 2003; Belzile et al, 2004). At $pH > 4$, Oxygen is the ultimate oxidant (direct) of sulphide minerals in presence of water, but at low $pH (< 4)$ sulphides are oxidized by ferric iron (Nordstrom and Alpers, 1999). Due its relatively poor ordered structure, pyrrhotite shows variations in chemical stoichiometry, and Nonstoichiometric and stoichiometric compositions exist in which x in the formula $Fe_{(1-x)}S$ can vary from 0.125 (Fe_7S_8) to 0 (FeS).



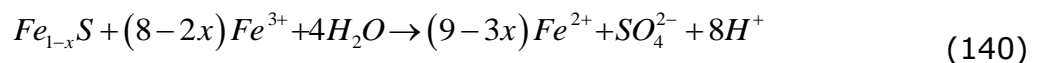
The ferrous iron is then oxidized to form ferric ions that can precipitate out solution to form ferric hydroxide at $pH > 4$.



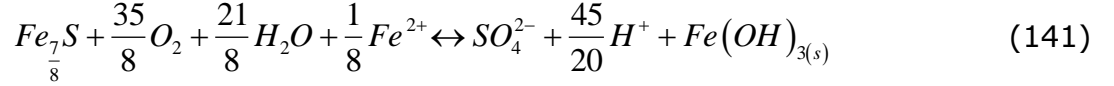
The ferric ions are then oxidized by Oxygen and precipitated as ferric hydroxides such as ferri-hydrates and goethite.



Ferric iron also acts as an oxidant for Pyrrhotite, causing more acidity in the system. If the reaction of Equation (137) occurred under severe acidic condition (very low pH), Fe^{3+} will not be completely oxidised and will remain in solution and maintain a cyclic reaction with reaction as shown in Equation (140).



Reaction of equation (140) is unlikely to occur as the values pH range generally between 6 and 8.5. Considering then ferrous irons and ferric ions oxidized simultaneously with reaction of (137), and then equations (138) and (139) can be thermodynamically combined with Equation. (137) and be represented with reaction shown in equation (141), for $x = \frac{1}{8}$.

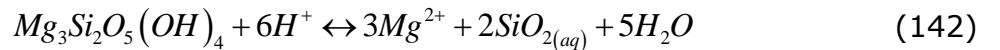


AMD buffering

AMD processes generally occur by co-existing buffering mechanisms that can prevent drops in the pH. More than 90% of the groundwater samples showed pH values that fluctuated between 6 and 8.5 (Figure 59) over the 04 years of monitoring. Under such measured pH ranges, Serpentinite, calcite and dolomite minerals can be dissolve, and buffer AMD. The Gabbro-Norite and Mottled Anorthosite of the Platreef's Hanging-wall, the Dolomite of the Footwall, and Serpentinite associated with the PGE, have a neutralizing (Buffering) capacity. This was established by K. L. Lishman (2009).

Serpentinite Buffering

In acidic water (pH<7), cations from the silicate minerals (Serpentinite) dissolve, and its dissolution (equation (142)) is followed by nucleation and precipitation of carbonate (Guthrie et al, 2001; Chizmeshya et al, 2003; Teire et al, 2007; Jarvis et al, 2009).



Calcite and Dolomite buffering

We investigate base on multivariate plots, the plausibility of Calcite and Dolomite dissolutions investigations as part of dominant acid buffering reactions in the groundwater system. The plot of $SO_4^{2-} + HCO_3^-$ versus $Mg^{2+} + Ca^{2+}$, will have a slope close to the 1:1 (Guler et al. 2002; Gomo et al. 2012), provided the dissolutions of calcite and dolomite are the dominant reactions in a system. Figure 60 shows a scatter plot of $SO_4^{2-} + HCO_3^-$ versus $Mg^{2+} + Ca^{2+}$ concentrations observed in the groundwater system during monitoring period. The plot with slope 1.01 is very close to the 1:1

equiline. This confirms the dominance of dolomite and calcite dissolution as acid buffering reactions in the system, at the point of observations.

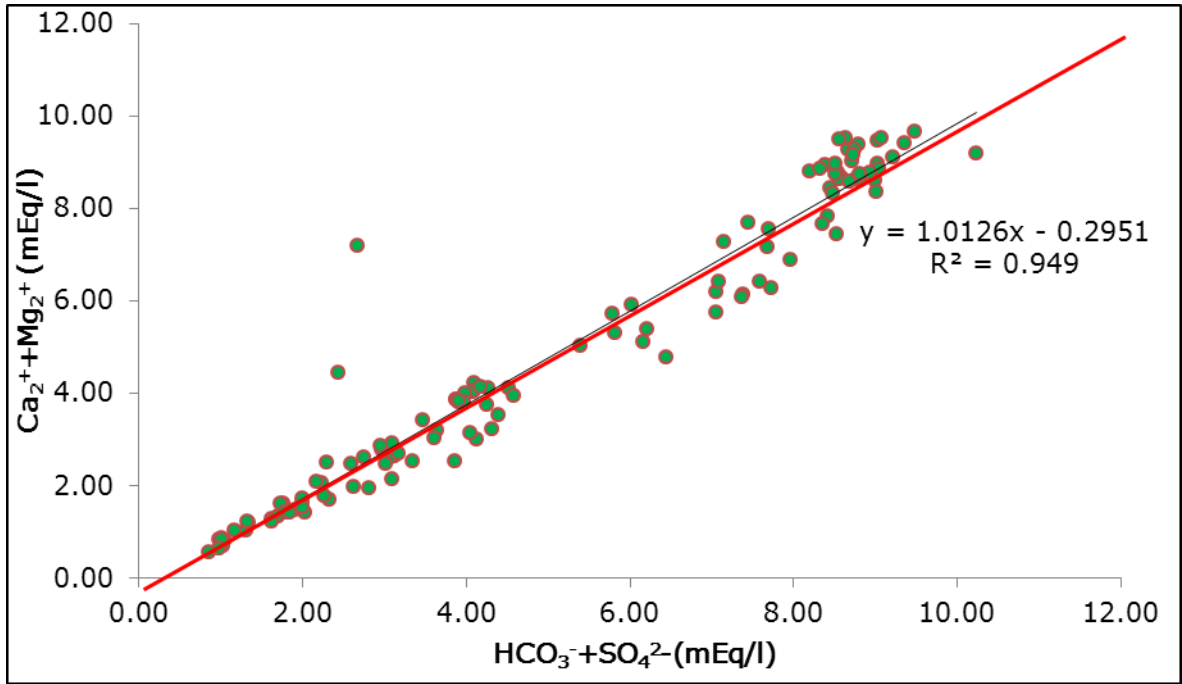
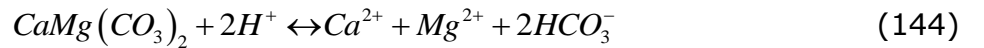


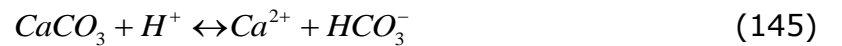
Figure 60: Scatter plot showing $(HCO_3^- + SO_4^{2-})$ against $(Ca^{2+} + Mg^{2+})$ concentrations measured during monitoring period.

Dolomite buffering

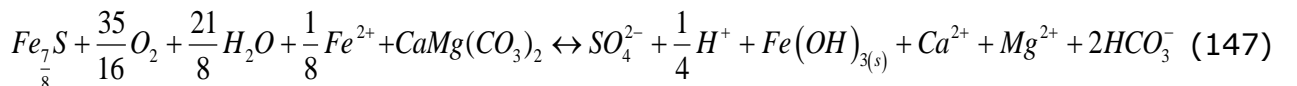
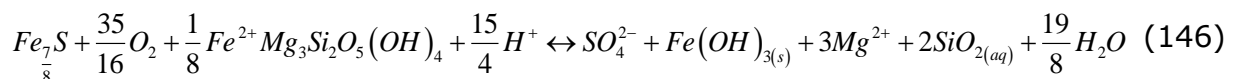
It has long been known that calcite and dolomite buffering processes are dominant in the pH range of 6.5–7.5 (Blowes et al., 1994 and Geller et al., 2000).

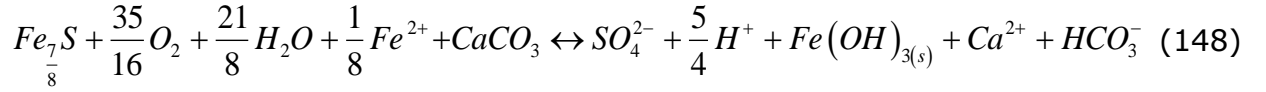


Calcite buffering



Considering the co-existing (simultaneous reactions) buffering mechanisms and AMD processes, as described above; Equations (142), (143), and (139) can be thermodynamically combined with Equation (141) and be represented with reactions shown in the following respective equations:





Note that the molar ratios between the investigated Major chemical elements of the Bicarbonate-Magnesium-Calcium (HCO_3^- ; Mg^{2+} ; and Ca^{2+}) will be produced from the chemical reactions of Equations (146), (147), and (148) which are independent of order of the structure of the sulfate bearing mineral (Pyrrhotite). So, for any value of x (between 0.125 and 0) in the formula $Fe_{(1-x)}S$, these molar ratios should be expected.

Equation (146) shows that when 1 mol of Pyrrhotite is oxidized and co-exist with weathering and dissolution of Serpentine minerals, 1 mol of SO_4^{2-} and 3 moles of Mg^{2+} will be released into the solution. The reaction in Equation (147) shows that for every 1 mol of Pyrrhotite oxidation, co-existence of dissolution of Dolomite will release 1 mol of SO_4^{2-} , 1 mol of Ca^{2+} , 1 mol Mg^{2+} , and 2 mols HCO_3^- into the solution. Equation (148) shows that the Calcite buffering of the acid produced by 1 mol of Pyrrhotite oxidation will release 1 mol of SO_4^{2-} , 1 mol of Mg^{2+} , and 1 mol HCO_3^- into the solution.

The reactions in Equations (146), (147, and (148) may occur simultaneously, resulting in the production of 3 Moles of SO_4^{2-} , 3 Moles of HCO_3^- , 4 Moles of Mg^{2+} and 2 Moles of Ca^{2+} in the system. Alternatively, the reactions may occur in pair as follow:

- Equations (147) and (146) suggest: When 2 Moles of SO_4^{2-} are produced, 2 Moles of HCO_3^- , 4 Mole of Mg^{2+} and 1 Mole of Ca^{2+} are produced in the system; (RPC12; RPC11; PC121S; PC122S);
- Equations (148) and (147) suggest: When 2 Moles of SO_4^{2-} are produced, 3 Moles of HCO_3^- , 1 Mole of Mg^{2+} and 2 Moles of Ca^{2+} are produced in the system;
- Equations (146) and (148) suggest: When 2 Moles of SO_4^{2-} are produced, 1 mol of HCO_3^- , 3 Moles of Mg^{2+} and 1 Moles of Ca^{2+} are produced in the system.

Figure 61 shows a scatter plot of observed HCO_3^- against Ca^{2+} and Mg^{2+} PPM during monitoring period. HCO_3^- is positively correlated to Ca^{2+} and Mg^{2+} with correlation

coefficients of 0.95 and 0.96 respectively, confirming that these three ions have the same linear time evolution in the groundwater system.

In a groundwater system controlled by the reactions of Equations (146), (147), and (148) the molar ratio of Ca^{2+} and Mg^{2+} to HCO_3^- should be 1:2; and the molar ratio of Mg^{2+} to Ca^{2+} should be 1:1.

Plots of Ca^{2+} against HCO_3^- , Mg^{2+} against HCO_3^- , and Ca^{2+} against Mg^{2+} will have slopes of 0.5, 0.5, and 1 respectively. These predictions are close to slopes (0.51, 0.5, and 0.99 respectively) of such plots for observed values which (Figure 61 and Figure 62).

Figure 62).

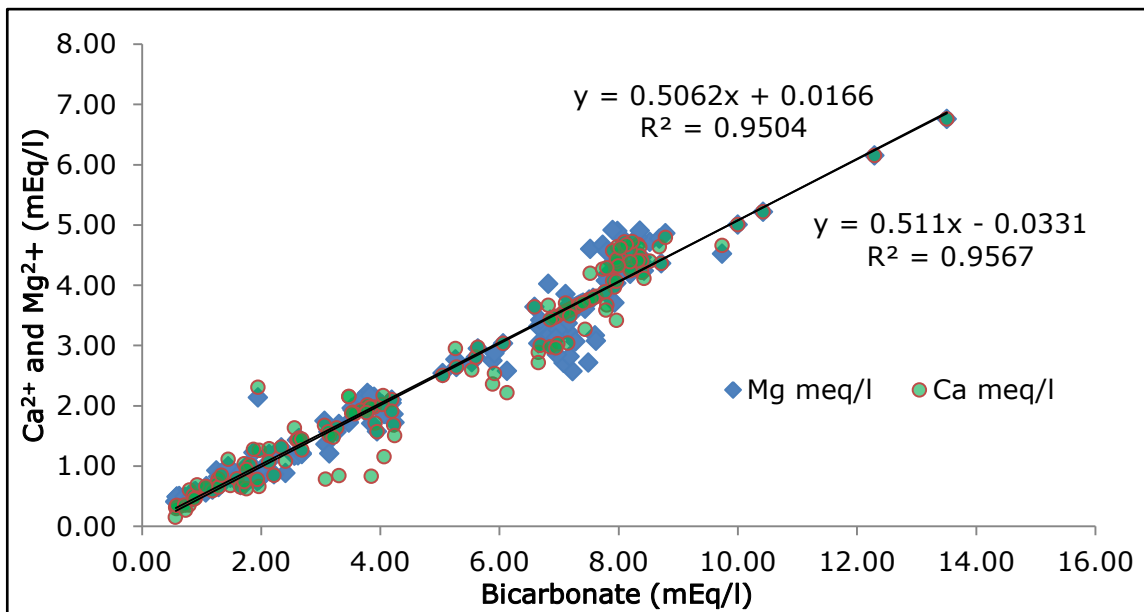


Figure 61: Scatter plot showing HCO_3^- against (Ca^{2+} and Mg^{2+}) concentrations measured during monitoring period.

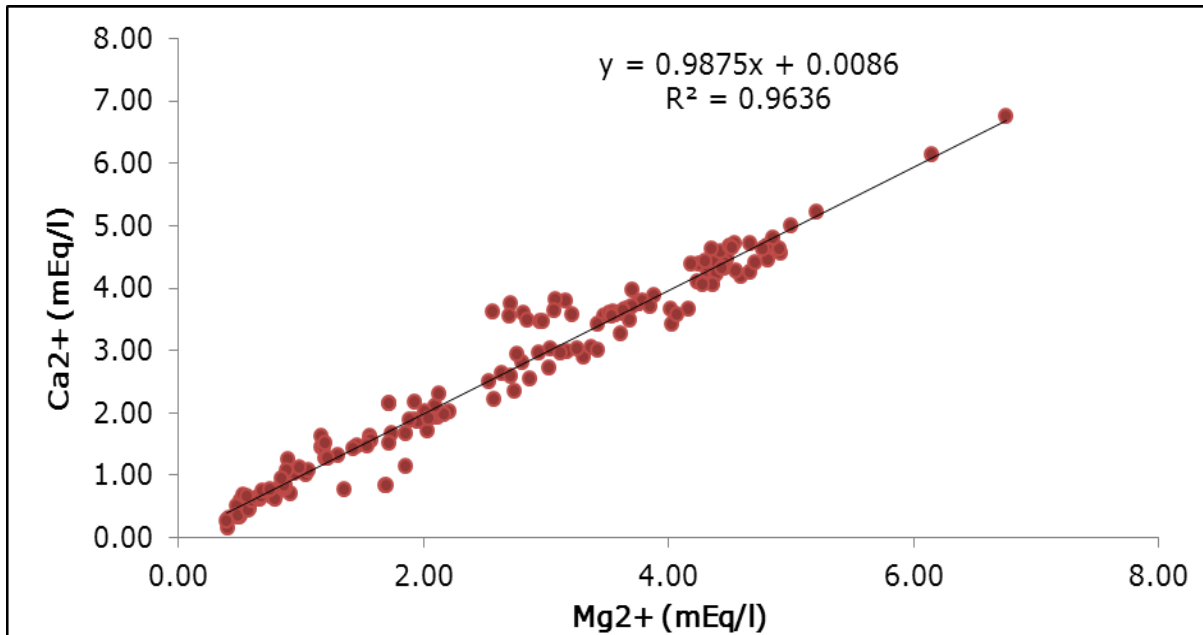


Figure 62: Scatter plot showing Ca^{2+} against Mg^{2+} concentrations measured during monitoring period.

We could not detect any other possible hydro-geochemical processes that can result in the Bicarbonate –Magnesium-Calcium water type.

Ions exchange

The plot of the observed concentrations of $SO_4^{2-} + HCO_3^-$ versus $Mg^{2+} + Ca^{2+}$. Figure 69 shows a shift to the right side of the 1:1 line ($SO_4^{2-} + HCO_3^-$), which is an indication of ion exchange processes taking place in the system (Mulican, 1997). The shift of plots to the right of the 1:1 line, and is assumed due to the decrease of Mg^{2+} and Ca^{2+} cations as they leave the groundwater system to occupy the exchange site left by Na^+ .

In addition, it is expected that if meteoric "NaCl" is the source of Na^+ in the groundwater system, then a plot of Na^+ against Cl^- in the groundwater should fall on the 1:1 evaporation line. The plot of Na^+ against Cl^- (Figure 63) shows that groundwater samples at the site are located above (on left of) the 1:1 evaporation line. This implies that rainfall is not the only source of Na^+ in the groundwater water system, which means that Na^+ concentration is increased by other occurring process such as ion exchange process. Jankowski and Beck (2000) reported that such shift of the plot from simple evaporation line is an indication addition of Na^+ into the aquifer system by ion exchange reactions.

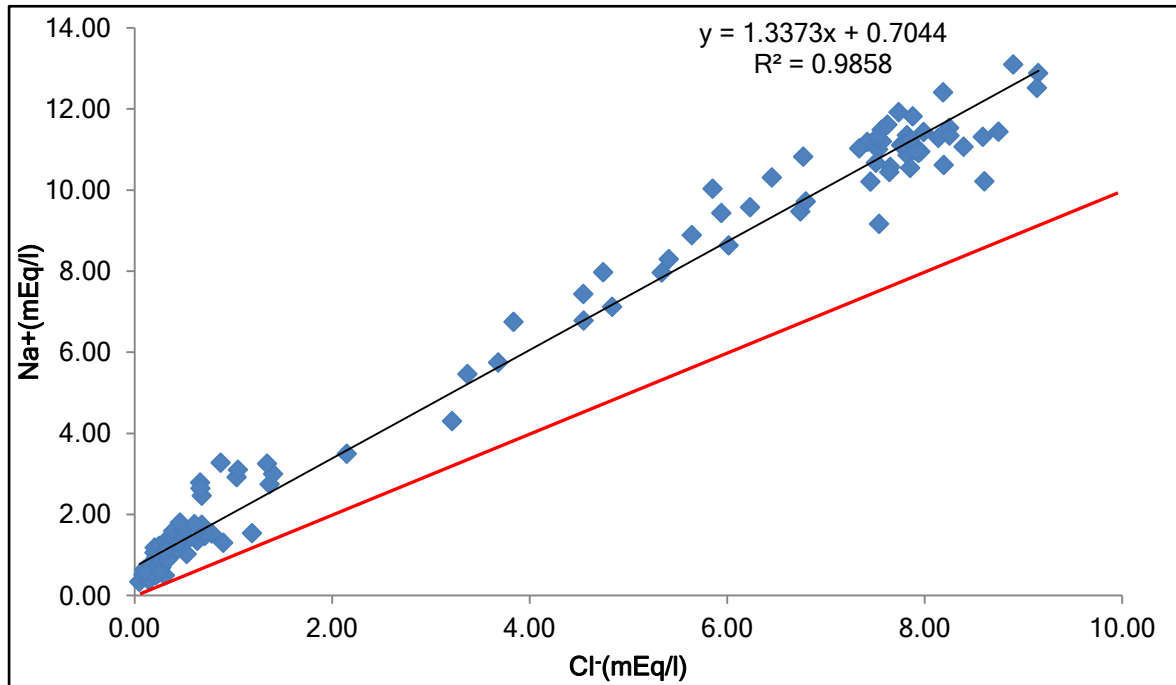


Figure 63: Scatter plot showing Cl^- against Na^+ concentrations measured during monitoring period.

Jankowski and Beck (2000) explained that in a system dominated by ion exchange processes, the plots of $(Mg^{2+} + Ca^{2+} - SO_4^{2-} - HCO_3^-)$ versus $(Cl^- - Na^+)$ should form a line with slope of -1. According to Jankowski and Beck, by subtracting chloride from sodium chloride (considering that Cl^- is a conservative ion, and assuming that all Cl^- comes from precipitation), groundwater that is not influenced by the ion exchange will plot close to zero on this axis. When $(SO_4^{2-} + HCO_3^-)$ concentration are subtracted from $(Mg^{2+}$

+ Ca^{2+}) concentrations, the dissolution of calcite, dolomite should also return values of zero assuming that dissolution occurs at the same rate and no ion exchange occurs.

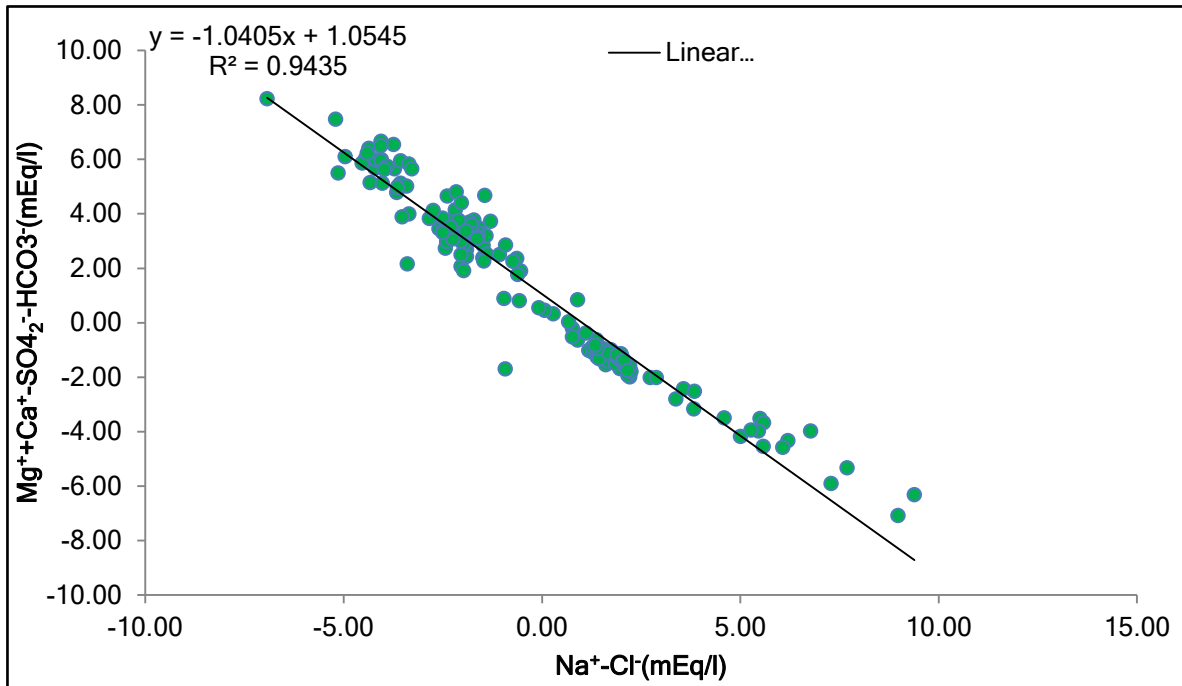


Figure 64: Scatter plot showing $(Mg^{2+} + Ca^{2+} - SO_4^{2-} - HCO_3^-)$ against $(Cl^- - Na^+)$ concentrations measured during monitoring period.

Figure 64 shows plot of observed $(Mg^{2+} + Ca^{2+} - SO_4^{2-} - HCO_3^-)$ versus $(Cl^- - Na^+)$, which displays a slope of -10.04 with a good fit of 94.35%. This enhances evidence for ion exchange reactions in the aquifer system.

6.2.6.4 Saturation state

The saturation Index (SI) is a useful measure of saturation of the water with respect to a given mineral. When the mineral solubility is in equilibrium (saturated) with the solution composition, the SI of the given mineral is equal to 0. Negative SI indicates that the mineral phase can dissolve and is under-saturated, while positive values reflect supersaturated hydro-geochemical conditions. Calcite and Dolomite are among mineral phases that are found to be controlling the geochemistry of Platreef's groundwater system within the monitoring area (mine). Using thermodynamic data contained in the database of the hydro-geochemical model PHREEQC (Parkhurst and Appelo, 1999), we calculated the SI for these two AMD buffering minerals (Calcite, Dolomite).

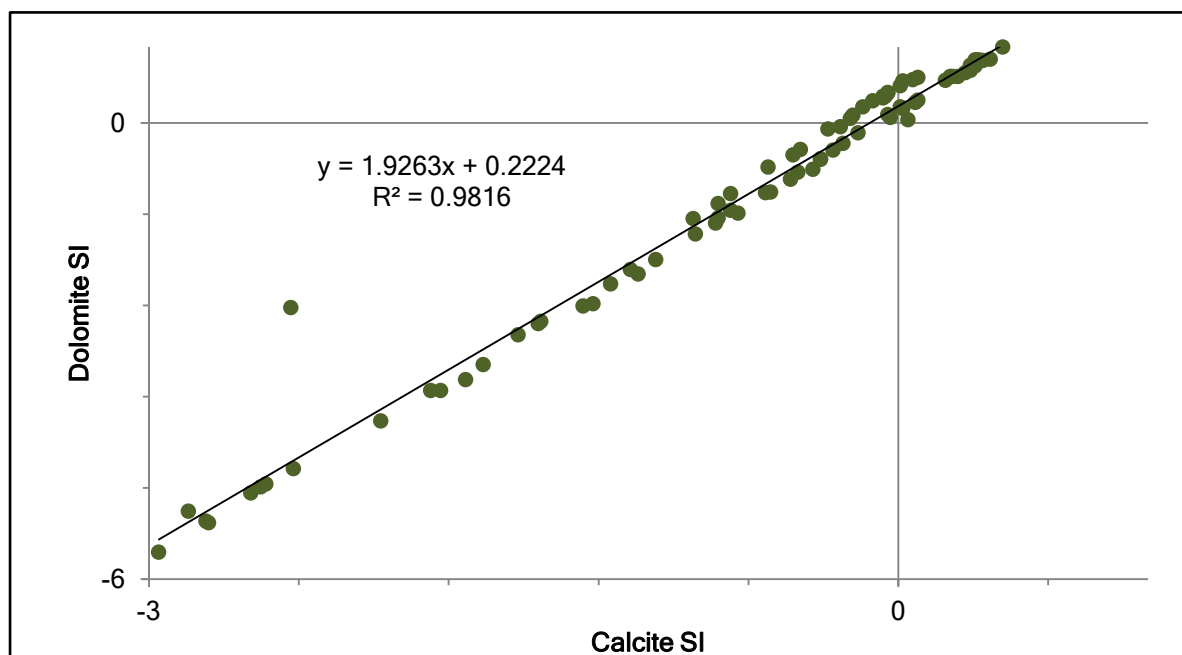


Figure 65: Scatter plot of Dolomite SI against Calcite SI.

As can be seen in Figure 65, Calcite and dolomite SI are following a positive linear trend with a correlation coefficient of 98%. This correlation confirms that the reactions of the two mineral are controlled by similar hydro-geochemical process (AMD buffering). We noticed that at pH value below 7, the mine's groundwater is under saturated with respect to both dolomite and calcite, and there is a constant increase of the SI of the Calcite and Dolomite minerals with pH (Figure 66). The alkalinity produced during the neutralisation of AMD by Calcite and Dolomite carbonates results in the increase in pH.

The plots of Calcite SI and Dolomite SI in function of the evolution of measured concentrations of Mg^{2+} and Ca^{2+} are presented in Figure 67 and Figure 68 respectively. The trends of the plots in Figure 67 and Figure 68 suggest that Mg^{2+} and Ca^{2+} in the mine's groundwater system would only occur up to certain points. At these points their respective aqueous solubility will become limited by the saturation of Calcite and Dolomite. Figure 67 shows that the mine's groundwater becomes definitively saturated with respect to Calcite at the concentrations above 2.5 mEq/L and 3.0 mEq/L for Mg^{2+} and Ca^{2+} respectively. The mine's groundwater becomes saturated with respect to Dolomite at the concentrations above 2 mEq/L and 3.0 mEq/L for Mg^{2+} and Ca^{2+} respectively (Figure 68).

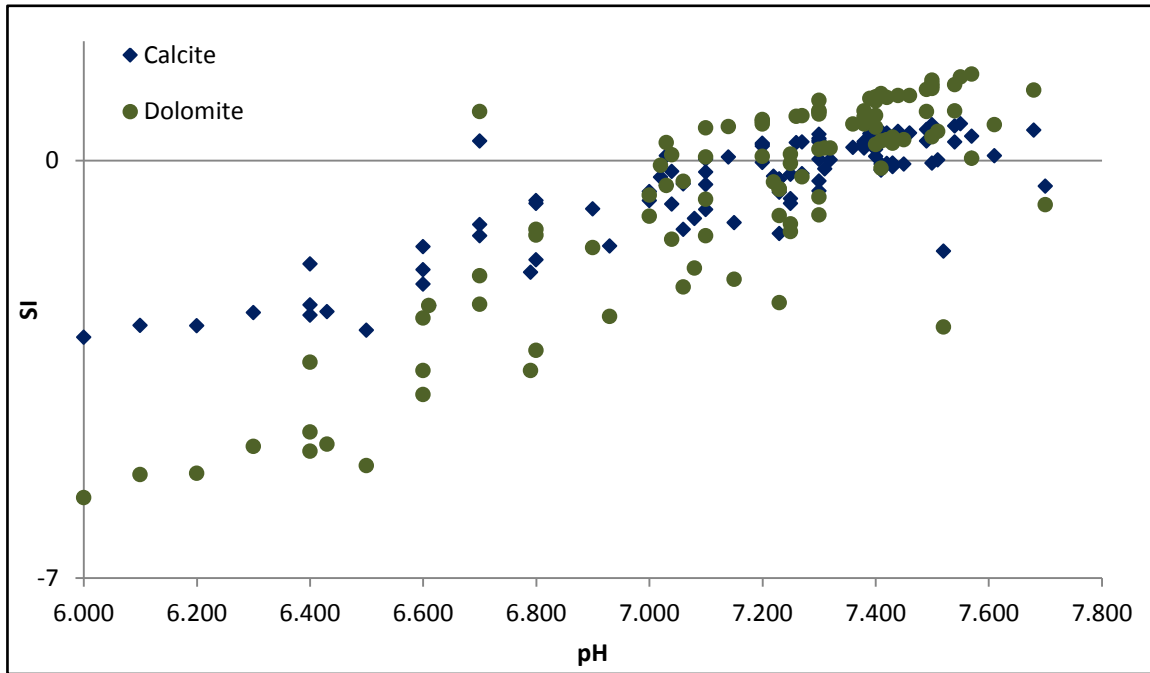


Figure 66: Scatter plot of pH against Dolomite and Calcite SI.

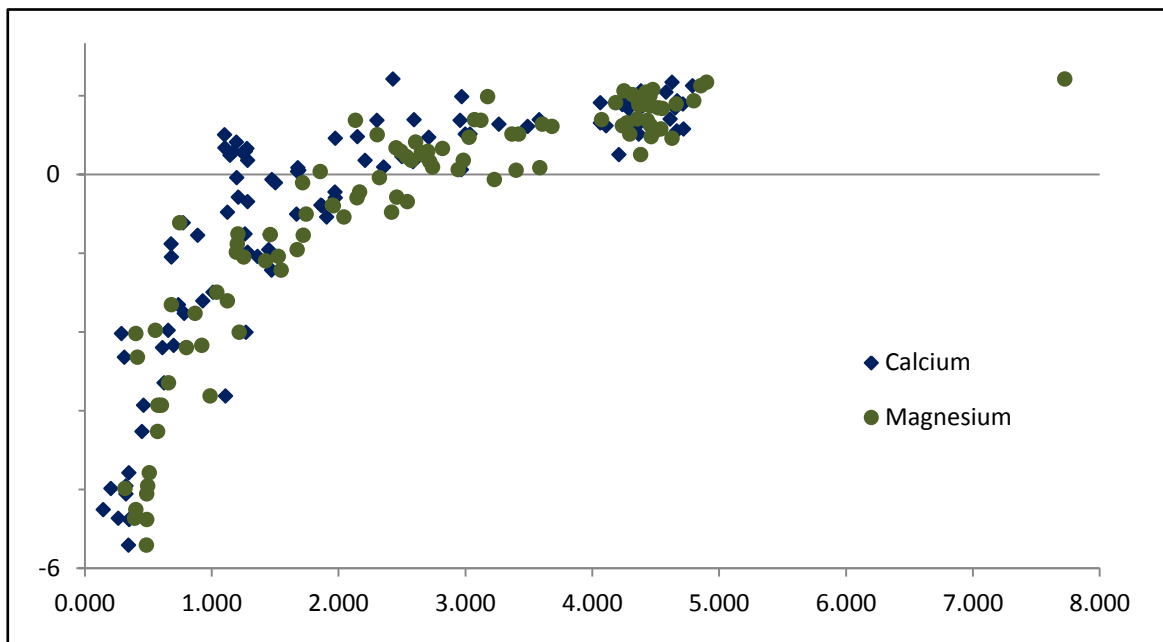


Figure 67: Scatter plot of Calcite SI against Mg^{2+} and Ca^{2+} .

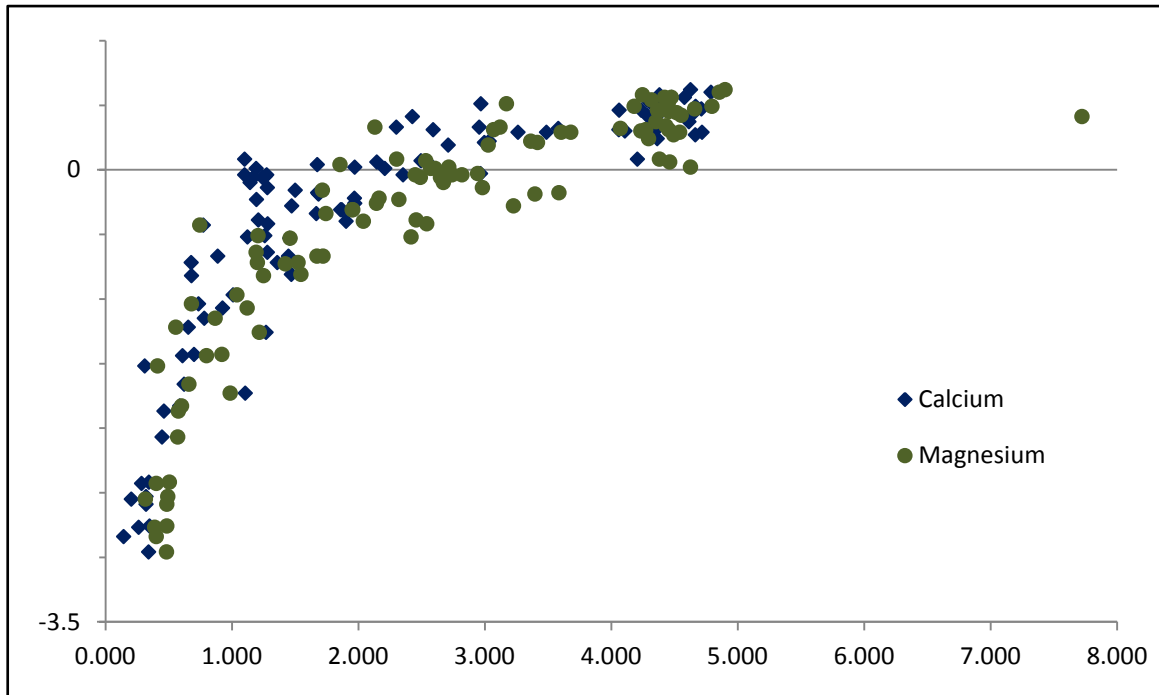


Figure 68: Scatter plot of Dolomite SI against Mg^{2+} and Ca^{2+} .

6.2.6.5 Groundwater quality

Metal

We have demonstrated above how the observed groundwater quality may have evolved from the oxidation of Pyrrhotite and subsequent buffering reactions (Serpentine, Dolomite, and Calcite). Following pyrite, pyrrhotite is the next most abundant iron sulphide in nature (K. L. Lishman., 2009; Belzile et al., 2004). It is well reported in literature (Johnson et al., 2000; Ekosse et al., 2004) that acidic water that is generated from oxidation of pyrrhotite may contain high concentrations of dissolved metals. Elevated concentrations of metals pose a potential threat of contaminating groundwater resource (Blowes and Ptacek, 1994; Rose and Cravotta, 1998). The levels of metal concentrations in a groundwater system that might have hydro-geochemically evolved through AMD were therefore assessed. Considering the geology in the area and the potential content of the waste materials (Rock dumps, tailing) focus was given to selected metals (Fe, Mn, Cu, Cd, Cr) that may dissolve into the water under acidic conditions, during monitoring period.

The descriptive statistics of metals that were detected in the Platreef's groundwater system during the monitoring period are summarized in Table 16.

Measured metals concentration were compared to SANS-241 (2015) and WHO (2011) drinking water quality guidelines. It appears that Fe and Mn that exceeded the SANS-241 (2015) drinking water quality target concentration in 03% and 12% of the samples respectively. With such low percentage of samples of concerns, one cannot directly infer the presence of such forte concentrations of these dissolved metals (Fe and Mn) in some of the groundwater samples to the effect of AMD metal leaching. Especially not when, no hydro-geochemical background (Pre-mining) data could be found as reference. Except for these very few samples with elevated Fe and Mn, the rest of the assessed metals are generally all below the SANS-241 (2015) and WHO (2011) drinking water quality guidelines. It can therefore be concluded that the calcite and dolomite minerals in the PGE and base metals deposits are buffering the AMD thus preventing the leaching of metals into the sampled groundwater system.

Table 16: Descriptive statistics of the metal concentration detected in the flooded underground mine ground water during the monitoring; also shown in the table is the SANS-241 (2015) and WHO (2011) drinking water quality guidelines.

	Count	Min	Max	Arithmetic Mean	Standard Deviation	SANS (2015)	WHO(2011)
Fe	1149	0.005	6.55	0.056	0.319	≤ 0.3	
Mn	1149	0.005	11.66	0.190	0.718	≤ 0.4	
Cu	1149	0.005	0.077	0.009896	0.002613279	≤ 2	
Cd	1149	0.0057	0.010	0.010	0.001	≤0.003	0.003
Cr	1149	0.01	0.03	0.023108	0.009505101	≤ 0.05	0.05

Total dissolved solids (TDS) and Total hardness

Figure 69 shows the groundwater quality classification for the platinum mine area based on TDS levels (WHO, 2003). 73% of the groundwater samples have TDS in the acceptable range (WHO, 2003; SANS-241, 2015) of for drinking purposes. Only 54% of the samples are classified between Excellent and Fair (WHO, 2003) groundwater quality. The samples (27%) that fall under Poor to High (WHO, 2003) classes of groundwater quality (greater than 900 mg/L) show also elevated concentration of SO_4^{2-} , Mg^{2+} , and Ca^{2+} ions which were found to be released during the carbonate AMD buffering process.

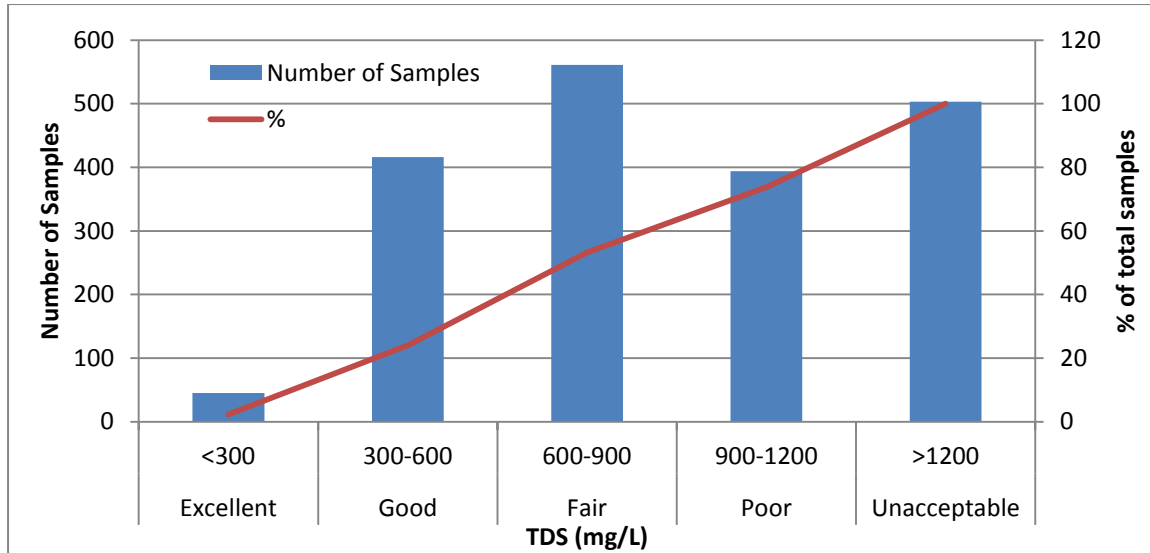


Figure 69: Classification of historical groundwater quality samples data based on TDS WHO (2003).

Figure 69 shows the groundwater quality classification for the monitored platinum mine area based on calculated total Hardness, and using TDS levels the index developed by McGowan (2000).

The elevated Mg^{2+} and Ca^{2+} concentrations released from the calcite and dolomite AMD buffering process, lead to a prevailing “Very hard” conditions (total hardness > 180 mg/L). This is confirmed by at 80% of the samples collected during the monitoring period in the platinum mine area, which are classified as very hard.

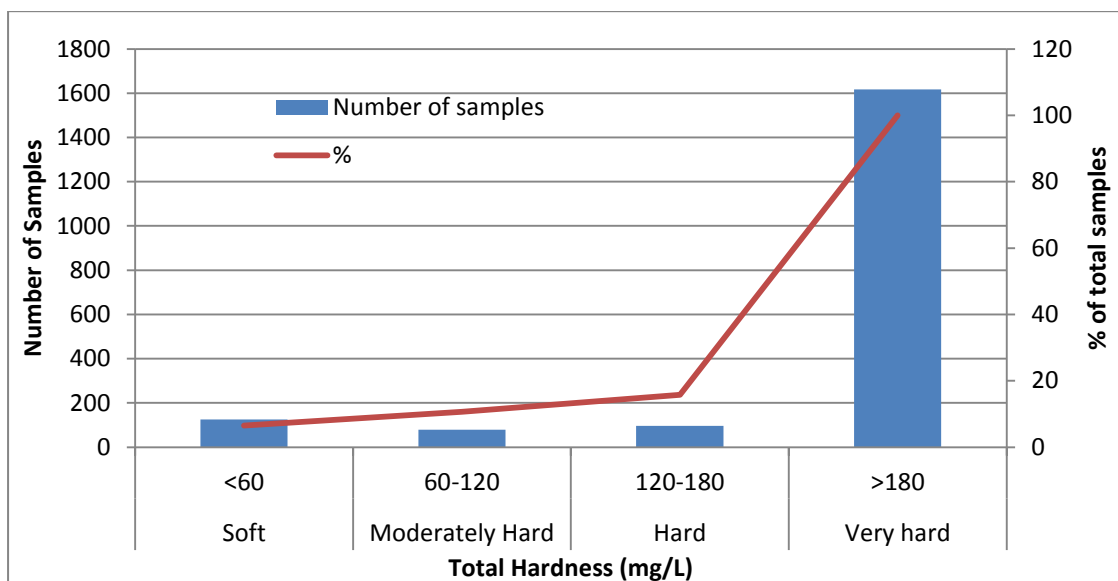


Figure 70: Classification of historical groundwater quality samples data based on Hardness Index (McGowan, 2000).

Although the buffering minerals (Serpentinite, calcite and dolomite) are important for reducing the AMD levels and minimizing the potential leaching of metals into the mine groundwater system they also presents the problem of elevated Total Dissolved Salt and Total hardness.

6.2.7 Groundwater recharge (Chloride Mass Balance Method) values

The groundwater system within the study area is mainly recharged via infiltration of precipitation, as confirmed by water qualities. The presence of black clay close to the surface does not seem to inhibit recharge from rainfall.

According to Vegter (1995), the recharge is 22 mm/a, which is equal to approximately 4% of mean annual precipitation. Different groundwater recharge rates were estimated for previous studies conducted in the area (at different periods). The methods used to estimate recharge in the previous studies included: (a) the Chloride Mass Balance (CMB) method; (b) the Saturated Volume Fluctuation (SVF) method; (c) the Cumulative Rainfall Departure (CRD) method; and (d) the extended model for Aquifer Recharge and soil moisture Transport through the unsaturated Hard rock (EARTH) method. Consistency was found in the recharge rates estimated from these different methods. Groundwater recharge was estimated between 2% and 4% of the mean annual rainfall (642 mm).

Using the water quality data from the hydrocensus, the recharge was calculated using the chloride mass balance method. Based on the above assessment of occurrence of ions exchange in the groundwater system, it was assumed that there is no other source of chloride other than the rainfall. We exclude recharge rates that were above 35mm/year (5% of total rainfall), as these were defined as unrealistic estimates. Figure 71 illustrates the spatial distribution of selected (142 in total) recharge in the catchment. The full detail on the calculated recharge is presented in appendix C Groundwater recharge rates in the catchment range between 0.10% and 5.56%, with a harmonic mean of 0.62% of the mean annual rainfall (642 mm). This corresponds to an annual recharge rates between 0.64 mm and 35.66 mm, with a harmonic mean of 3.95 mm.

We could not observe any spatial correlation between the variability of the recharge rates and the locations of the lineaments. This suggests the occurrence of preferential recharge in the linear fractured zones.

6.2.7.1 Artificial recharge

Water stored in the tailings and return water dams may constitute sources of artificial recharge to the aquifer system(s). The previous studies also indicated that although there were slight differences between the calculated recharge rates, the results compared well from one method to the other.

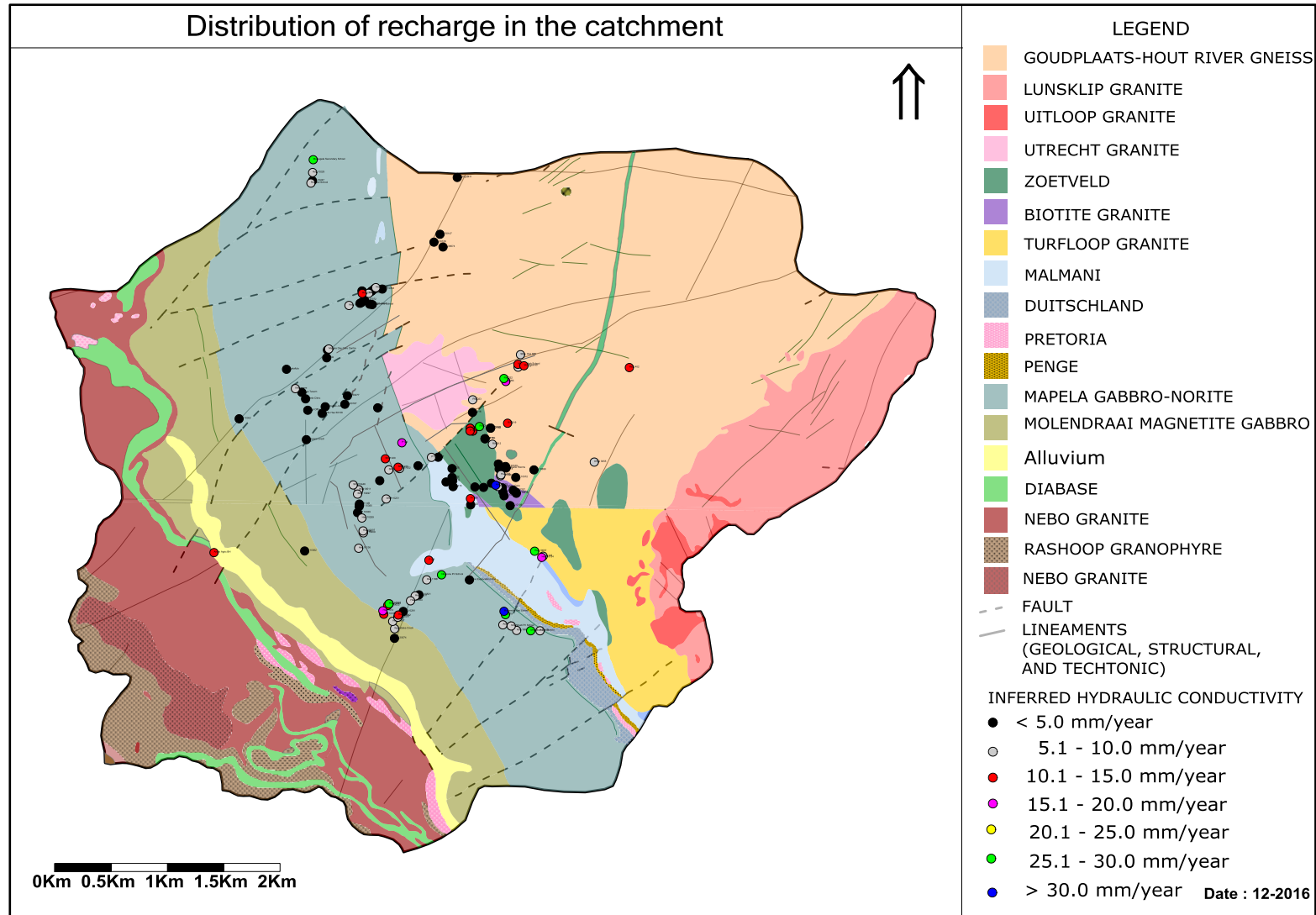


Figure 71: Spatial distribution of the estimated recharge using Chloride Mass Balance method in the catchment

7 Conceptual and numerical geohydrological model of the Platreef

7.1 Objective of the Modelling

The ultimate goal of the present numerical modelling investigation is to demonstrate how one can model spatial heterogeneity in aquifers, based on most commonly available tools and data in mining environments of South Africa. The purpose of this type of model is to simulate mining impact on groundwater flow and associated mass transport, and to predict some of the groundwater related scenarios (Dewatering, Contaminant migration,).

Spatial variability of hydraulic parameters as quantified above has to be included in the model. Special focus is given to the geo-statistical characters. Current trends (Stochastic, Discrete) in the modelling of flow in fractured igneous rocks, in the South African opencast mining environments, are also part of the interests of the present numerical modelling investigation. Three numerical Software models were assessed on their capabilities to quantify and model discontinuities in groundwater flow.

The location and scale of the study were chosen according to available data and experiences acquired in the area.

7.2 Conceptual geohydrological models

The construction of a conceptual model of the problem and the relevant aquifer domain, constitute the foundation for the modelling of any system. The conceptual model is a simplified representation of the essential hydrological features and the behaviour of the physical hydrogeological system, to an adequate degree of detail. A set of assumptions are considered to reduce the real problem and the real domain to simplified versions that are acceptable in view of the objectives of the modelling.

Many conceptual hydrogeological models were developed in the past as part of groundwater models in the study area, for different projects. These projects include the "Annual Numerical Groundwater Model Update" for the Mogalakwena Mine located in the catchment.

The current level of site characterization (including existing groundwater models) was used to simplify the description of the aquifer systems.

The present site conceptualization is for predicting the potential impacts of the opencast mining activities on the aquifer systems associated with the Platreef PGE deposits by considering the spatial changes (heterogeneity). It aims to construct equivalent but simplified conditions for the real world problem, which are acceptable in view of the objectives of the modelling. The following is included:

- The known geological and geohydrological features and characteristics of the area;
- The static water level elevations in the study area;
- The interaction of the geology and geohydrology on the boundary of the study area;
- A description of the processes and interactions taking place within the study area that will influence the movement of groundwater; and
- Any simplifying assumptions necessary for the development of a numerical model and the selection of a suitable numerical code.

As generally observed, groundwater flow and aquifer occurrence (development) are closely linked to the geology and structural features of an area. It is therefore assumed that the surface geology and the collected aquifer parameters form the basis on which the conceptual hydrogeological model is spatially based.

7.2.1 Soils and unsaturated zone

The soils are of moderate natural fertility. Recent studies conducted in the catchment (SRK, 2012; SRK, 2013) described the soil as generally moderate natural fertility. The soils are classified as follow:

- Sandy, loamy soils are found on the flatter areas (Hutton and Shortlands forms);
- At the sloppy area, shallower rocky soils (Mispha forms) are generally dominant;
- And the clay (sandy clay) soils (Arcadia form) are found associated with depressions. The surface rockiness together with the marginal mean annual rainfall and other climatic conditions attributes to the low agricultural potential of the soils.

Based on existing borehole logs, and field observations, the top soil of the area consists mostly of the clay and sand of multiple colours (whitish, blackish, brown). This soil has developed as residual soil from either the igneous or sedimentary rocks. This soil may extend to 3.0 m below ground level, but is also inexistent at some places.

7.2.2 Hydro-stratigraphic units, types, and thicknesses

The top subsurface geology (up to 180 mbgl) is characterized by a well-developed igneous layering of Gabbro-Norite (of Rustenburg layered Suit of the Bushveld Complex), Granite (of Utrecht, and Mashashane Suit), Pyroxinite, and Gneiss (and Goudplaats-Hout River Suit). These igneous formations are known to be disturbed by dolerite dykes and diabase dykes of variable sizes, as well as by faults.

As per the regional hydro-stratigraphy, three dominants hydro-stratigraphic units (Alluvial deposits; Shallow weathered aquifer system; and Shallow and Deeper Localized fracture aquifer system) are found in the catchment.

We describe here some particularity of such hydro-stratigraphic units within the study area.

7.2.2.1 Alluvial Aquifers

The alluvial deposits occur along the main surface water drainage. According to existing geological maps, and based on field observations, the only substantial deposits of alluvium occur along the major catchment surface drainage course: "Mogalakwena River". The water flowing down this river will recharge the shallow alluvial aquifers, which in turn will drain downwards to the weathered and fractured aquifers due to their inter-connectivity. The alluvial deposits typically consist of red or sandy clay (calcified in places) which overlies sand, gravel and pebbles. Sustainable yields from boreholes drilled into this aquifer vary between 0.5 ℓ/s and 9 ℓ/s .

Considering the limited extent of an alluvial deposit (along the Rivers) spatially and vertically, compared to the weathered and fractured aquifers of the foot wall granite, and of hanging wall Gabbro-Norite, it will not be incorporated in the present modelling exercises.

7.2.2.2 Shallow Weathered Aquifer

The top soil is generally underlain by a sedimentary layer which may extend up to 9.0 m below ground level, with an average thickness of 3.0 m. This thin sedimentary layer forms the roof of the weathered/fractured igneous rocks and will be considered to be part of the shallow weathered aquifer. One of the previous models developed for the catchment considers this type of sedimentary layer as a sandy aquifer. However, the limited average thickness (less than 08 m) of such a layer, and the saturated level (depth to groundwater levels) of the aquifer, do not suggest a well-developed separate sandy aquifer, but rather, pockets of sandy aquifers within the weathered/fractured aquifer.

Based on previous investigations in the Limpopo plateau and field characterisation (boreholes drilling logs analysis) in the study area, the starting depths of the weathering and fracturing in the igneous rocks range between 1 and 23 mbgl, with an average of 6.5 mbgl. Weathering/ fracturing zones in the igneous rocks were found to have an average thickness of 20 m and occurred up to 50 mbgl.

Fractures were found to occur from 3 mgbl, with a depth of up to 105 mbgl. However, most of the fractures were found to occur in the weathering zone at depths between 10 and 40 mbgl. The highest fracture frequency is encountered in the weathering zone between 15 and 20 mbgl.

This aquifer is unconfined to semi-confined and is recharged by rainfall. Evidence of this is provided by the correlation between groundwater level elevation and topography.

The shallow weathered aquifer is comprised of lower permeable rock material.

The regional groundwater gradient is predominantly toward the Mogalakwena River, following the topography. The depths to groundwater level are found to be in average of 9 mbgl. Such measured water levels are a function of the product of the combined saturated aquifers (weathered and fractured) thickness, the hydraulic conductivity (transmissivity) and effective aquifer recharge.

7.2.2.3 Deeper Fractured Aquifer

A deeper fractured rock aquifer formed by competent rocks of the Goudplaats-Hout River Gneiss Suit, Granites of the Mashashane Suit and Mashashane Suit, that has been subjected to fracturing associated with tectonic movements that took place during intrusion of the Bushveld igneous Complex, Diabase dykes and sills.

There is insufficient information available to confirm the exact thickness of the deeper fractured aquifer, but considering previous investigations in the area and the objectives of the model (impacts of open cast mine) we limit the deeper fractured aquifer at 100 m below the bottom of the shallow weathered aquifer.

The deeper fractured aquifer is expected to be unconfined to semi-confined , as available geological logs in the area did not show any impermeable layer between the two aquifer systems.

7.2.3 Aquifers domain and boundaries

In groundwater modelling, the identification of the modelled area and its boundaries is one of the most important and demanding tasks.

At the present level of site characterisation, no evidence of subsurface no-flow boundaries has been clearly identified. Also, there is a good correlation between the groundwater level elevations and the surface topography. We then, consider that the groundwater system extends over the geometry of the surface water system within the catchment. As the PGE deposits within the catchment are located in the eastern watershed area of the Mogalakwena River (Perennial), the model domain is limited to only this watershed. The water divide of the quaternary catchment boundary and the Mogalakwena River, coincides with and form the model perimeter boundary. The internal model boundaries are formed by the main streams (Groot-Sandsloot River, Mohlosane River, and Wit River) feeding into the Mogalakwena River.

Some of potential tailings infrastructure and open pits may also straddle multiple sub-catchment divides. We therefore include large areas of the surface water sub-catchments of the main water courses that drain the catchment cross, with particular attention to the

ones crossing the Platreef (Mogalakwena River, Groot–Sandsloot River, Mohlosane River, and Wit River) into the modelling domain.

So, most of the groundwater recharges occurring within the study area are expected to discharge (internally) to the:

- Surface drainage systems via SPRINGS;
- Base of the main river drainage systems (Mogalakwena River, Groot–Sandsloot River, Mohlosane River, and Wit River); and
- Mining pits causing flooding of pits' floor.

The thickness of the unsaturated zone is determined by the depths to groundwater levels varying between 3 mbgl and 33 mbgl (close to dewatered open pits). We consider a saturated zone extending from the groundwater levels down to 150 m below groundwater levels. Although the bottom of the ore body is known to extend up to 500 mbgl, the formations below 50 mbgl generally contain very little water. Moreover, below 250 mbgl may be considered dry.

7.2.4 Hydraulic Parameters

7.2.4.1 Hydraulic conductivity values

The current level of site characterization gives a wide range of aquifer flow parameters (Transmissivity or Hydraulic Conductivity).

We consider results from different hydraulic tests (slug, and pumping tests) conducted previously and recently in the catchment to infer hydraulic conductivity values. We assume that the data and inferred aquifer parameters are correct. In total, 72 hydraulic conductivity values (including dry boreholes) are estimated from hydraulic tests. These values appear to vary spatially by 04 orders of magnitude as illustrated in Figure 72 and Figure 73.

55% of inferred hydraulic conductivities were found to vary between 0.1 m/day and 50 m/day. However, only 30% of the tested boreholes proved to have hydraulic conductivity values above 10 m/day, and 15% vary between 10 m/day and 50 m/day (Figure 72). This spatial variability in hydraulic conductivity values was expected. Furthermore, the geological setting is complex due to the different intrusions into the older rocks, and

faulting which probably enhanced the development of higher hydraulic conductivity zones.

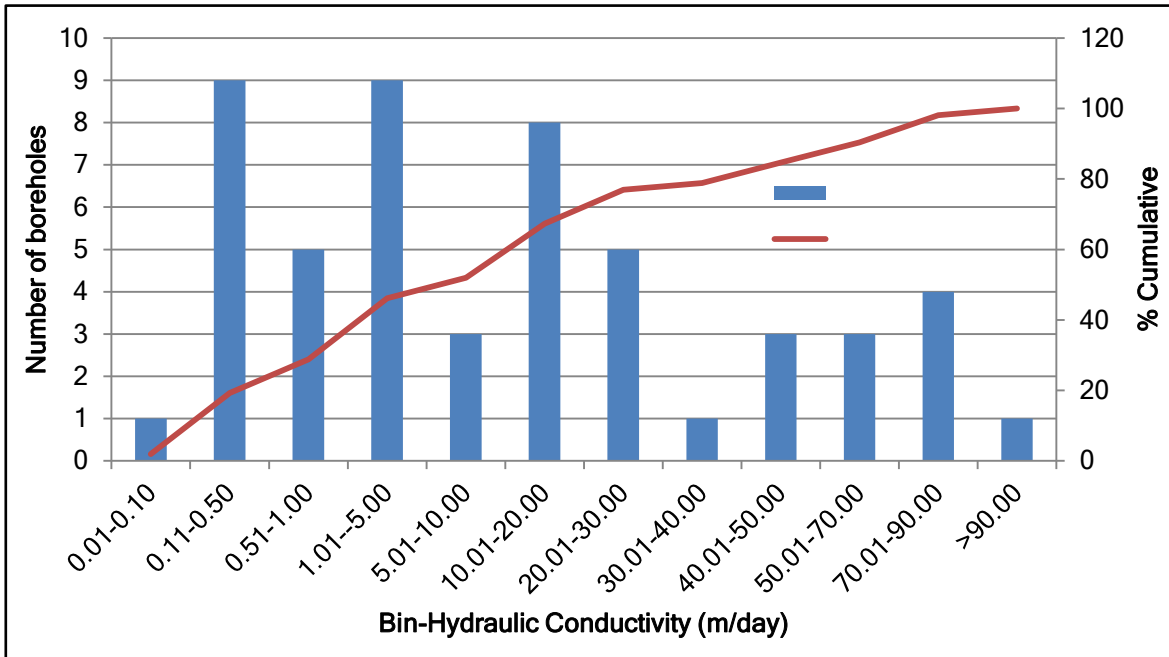


Figure 72: Available Hydraulic conductivity frequency in the catchment

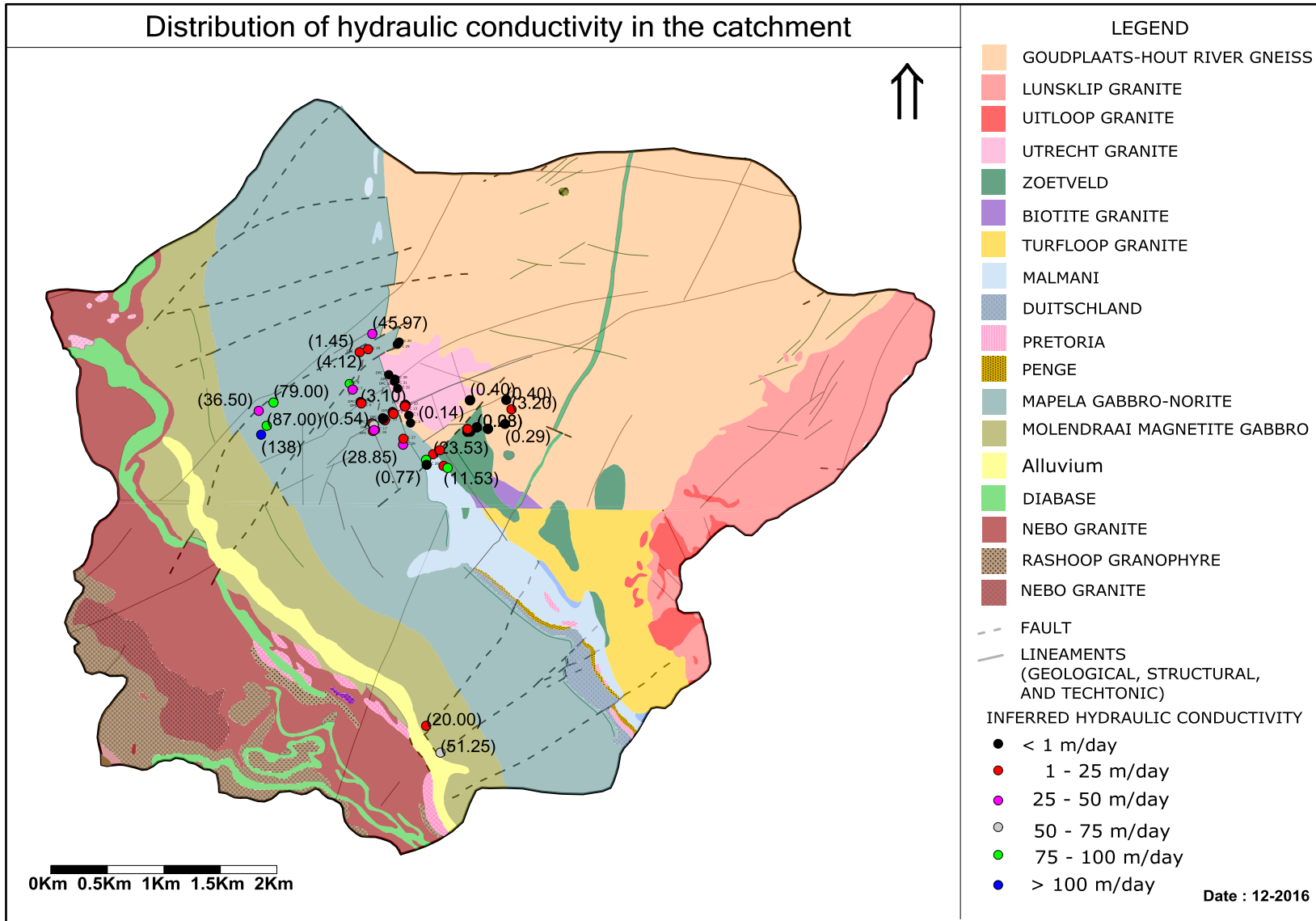


Figure 73: Spatial distribution of available estimated Hydraulic conductivity in the catchment

One of the main aspects of the conceptual model in the present research is how this available filed data can be transferred into a representative form of the aquifer, which can be defined and simulated by the selected software packages.

The previously developed numerical models for the area assume homogeneous layers of constant conductivity (transmissivity), which are crossed by lineaments (faults). However, no tangible heterogeneous features of discontinuities, anisotropy, and long tail can be seen in the shapes of the cone of depressions (drawdowns) and potential pollutions plumes. Although a state of the art investigation cannot guarantee detection of all fracture zones in the catchment, we expect to see the effect of heterogeneous features in the predictions made from numerical model simulation, in such fractured aquifer flow systems.

No abrupt transition feature is observed in the groundwater drainage. This can be associated to spatial rocks units' variability. In addition to this, data collected are spatially limited. We propose a single domain stochastic model (Long and Billaux, 1987; Geier et al, 1989) combined with discrete fractured areas along the main lineaments (Fault and thin dykes). These lineaments are confirmed to be associated with discontinuous, but relatively denser fractures networks, forming a preferential flow for groundwater and mass transport.

It is worthy to mention that even this quantified variability in aquifer hydraulic conductivity values is more representative of the aquifer systems in the main fractured zones (associate with the lineaments and contacts zones). Most (>90%) data were collected from boreholes which intersect such fractured zones. Using only this data for numerical modelling simulations may result in overestimating groundwater flow movement. To mitigate such bias, we attributed to all known dry (no water strike, no seepage) boreholes (20 in total), a very low theoretical hydraulic conductivity value (9.10^{-5} m/day). Assuming a lack of sufficient budget (time, and financial), and other constraints (production, safety, and others mining activities) do not prevail, we still however advise to drill the same number of boreholes (drilled) in both the main fractured zones and the known dense rock mass (no fractured zones) for a more representative and efficient model.

7.2.4.2 Storativity

Although available analytical methods of the interpretation of the pumping tests data are not recommended for estimating storage capacity in such a fractured aquifer, the values of storage inferred values from such analytical modelling sound in the range of the ones publically available. The storage capacity inferred from the above conducted pumping test fall well in the same range of what was considered in previous groundwater studies (van der Westhuizen, 2002a, and the annual model update by AEC (2011, 2012, 2013)) in the catchment. The program RPTSOLV, which is a 2-dimensional numerical model especially designed for estimating the storage coefficient in fractured aquifers, is another alternative method for first estimation of the storage coefficient of the matrix, especially in dual porosity environment. The spatial variability of storage capacity values in the studied area is not of much importance in the present study, and therefore was simplified in the conceptual model as presented in Table 17. These values will be used as first estimation of the storage coefficient.

Table 17: Summary on the aquifers storativity values

Aquifer	Storativity
Weathered aquifer (norite/granite)	$2 * 10^{-3}$
Fractured aquifer (norite/granite)	$3 * 10^{-4}$
Faults	$1 * 10^{-4}$

7.2.4.3 Recharge

All previous numerical models developed for the area, consider a constant recharge value. This was calculated either from one borehole, or from the average (Harmonic mean) of multiple estimations from different points. The spatial variability in the recharge rates is of interest in the present study. The recharge rates (Count: 142) as calculated across the catchment, are used for the modelling of the aquifers. 50% of the estimated recharge rates are below 5 mm/year, and less than 10% are above 15 mm/year (Figure 71 and Figure 74). As for the considered hydraulic conductivity values, the estimated recharge rates are likely to be more representative of the fractured networks intersected by the boreholes used for their estimation.

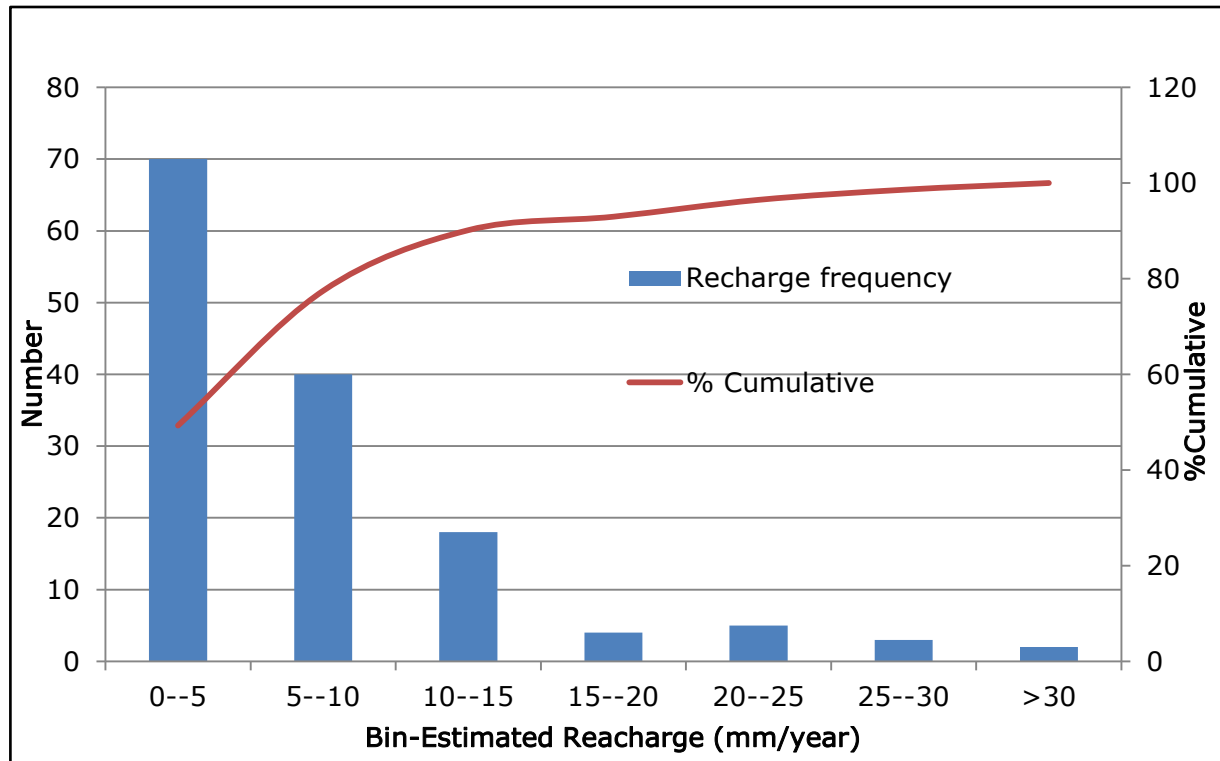


Figure 74: Frequency distribution of estimated recharge using Chloride Mass Balance method

We assumed that the recharge rates estimated are effective, and have already overcome the effect of evapotranspiration losses from the groundwater systems.

7.3 Numerical model

Three numerical models were constructed to represent the conceptual groundwater system of the study area as presented above using 03 different numerical groundwater modelling software packages. The purpose of these is to compare the capabilities of selected software in accounting heterogeneities for determining the potential impacts (dewatering and pollution) from mining of PGE of the Platreef, on the groundwater regime of the area.

7.3.1 Software codes

The appropriate modelling code and GUI to be selected should have the capability to adequately represent the essential features and flow processes of the groundwater system being studied. Main factors that need to be considered when selecting an appropriate modelling code are:

- Capability of the model to represent the conceptual model features
- Importance of gradients (horizontal, vertical)
- The type of flow system (Saturated and/or unsaturated)
- Importance of density-dependent flow
- The type of aquifer system (equivalent porous medium, fractured, and/or solutioned media)
- Finite difference or finite element model
- Available and level application of modelling features
- Cost
- End-user requirements

The codes selected for conducting the modelling of the study area are all commercially available and widely distributed. In the present study, they are assessed based on their respective capabilities in handling heterogeneities.

The 03 numerical Software models that have been selected to be assessed are:

- a) Processing MODFLOW Pro 2005: Originally developed by the US Geological Survey (McDonald and Harbaugh, 1996). MODFLOW is the industry-leading public domain numerical flow model, although it shows some limitations for some modelling study. The code has been verified against many analytical solutions, and has been used to successfully simulate a wide range of hydrogeological systems across the world, the source code is in the public domain and there are several relatively cheap or free (Processing MODFLOW for Windows PMW) GUIs available. There are also several text books that detail modelling methodologies with MODFLOW (notably Anderson and Woessner, 1992), and there are regular conferences held in the USA on MODFLOW projects.
- b) FEFLOW 6.1: This software is developed since 1979 by the WASY Institute for Water Resources Planning and Systems Research Ltd (Germany), and is has been continuously improved. It is an interactive groundwater modelling system for three and two-dimensional, areal and cross-sectional, fluid density-coupled, thermohaline or uncoupled, variably saturated, transient or steady state flow, mass and heat transport in subsurface water resources with or without one or

multiple free surfaces. The software is known worldwide as an efficient groundwater-modelling tool at universities, research institutes, government offices, and engineering and environmental companies.

- c) **SPRING 4: Simulation of Processes in Groundwater (SPRING)** was initially developed by the Ruhr University of Bochum, and allows for the calculation of three-dimensional groundwater flow, surface water hydrology, heat and contaminant transport models. The software has been proven for more than 37 years, especially in Europe.

7.3.2 Model area and boundaries conditions

A model boundary is the interface between the modelled area and the surrounding environment, and conditions on the boundaries have to be specified. Boundaries occur at the edges of the modelled area and at locations in the modelled area where external influences are represented, such as rivers; wells; and leaky impoundments.

The conceptual model and the hydrogeological framework data are used together to define the boundary conditions. The hydrogeological stresses are known to provide the temporal and spatial data for the solution of the hydraulic equation, and also help in completing the definition of the boundary condition.

Primary criteria for selecting hydraulic boundary conditions are topography, hydrology, geology, and observed groundwater drainage pattern. The topography, geology, or both, may yield boundaries such as impermeable strata or potentiometric surface controlled by surface water, or recharge/discharge areas such as inflow boundaries along mountain ranges. The groundwater flow system allows the specification of boundaries in situations where natural boundaries are a great distance away. Boundary conditions may vary with time. The topography, hydrology, and groundwater drainage were mainly used in the identification of the lateral boundary, whereas available geology and hydrogeology information were used for the aquifer layer thickness. Boundaries in groundwater models have been specified as (Figure 75):

- Dirichlet (constant head) boundary condition was set along the Mogalakwena River on the western boundary.

- All other external boundaries coincide with quaternary catchment boundary and are therefore considered as no-flow boundaries (Neumann (or specified flux=0) boundary conditions;
- Non-perennial tributary streams of the Mogalakwena Rivier (Groot-Sandsloot River, Mohlosane River, and Wit River) were considered in the model as Cauchy (3rd-kind conditions or a combination of Dirichlet and Neuman) boundaries;

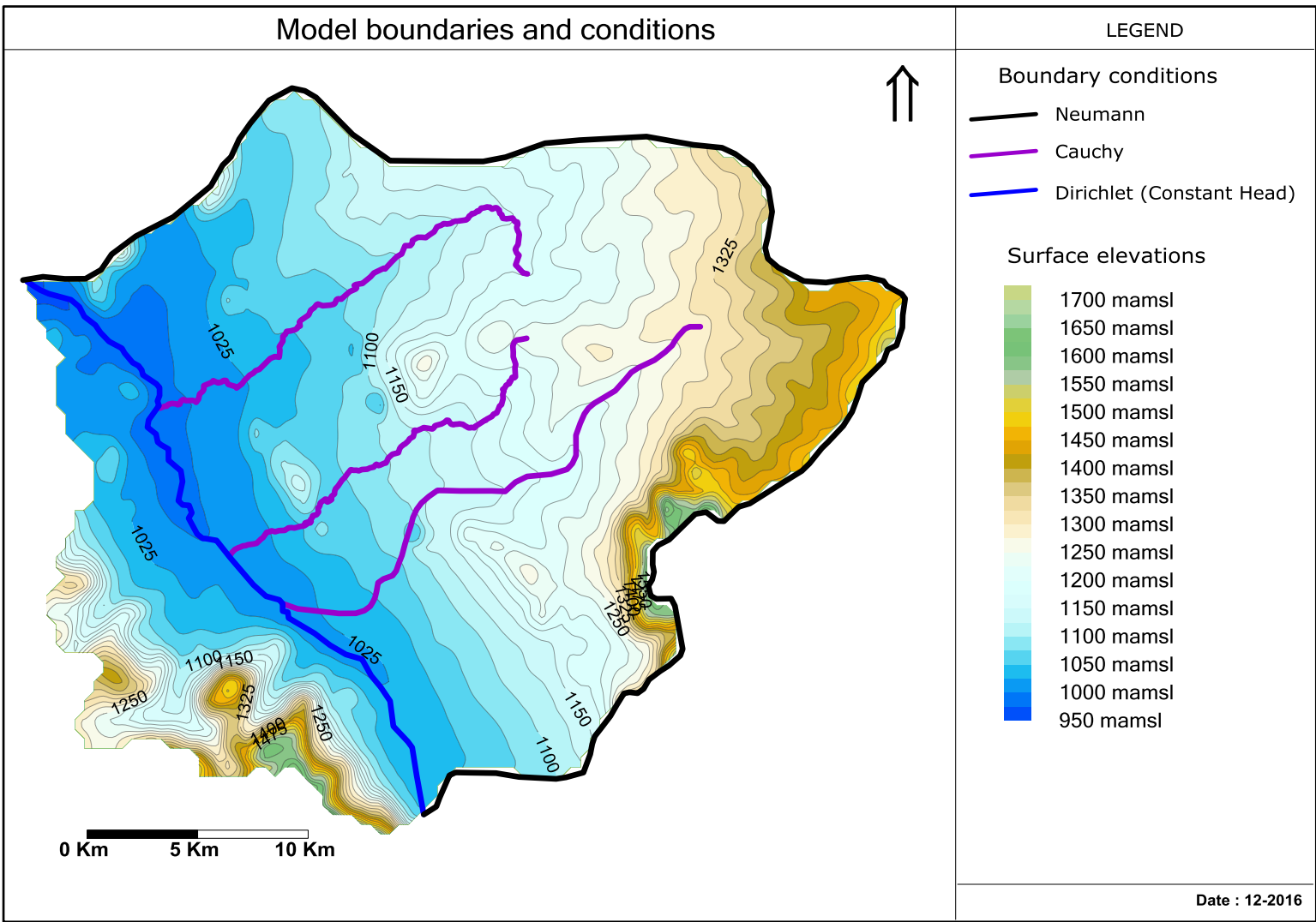


Figure 75: Numerical models boundary conditions

7.3.3 Discretisation of the Model Area

After the definition of boundary conditions, suitable mesh or grid was developed for the aquifer. In Processing MODFLOW Pro, the grid (mesh) is constructed with "finite differences", whereas "finite elements" are used in the SPRING and FEFLOW.

The generations of finite elements (FEFLOW, and SPRING) were not straight forward. Computational difficulties were faced, due to the very well connected nature of the fractures populations in the model. Larger (and longeur) fractures in the population were prioritize at the phase of finite element generations, and variable transmissivity technic was used for individual fractures.

All the models consist of two layers with constant thicknesses of 50 m for the weathered aquifer and 100 m for the fractured rock aquifer. In real word however, the thicknesses are surely not constant. This uncertainty in the quantification of the aquifers thicknesses is to be compensated for, by adjustment of the hydraulic conductivity values during model calibration.

7.3.3.1 MODFLOW

Finite differences divide the aquifer into a rectangular grid of nodes defining the corners or the centres of model cells. The mesh constructed for the model consisted of 465 rows and 525 columns. The horizontal extent of the model chosen was large enough to avoid boundary effects (43000 m x 37000 m). The sizes of the cells vary from 100 m x 100 m outside the domain of concern, to 10 m x 10 m within the domain of the target site. Special attention was given to the grid expansion factor (ratio of larger to smaller adjacent nodal spacing) to do not exceed 1.5.

The coordinates for the modelled area are from 675058, 7363796 (Min x, Max y) to 717558, 7327296 (Max x, Min y). The interpolated groundwater elevations were used to define the top of the first layer, which is unconfined.

7.3.3.2 FEFLOW

Finite elements divide the aquifer into a mesh of node points forming polygonal (triangular) cells, with which special head and flux boundaries were aligned. A finite element network (grid) was designed to provide a high resolution of the numerical

solution, and to accommodate the model area. FEFLOW pre-processing software allows for the generation of triangular shape grids consisting of 142098 elements, 107616 nodes, and 213840 joint faces. The topographic elevations were used for the elevations of the top slice. 3D-views of the modelling area are given in Figure 76 and Figure 77.

The positions of the different internal boundary, TSF's, and high conductive features (faults and fractures along dykes and others lineaments) as characterised above, were incorporated in the modelling grid. 2930 joint faces were used to incorporate selected high conductive features.

The construction of finite element mesh in FEFLOW is first designed in the Supermesh, where: outer model boundary, geometrical features, areas, courses of rivers are defined with points, lines, and polygones upon which boundary conditions or material properties may be assigned.

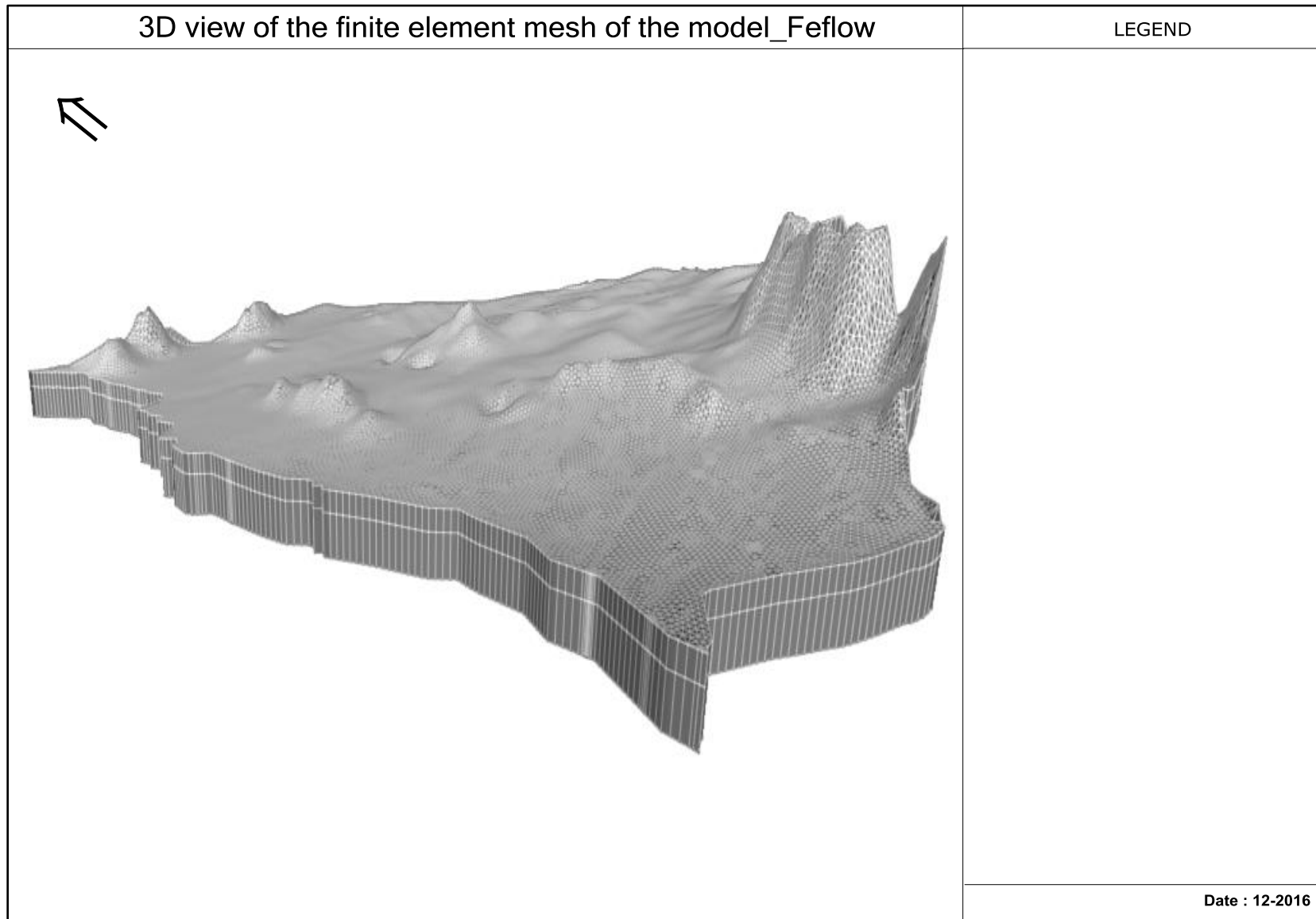


Figure 76: 3D view of the aquifer geometry build from Finite Element Mesh in FEFLOW.

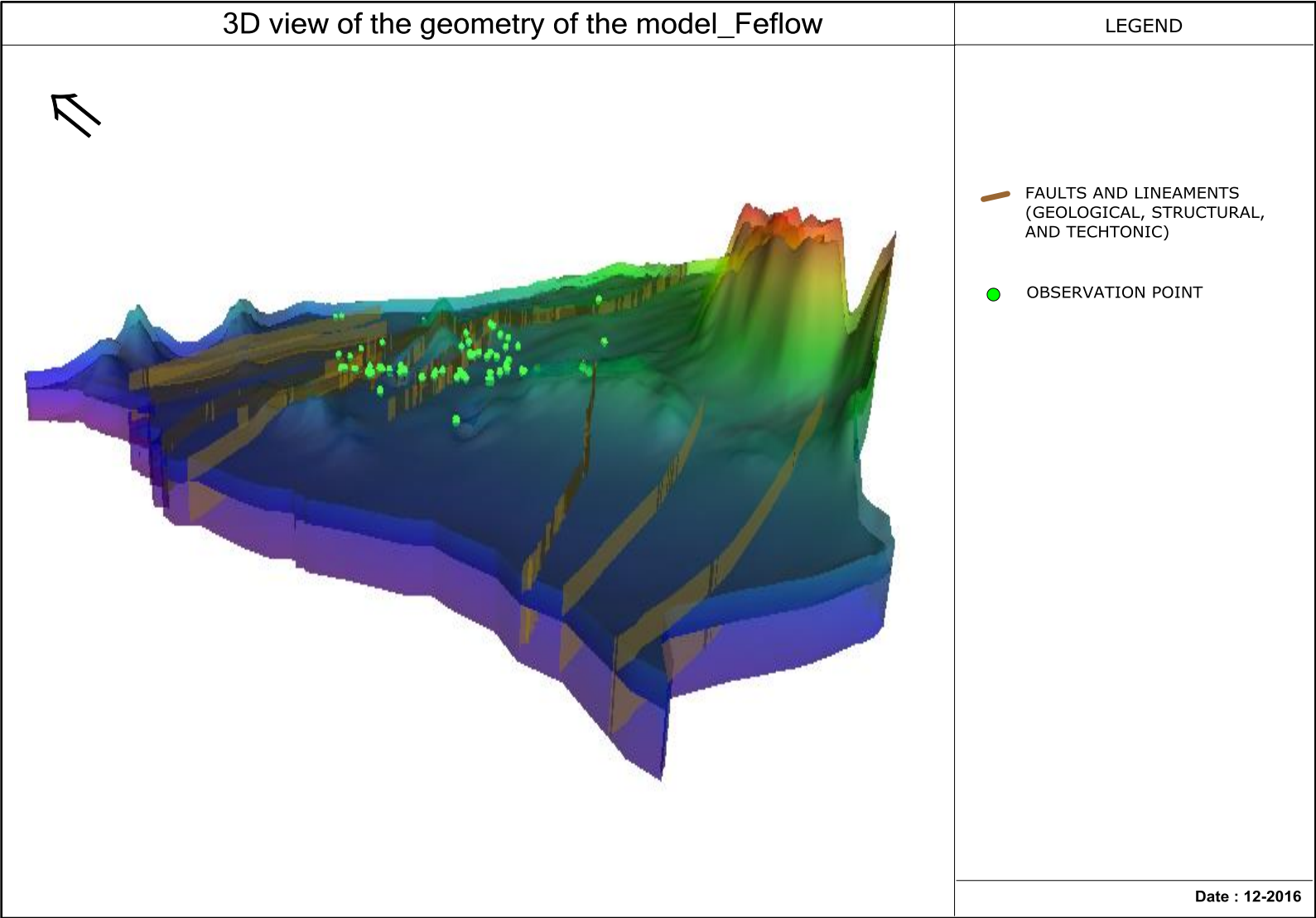


Figure 77: 3D view of the aquifer geometry build from Finite Element Mesh in FEFLOW

7.3.3.3 SPRING

Although the model grid is formed of finite elements, we attract the attention that in SPRING the systematic building of the model mesh follows a longer sequential approach than in FEFLOW.

Raw data have to firstly be transformed into structures. Relevant structures become contours which are used to create nodes that will form the elements of the mesh of the model. Spring pre-processing software allows for the generation of triangular shape grids consisting of 534 structures, 441 contours, 91578 nodes, and 7796 elements and special features (fractures, etc.).

A very interesting point in construction of the model geometry, using SPRING pre-processing software, is that the 3D settings are only allowed after assignment of aquifer flow parameters of 2D

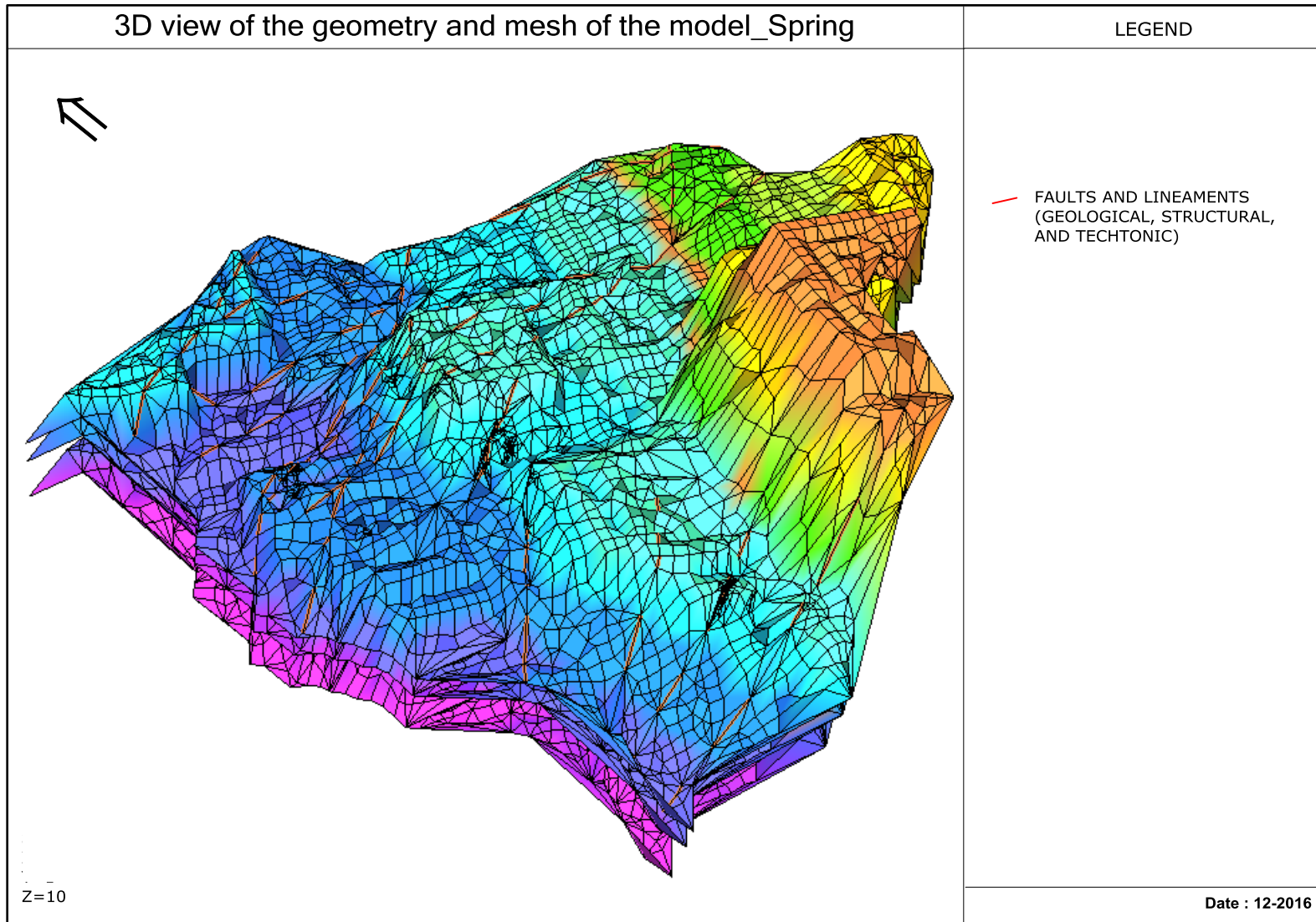


Figure 78: 3D view of the aquifer geometry and mesh build from Finite Element Mesh in SPRING

7.3.4 Numerical Flow Model

A steady state groundwater flow model was constructed to simulate undisturbed groundwater heads distribution, based on the generalised steady state conditions, groundwater flow equation as follows:

$$\frac{\partial}{\partial x} \left(K_x \frac{\partial h}{\partial x} \right) + \frac{\partial}{\partial y} \left(K_y \frac{\partial h}{\partial y} \right) + \frac{\partial}{\partial z} \left(K_z \frac{\partial h}{\partial z} \right) \pm W = 0 \quad \dots \dots (149)$$

Where: h is the hydraulic head; $K_x, K_y, \text{ and } K_z$ represent the hydraulic Conductivity; t is the time ; and W is the source (recharge) or sink (pumping) per unit area.

These conditions serve as initial heads for the transient simulations of groundwater flow, in which changes with time are simulated, using the three-dimensional groundwater flow model equation. The 03 software packages used for simulations in the present modelling study are based on three-dimensional groundwater flow and may be described by the following equation:

$$\frac{\partial}{\partial x} \left(K_x \frac{\partial h}{\partial x} \right) + \frac{\partial}{\partial y} \left(K_y \frac{\partial h}{\partial y} \right) + \frac{\partial}{\partial z} \left(K_z \frac{\partial h}{\partial z} \right) \pm W = S \frac{\partial h}{\partial t} \quad \dots \dots (150)$$

Where: S is the storage coefficient; t is the time; and W is the source (recharge) or sink (pumping) per unit area.

7.3.5 Models Hydraulic properties

7.3.5.1 Initial Hydraulic Heads

The grip of Bayesian interpolated groundwater elevations was used to set initial hydraulic head condition for Processing MODFLOW Pro. The initial head conditions were interpolated from the measured groundwater levels using the Akuna, and the Gaussian techniques for FEFLOW and SPRING respectively. The same hydraulic heads apply for both model layers.

7.3.5.2 Hydraulic conductivity

Figure 79 and Figure 80 show the different variogram plots (experimental and model) of the available hydraulic conductivity values. Specific information that can be expected

from such available field parameters, for the definition of the single domain stochastic model are summarized in Table 18. These parameters were then used for the generation of multiples geostatistical correlated fields of the first layer which serve in the steady state calibration of the models. The conductivity values of the second layer and the vertical hydraulic conductivity values were grouped to the values of the first layer by factors of 0.5 and 0.1 respectively.

The faults were given a constant hydraulic conductivity of 4 m/day, and the minor groundwater flow associated with dykes was given a constant hydraulic conductivity value of 1 m/day.

Table 18: Inferred statics and stochastic parameters from spatial conductivity

Model Variogram	Mean Log(k)	Average	Standard deviation Log(k)	Correlation length (Slope)	Anisotropy ratio	Anisotropy angle
Wet boreholes	0.72	21.17	0.90	0.15	2	145.90
Wet and dry boreholes	-0.49	15.29	2.17	0.16	2	140.80

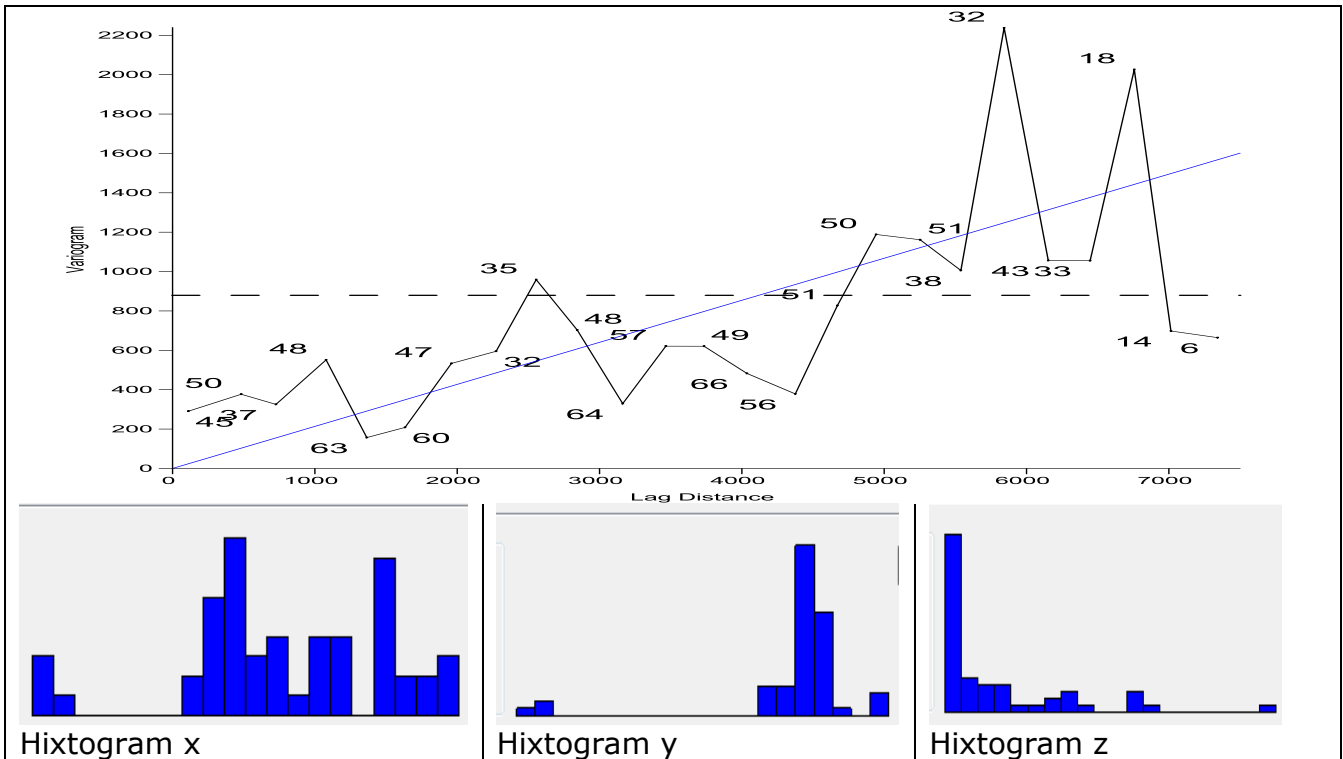


Figure 79: Experimental (black) and linear model (blue) variogram of the available conductivity without dry boreholes

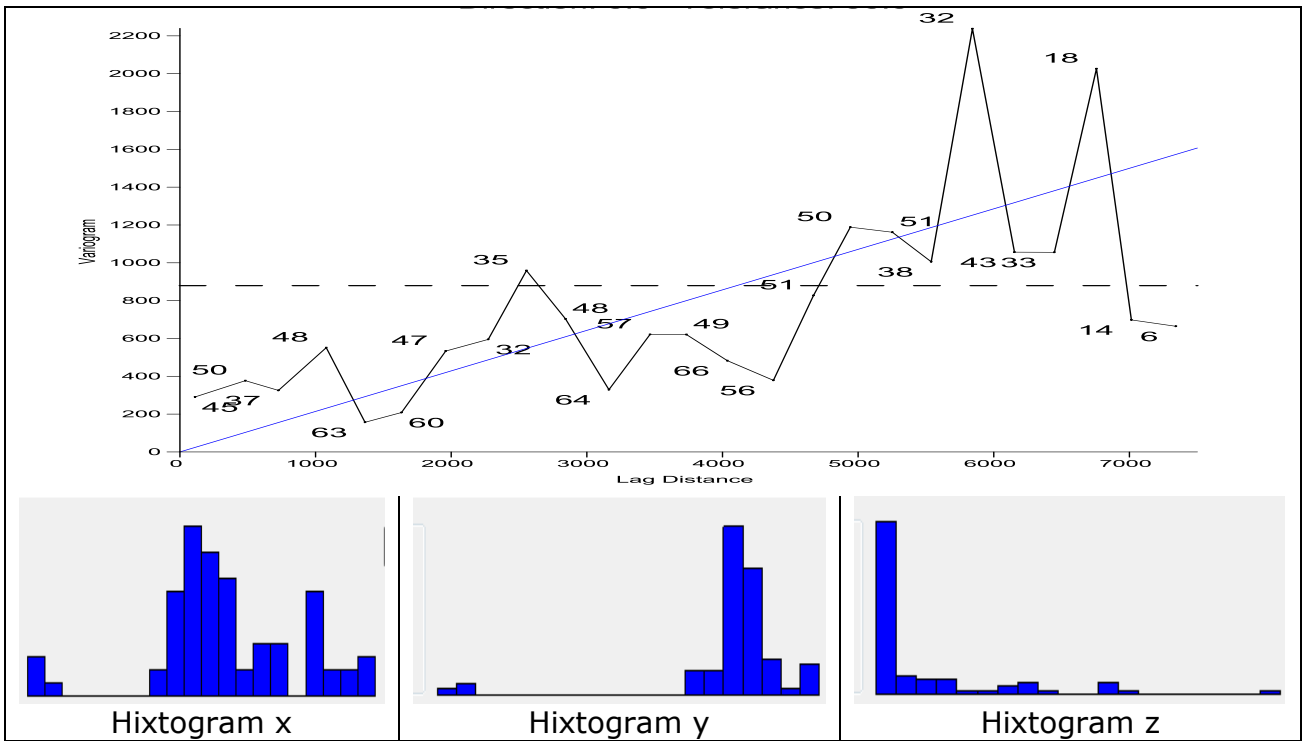


Figure 80: Experimental and linear model variogram of the available conductivity with dry drilled boreholes

7.3.5.3 Recharge

Figure 81 shows the variogram (experimental and model) plot of the available recharge rates. Unlike the hydraulic conductivity values which variogram was characterised by a linear variogram model, the variogram of the recharge rates is characterised by a logarithmic variogram model. Table 19 summarises the parameters that are used for the generation of fields of recharge rates used in the calibration of the models.

Table 19: Inferred statics and stochastic parameters from spatial Recharges

Mean Log(k)	Average	Standard deviation Log(k)	Correlation length (Slope)	Anisotropy ratio
0.73	7.42	0.03	9.38×10^{-8}	2

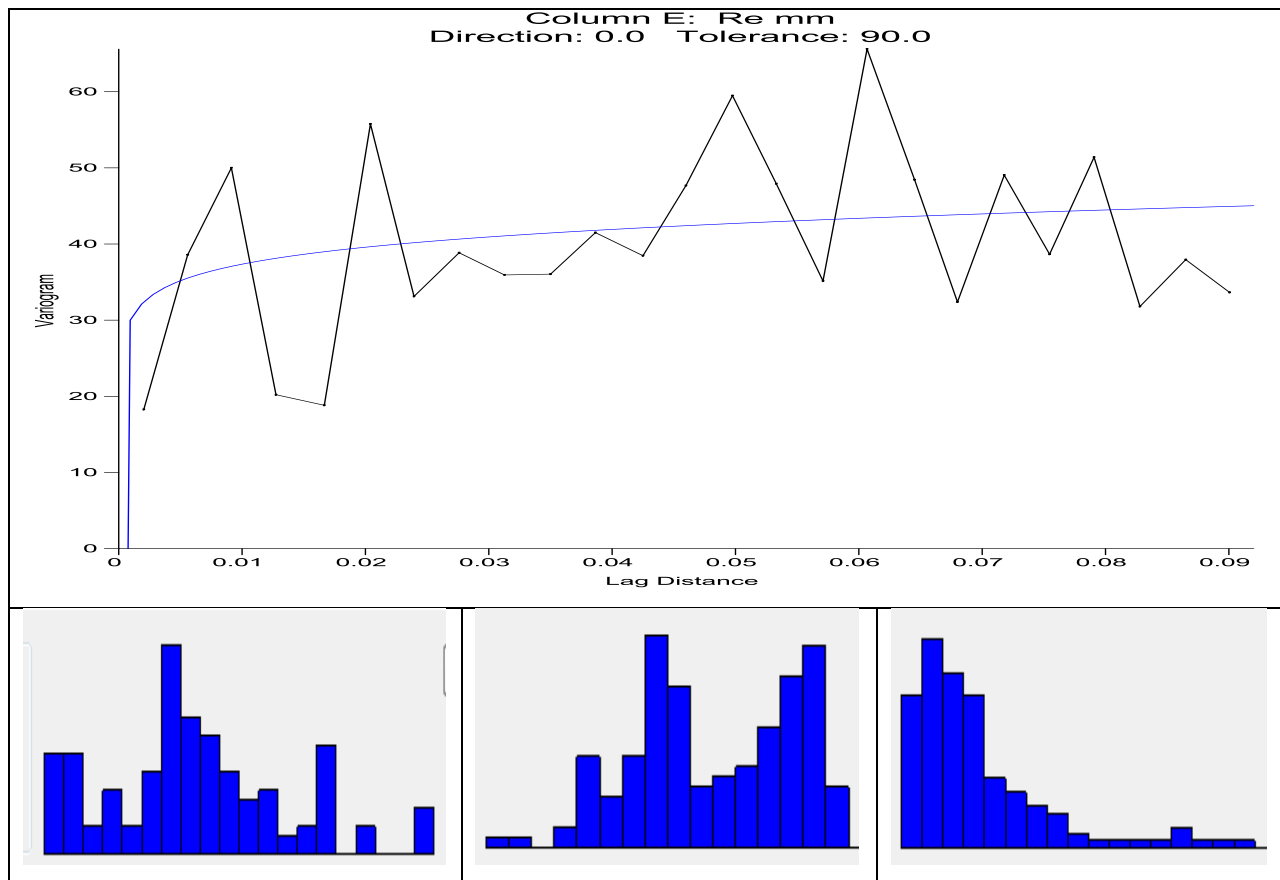


Figure 81: Experimental and linear model variogram of the available recharge rates

7.3.6 Calibrations of Steady state flow models, and model errors

Widely used methodology (Spitz and Moreno., 1996; and ASTM) was followed for calibration of the model. The model was calibrated using groundwater levels collected during the hydrocensus. Figure 82 shows the locations of boreholes used for calibration purposes.

Steady state calibration was accomplished by varying the generated fields for hydraulic conductivity values and also for the recharge rates, until a reasonable match between the measured groundwater elevations and the simulated groundwater elevations was obtained. Figure 83, Figure 84, and Figure 85 show the simulated hydraulic heads for the steady state calibration of the respective models. The generated hydraulic conductivity fields assigned to the weathered aquifer for the best match between measured and simulated elevations are presented in Figure 86 to Figure 88. At the best fit (calibration) between measured and simulated, Faults were assigned a hydraulic conductivity of 5 m/day, Lithological contacts were assigned a hydraulic conductivity value of 3 m/day, and the Dykes were assigned a value of 1 m/day.

The residual (difference) between the simulated and the observed hydraulic head was calculated for each observation borehole (Table 20, Table 21, and Table 22). Three common methods were used to assess the error in the model calibration: (a) the residual mean error (ME), (b) the residual mean absolute error (MAE), and (c) the residual root mean squared (RMS) error. A small ME is not necessarily an indication of a good calibration, because negative and positive residuals can cancel each other out, resulting in a small ME. The MAE addresses this as the mean of the absolute value of the differences in measured and simulated water levels. The RMS error is the ratio to the total water level change across the model domain (Anderson and Woessner, 1992). The RMS error is the average of the squared differences in measured and simulated water levels. If the ratio is small, the errors are only a small part of the overall model response.

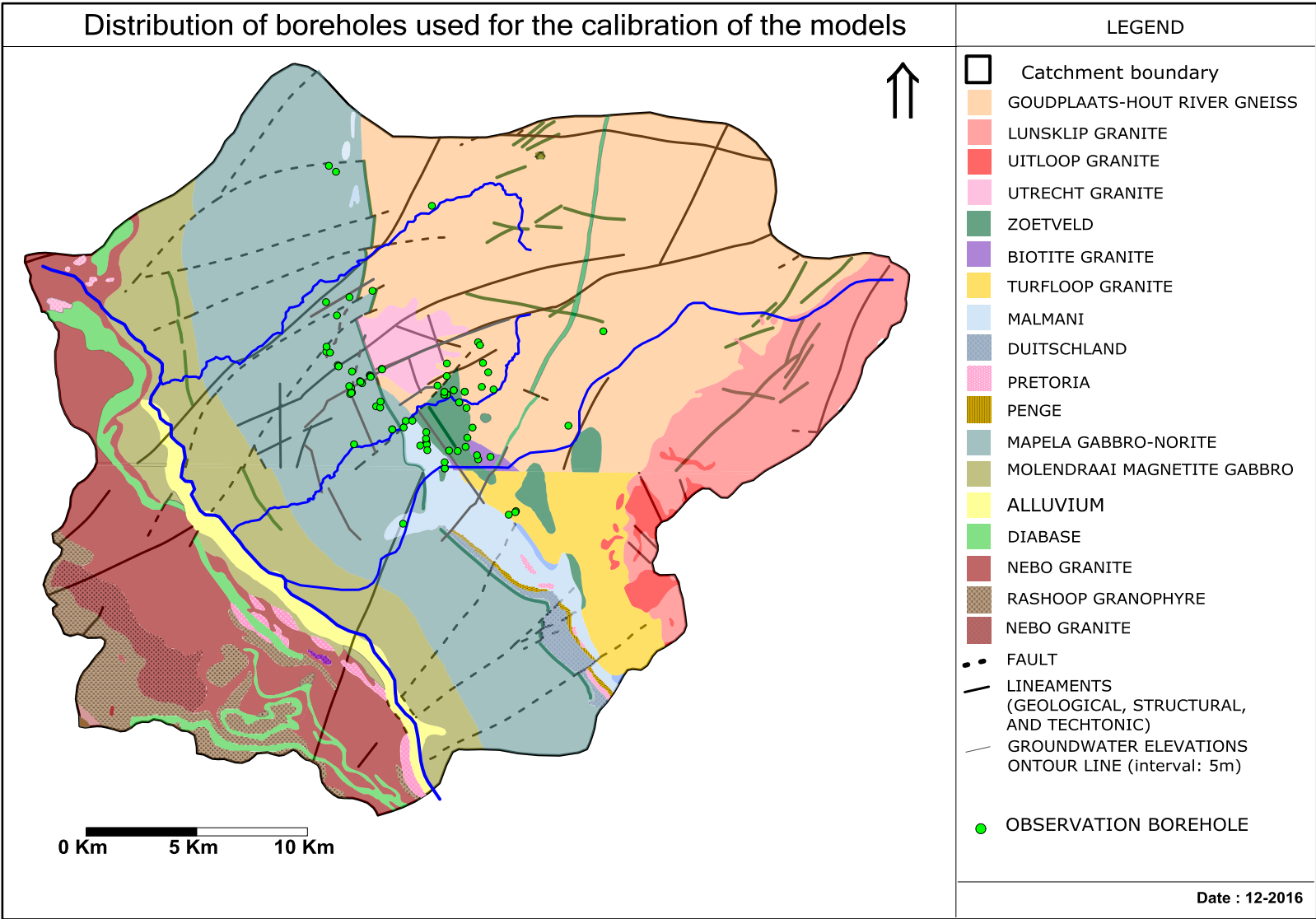


Figure 82: Locations of the boreholes used for the calibration of the steady state models.

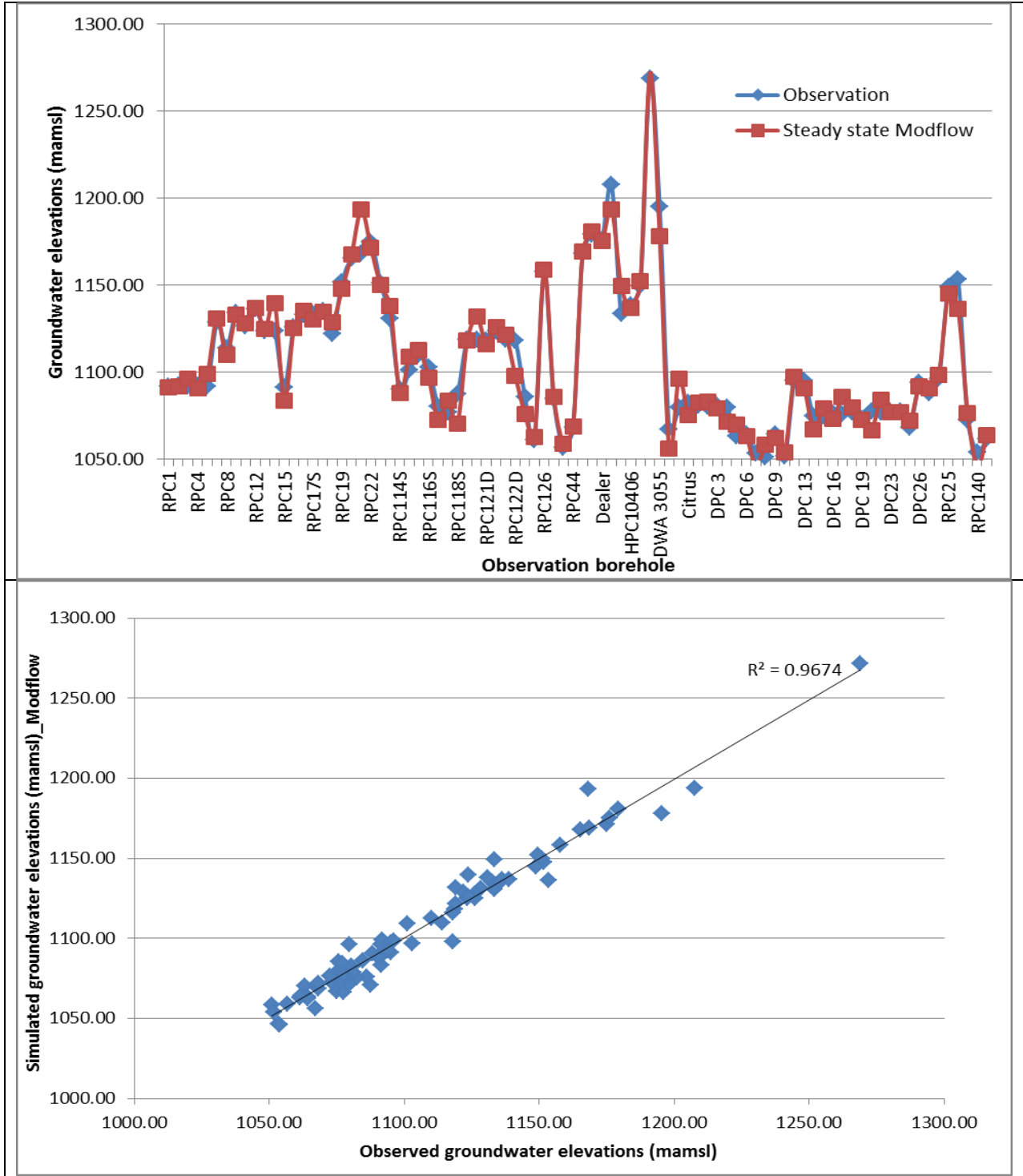


Figure 83: Observed groundwater elevations versus simulated elevations MODFLOW

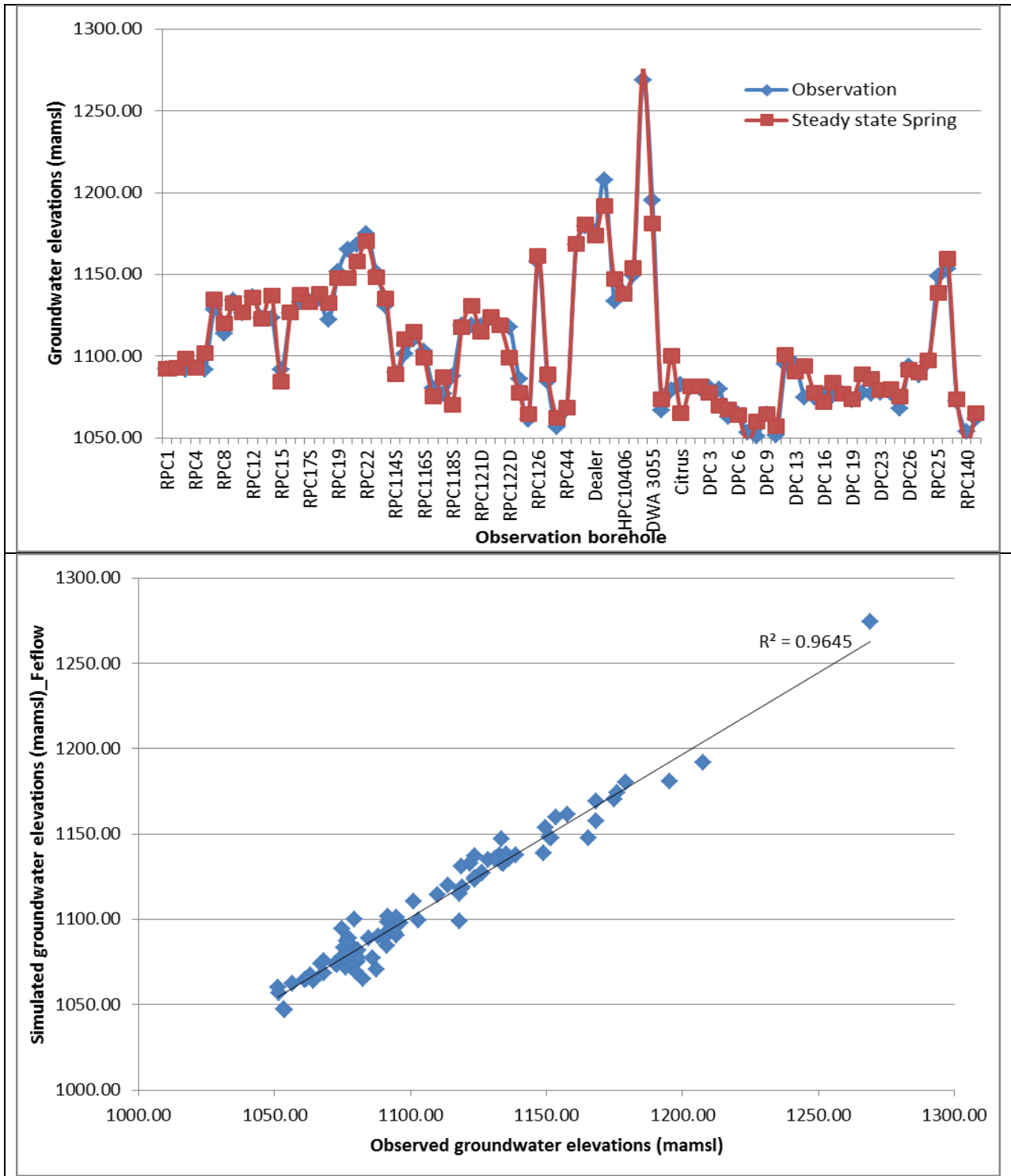


Figure 84: Observed groundwater elevations versus simulated elevations FEFLOW

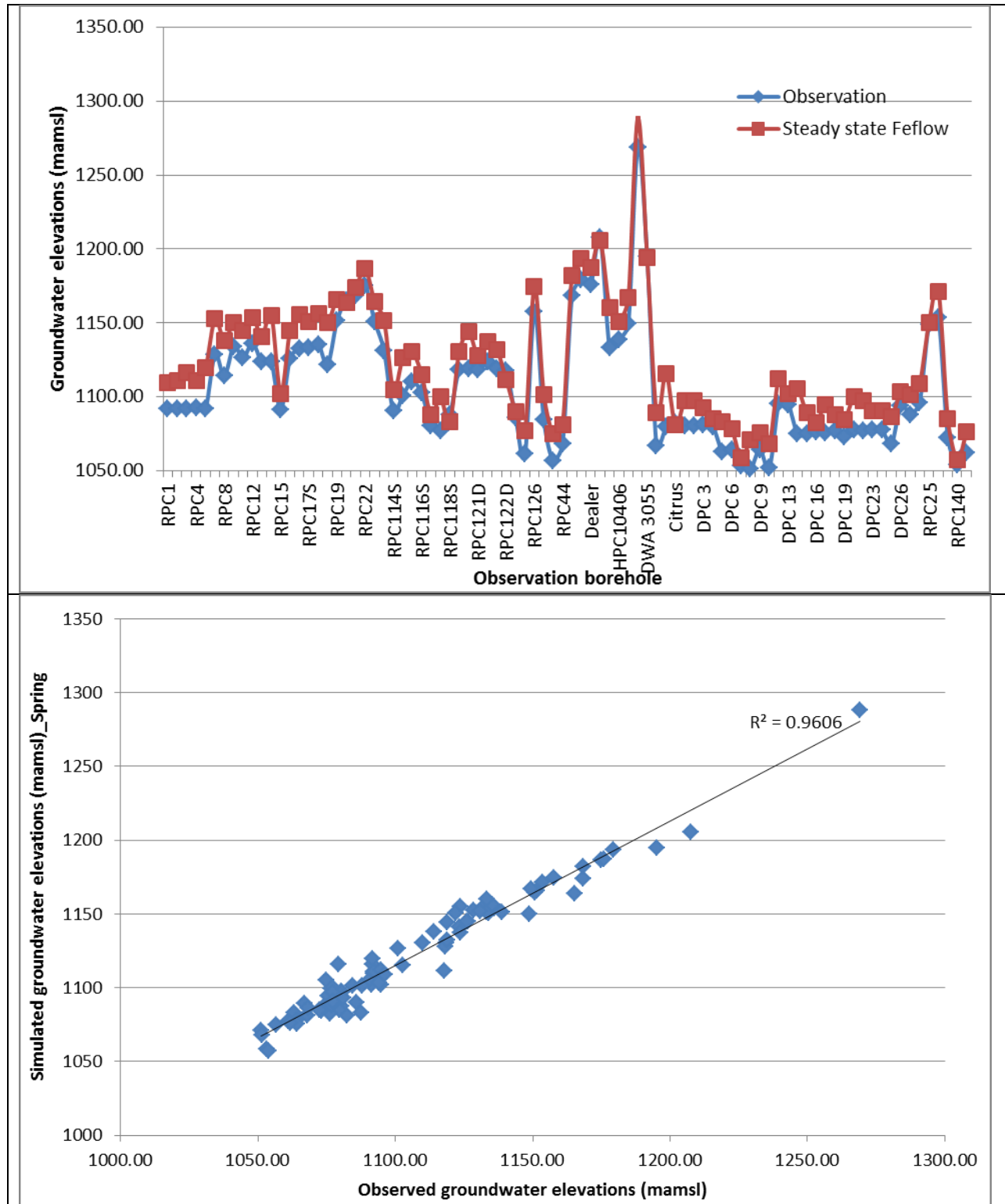


Figure 85: Observed groundwater elevations versus simulated elevations SPRING

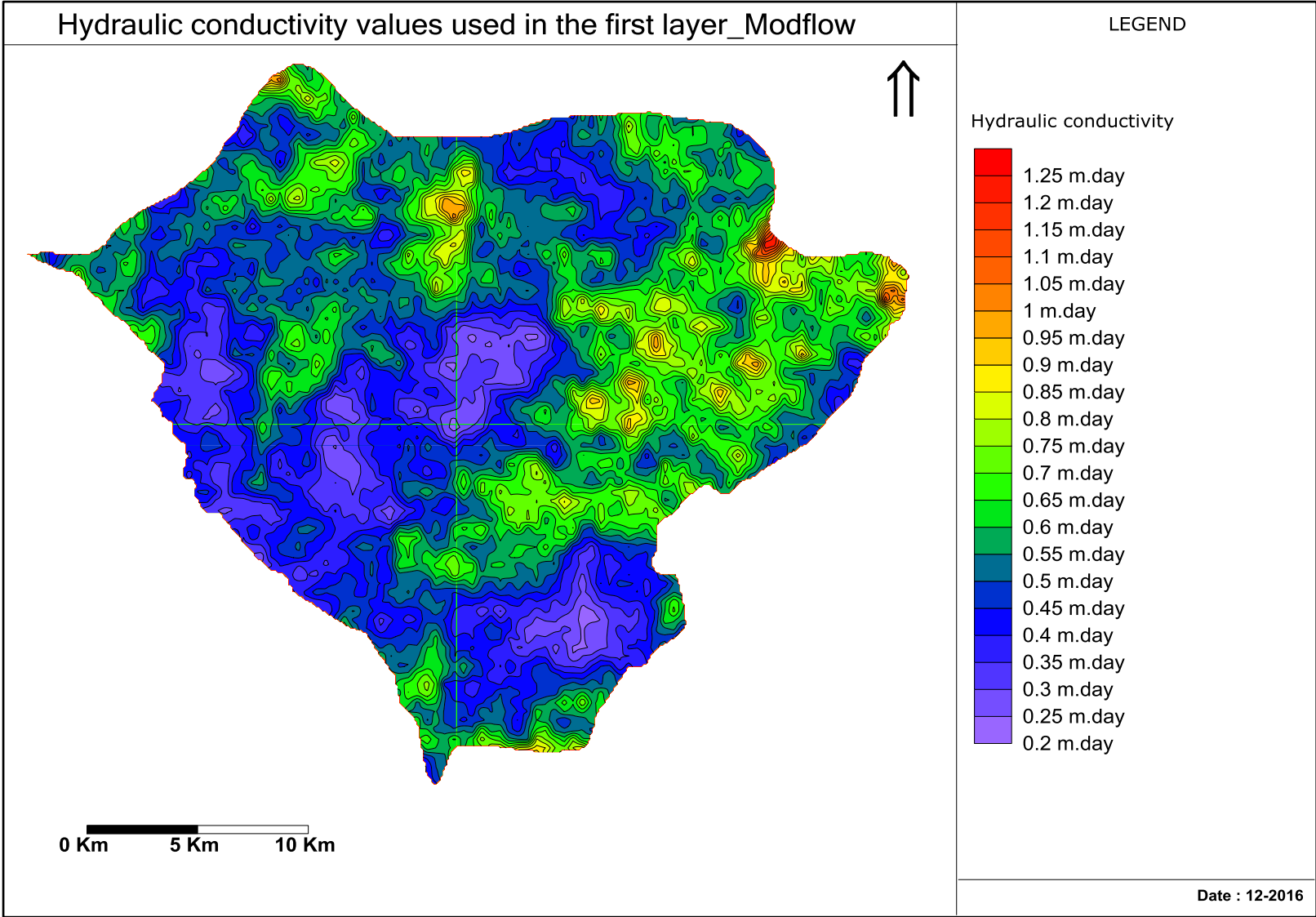


Figure 86: Hydraulic conductivity values used for the calibration in MODFLOW

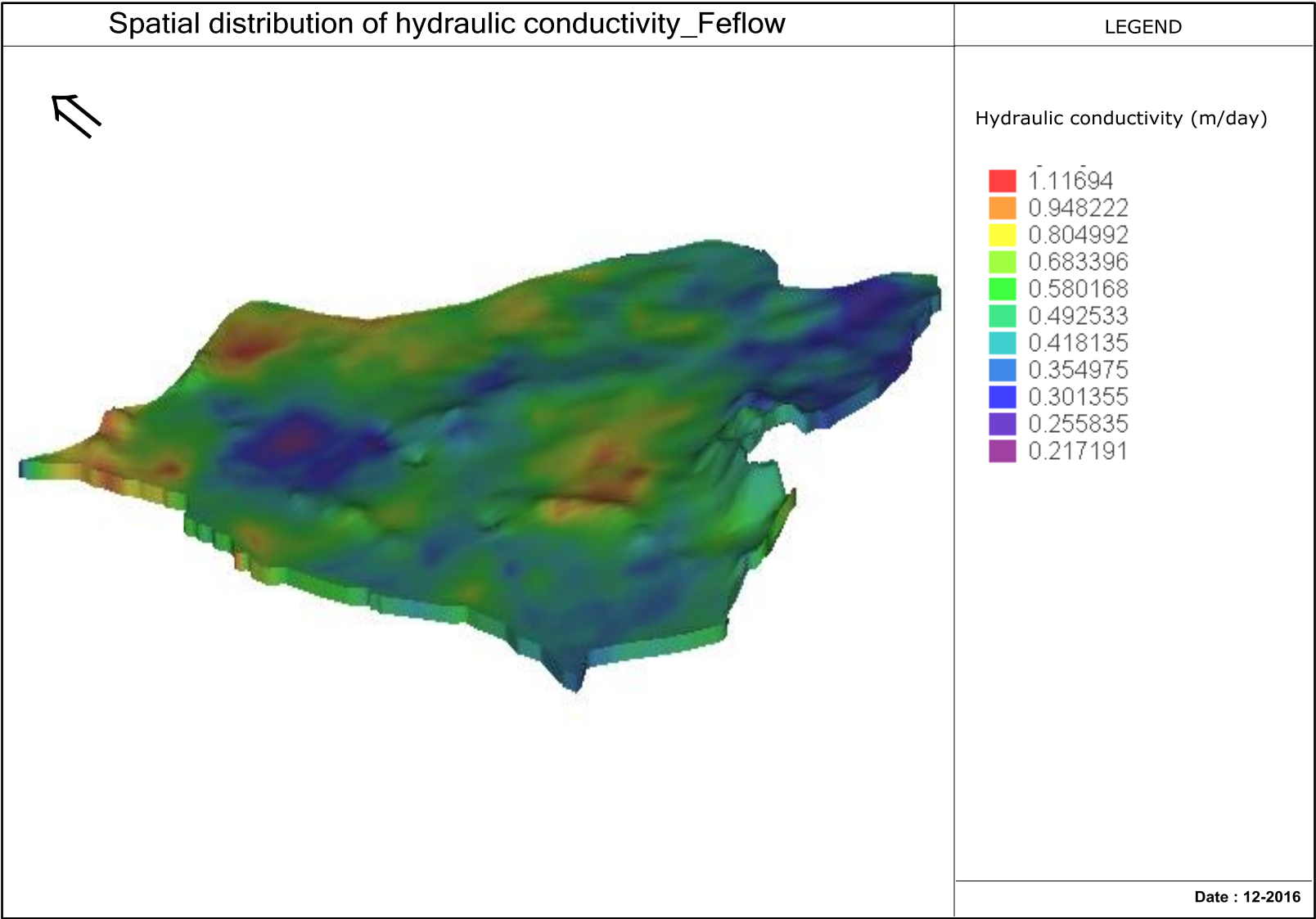


Figure 87: Hydraulic conductivity values used for the calibration in FEFLOW

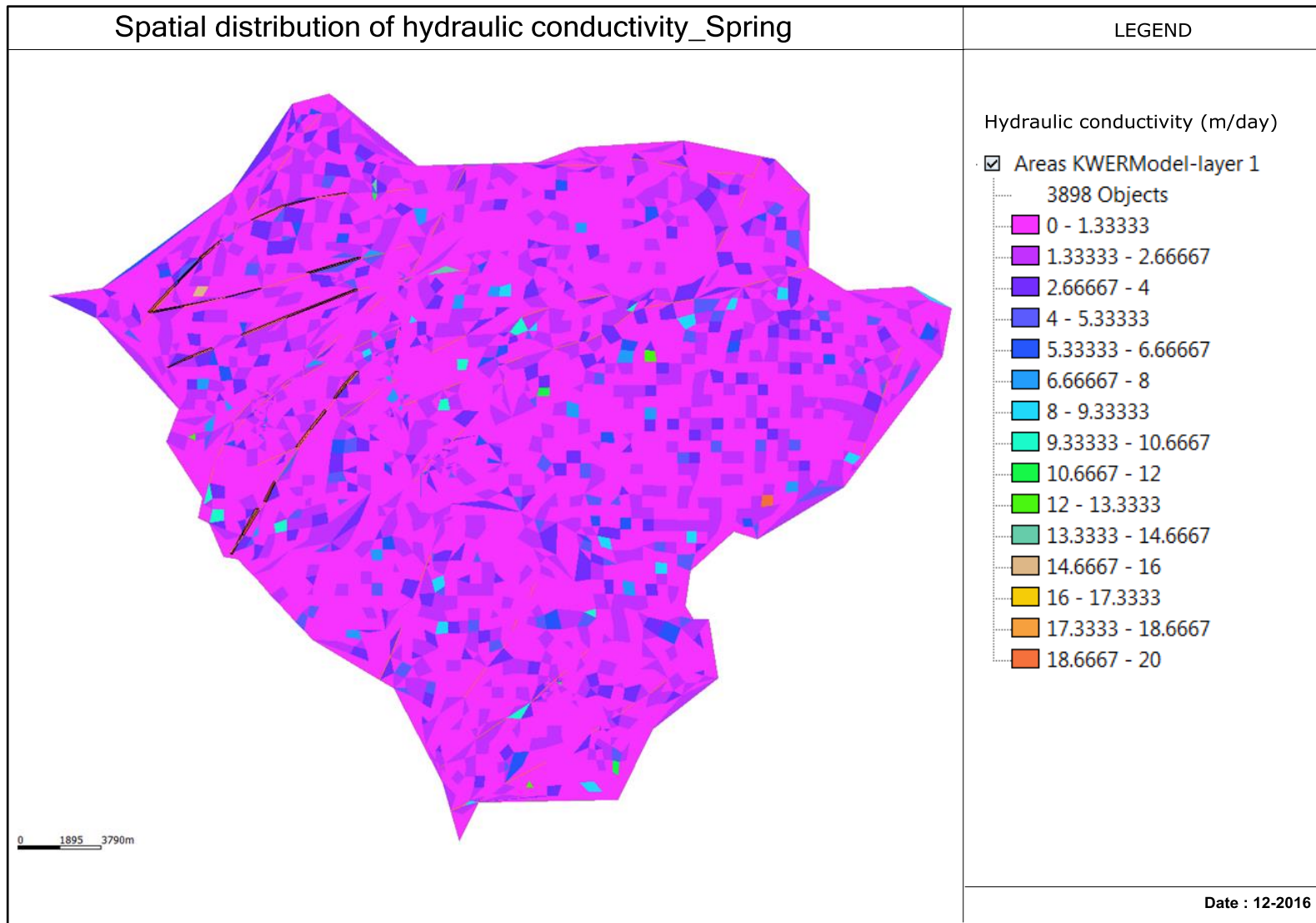


Figure 88: Hydraulic conductivity values used for the calibration in SPRING

These errors were calculated for each Model as follow:

$$ME = \frac{\sum_i^n (h_{obs} - h_{sim})}{n} \quad (151)$$

$$MAE = \frac{\left| \sum_i^n (h_{obs} - h_{sim}) \right|}{n} \quad (152)$$

$$RMS = \frac{\left(\sum_i^n (h_{obs} - h_m) \right)^2}{n} \quad (153)$$

n is the number of observations considered for calibration; h_{obs} is the measured hydraulic head; and h_{sim} is the simulated hydraulic head.

Calculated Errors for the data set from each Model are presented from Table 20 to Table 22. The Mean calculated Mean error vary between -14.92 and 0.045 m for the data of the 03 Models. The Mean Absolute Error for the data, vary between 5.63 and 15.63 .

Table 20: Calculated errors for the calibrated model in MODFLOW

Borehole	Observed elevations	Simulated elevations	$(h_{obs} - h_{sim})$	$ (h_{obs} - h_{sim}) $	$(h_{obs} - h_m)^2$
	mamsl	mamsl	m	m	m
RPC1	1092.056	1091.056	1.000	1.000	1.000
RPC2	1092.132	1091.632	0.500	0.500	0.250
RPC3	1091.56	1096.36	-4.800	4.800	23.040
RPC4	1092.548	1090.548	2.000	2.000	4.000
RPC5	1091.82	1098.82	-7.000	7.000	49.000
RPC7	1128.479	1130.979	-2.500	2.500	6.250
RPC8	1113.949	1109.949	4.000	4.000	16.000
RPC10	1134.059	1132.859	1.200	1.200	1.440
RPC11	1126.3	1127.9	-1.600	1.600	2.560
RPC12	1136.202	1137.002	-0.800	0.800	0.640
RPC13	1123.496	1124.996	-1.500	1.500	2.250
RPC13S	1123.528	1139.528	-16.000	16.000	256.000
RPC15	1091.507	1083.507	8.000	8.000	64.000
RPC16	1126.038	1125.238	0.800	0.800	0.640
RPC17D	1132.778	1135.378	-2.600	2.600	6.760
RPC17S	1133.431	1130.431	3.000	3.000	9.000
RPC18S	1135.407	1134.907	0.500	0.500	0.250
RPC18D	1122.045	1128.845	-6.800	6.800	46.240
RPC19	1151.636	1147.636	4.000	4.000	16.000
RPC20	1165.326	1167.826	-2.500	2.500	6.250
RPC21	1168.275	1193.275	-25.000	25.000	625.000

Borehole	Observed elevations	Simulated elevations	$(h_{obs} - h_{sim})$	$ (h_{obs} - h_{sim}) $	$(h_{obs} - h_m)^2$
	mamsl	mamsl	m	m	m
RPC22	1175.011	1171.511	3.500	3.500	12.250
RPC23D	1150.99	1149.99	1.000	1.000	1.000
RPC24	1130.87	1137.87	-7.000	7.000	49.000
RPC114S	1090.246	1088.046	2.200	2.200	4.840
RPC115S	1101.037	1109.037	-8.000	8.000	64.000
RPC115D	1110.098	1112.598	-2.500	2.500	6.250
RPC116S	1102.791	1096.791	6.000	6.000	36.000
RPC117	1080.316	1072.316	8.000	8.000	64.000
RPC118	1076.693	1083.693	-7.000	7.000	49.000
RPC118S	1087.581	1070.581	17.000	17.000	289.000
RPC120D	1118.62	1118.12	0.500	0.500	0.250
RPC120S	1118.896	1131.896	-13.000	13.000	169.000
RPC121D	1118.149	1116.149	2.000	2.000	4.000
RPC121S	1123.602	1126.102	-2.500	2.500	6.250
RPC122S	1118.992	1121.492	-2.500	2.500	6.250
RPC122D	1117.938	1097.938	20.000	20.000	400.000
RPC124	1086	1076	10.000	10.000	100.000
RPC125	1061.22	1062.82	-1.600	1.600	2.560
RPC126	1157.77	1158.57	-0.800	0.800	0.640
RPC127	1084.52	1086.02	-1.500	1.500	2.250
RPC128	1056.58	1059.08	-2.500	2.500	6.250
RPC44	1068.03	1068.53	-0.500	0.500	0.250

Borehole	Observed elevations	Simulated elevations	$(h_{obs} - h_{sim})$	$ (h_{obs} - h_{sim}) $	$(h_{obs} - h_m)^2$
	mamsl	mamsl	m	m	m
SRK5S	1168.32	1169.12	-0.800	0.800	0.640
Machikiri	1179.34	1180.94	-1.600	1.600	2.560
Dealer	1176.118	1175.118	1.000	1.000	1.000
HPC10057	1207.591	1193.591	14.000	14.000	196.000
HPC10364	1133.457	1149.457	-16.000	16.000	256.000
HPC10406	1138.694	1136.694	2.000	2.000	4.000
HPC10319	1149.509	1152.009	-2.500	2.500	6.250
RBK 402	1268.974	1271.474	-2.500	2.500	6.250
DWA 3055	1195.223	1178.223	17.000	17.000	289.000
HO3-2847	1066.938	1055.938	11.000	11.000	121.000
BH W14	1079.457	1096.457	-17.000	17.000	289.000
Citrus	1082.498	1075.498	7.000	7.000	49.000
DPC 1	1080.682	1082.182	-1.500	1.500	2.250
DPC 2	1080.401	1082.901	-2.500	2.500	6.250
DPC 3	1080.908	1078.908	2.000	2.000	4.000
DPC 4	1079.588	1071.588	8.000	8.000	64.000
DPC 5	1063.069	1070.069	-7.000	7.000	49.000
DPC 6	1064.277	1063.277	1.000	1.000	1.000
DPC 7	1053.373	1046.373	7.000	7.000	49.000
DPC 8	1051.146	1058.146	-7.000	7.000	49.000
DPC 9	1064.284	1062.284	2.000	2.000	4.000
DPC 11	1051.642	1054.142	-2.500	2.500	6.250

Borehole	Observed elevations	Simulated elevations	$(h_{obs} - h_{sim})$	$ (h_{obs} - h_{sim}) $	$(h_{obs} - h_m)^2$
	mamsl	mamsl	m	m	m
DPC 12	1094.947	1097.447	-2.500	2.500	6.250
DPC 13	1094.907	1090.907	4.000	4.000	16.000
DPC 14	1074.907	1066.907	8.000	8.000	64.000
DPC 15	1074.904	1078.904	-4.000	4.000	16.000
DPC 16	1076.328	1073.328	3.000	3.000	9.000
DPC 17	1075.663	1085.663	-10.000	10.000	100.000
DPC 18	1076.939	1079.439	-2.500	2.500	6.250
DPC 19	1073.138	1072.538	0.600	0.600	0.360
DPC 21	1077.443	1066.443	11.000	11.000	121.000
DPC22	1077.166	1084.166	-7.000	7.000	49.000
DPC23	1077.752	1076.752	1.000	1.000	1.000
DPC24A	1077.361	1076.861	0.500	0.500	0.250
DPC24	1068.191	1071.991	-3.800	3.800	14.440
DPC26	1094.017	1092.017	2.000	2.000	4.000
DPC27	1088.086	1090.586	-2.500	2.500	6.250
DPC28	1096.097	1098.597	-2.500	2.500	6.250
RPC25	1148.871	1144.871	4.000	4.000	16.000
RPC26	1153.454	1136.454	17.000	17.000	289.000
RPC139	1072.378	1076.378	-4.000	4.000	16.000
RPC140	1053.847	1045.847	8.000	8.000	64.000
RPC141	1061.82147	1064.021	-2.200	2.200	4.840
		$\sum_i^n 0$	3.900	448.700	4674.950

Borehole	Observed elevations	Simulated elevations	$(h_{obs} - h_{sim})$	$ (h_{obs} - h_{sim}) $	$(h_{obs} - h_m)^2$
	mamsl	mamsl	m	m	m
		Errors	ME=0.045	MAE=5.217	RMS=54.360

Table 21: Calculated errors for the calibrated model in FEFLOW

Borehole	Observed elevations	Simulated elevations	$(h_{obs} - h_{sim})$	$ (h_{obs} - h_{sim}) $	$(h_{obs} - h_m)^2$
	mamsl	mamsl	m	m	m
RPC1	1092.056	1109.703	-17.647	17.647	311.406
RPC2	1092.132	1110.792	-18.660	18.660	348.183
RPC3	1091.56	1116.083	-24.523	24.523	601.356
RPC4	1092.548	1110.707	-18.159	18.159	329.736
RPC5	1091.82	1119.584	-27.764	27.764	770.851
RPC7	1128.479	1152.636	-24.157	24.157	583.573
RPC8	1113.949	1137.881	-23.932	23.932	572.743
RPC10	1134.059	1150.491	-16.432	16.432	270.002
RPC11	1126.3	1144.966	-18.666	18.666	348.421
RPC12	1136.202	1153.672	-17.470	17.470	305.186
RPC13	1123.496	1141.015	-17.519	17.519	306.918
RPC13S	1123.528	1155.216	-31.688	31.688	1004.126
RPC15	1091.507	1102.063	-10.556	10.556	111.426
RPC16	1126.038	1144.802	-18.764	18.764	352.091
RPC17D	1132.778	1155.570	-22.792	22.792	519.482
RPC17S	1133.431	1151.070	-17.639	17.639	311.121
RPC18S	1135.407	1156.106	-20.699	20.699	428.429
RPC18D	1122.045	1150.477	-28.432	28.432	808.355

Borehole	Observed elevations	Simulated elevations	$(h_{obs} - h_{sim})$	$ (h_{obs} - h_{sim}) $	$(h_{obs} - h_m)^2$
	mamsl	mamsl	m	m	m
RPC19	1151.636	1165.952	-14.316	14.316	204.937
RPC20	1165.326	1163.739	1.587	1.587	2.520
RPC21	1168.275	1173.883	-5.608	5.608	31.448
RPC22	1175.011	1186.596	-11.585	11.585	134.210
RPC23D	1150.99	1164.310	-13.320	13.320	177.419
RPC24	1130.87	1151.538	-20.668	20.668	427.166
RPC114S	1090.246	1104.656	-14.410	14.410	207.662
RPC115S	1101.037	1126.406	-25.369	25.369	643.592
RPC115D	1110.098	1130.516	-20.418	20.418	416.894
RPC116S	1102.791	1115.025	-12.234	12.234	149.665
RPC117	1080.316	1087.761	-7.445	7.445	55.432
RPC118	1076.693	1099.781	-23.088	23.088	533.064
RPC118S	1087.581	1082.969	4.612	4.612	21.268
RPC120D	1118.62	1130.574	-11.954	11.954	142.907
RPC120S	1118.896	1144.010	-25.114	25.114	630.720
RPC121D	1118.149	1127.568	-9.419	9.419	88.710
RPC121S	1123.602	1137.134	-13.532	13.532	183.125
RPC122S	1118.992	1131.963	-12.971	12.971	168.244
RPC122D	1117.938	1111.668	6.270	6.270	39.319
RPC124	1086	1089.972	-3.972	3.972	15.773
RPC125	1061.22	1077.139	-15.919	15.919	253.412
RPC126	1157.77	1174.547	-16.777	16.777	281.477

Borehole	Observed elevations	Simulated elevations	$(h_{obs} - h_{sim})$	$ (h_{obs} - h_{sim}) $	$(h_{obs} - h_m)^2$
	mamsl	mamsl	m	m	m
RPC127	1084.52	1101.630	-17.110	17.110	292.758
RPC128	1056.58	1074.872	-18.292	18.292	334.596
RPC44	1068.03	1080.894	-12.864	12.864	165.471
SRK5S	1168.32	1182.188	-13.868	13.868	192.326
Machikiri	1179.34	1193.644	-14.304	14.304	204.615
Dealer	1176.118	1187.246	-11.128	11.128	123.839
HPC10057	1207.591	1205.436	2.155	2.155	4.646
HPC10364	1133.457	1160.264	-26.807	26.807	718.639
HPC10406	1138.694	1150.890	-12.196	12.196	148.741
HPC10319	1149.509	1166.895	-17.386	17.386	302.283
RBK 402	1268.974	1288.304	-19.330	19.330	373.651
DWA 3055	1195.223	1194.437	0.786	0.786	0.618
HO3-2847	1066.938	1089.291	-22.353	22.353	499.662
BH W14	1079.457	1115.699	-36.242	36.242	1313.467
Citrus	1082.498	1080.875	1.623	1.623	2.633
DPC 1	1080.682	1097.204	-16.522	16.522	272.972
DPC 2	1080.401	1097.425	-17.024	17.024	289.833
DPC 3	1080.908	1092.878	-11.970	11.970	143.291
DPC 4	1079.588	1084.964	-5.376	5.376	28.905
DPC 5	1063.069	1082.921	-19.852	19.852	394.102
DPC 6	1064.277	1078.089	-13.812	13.812	190.782
DPC 7	1053.373	1058.488	-5.115	5.115	26.163

Borehole	Observed elevations	Simulated elevations	$(h_{obs} - h_{sim})$	$ (h_{obs} - h_{sim}) $	$(h_{obs} - h_m)^2$
	mamsl	mamsl	m	m	m
DPC 8	1051.146	1070.909	-19.763	19.763	390.563
DPC 9	1064.284	1075.602	-11.318	11.318	128.108
DPC 11	1051.642	1067.869	-16.227	16.227	263.300
DPC 12	1094.947	1112.201	-17.254	17.254	297.690
DPC 13	1094.907	1102.040	-7.133	7.133	50.878
DPC 14	1074.907	1105.441	-30.534	30.534	932.326
DPC 15	1074.904	1088.880	-13.976	13.976	195.339
DPC 16	1076.328	1082.731	-6.403	6.403	41.002
DPC 17	1075.663	1094.709	-19.046	19.046	362.738
DPC 18	1076.939	1087.904	-10.965	10.965	120.226
DPC 19	1073.138	1084.462	-11.324	11.324	128.229
DPC 21	1077.443	1099.947	-22.504	22.504	506.408
DPC22	1077.166	1097.242	-20.076	20.076	403.038
DPC23	1077.752	1090.245	-12.493	12.493	156.065
DPC24A	1077.361	1090.861	-13.500	13.500	182.248
DPC24	1068.191	1086.438	-18.247	18.247	332.965
DPC26	1094.017	1103.163	-9.146	9.146	83.654
DPC27	1088.086	1101.209	-13.123	13.123	172.213
DPC28	1096.097	1108.810	-12.713	12.713	161.630
RPC25	1148.871	1150.100	-1.229	1.229	1.511
RPC26	1153.454	1171.286	-17.832	17.832	317.979
RPC139	1072.378	1084.806	-12.428	12.428	154.453

Borehole	Observed elevations	Simulated elevations	$(h_{obs} - h_{sim})$	$ (h_{obs} - h_{sim}) $	$(h_{obs} - h_m)^2$
	mamsl	mamsl	m	m	m
RPC140	1053.847	1057.450	-3.603	3.603	12.979
RPC141	1061.82147	1076.349	-14.527	14.527	211.044
		$\sum_i^n ()$	-1283.498	1317.566	24722.948
		Errors	ME= -14.924	MAE=15.321	RMS=287.476

Table 22: Calculated errors for the calibrated model in SPRING

Borehole	Observed elevations	Simulated elevations	$(h_{obs} - h_{sim})$	$ (h_{obs} - h_{sim}) $	$(h_{obs} - h_m)^2$
	mamsl	mamsl	m	m	m
RPC1	1092.056	1091.99	0.067	0.067	0.005
RPC2	1092.132	1093.07	-0.938	0.938	0.880
RPC3	1091.56	1098.32	-6.764	6.764	45.756
RPC4	1092.548	1092.99	-0.438	0.438	0.192
RPC5	1091.82	1101.80	-9.982	9.982	99.632
RPC7	1128.479	1134.62	-6.145	6.145	37.760
RPC8	1113.949	1119.97	-6.022	6.022	36.267
RPC10	1134.059	1132.49	1.566	1.566	2.451
RPC11	1126.3	1127.01	-0.707	0.707	0.500
RPC12	1136.202	1135.65	0.550	0.550	0.302
RPC13	1123.496	1123.08	0.413	0.413	0.170
RPC13S	1123.528	1137.19	-13.658	13.658	186.531
RPC15	1091.507	1084.40	7.105	7.105	50.481
RPC16	1126.038	1126.84	-0.806	0.806	0.650

Borehole	Observed elevations	Simulated elevations	$(h_{obs} - h_{sim})$	$ (h_{obs} - h_{sim}) $	$(h_{obs} - h_m)^2$
	mamsl	mamsl	m	m	m
RPC17D	1132.778	1137.54	-4.759	4.759	22.652
RPC17S	1133.431	1133.07	0.363	0.363	0.132
RPC18S	1135.407	1138.07	-2.662	2.662	7.086
RPC18D	1122.045	1132.48	-10.434	10.434	108.873
RPC19	1151.636	1147.85	3.789	3.789	14.359
RPC20	1165.326	1147.64	17.691	17.691	312.967
RPC21	1168.275	1157.71	10.566	10.566	111.643
RPC22	1175.011	1170.33	4.677	4.677	21.878
RPC23D	1150.99	1148.20	2.788	2.788	7.770
RPC24	1130.87	1135.52	-4.649	4.649	21.616
RPC114S	1090.246	1088.96	1.282	1.282	1.644
RPC115S	1101.037	1110.56	-9.525	9.525	90.729
RPC115D	1110.098	1114.64	-4.545	4.545	20.661
RPC116S	1102.791	1099.26	3.531	3.531	12.468
RPC117	1080.316	1075.17	5.151	5.151	26.532
RPC118	1076.693	1087.10	-10.408	10.408	108.336
RPC118S	1087.581	1070.41	17.175	17.175	294.967
RPC120D	1118.62	1117.68	0.939	0.939	0.882
RPC120S	1118.896	1131.02	-12.127	12.127	147.064
RPC121D	1118.149	1114.69	3.454	3.454	11.932
RPC121S	1123.602	1124.20	-0.593	0.593	0.352
RPC122S	1118.992	1119.06	-0.067	0.067	0.005

Borehole	Observed elevations	Simulated elevations	$(h_{obs} - h_{sim})$	$ (h_{obs} - h_{sim}) $	$(h_{obs} - h_m)^2$
	mamsl	mamsl	m	m	m
RPC122D	1117.938	1098.91	19.033	19.033	362.248
RPC124	1086	1077.36	8.640	8.640	74.650
RPC125	1061.22	1064.62	-3.397	3.397	11.537
RPC126	1157.77	1161.35	-3.578	3.578	12.801
RPC127	1084.52	1088.94	-4.418	4.418	19.515
RPC128	1056.58	1062.37	-5.785	5.785	33.471
RPC44	1068.03	1068.35	-0.315	0.315	0.099
SRK5S	1168.32	1168.94	-0.616	0.616	0.379
Machikiri	1179.34	1180.31	-0.972	0.972	0.945
Dealer	1176.118	1173.96	2.159	2.159	4.663
HPC10057	1207.591	1192.02	15.570	15.570	242.411
HPC10364	1133.457	1147.16	-13.707	13.707	187.890
HPC10406	1138.694	1137.85	0.839	0.839	0.704
HPC10319	1149.509	1153.75	-4.240	4.240	17.978
RBK 402	1268.974	1274.31	-5.340	5.340	28.514
DWA 3055	1195.223	1181.10	14.124	14.124	199.484
HO3-2847	1066.938	1073.71	-6.767	6.767	45.795
BH W14	1079.457	1099.93	-20.472	20.472	419.114
Citrus	1082.498	1065.35	17.150	17.150	294.123
DPC 1	1080.682	1081.56	-0.881	0.881	0.776
DPC 2	1080.401	1081.78	-1.382	1.382	1.910
DPC 3	1080.908	1077.27	3.640	3.640	13.253

Borehole	Observed elevations	Simulated elevations	$(h_{obs} - h_{sim})$	$ (h_{obs} - h_{sim}) $	$(h_{obs} - h_m)^2$
	mamsl	mamsl	m	m	m
DPC 4	1079.588	1069.41	10.180	10.180	103.623
DPC 5	1063.069	1067.38	-4.310	4.310	18.579
DPC 6	1064.277	1064.07	0.206	0.206	0.042
DPC 7	1053.373	1047.58	5.788	5.788	33.503
DPC 8	1051.146	1059.92	-8.773	8.773	76.970
DPC 9	1064.284	1064.58	-0.296	0.296	0.088
DPC 11	1051.642	1056.90	-5.258	5.258	27.649
DPC 12	1094.947	1100.92	-5.977	5.977	35.727
DPC 13	1094.907	1090.83	4.073	4.073	16.589
DPC 14	1074.907	1094.21	-19.305	19.305	372.665
DPC 15	1074.904	1077.77	-2.862	2.862	8.191
DPC 16	1076.328	1071.66	4.668	4.668	21.794
DPC 17	1075.663	1083.55	-7.891	7.891	62.265
DPC 18	1076.939	1076.80	0.143	0.143	0.020
DPC 19	1073.138	1073.38	-0.240	0.240	0.058
DPC 21	1077.443	1088.76	-11.312	11.312	127.966
DPC22	1077.166	1086.07	-8.903	8.903	79.269
DPC23	1077.752	1079.12	-1.369	1.369	1.874
DPC24A	1077.361	1079.73	-2.372	2.372	5.625
DPC24	1068.191	1075.34	-7.150	7.150	51.122
DPC26	1094.017	1091.95	2.067	2.067	4.274
DPC27	1088.086	1090.01	-1.923	1.923	3.698

Borehole	Observed elevations	Simulated elevations	$(h_{obs} - h_{sim})$	$ (h_{obs} - h_{sim}) $	$(h_{obs} - h_m)^2$
	mamsl	mamsl	m	m	m
DPC28	1096.097	1097.56	-1.460	1.460	2.133
RPC25	1148.871	1138.56	10.311	10.311	106.309
RPC26	1153.454	1159.60	-6.145	6.145	37.758
RPC139	1072.378	1073.72	-1.342	1.342	1.801
RPC140	1053.847	1046.55	7.293	7.293	53.192
RPC141	1061.82147	1065.32	-3.500	3.500	12.251
		$\sum_i^n ()$	-70.499	484.482	5043.421
		Errors	ME=-0.820	MAE=5.634	RMS=58.644

7.3.7 Sensitivity analysis of the steady state models

We demonstrate in the present section the sensitivity of the models to the conductivity field. The double and half of the conductivity values in the fields which were used for the steady state calibrations were calculated and used to simulated steady state flow. The effects of these changes on simulated hydraulic heads are depicted from Figure 89 to Figure 91.

The sensitivity of the models to the Hydraulic conductivity fields show that an increase in hydraulic conductivity values, have to be compensated by a decrease in Recharge rate. This is illustrates the non-uniqueness of the solution of the groundwater flow equation used for the numerical models.

7.3.7.1 Storativity

For transient state calibration and simulation of models scenarios, storativity is required. The specific storage values as described in the conceptual model were used as initial conditions for transient state calibration of the models.

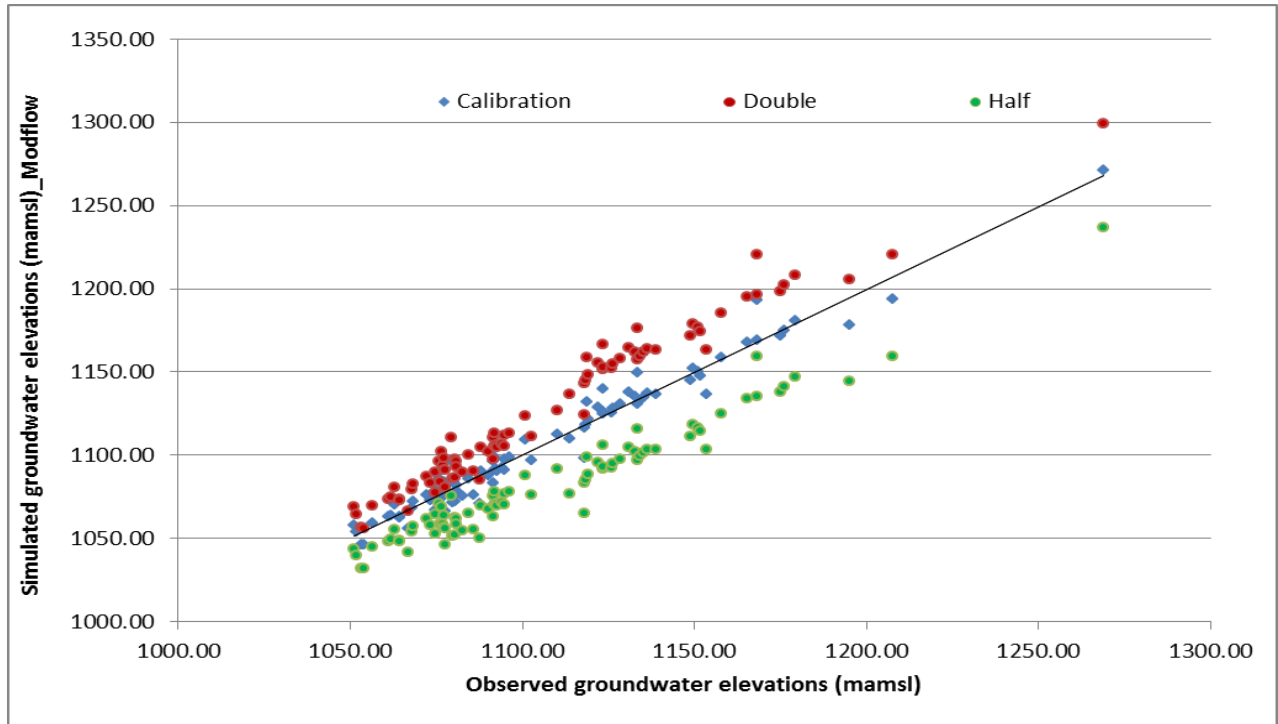


Figure 89: Sensitivity of MODFLOW model to double calibrated K

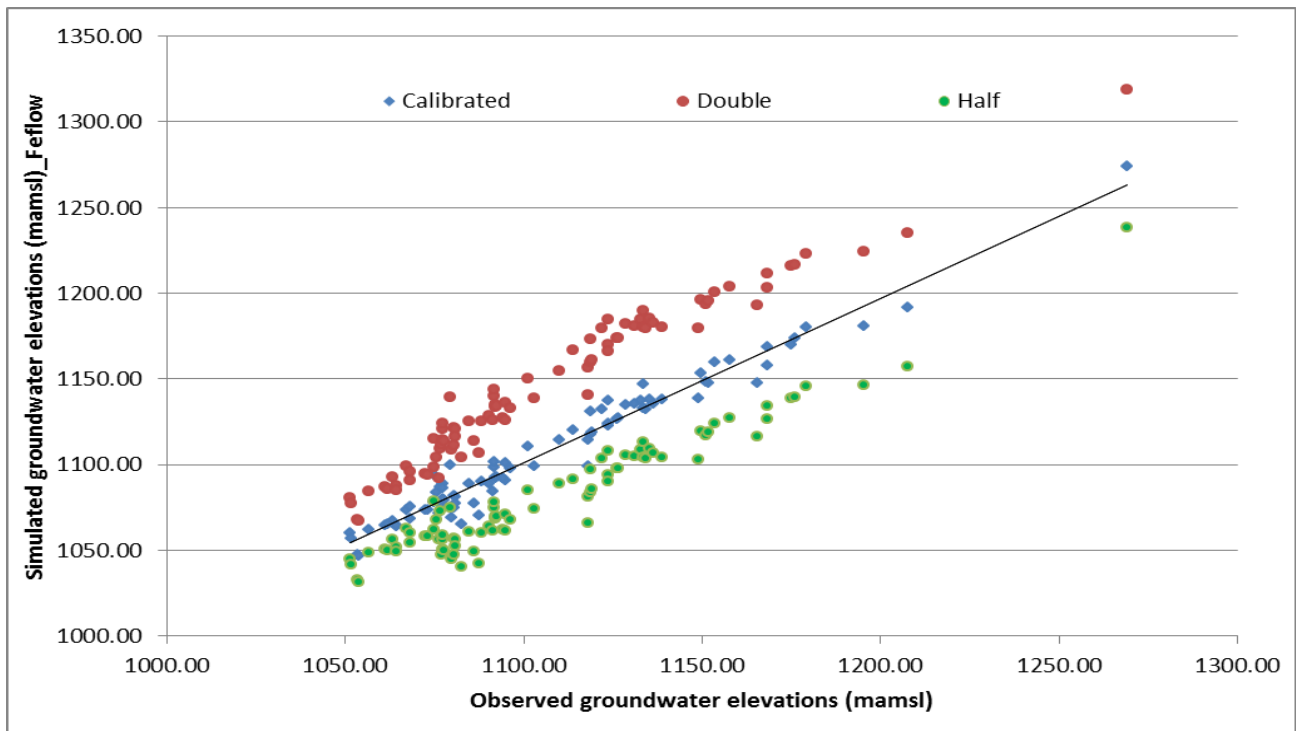


Figure 90: Sensitivity of FEFLOW model to double calibrated K

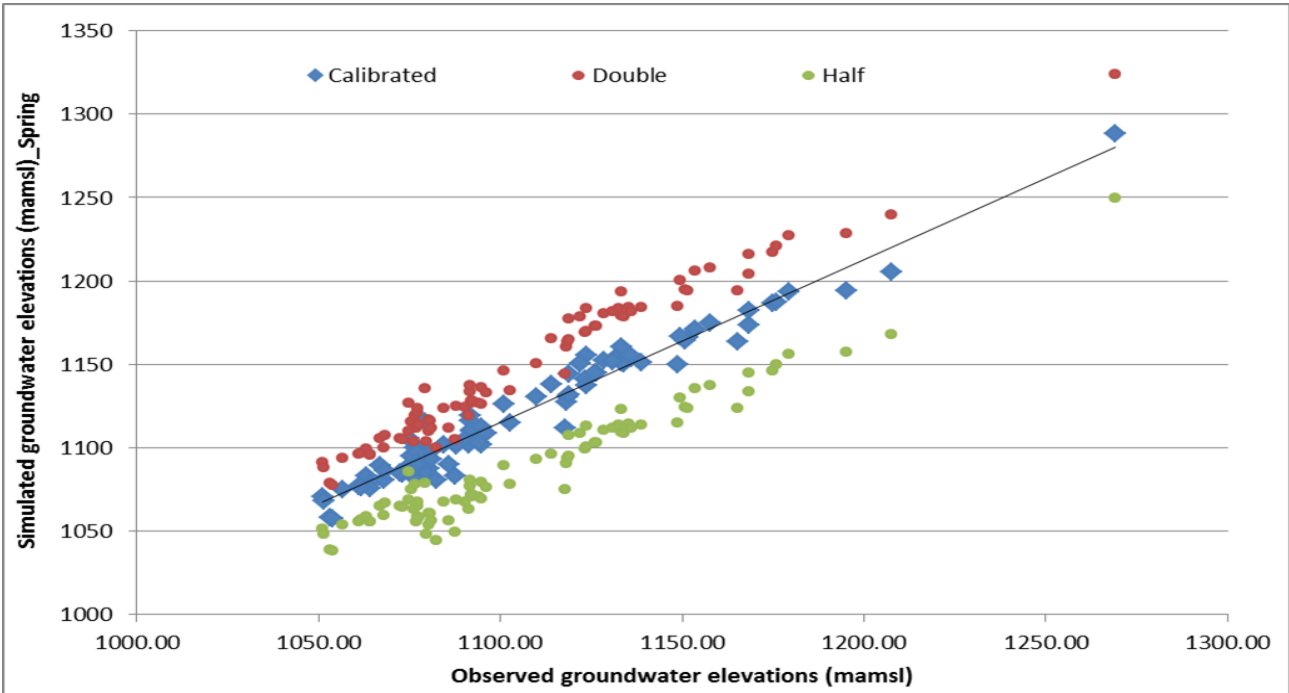


Figure 91: Sensitivity of SPRING model to half calibrated K

7.3.8 Transport numerical model

Mass transport modelling consists of the simulation of water contamination or pollution due to deteriorating water quality in response to man's disturbance of the natural system. Only the mechanical dispersion and molecular diffusion are of interest here. Advection and the Hydrodynamic dispersion are well known to be most important processes involved in the transport through a medium. Other phenomena (sorption, adsorption, deposition, ion exchange, etc.) may affect the concentration distribution of a contaminant as it moves through a medium, but are not of interest in the present study. Since fractured flow characteristics will prevail in the aquifer system, the effect of retardation will be reduced. Contaminant migration is therefore assumed to be governed by only advection and hydrodynamic dispersion. However, it is worthy to mention this assumption will provide a worst-case scenario in terms of travel distance of contaminants.

The effective porosity is required to calculate the average linear velocity of groundwater flow, which in turn is needed to track water particles and to calculate contaminant concentrations in the groundwater. The kinematic porosity of the aquifer and the

longitudinal dispersivity are among the biggest uncertain parameters used during transport modelling of pollutants.

Bear and Verruijt (1992) estimated the average transversal dispersivity to be 10 to 20 times smaller than the average longitudinal dispersivity. The transport model input parameters are summarized in Table 23. These values were chosen as per previous model in the area.

Table 23 Summary on the input for transport simulation

Effective Porosity	Longitudinal Dispersivity	Transversal Dispersivity
--	(m)	(m)
0.06	75	7.5

7.3.8.1 Mass transport in MODFLOW

The modular three dimensional transport model of multi-species (MT3DS) mode was used to provide numerical solutions for the concentration values in the aquifer in time and space. This widely used fate and transport model was created by Zheng and Wang (1999). General equation of fate and transport in three dimensions solved by MT3DMS is:

$$\frac{\partial}{\partial x_i} \left(\theta D_{ij} \frac{\partial C^k}{\partial x_j} \right) - \frac{\partial}{\partial x_{i,j}} (\theta v_i C^k) + q_s C_s^k + \sum R_n = \frac{\partial(\theta C^k)}{\partial t} \quad (154)$$

Where C^k is the dissolved concentration of the k species (ML^{-3}), θ is the porosity (dimensionless), t is the time, $x_{i,j}$ is the distance along the respective Cartesian coordinate axis, D_{ij} is the hydrodynamic dispersion tensor, $v_i = \frac{q_i}{\theta}$, q_i is the volumetric flow rate per unit volume flux of aquifer representing fluid sources (positive) and sinks (negative), C_s^k is the concentration of the source or sink flux for species k ; $\sum R_n$ is the chemical reaction term. Flow model input parameters (Boundaries conditions,

hydraulic conductivity, Recharge, Specific Storage, and Specific Yield) values that serve in flow calibrations were specified for the aquifer.

7.3.8.2 Mass transport in FEFLOW

Bear and Verruijt (1992) expressed the equation of hydrodynamic dispersion or the advection-dispersion equation (or the mass balance equation) of a pollutant (contaminant) as:

$$\frac{\delta nc}{\delta t} = - \Delta \bullet q_{c,total} - f + n\rho\Gamma - P_c + R_c \dots\dots\dots (155)$$

where: n^c is mass of pollutant per unit volume of porous medium; n porosity of saturated zone; c concentration of pollutant (mass of pollutant per unit volume of liquid (water)); $\Delta \bullet q_{c,total}$ is the excess of inflow of a considered pollutant over outflow, per unit volume of porous medium, per unit time; f is the quantity of pollutant leaving the water (through adsorption, ion exchange etc.); $n\rho\Gamma$ is the mass of pollutant added to the water (or leaving it) as a result of chemical interactions among species inside the water, or by various decay phenomena; Γ is the rate at which the mass of a pollutant is added to the water per unit mass of fluid; ρ is the density of pollutant; P_c is the total quantity of pollutant withdrawn (pumped) per unit volume of porous medium per unit time; R_c is the total quantity of pollutant added (artificial recharge) per unit volume of porous medium per unit time.

7.3.8.3 Mass transport in SPRING

SPRING makes use of inverted flow fields to calculate the contamination transport. The method considers the storage, the advection, dispersion, and diffusion processes, to simulate/calculate contaminant from sources, and water particle tracking.

$$(nS_w\rho) \frac{\partial c}{\partial t} + \rho v_i \frac{\partial c}{\partial x_i} - \frac{\partial(nS_w\rho(D_{ij} + D_{mol}\delta_{ij}) \frac{\partial c}{\partial x_i})}{\partial x_i} = q(c^* - c) \quad (156)$$

The right term of the equation constitutes the source. $(nS_w\rho)\frac{\partial c}{\partial t}$ is the storage term.

$\rho v_i \frac{\partial c}{\partial x_i}$ represents the advection. The diffusion and dispersion are accounted for in

$$\frac{\partial(nS_w\rho(D_{ij} + D_{mol}\delta_{ij})\frac{\partial c}{\partial x_i})}{\partial x_i}.$$

7.4 Models Results and discussion

The two most common scenarios of groundwater modelling for the impact assessment of the opencast mines are simulated to demonstrate typical effects of linear discontinuities (relative more conductive) on:

- The changes (drainage) in the groundwater system due to active mining opencast areas (Dewatering) ;
- The changes (quality) in the groundwater system due to ore processing residual/waste (tailings).

7.4.1 Cone of depression

In the rock blocks (Granite, and Gabbro-Norite), the cone of depression extends up to 1.5 km away from the pits when pit floor reaches 35 mbgl and is dewatered. The simulated cone of depressions is shown in Figure 92. The effect of linear conductive fractured zones can be clearly as the cone extends up to 5 km away from the pits. This is a result of relatively higher pit inflow rates coming from such linear features.

The irregular shape with the elongation of the cone of depression along the relatively more hydraulic conductive features that cross the pits could have been easily depicted from field measurement around active opencast mine; provided that sufficient monitoring (observation) boreholes were available. The regular oval/elliptical shape usually presented by many of the modelling report is not realistic and is due to the spatial homogenisation (constant conductivity/recharge) of the conceptual flow model.

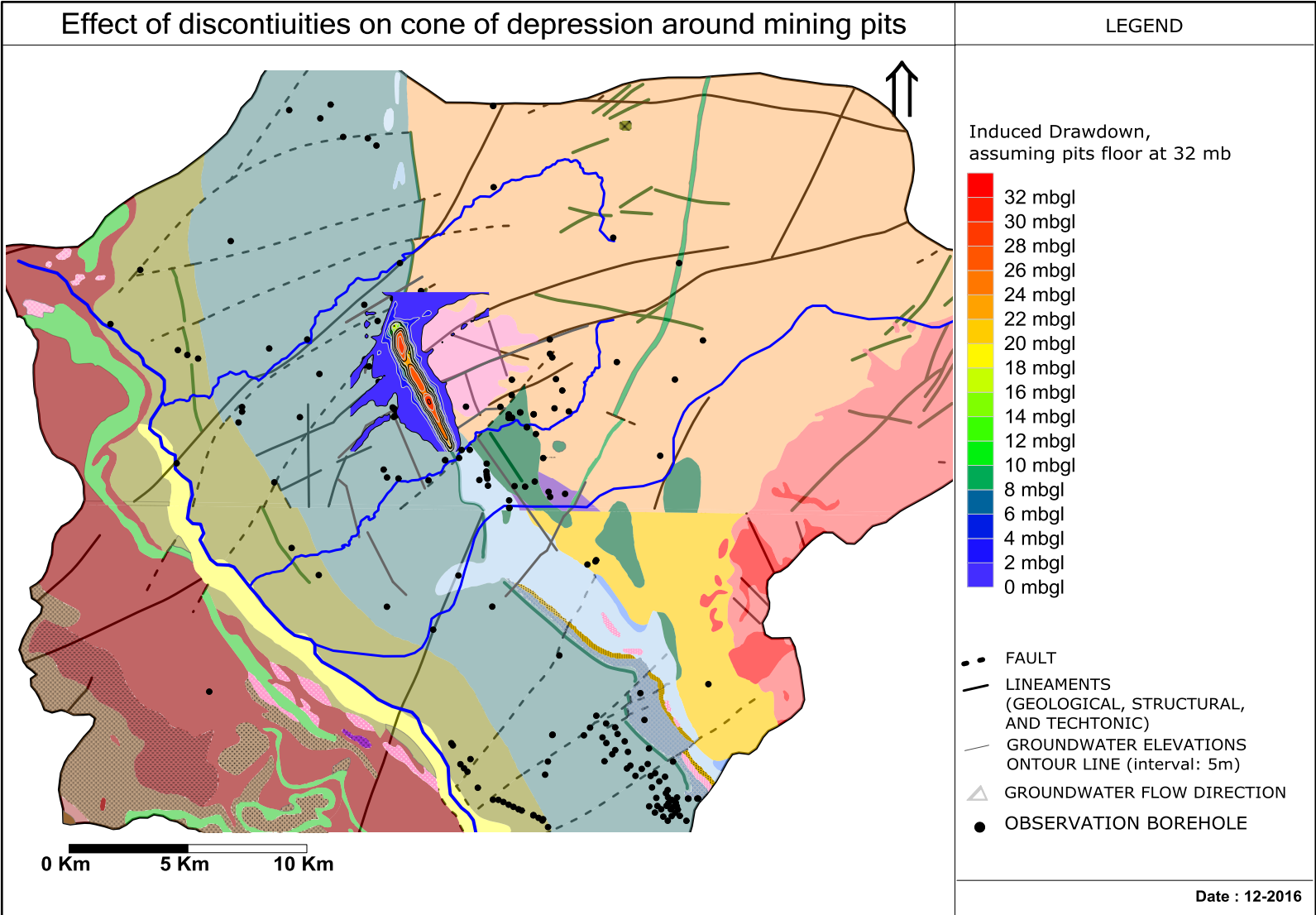


Figure 92: Cone of depression around active opencast mine in a typical fractured crystalline aquifer.

7.4.2 Contaminants transport simulation

Groundwater flow is dependent on the water heads gradient. During active mining, groundwater flow is towards the open pit. Any pollution plumes emanating from contaminations source in dewatering catchment area will move towards the open pit. If the source of the contaminant is outside of the dewatering catchment area, pollution plumes moves down gradient toward the discharge point. In both cases contamination plume migration in the fractured crystalline rock aquifer is expected to be influenced by linear features, depending on their hydraulic function. We demonstrate with two scenarios, the importance of considering the hydraulic function of the linear features crossing tailing dam, or intersecting the path of a contamination plume.

The first scenario considers an existing tailing dam as a source. At that source initial contaminant concentrations were assigned. The Total Dissolved Solids value was used as concentration of the contaminant. The mass transport model was used to predict salt concentration values of the contaminant in the aquifer in time and space. As illustrated in Figure 93, the existing tailing (source) is being developed in an area crossed by lineament LN4 in the SW-NE direction. LN4 is known to a Dyke, and a number of boreholes were drilled inside and at the side in the baking zones. The results of drilling and different hydraulic tests have shown that this linear feature is associated with higher groundwater occurrence than the rock blocks (Granite, Gabbro-Norite), and that was considered in the calibration of the flow model. Based on simulation results, after a period of 10 years with the pollution plume migration in the weathered/fractured aquifer, the extent of the cone of depression would reach between 500 m and 700m away from and mainly down gradient to the source (Figure 93). This prediction is in agreement with the results of previous model which consider constant conductivity and recharge across the model area. However, unlike the previous model, the present models accounts for variability in the aquifer flow, and the simulated contamination plume shows clearly the long tail along the crossing lineament LN4. Along LN4, the pollution plume would migrate up 1.2 km after 10 years. This suggests that the contaminants would move faster along the Dyke than in the weathered rocks. In the second scenario, an arbitrary potential source of groundwater contamination source was chosen in the catchment at the angle of intersection of 03 lineaments (LN1, LN2, and

LN3) of different types. LN1 is a Dyke which in this scenario was explicitly treated as lower conductive lineaments, LN2 represents lithological contact, and LN3 represents a fault. We first consider these 03 lineaments that cross the pollution plume path, and simulate the models for 10 years. As clearly depicted in Figure 94 LN1 would act as a barrier and salt would accumulate along it. The pollution plume would preferentially migrate into LN2 which has groundwater head gradient advantages over LN3. However, if the lithological contact zone is not that much hydraulically conductive, then as it is seen in Figure 95, the preferential flow for the migration of the pollution plume will be LN2.

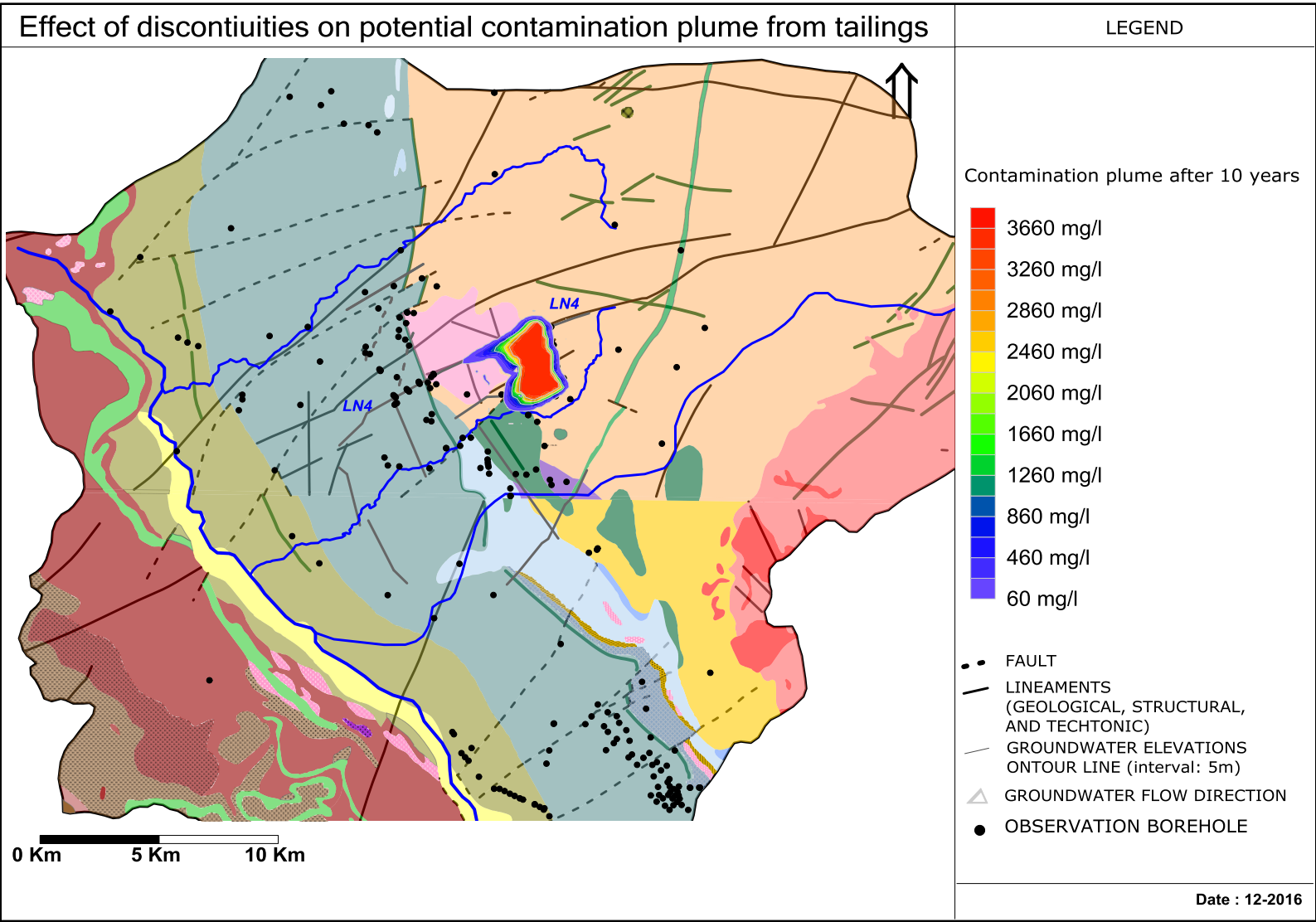


Figure 93: Simulated contamination plume from existing tailings dam after 10 years.

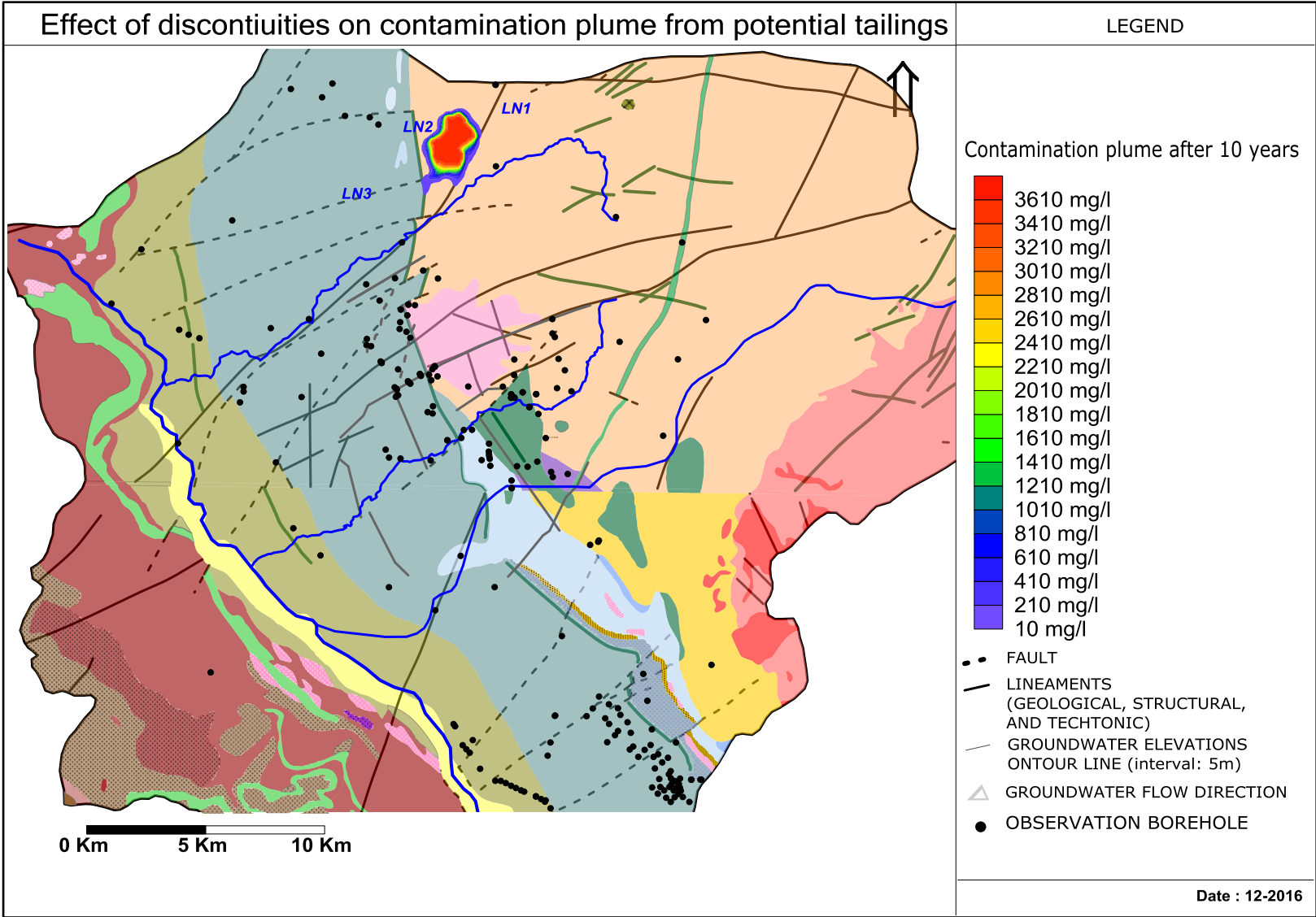


Figure 94: Simulated contamination plume from potential tailings dam after 10 years with contact zone activated included

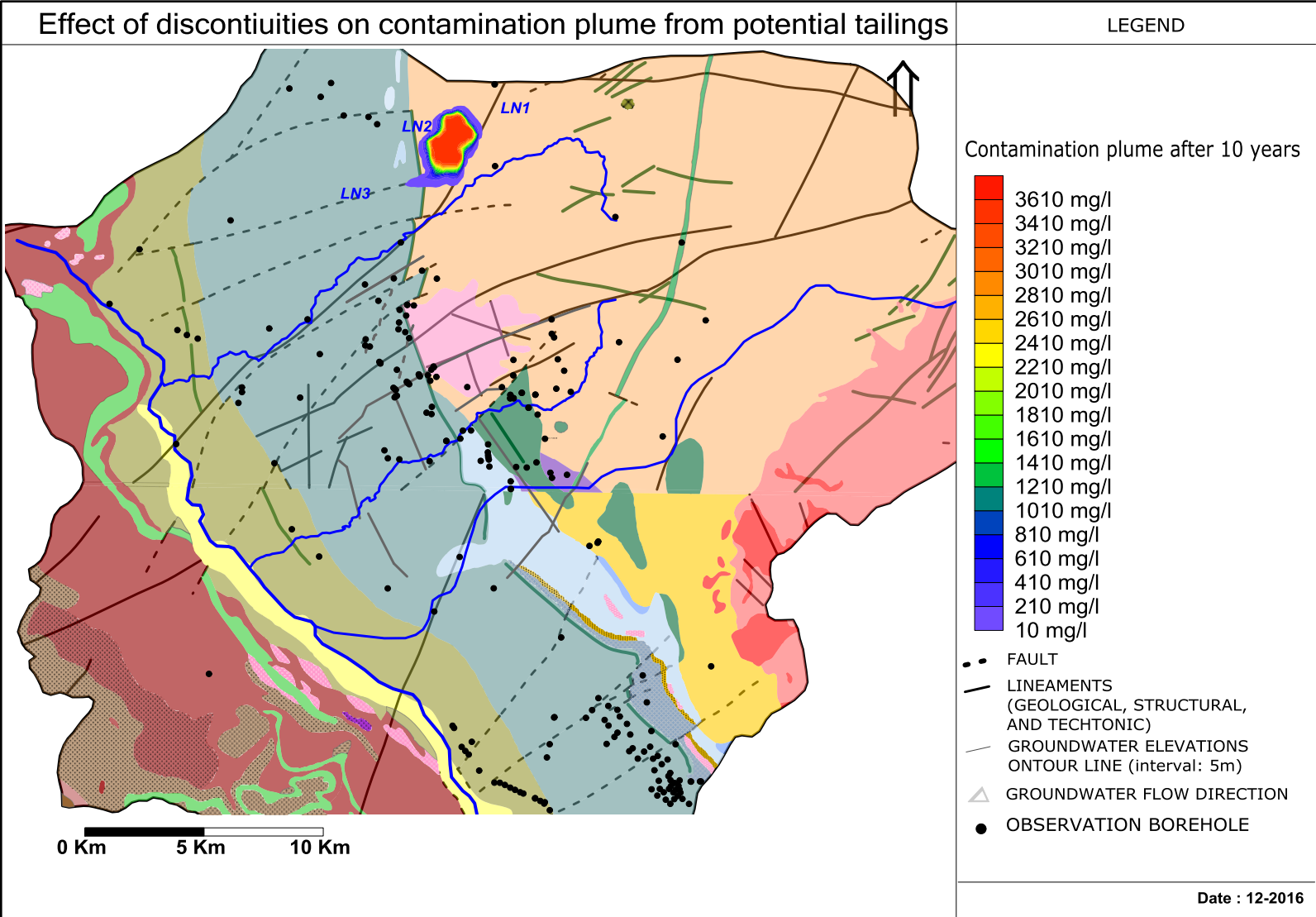


Figure 95: Simulated contamination plume from potential tailings dam after 10 years with contact zone activated included

8 General Conclusion

"If the rock properties were constant in space, and/or easy to determine, hydrogeology would be a rather boring job" Gh. de Marsily, et al (2005). Heterogeneity can be quantified and accounted for either in the form of homogeneous equivalent properties (averaging) or in the form of the spatial variability of the rock properties from geologic observations and local measurements. It is confirmed that a minimum level of heterogeneity (discontinuity) has to be considered in geohydrological studies for both environmental compliance and production in mining projects. It is also important to stress that commonly available geohydrological data in mining environments allow for this minimum level of heterogeneity to be accounted for. To add, the current progress in mathematical models (new differentiation tools) together with current level of computers' capacities (model/software) should allow us to define and account for such discontinuities in aquifers. The expert/modeller has to be associated with the design and supervision of the data collection phase for such an objective to be fully accomplished. Modelling of heterogeneity really requires an informed and a conscious willingness to better the characterize geology of the sites of interest. Only a sound understanding of rock structures can clearly pose the problem which will then be used to define hydraulic equations to be solved by mathematical models. In the present thesis 02 new mathematical/analytical models which assume fractal behaviours of the aquifers were firstly proposed. Heterogeneity in a typical South African crystalline rock (Bushveld Complex) aquifer was assessed. From this, a methodical level for quantifying and modelling heterogeneity in an aquifer was deduced.

The model of fractured fractal flow is perhaps one of the most difficult physical problems within the field of Geohydrology due the multiples complexities. To model these complexities one will have to use the suitable concept of differentiation. A modified fractured fractal flow model using the Atangana-Baleanu fractional derivative is suggested. The new fractional differentiation is more natural and more suitable to model real world problems due to the wider applicability of the generalized Mittag-

Leffler function. The existence and the uniqueness of the proposed solution were demonstrated, and three numerical schemes to derive the numerical solution of the modified model were suggested. The proposed new fractal flow was then successfully applied to fit groundwater level drawdowns from 04 constant pumping discharge tests in a typical fractured crystalline rock aquifer, as part site characterisation.

The fractal flow model in dual media appear to be more complex than the fractal flow model, since it accounts for flow within the fractured network as well as flow within the matrix rock. In addition to heterogeneity in the fractures, one has to account for the heterogeneity, elasticity or visco-elastic of matrix rock as well. A modified Dual medium fractal model is proposed by replacing the local derivative with the non-local operator with power and Mittag-Leffler law. This replacement is also done by a combination of the two laws which is the power-Mittag-Leffler law. The existence of the solution of the modified model was analysed numerically using the Upwind for second and third order approximation in space; and thereafter, the power, Mittag-Leffler to Mittag-Leffler-Power laws are compared.

The groundwater characterisation was completed around the open pits of an operating mine and the following conclusions were reached:

- Magnetic and Electromagenetic methods were applied with great success to delineate dykes and structures.
- Drilling along Dykes revealed that although some water strikes were encountered in the dykes, very limited water strikes were encountered on the edges of the dykes. The big dykes were found to be very tight and fresh, and would probably act as a competent barrier in terms of groundwater flow in the investigated area. The smaller dyke has similar properties. Structures intercepting the dykes were found to conduct groundwater. The highest yielding boreholes were encountered at positions close to or on faults, and the dykes are associated with secondary faulting. The shallow weathering in all the boreholes indicated water strikes at depths not exceeding 50mbgl. Groundwater was found to occur mainly at depths between 10 and 50 mbgl, however, deeper flowing zones may primarily be present in Faults
- Pump testing revealed Transmissivity values ranging from 3 to 160 m²/day;

- The dominant hydrogeochemical processes contributing to the evolution of the main hydrochemical groundwater type and quality of the crystalline aquifer in the open pit platinum mine were identified and described. It was also shown that the mine is characterised by a Bicarbonate Magnesium Calcium hydro-geochemical type. It was established that the Bicarbonate Magnesium Calcium hydro-geochemical type evolves from the buffering of AMD by serpentinite, calcite, and dolomite carbonate minerals. It was further demonstrated the occurrence of ion exchanges in the groundwater system which results in decrease of Mg^{2+} and Ca^{2+} cations.

From the modelling results using PHREEQC it is found that Mg^{2+} and Ca^{2+} that evolve from carbonate AMD buffering process in the mine's groundwater system would only occur up to the certain points. At these points their respective aqueous solubility will become limited by the saturation of Calcite and Dolomite. Although the buffering minerals (Serpentinite, calcite and dolomite) are important for reducing the AMD levels and minimizing the potential leaching of metals into the mine groundwater system they also present the problems of elevated Total Dissolved Salt and Total hardness in the groundwater system.

- The variability of recharge rates was estimated using the Chloride Mass Balance method. Estimated recharge rates were between 0.64 mm and 35.66 mm compared with recharge rates estimated in previous studies in the region using different methods.

It was also demonstrated how spatial heterogeneity in aquifers can be modelled based on most commonly available tools and data in mining environments of South Africa. Sufficient information on heterogeneity of the aquifer was inferred from a long site characterisation for a long term pit dewatering project. Spatial variability of hydraulic parameters (hydraulic conductivity and recharge) were used to account for heterogeneity in the aquifer. Geostatistical tools were used to analyse the estimated hydraulic conductivity and recharges. This allowed for the generation of statistically correlated fields of hydraulic conductivity and recharge rates. The multiples generated correlated fields which were then used in the calibrations of three groundwater

numerical models using MODFLOW Processing Pro 2005, FEFLOW 6.1, and SPRING 4. The calibrated groundwater heads for the three Models compare well with measured heads in the catchment. Errors associated with each model were estimated and the sensitivity of each model to changes in hydraulic conductivity was established. The models were then used to demonstrate the effect of heterogeneity in the common scenarios that are simulated in numerical groundwater study for open pit mines. The extent of the impacts appear to be magnified at different degrees along the linear discontinuities. Such behaviour in the aquifer is normal, and should be expected especially when the presence of conductive linear features in the study area is confirmed. It is also concluded that MODFLOW, FEFLOW, or SPRING all have the capacity of accounting for heterogeneity in the modelling of the investigated fractured crystalline aquifer, even if there is relatively limited available data as in the case of the case study of the present thesis. Better modelling of the complex aquifer system can still be developed (Multiple zoning stochastic, Markov chain, Genetic models, etc.), provided the modeller leads the design and the collection of the required data.

The future of modelling of heterogeneity in aquifers is definitively in the designing of new in situ testing (hydraulic and mass transport) procedures with new corresponding mathematical models. New trends in mathematical differentiation offer opportunity to explore more flexible and practical mathematical model solutions; and this applies to both analytical and numerical modelling.

9 References

1. Acworth, R.I. (1987). The development of crystalline basement aquifers in a tropical environment. *Q. J. Eng. Geol.*, 20: 265-272.
2. Ahmet Apaydin, (2010) Relation of tectonic structure to groundwater flow in the Beypazari region, NW Anatolia, Turkey. *Hydrogeology Journal*. DOI 10.1007/s10040-010-0605-1.
3. American Water Works Association and Water Environment Federation, 2005. *Standard Methods for the Examination of Water and Wastewater*. Washington, DC 20001-3710.
4. Anhaeusser, C.R. (1992). Structures in granitoid gneisses and associated migmatites close to the boundary of the Limpopo Belt, South Africa. *Precambrian Res.*, 55: 81-92.
5. Armstrong, R. A., Compston, W., Retief, E. A. and Williams, I. S. 1990. Geochronological constraints on the evolution of the Witwatersrand basin (South Africa), as deduced from single zircon U/Pb ion microprobe studies. In: J. S. Clover and S. E. Ho (eds.), *3rd Int. Archean Symp., Extended Abstract volume*, pp. 287-288.
6. A.R. Byea, and F.G. Bellb Chilton. 2001. Stability assessment and slope design at Sandsloot open pit, South Africa. *International Journal of Rock Mechanics & Mining Sciences* 38 (2001) 449–466.
7. Atangana A. Derivative with two fractional orders: A new avenue of investigation toward revolution in fractional calculus: *Eur. Phys. J. Plus* 2016, 131: 373.
8. Atangana A., Dumitru B. "New fractional derivatives with non-local and non-singular kernel: Theory and application to heat transfer model, *Thermal Science*, Year 2016, Vol. 20, No. 2, pp. 763–769.
9. A.R. Byea, F.G. Bell. 2001. Stability assessment and slope design at Sandsloot open pit, South Africa. *International Journal of Rock Mechanics & Mining Sciences* 38 (2001) 449–466.

10. Badr Saad T. Alkahtani, " Chua's circuit model with Atangana–Baleanu derivative with fractional order Chaos, Solitons & Fractals", Volume 89, August 2016, Pages 547–551.
11. Barenblatt, G.E., Zheltov, I.P., and Kochina, I.N. 1960. Basic Concepts in the Theory of Homogeneous Liquids in Fissured Rocks. *J. Appl. Math. Mech.* 24: 1286-1303.
12. Barker, J.A. (1988). A Generalized Radial Flow Model for Hydraulic Tests in Fractured Rock. *Water Resources Res.*, 24(10): 1796-1804.
13. Bernard S, Delay F, Porel G. A new method of data inversion for the identification of fractal characteristics and homogenization scale from hydraulic pumping tests in fractured aquifers. *J Hydrol*; in press. doi:10.1016/j.jhydrol.2006.01.008.
14. Bell, F.G., Bullock, S.E.T., Hälbich, T.F.J., Lindsay, P., 2001. Environmental impacts associated with an abandoned mine in the Witbank Coalfield, South Africa. *Int. J. Coal Geol.* 45, 195–216.
15. Belzile, N.; Chen, Y.W.; Cai, M.F. and Li, Y. (2004). A review of pyrrhotite oxidation. *Journal of Geochemical Exploration*, 84: 65-76.
16. Benner, S.G., Gould, W.D., Blowes, D.W., 2000. Microbial populations associated with the generation and treatment of acid mine drainage. *Chem. Geol.* 169, 435-448.
17. Black, J.H. (1994). Hydrogeology of fractured rocks – a question of uncertainty about geometry. *Applied Hydrogeology.*, 2(3): 56-70.
18. Blenkinsop, T.G. and Rollinson, H.R., 1992. North Limpopo Field Workshop, Field Guide and Abstracts Volume. Geological Society of Zimbabwe, 56 pp.
19. Blowes, D.W., Ptacek, C.L., Frind, E.O., Johnson, R.H., Robertson, W.D., Molson, J.W., 1994. Acid-neutralization reactions in inactive mine tailings impoundments and their effect on the transport of dissolved metals. *Proc. Int. Land Reclam. Mine Drain. Conf. Pitt.* 1, 429–438.
20. Blowes D.W.; Ptacek, C.J., Jamvor, L.J. and Weisener, C.G. (2003). The Geochemistry of Acid Mine Drainage. In: Holland, H.D. and Turekian, K.K. (Eds.), *Treatise on Geochemistry*. Elsevier, New York, 9:149-204.

21. Bourdet, D. et al. 1984. New Type Curves Aid Analysis of Fissured Zone Well Tests. *World Oil* (April).
22. Brandl, G (1986). The geology of Pietersburg area. Explanation of sheet 2328 Scale 1:250 000. Geological Survey of South Africa, Pretoria, 43p.
23. Buchanan, D.L. (1988). Platinum-group element exploration. *Developments in Economic Geology*, 26. Elsevier, Amsterdam, 73-76.
24. Burdon, D.J., Malzoum, J., 1958. Some chemical types of groundwater from Syria. In: *Proceedings of the UNESCO Symposium, Teheran*, pp. 73–90.
25. Caputo M , Fabrizio M . A new definition of fractional derivative with- out singular kernel. *Progr Fract Differ Appl* 2015;1:73–85 .
26. Chinoda, G., Matura, N., Moyce, W. and Owen, R. 2009. Baseline Report on the Geology of the Limpopo Basin Area, a contribution to the Challenge Program on Water and Food Project 17 "Integrated Water Resource Management for Improved Rural Livelihoods: Managing risk, mitigating drought and improving water productivity in the water scarce Limpopo Basin". WaterNet Working Paper 7. WaterNet, Harare.
27. Chizmeshya, A., McKelvy, M., Wolf, G., Carpenter, R., Gormley, D., 2003. Enhancing the atomic-level understanding of CO₂ mineral sequestration mechanisms via advanced computational modeling. In: *Tech. Rep. Arizona State University Center for Solid State Science. Arizona State University Center for Solid State Science.*
28. Cooper, H.H. and C.E. Jacob, 1946. A generalized graphical method for evaluating formation constants and summarizing well field history, *Am. Geophys. Union Trans.*, vol. 27, pp. 526-534.
29. Courant, Richard; Isaacson, E; Rees, M. (1952). "On the Solution of Nonlinear Hyperbolic Differential Equations by Finite Differences". *Comm. Pure Appl. Math.* 5: 243..255
30. Davis, P. J. (1959). "Leonhard Euler's Integral: A Historical Profile of the Gamma Function". *American Mathematical Monthly.* 66 (10): 849–869. doi:10.2307/2309786. Retrieved 3 December 2016.

31. Delinom RM (2009) Structural geology controls on groundwater flow: Lembang Fault case study, West Java, Indonesia. doi:10.1007/s10040-009-0453-z.
32. Department of Water Affairs and Forestry. (2006). Groundwater Resource Assessment II – Task 3, Recharge. Department of Water Affairs and Forestry, Pretoria.
33. de Swaan O., A. 1976. Analytical Solutions for Determining Naturally Fractured Reservoir Properties by Well Testing. SPE J. 16 (3): 117–122. SPE-5346-PA.
34. De Wit, M. J. and Roering, C. 1990. Episodes of formation and stabilization of the Kaapvaal craton in the Archean: an overview based on some selected recent data. In: J. M. Barton (ed.), The Limpopo Belt: A Field Workshop on Granulites and Deep Crustal Tectonics, Extended Abstract Vol. Rand Afrikaans University, Johannesburg and Foundation for Research and Development, Pretoria, pp. 42-52.
35. Du Toit, W.H. (2001). An investigation into the occurrence of groundwater in the contact aureole of large granite intrusions (batholiths) located west and northwest of
36. Debnath, L. (2004). "A brief historical introduction to fractional calculus". International Journal of Mathematical Education in Science and Technology. 35 (4): 487–501
37. Dziembowski, Z.M. (1976). Die geohydrologie van die Dendrongebied, distrik Pietersburg. Report GH 2878. Directorate Geohydrology, Department of Water Affairs and Forestry, Pretoria.
38. Ekosse, G., Van Den Heever, D.J.; De Jager, L. and Totolo, O. (2004). Mineralogy of Tailings Dump around Selebi Phikwe Nickel-Copper Plant, Botswana. Journal of Applied Sciences and Environmental Management, 8(1):37-44.
39. Fetter, C.W., 1988, Applied hydrogeology (2nd ed.): Columbus, Ohio, Merrill Publishing, 592 p.
40. Fisher RS, Mulican WF III (1997) Hydrochemical evolution of sodium-sulfate and sodium-chloride groundwater beneath the northern Chihuahuan desert, Trans-Pecos, Texas, USA. Hydrogeol J 10:455–474

41. Foose, M.P.; Zientek, M.L., and Klein, D.P. (1995). Magmatic Sulfide Deposits. In: du Bray, E.A. (Ed.), Preliminary compilation of descriptive geoenvironmental mineral deposit models, Open-File Report 95-831. U.S. Department of the Interior: U.S. Geological Survey.
42. Freeze, R.A., and Cherry, J.A., 1979, Groundwater: New Jersey, Prentice Hall.
43. Geier, J.E., K Lee, and W.S. dershwitz, 1989. "Field Validation of Conceptual Models for Fractures Geometry". Rock Mechanics and Rock Engineering.
44. Geller, W., Friese, K., Herzsprung, P., Kringel, R., Schultze, M., 2000. Limnology of sulphur-acidic mining lakes. II Chemical properties: the main constituents and buffering systems. Verhandlungen des Internationaly Verein Limnologie 27, 2475–2479.
45. Gerrit van Tonder and Yongxin Xu, Eddie van Wyk. 2001. A guide for the estimation of groundwater rehxarge in South Africa. Presented at the Workshop on Recharge At the University of Pretoria. DWAF.
46. Gomez-Aguilar JF, Escobar-Jimenez RF, Lopez-Lopez MG , Alvarado-Martinez VM, Cordova-Fraga T., 2016 Electromagnetic waves in conducting media described by a fractional derivative with non-singular kernel , Journal of Electromagnetic Waves and Applications, 1-11.
47. Gomo, M., van Tonder, J.G., Steyl, G., 2012. Investigation of the hydrogeochemical processes in an alluvial channel aquifer located in a typical Karoo Basin of Southern Africa. Environ. Earth Sci.. <http://dx.doi.org/10.1007/s12665-012-2118-9>.
48. Guler C, Thyne GD, McCray JE, Turner AK (2002) Evaluation of graphical and multivariate statistical methods for classification of water chemistry data. Hydrogeol J 10:455–474
49. Gustafson, G. and Krásný, J. 1994. Crystalline rock aquifers: Their occurrence, use and importance. Applied Hydrogeology, 2: 64-75.
50. Guthrie, G.D., Carey, J.W., Bergfeld, D., Chipera, S., Ziock, H.-J., Lackner, K., 2001. Geo- chemical aspects of the carbonation of magnesium silicates in aqueous medium. In: NETL Meeting on Carbon Capture and Sequestration.

51. Harris C, Chaumba JB (2001) Crustal contamination and fluid-rock interaction during the formation of the Platreef, northern lobe of the Bushveld Complex, South Africa. *J Petrol* 42:1321–1347.
52. Hantush, M.S., 1961a. Drawdown around a partially penetrating well, *Jour. of the Hyd. Div., Proc. of the Am. Soc. of Civil Eng.*, vol. 87, no. HY4, pp. 83-98.
53. Hantush, M.S., 1961b. Aquifer tests on partially penetrating wells, *Jour. of the Hyd. Div., Proc. of the Am. Soc. of Civil Eng.*, vol. 87, no. HY5, pp. 171-194.
54. Havlin S. and Ben-Avraham D., 1987. Diffusion in disordered media. *Advances in Physics*: 36(6), 695.
55. Harbaugh, A.W., and McDonald, M.G., 1996, User's documentation for MODFLOW-96 an update to the U.S. Geological Survey modular finite-difference ground-water flow model: U.S. Geological Survey Open-File Report 96-485, 56 p.
56. Hirata, T. (1989), Fractal dimension of fault system in Japan: Fractal structure in rock fracture geometry at various scales, *Pure Appl. Geophys.*, 121, 157–170.
57. H. K. Versteeg & W. Malalasekera (1995). An introduction to Computational Fluid Dynamics. Chapter 5, page 104.
58. H.K Versteeg & W. Malalasekera. An introduction to Computational Fluid Dynamics. Chapter:5. Page 105.
59. Iain McDonald, David A. Holwell, Paul E. B. Armitage. 2005. Geochemistry and mineralogy of the Platreef and "Critical Zone" of the northern lobe of the Bushveld Complex, South Africa: implications for Bushveld stratigraphy and the development of PGE mineralisation. *Mineralium Deposita* (2005)40: 526–549. DOI 10.1007/s00126-005-0018-6.
60. Igor Shiklomanov, 1993. "World fresh water resources" in Peter H. Gleick (editor), 1993, *Water in Crisis: A Guide to the World's Fresh Water Resources* (Oxford University Press, New York).
61. Jankowski J, Beck P (2000) Aquifer heterogeneity: hydrogeological and hydrochemical properties of the Botany Sands aquifer and their impact on contaminant transport. *Aust J Earth Sci* 47(1):45–64.

62. Jarvis, K., Carpenter, R., Windman, T., Kim, Y., Nunez, R., Alawneh, F., 2009. Reaction mechanisms for enhancing mineral sequestration of CO₂. *Environmental Science and Technology* 43 (16) ,6314–6319.
63. Johnson, R.H.; Blowes, D.W.; Robertson, W.D. and Jambor, J.L. (2000). The hydrogeochemistry of the Nickel Rim mine tailings impoundment, Sudbury, Ontario. *Journal of Contaminant Hydrology*, 4: 49-80.
64. Jolly, J.L. (1986). Borehole/irrigation survey and groundwater evaluation of the Doringlaagte drainage basin, Dendron (N.Tvl.). Report GH 3495. Directorate Geohydrology, Department of Water Affairs and Forestry, Pretoria.
65. Katherine Louise Lishman, 2009. The acid mine drainage potential of the Platreef, Northern Limb of the Bushveld Complex, South Africa. A dissertation submitted to the Faculty of Science, University of the Witwatersrand, in fulfilment of the requirements for the degree of Master of Science.
66. Kinnaird, J.A. and McDonald, I. (2005). Mineralisation in the northern limb of the Bushveld Complex. *Applied Earth Science (Trans. Inst. Min. Metall. B)*, 114: B194-B198.
67. Koca I, 2015. A method for solving differential equations of q-fractional order. *Appl Math Comput*: 266 ,1–5
68. Koca I., Abdon Atangana, 2016, Solutions of Cattaneo-Hristov model of elastic heat diffusion with Caputo-Fabrizio and Atangana- Baleanu fractional derivatives, *Thermal Science*, DOI:10.2298/TSCI160102102M
69. Leveinen, J. (2000), Composite model with fractional flow dimensions for well test analysis in fractured rocks, *J. Hydrol.*, 234(3–4), 116–141.
70. Long, J.C.S and D Billaux, 1987. "From field data to fractures network modelling: an example incorporating spatial structures". *Water Resources Research*, Vol. 23, pp. 1201-1216.
71. Martin Holland, 2011. Hydrogeological characterisation of crystalline basement aquifers within the Limpopo Province, South Africa. PhD Thesis. University of Pretoria.

72. McCourt, S. and Van Reenen, D. D. 1992. Structural geology and tectonic setting of the Sutherland greenstone belt, Kaapvaal Craton, South Africa. *Precambrian Res.* V. 55, pp. 93-110.
73. McGowan, W., 2000. *Water Processing: Residential, Commercial, Light-Industrial*, 3rd ed. Water Quality Association, Lisle, Illinois, USA.
74. Mkweli, S., Kamber, B. and Berger, M. 1995. A westward continuation of the Zimbabwe craton-NMZ tectonic break and new age constraints on the timing of the thrusting. *Journal of the Geological Society of London*, V. 152, pp. 77-83.
75. Moench, A.F. (1984). Double-porosity models for a fissured groundwater reservoir with fracture skin. *Water Resour. Res.*, 20(7): 831-846.
76. Moench, A.F. (1997). Flow to a well of finite diameter in a homogeneous, anisotropic water-table aquifer. *Water Resour. Res.*, 33(6): 1397-1407.
77. Nel, M. (2000). *Geohidrologiese evaluering van 'n gedeelte van die Sand Rivier opvanggebied Pietersburg distrik, Noord Provinsie*. GH 3947. Directorate Geohydrology, Department of Water Affairs and Forestry, Pretoria.
78. Neuman, S.P., 1974. Effect of partial penetration on flow in unconfined aquifers considering delayed gravity response, *Water Resour. Res.*, 10(2): 303-312.
79. Nordstroom, D.K., Alpers, C.N., 1999. Geochemistry of acid mine waters. In: Plumlee, G.S., Logston, M.D. (Eds.), *The Environmental Geochemistry of Mineral Deposits: Part A. Processes, Methods, and Health Issues*. Society of Economic Geologists, Littleton, CO., *Reviews in Economic Geology*, vol. 6A. pp. 133-160.
80. Oldham, Keith B.; Spanier, Jerome (1974). *The Fractional Calculus; Theory and Applications of Differentiation and Integration to Arbitrary Order*. Mathematics in Science and Engineering. V. Academic Press. ISBN 0-12-525550-0.
81. Orpen, W.R.G. (1986). A preliminary evaluation of the possible groundwater resources within a radius of 30 km of Pietersburg for use by the municipality. Report GH 3465. Directorate Geohydrology, Department of Water Affairs and Forestry, Pretoria.
82. O'Shaughnessy, B., and I. Procaccia (1985), Diffusion on fractals, *Phys. Rev. A*, 32(5), 3073-3083.

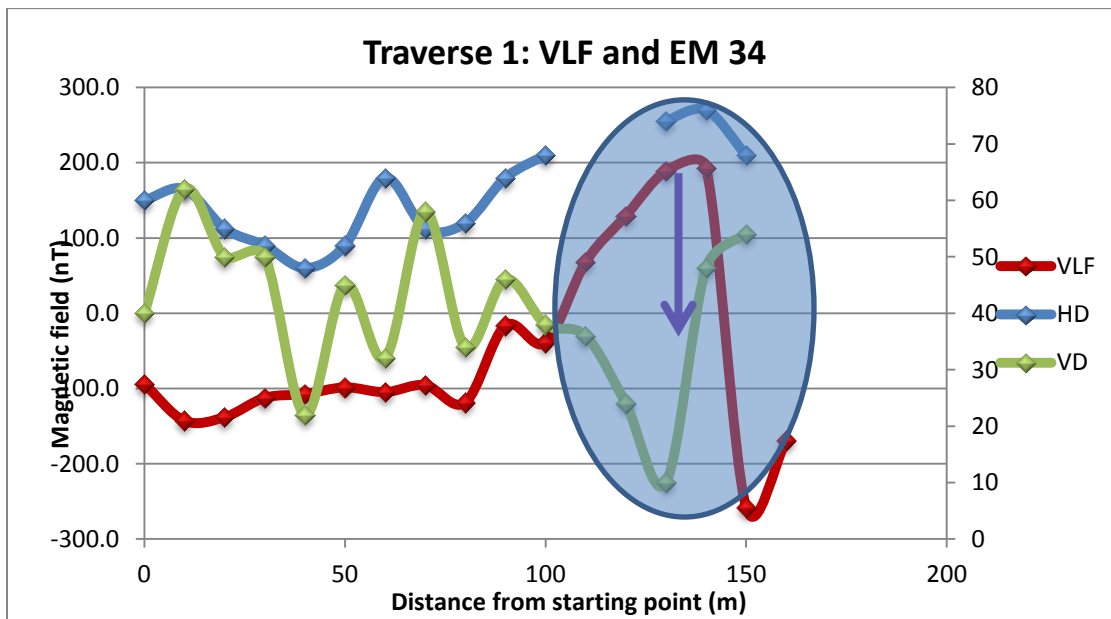
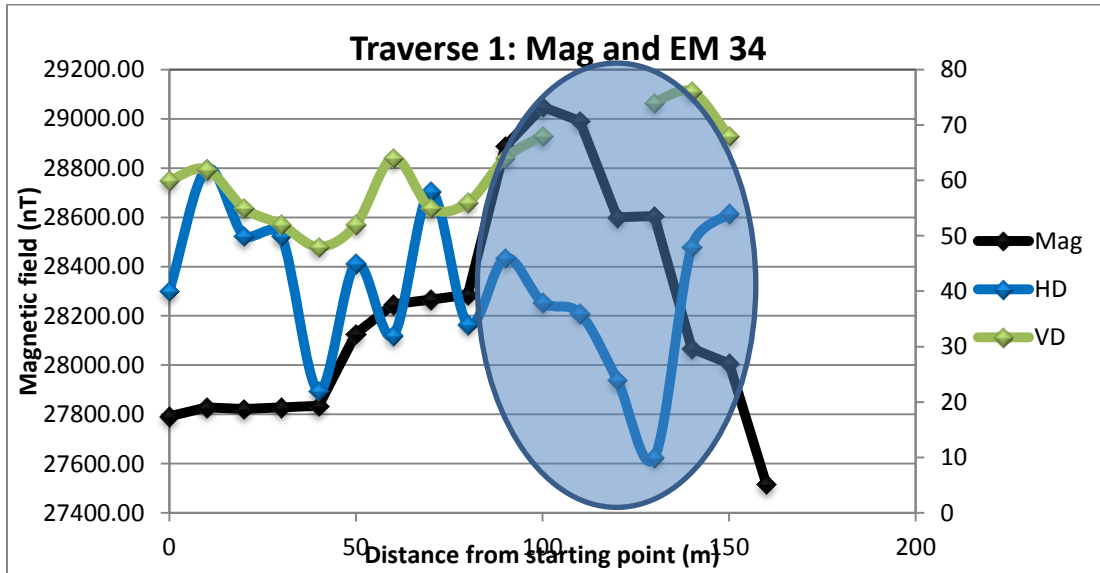
83. Parkhurst, D.L., Appelo, C.A.J., 1999. PHREEQC for windows version 1.4.07. A hydrogeochemical transport model. US Geological Survey Software. Washington.
84. Pietersburg. Report GH 3923. Directorate Geohydrology, Department of Water Affairs and Forestry, Pretoria.
85. Piper, A.M. (1944). A graphic procedure in the geochemical interpretation of water-analyses. Transactions, American Geophysical Union 25: doi: 10.1029/TR025i006p00914. issn: 0002-8606.
86. P.J. and Foster, S.S.D. (1995). Hydrological characterization and water-supply potential of basement aquifers in tropical Africa. Hydrogeol J., 3: 36-49.
87. Renard, P., Glenz, D. And Mejias, M. (2009). Understanding diagnostic plots for well-test interpretation. Hydrogeol. J., 17: 589-600.
88. Roering, C. Van Reenen, D.D., Smit, C.A., Barton, J.M. Jr., De Beer, J.H., De Wit, M.J., Stettler, E.H. Van Schalwyk, J.F. Stevens, G. and Pretorius, S.J. (1992). Tectonic model for the evolution of the Limpopo Belt. Precambrian Research, 55: 539-552.
89. Rose, A.W., Cravotta III, C.A., 1998. Geochemistry of coal mine drainage. In: Brady, K.B.C., Smith, M.W., Schueck, J. (Eds.), Coal Mine Drainage Prediction and Pollution in Pennsylvania. Bureau of Mining and Reclamation, Pennsylvania Department of Environmental Protection, Harrisburg.
90. Ross, B. (1975). "A brief history and exposition of the fundamental theory of fractional calculus". Fractional Calculus and Its Applications. Lecture Notes in Mathematics. 457: 1-36
91. SACS (1980). Lithostratigraphy of the Republic of South Africa, South West Africa/Namibia, and the Republics of Bophuthatswana, Transkei and Venda. In: Kent, L. E. (ed.) Stratigraphy of South Africa, Part 1. Pretoria: Geological Survey of South Africa, p. 690.
92. SANS 241-1:2015. Drinking Water, Part1: Microbiological, physical, aesthetic, and chemical determinands. The South African Bureau of Standards, ISBN 978-0-626-29841-8. Pretoria, South Africa.

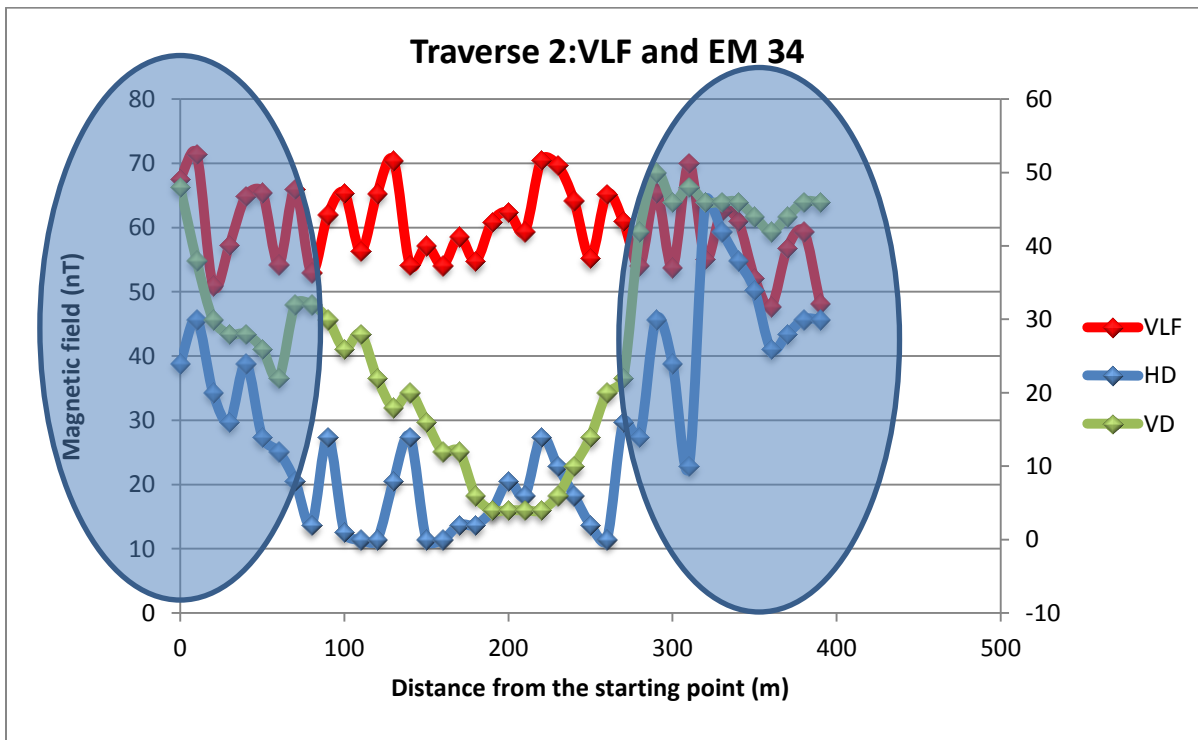
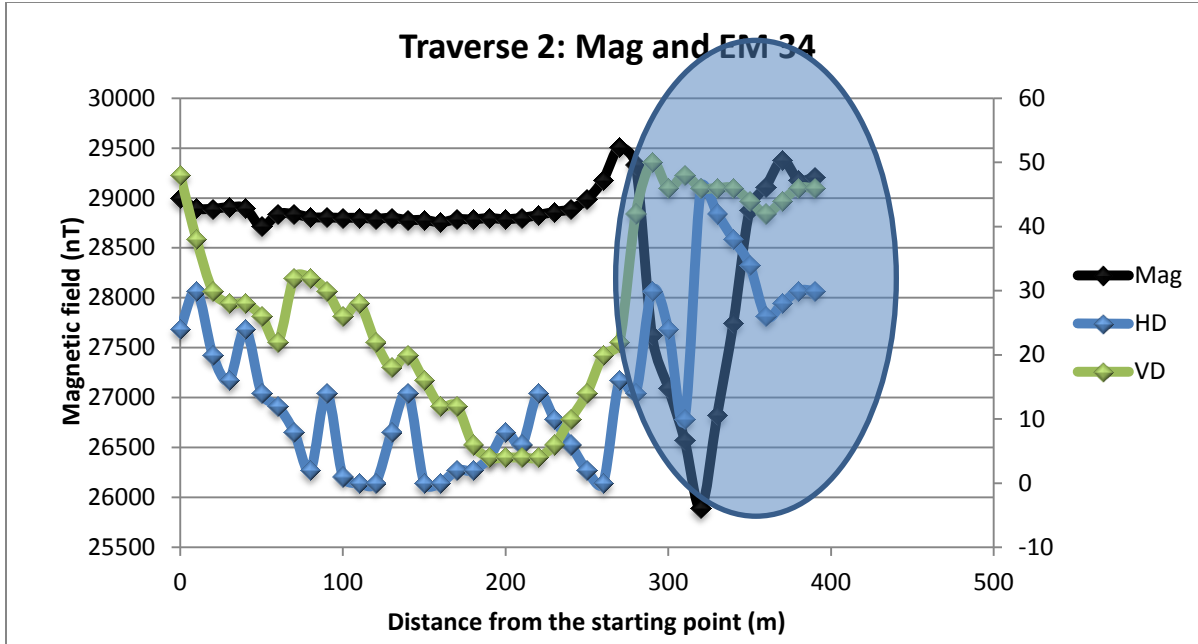
93. Serra, K., Reynolds, A.C., and Raghavan, R. 1983. New Pressure Transient Analysis Methods for Naturally Fractured Reservoirs (includes associated papers 12940 and 13014). *J Pet Technol* 35 (12): 2271-2283.
94. Stuart, G. W., and Zengeni, T.G. 1987. Seismic crustal structure of the Limpopo Mobile Belt, Zimbabwe. *Tectonophysics*, V. 144, pp. 323-335.
95. Spitz, K., and Moreno, J., 1996. A practical guide to groundwater and solute transport modelling. John Wiley and Sons, Inc.
96. Soregaroli, B.A. and Lawrence, R.W. (1998). Update on Waste Rock Characterization Studies, Proc. Mine Design, Operations and Closure Conference, Polson, Montana.
97. Tawanda D. Manyeruke, Wolfgang D. Maier, Sarah-Jane Barnes. 2005. Major and trace element geochemistry of the Platreef on the farm Townlands, northern Bushveld Complex. *South African Journal of Geology*, Volume 108 Page 381-396.
98. Teir, S., Revitzer, H., Eloneva, S., Goelholm, C.-J., Zevenhoven, R., 2007. Dissolution of natural serpentinite in mineral and organic acids. *International Journal of Mineral Processing* 83, 36-46.
99. Theis, C.V., 1935. The relation between the lowering of the piezometric surface and the rate and duration of discharge of a well using groundwater storage, *Am. Geophys. Union Trans.*, vol. 16, pp. 519-524.
100. Timmerman, K.M.G., L.R.A. and Orpen, W.R.G. 1983. Geohydrological investigation for the proposed military base near Louis Trichardt. Report GH 3286. Directorate Geohydrology, Department of Water Affairs and Forestry, Pretoria.
101. Van Reenen, D. D., Roering, C., Ashwal, L. D. and De Wit, M. J. (eds) 1992. The Archean Limpopo granulite belt: Tectonics and deep crustal processes. *Precambrian Research*, V. 55, 587 pp.
102. Van Tonder, G. Bardenhagen, I., Riemann, K. Van Bosch, J., Dzanga, P and Xu, Y. (2002). Manual on pumping test analysis in fractured rock aquifers. WRC Report No. 1116/1/02. Water Research Commission. Pretoria.
103. Vearncombe, J. R. 1991. The Murchison Belt, Kaapvaal Craton: A possible source for Witwatersrand gold. In: S. E. Ho and J. E. Cloves (eds.), Proc. 3rd Int. Archean

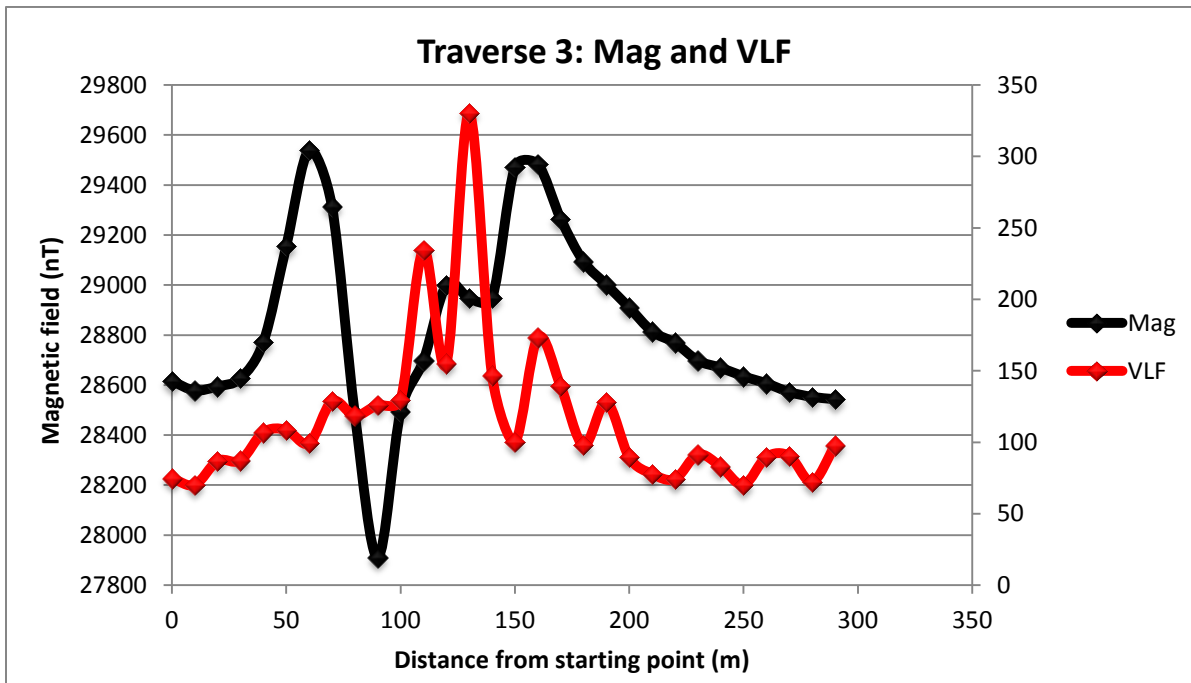
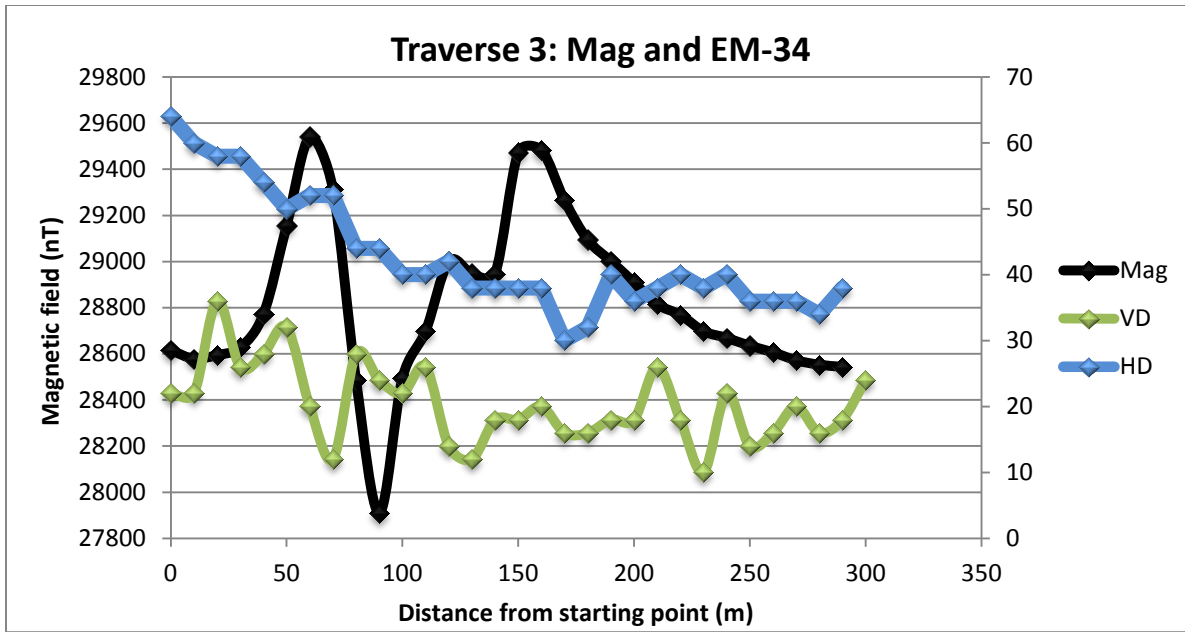
- Sym., Perth, 1990. Geological Department and University Extension, University of West Australia, publication 22.
104. Vegter, J.R. (2003a) Hydrogeology of groundwater regions, Region 7, Polokwane/Pietersburg Plateau. WRC Report No. TT 209/03. Water Research Commission, Pretoria.
105. Vermeulen, D., Usher, B., 2009. Operation and monitoring guidelines and the development of a screening tool for irrigating with coal mine water in Mpumalanga Province, South Africa. *Water SA* 35 (4), 379–386.
106. Viljoen MJ, Schürmann LW (1998) Platinum-group metals. In: Wilson MGC, Anhaeusser CR (eds) *The mineral resources of South Africa. Coun Geosci Handbook* 16:532–568.
107. Walton, W.C., 1962, selected analytical methods for well and aquifer evaluation: Illinois State Water Survey, Bulletin 49.
108. Warren, J.E. and Root, P.J. 1963. The Behavior of Naturally Fractured Reservoirs. *SPE J.* 3 (3): 245–255. SPE-426-PA
109. White JA (1994) The Potgietersrus prospect – geology and exploration history. In: Anhaeusser CR (ed) *Proceedings XVth CMMI Congress. S Afr Inst Min Metall, Johannesburg, vol. 3, pp 173–181.*
110. WHO, 2003. Total dissolved solids in drinking-water. Background document for development of WHO Guidelines for Drinking-water Quality. WHO/SDE/WSH/03.04/16. Geneva, Switzerland.
111. WHO, 2011. *Guidelines for Drinking-water Quality (fourth ed.)*. ISBN 978 92 4154815 1. Geneva, Switzerland.

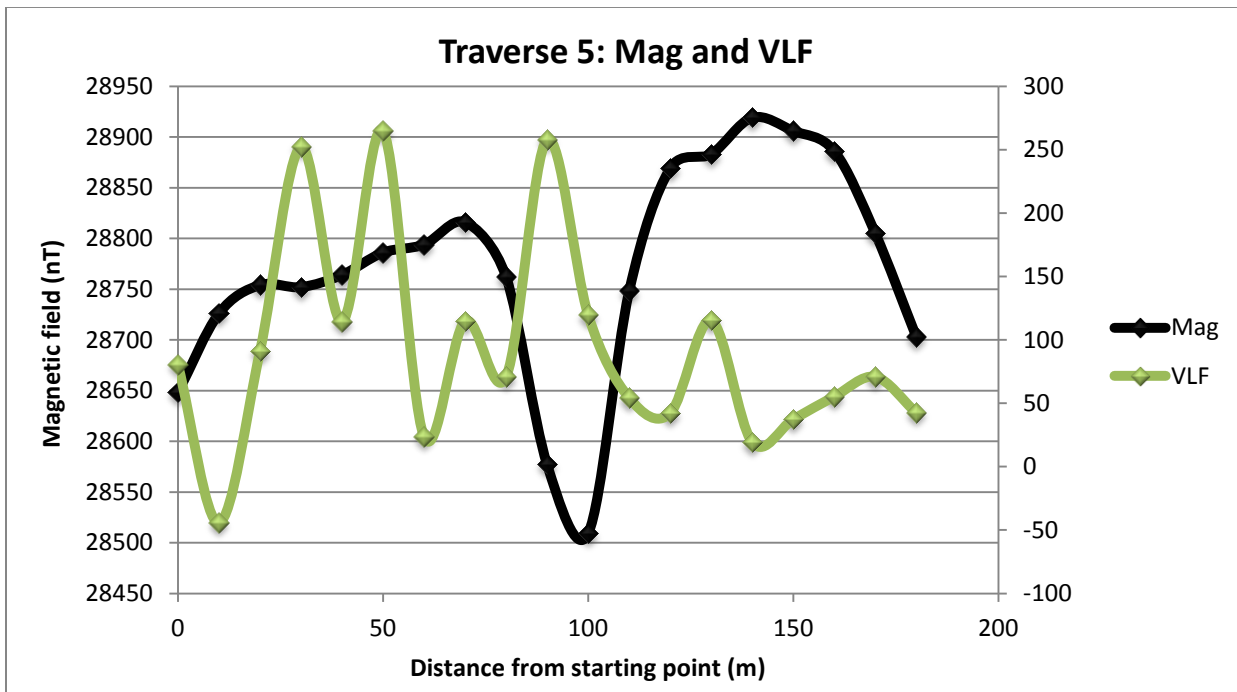
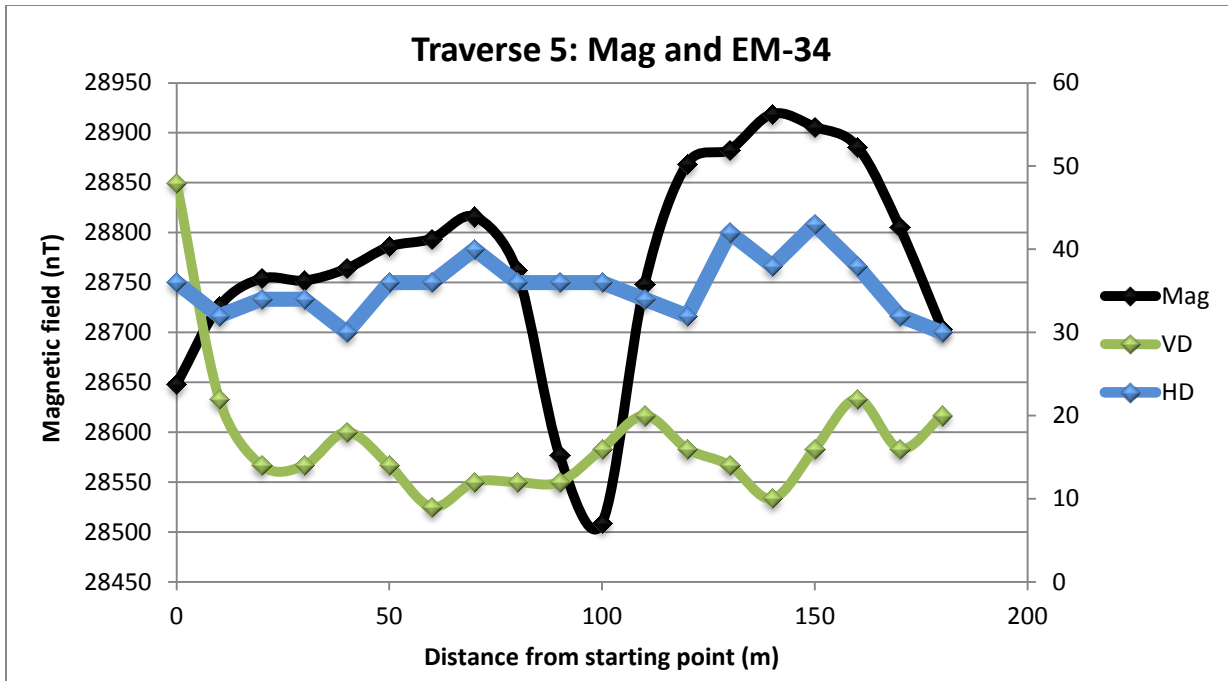
10 Appendices

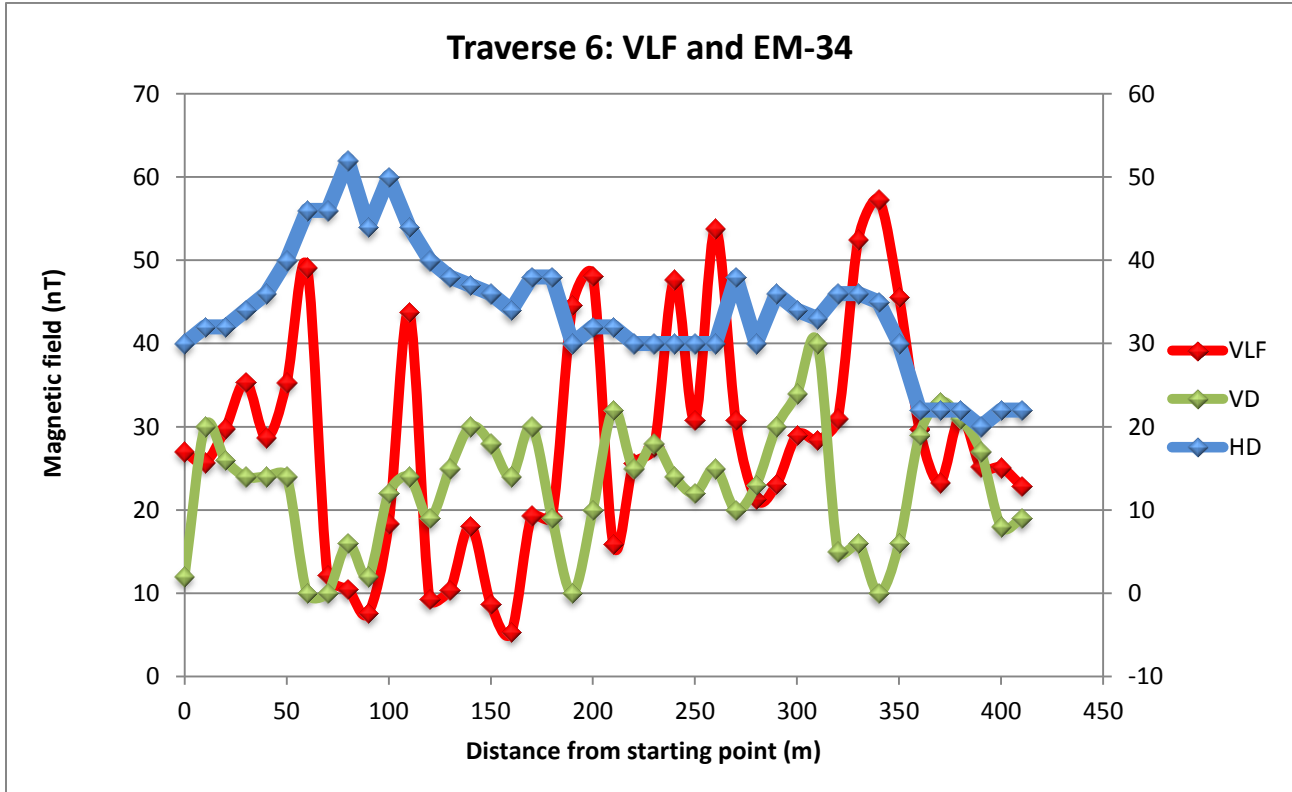
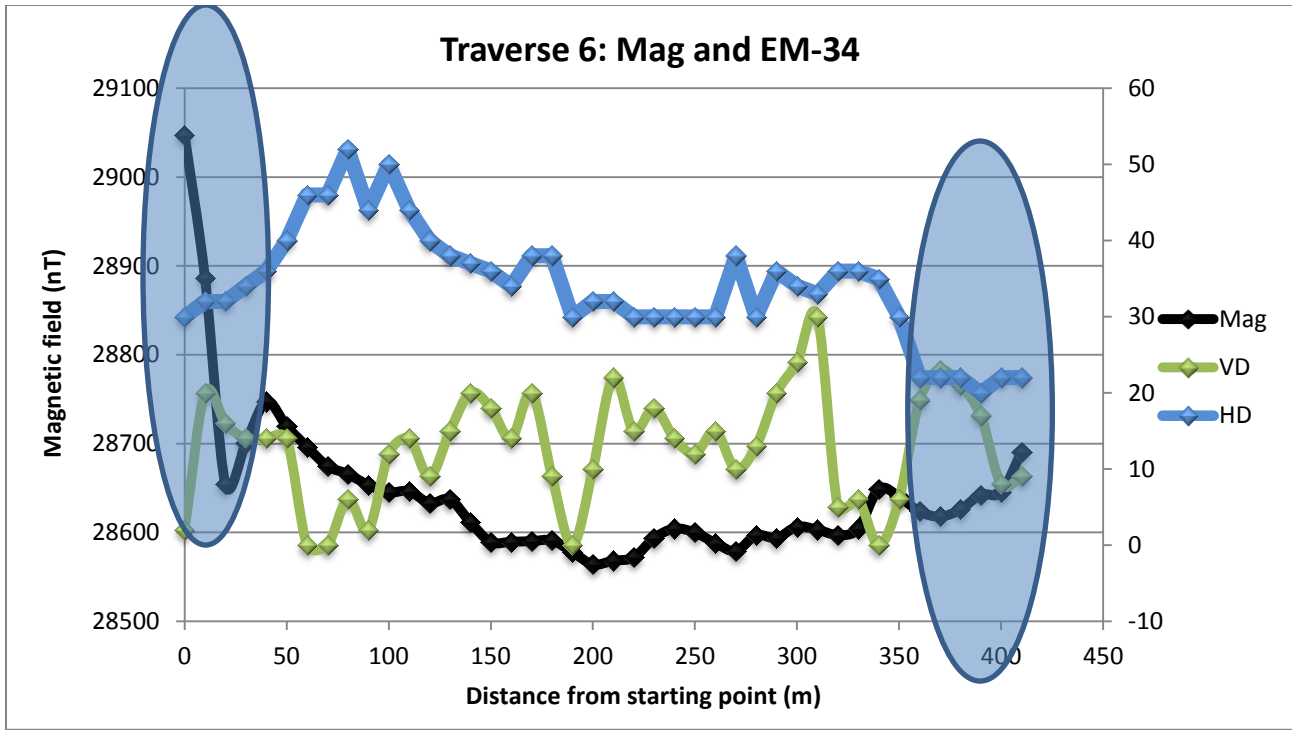
10.1 Appendix A: Geophysical survey results

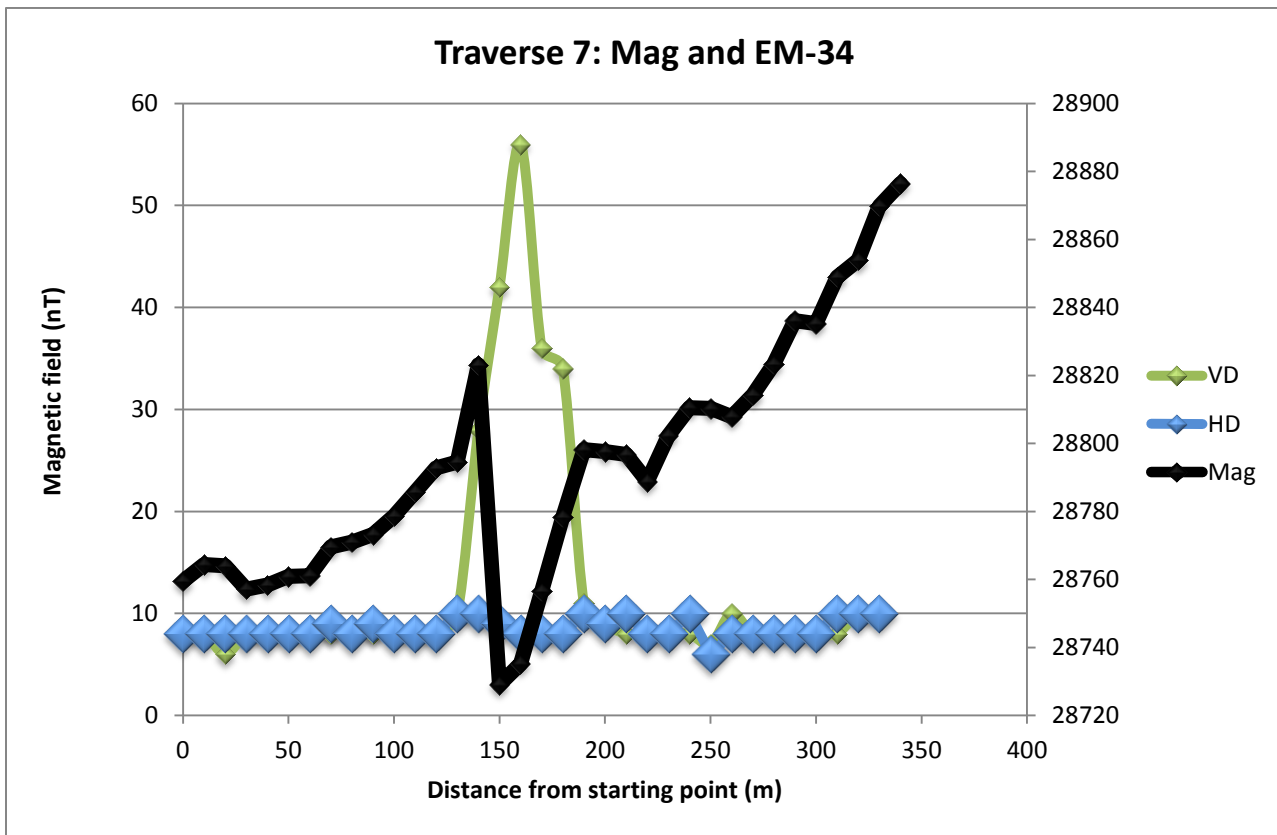
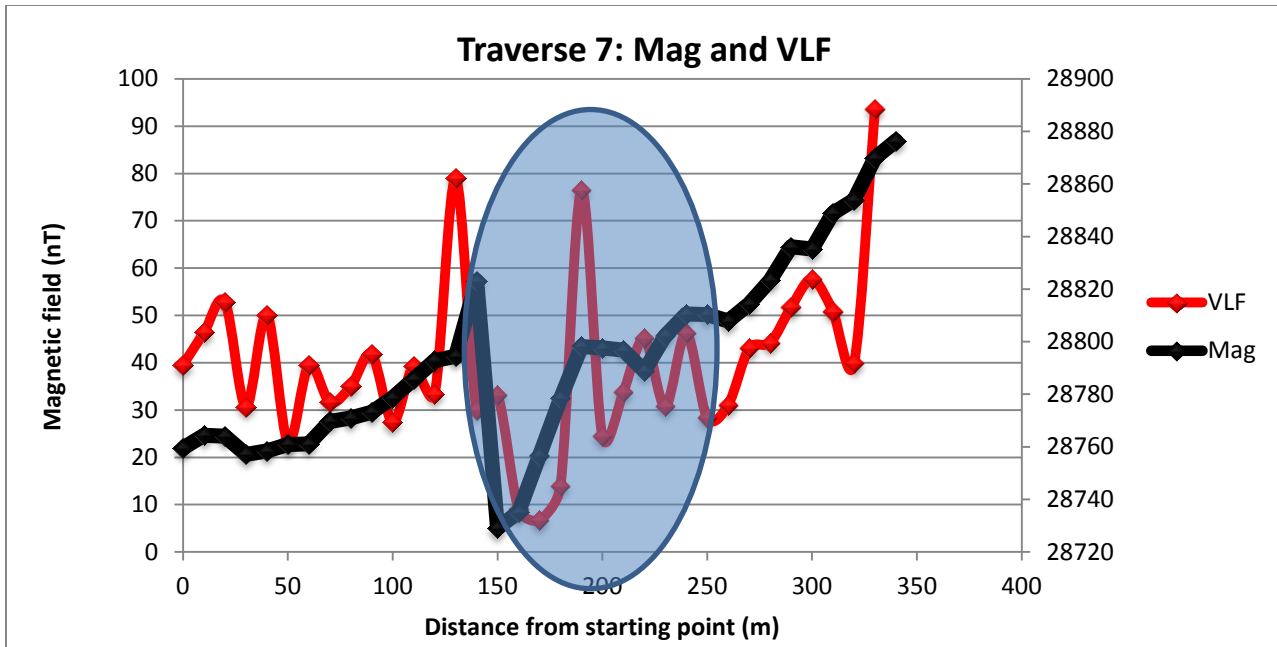


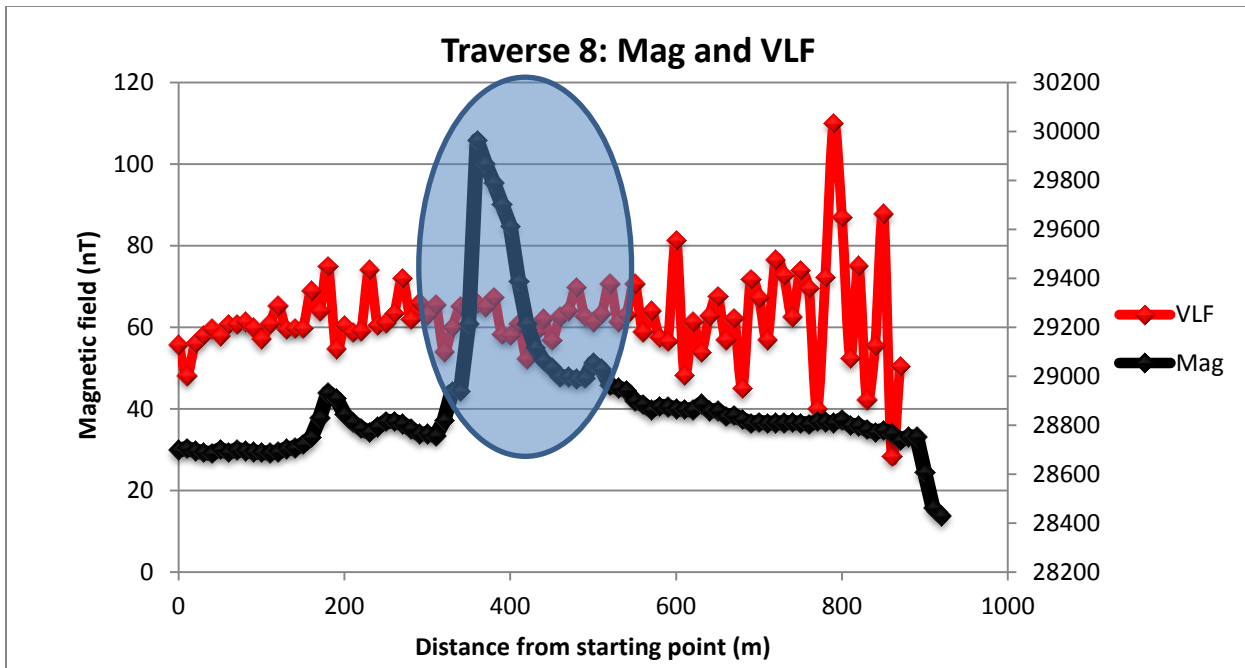
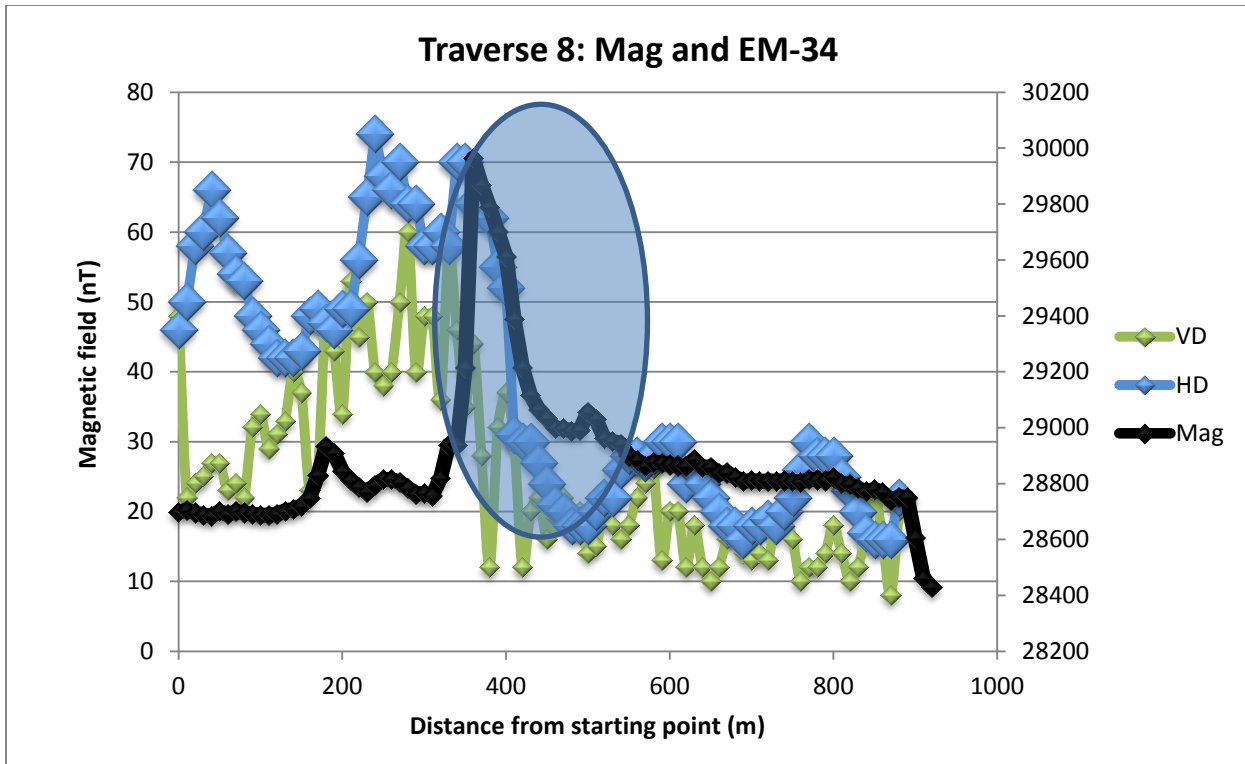


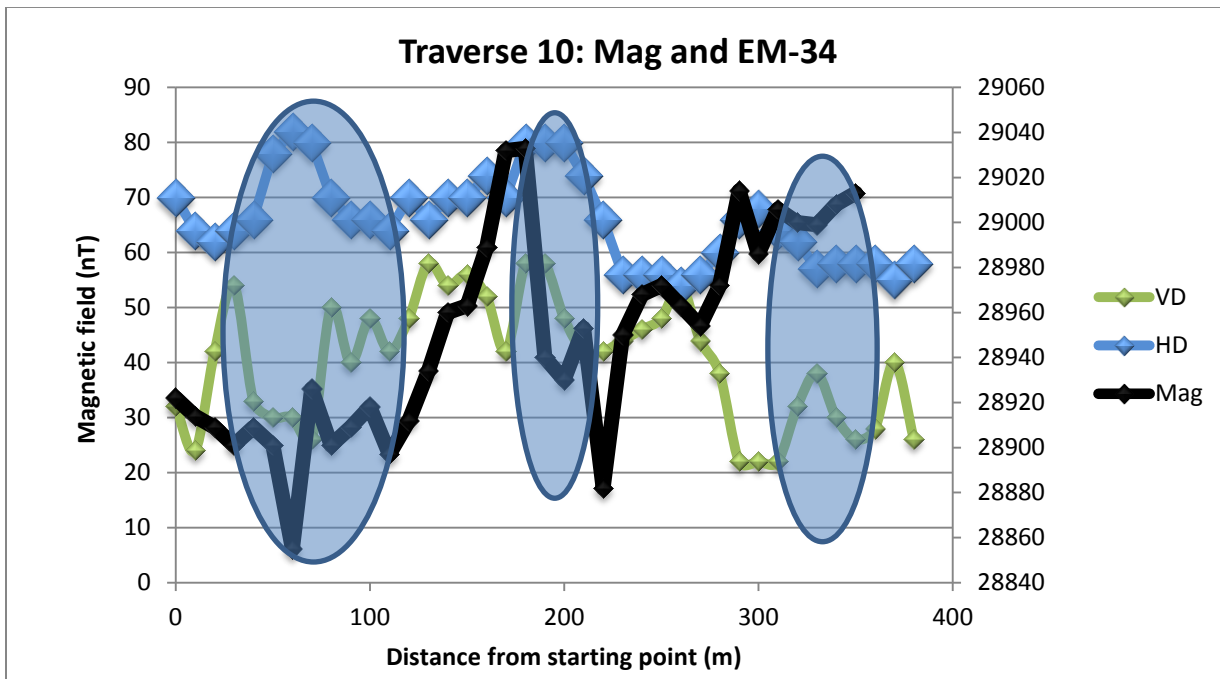
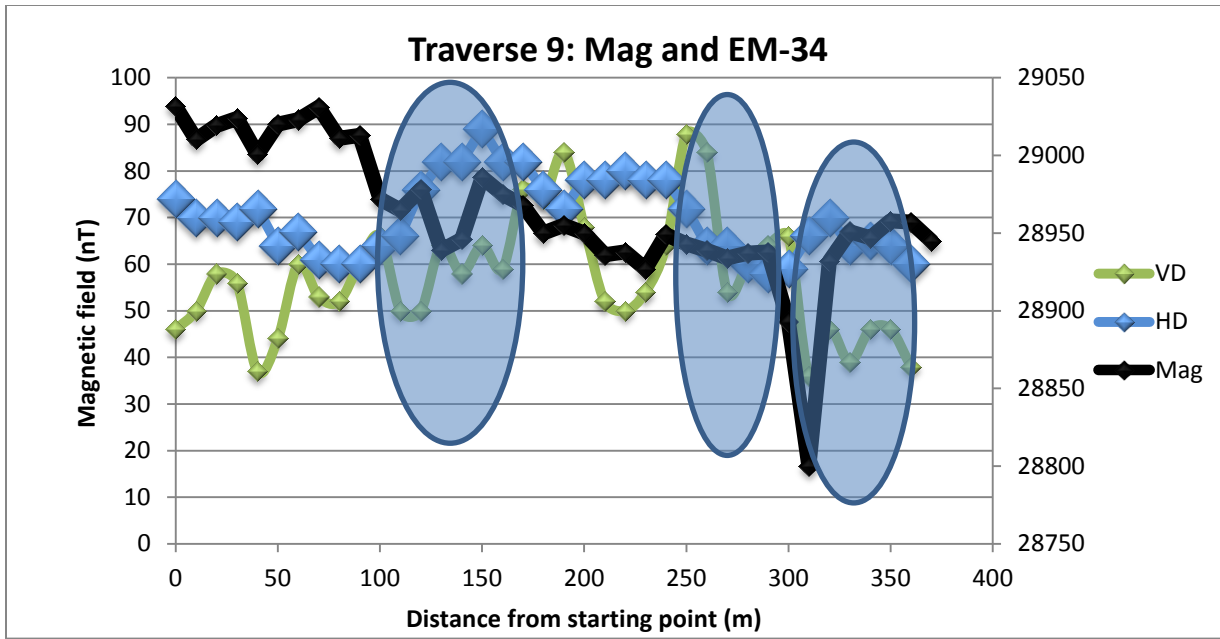


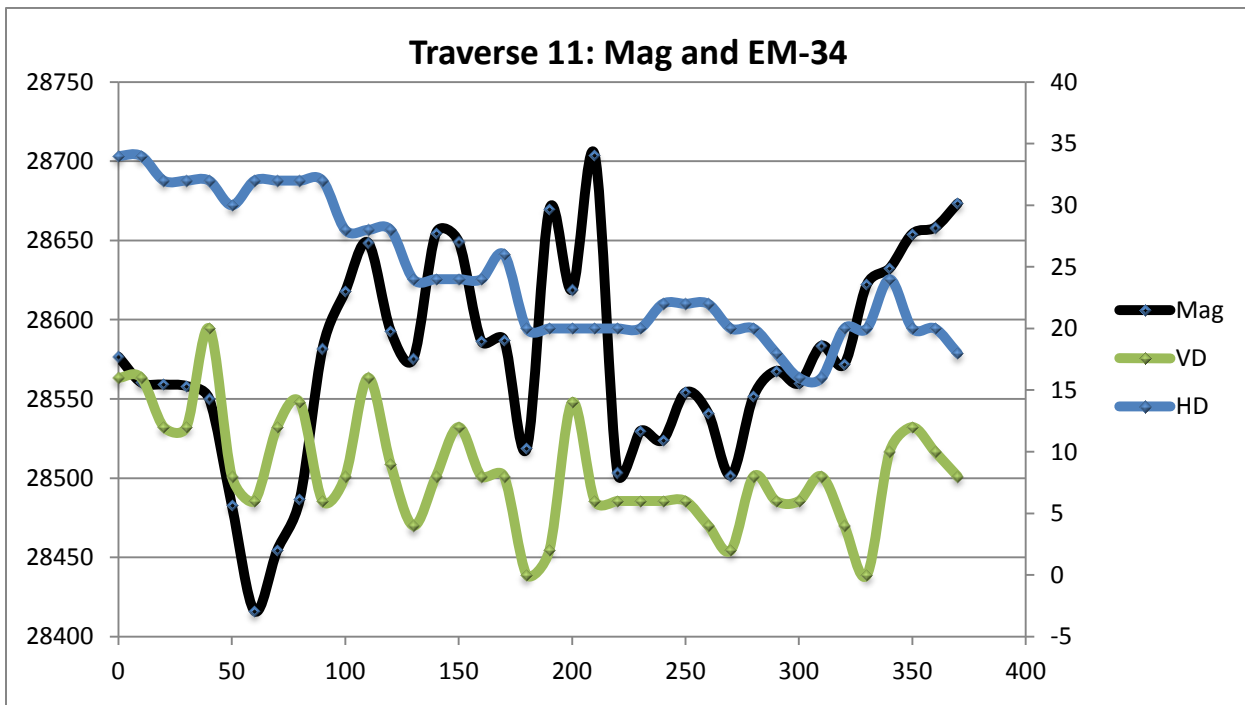
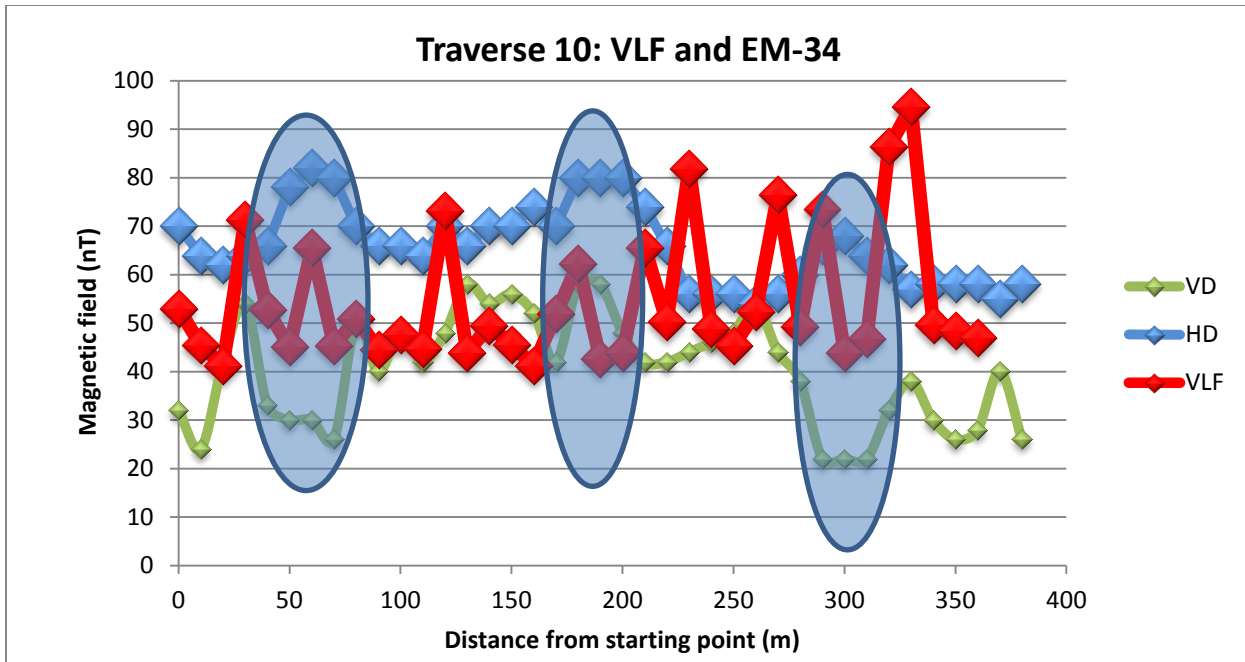


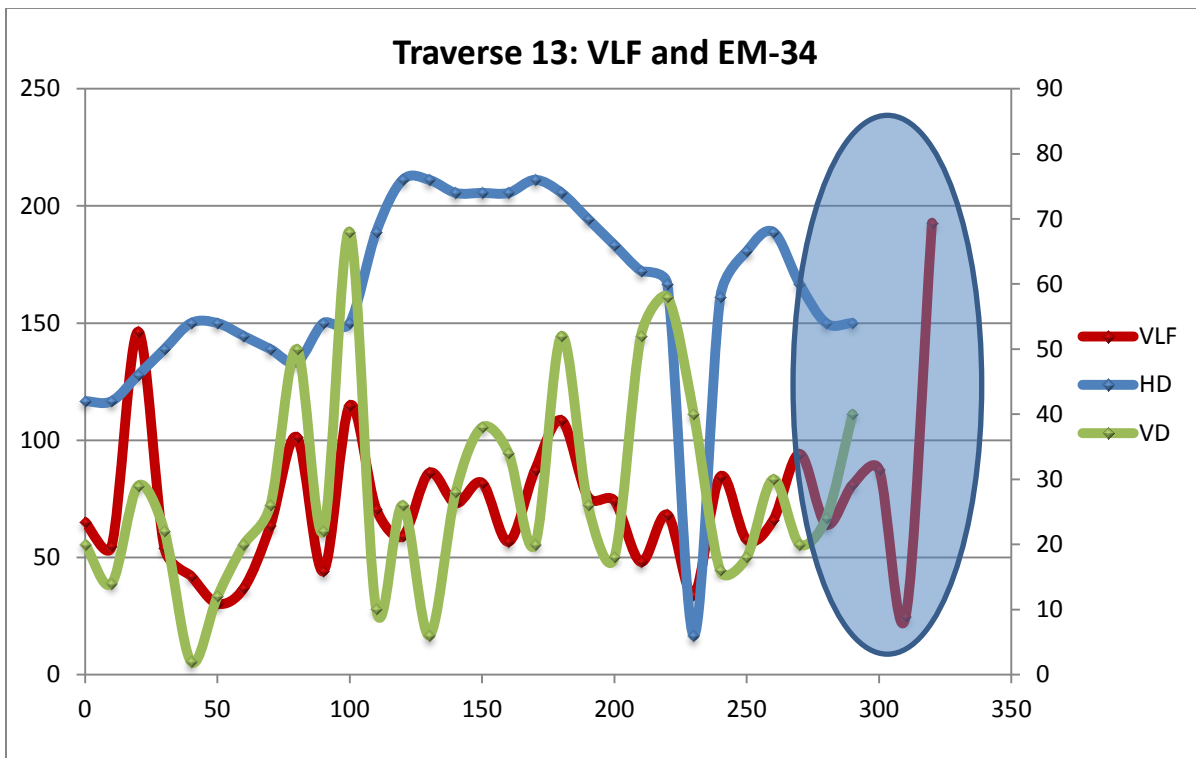
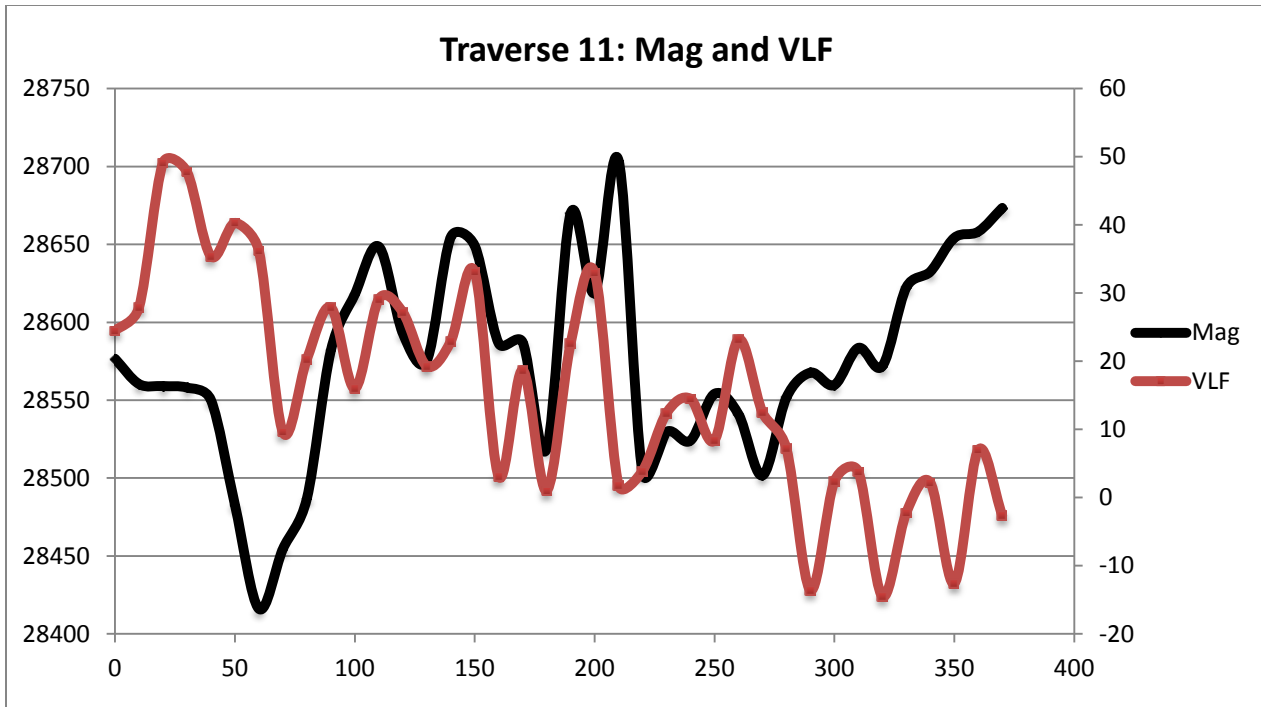


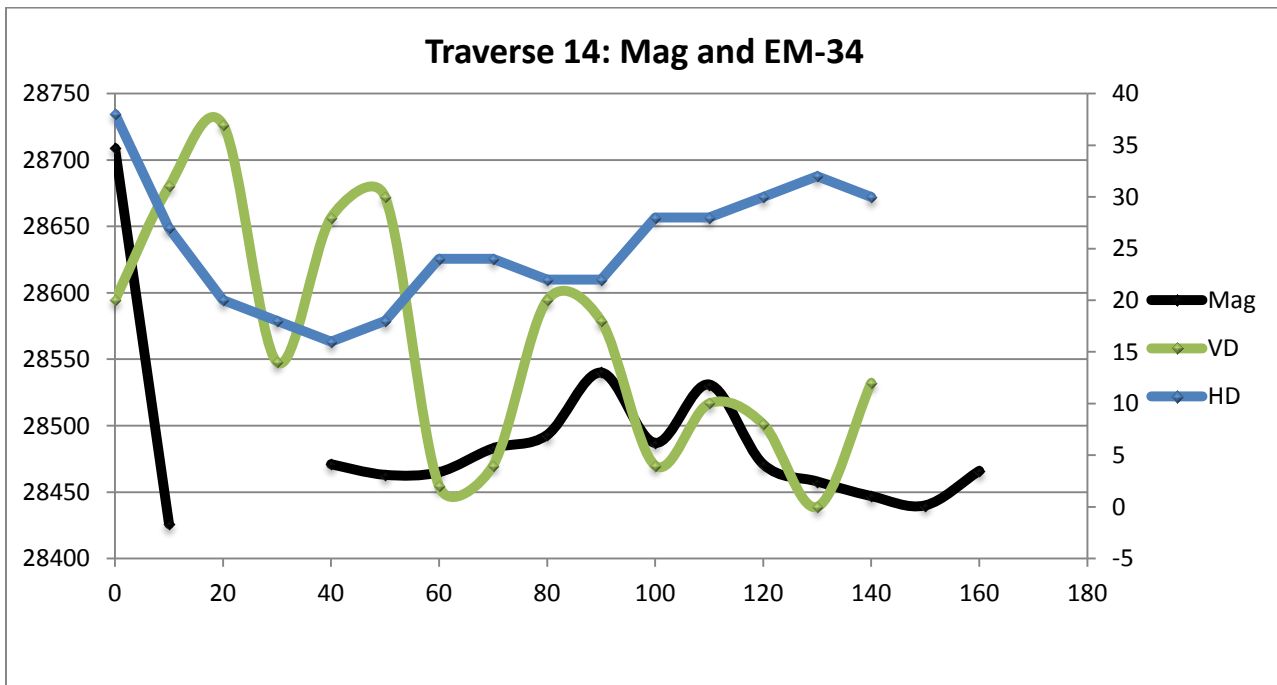
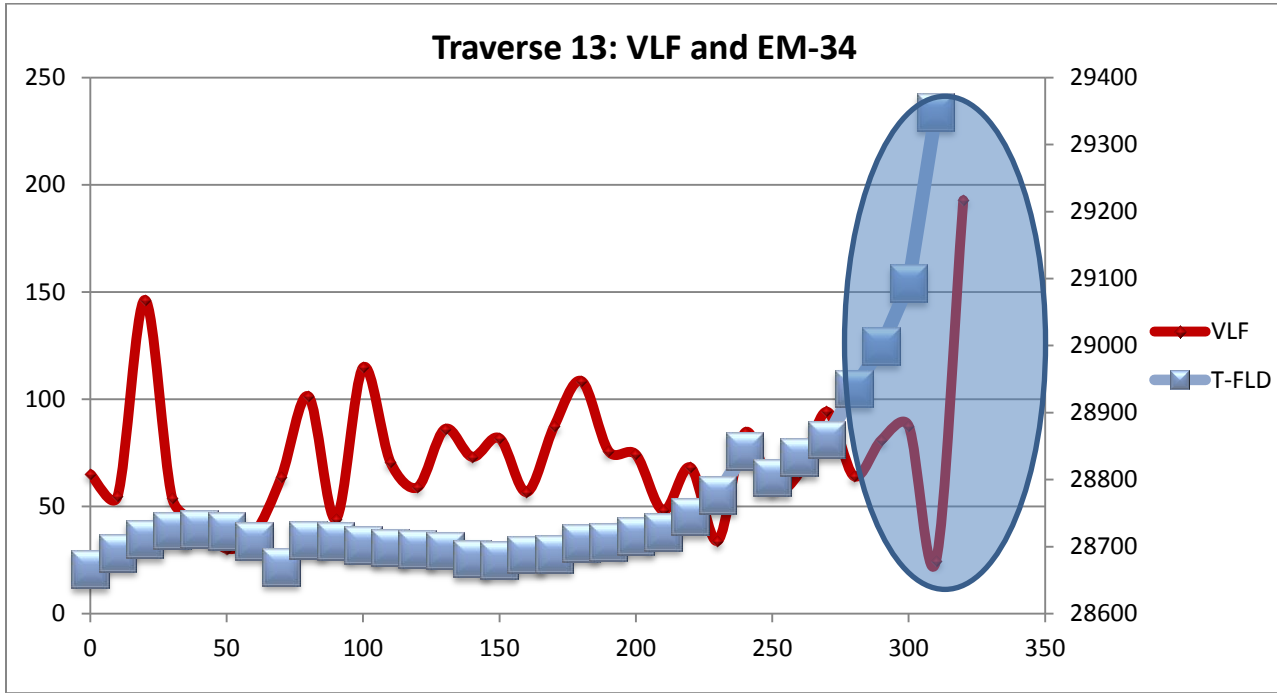


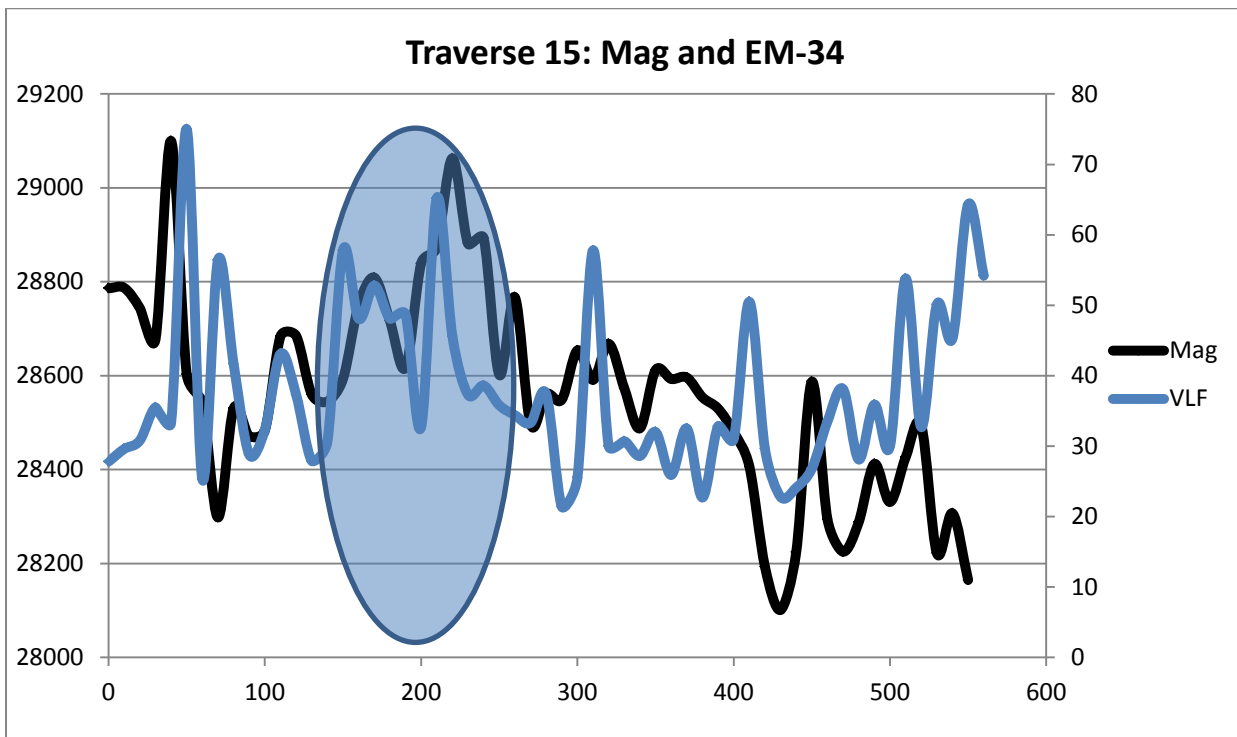
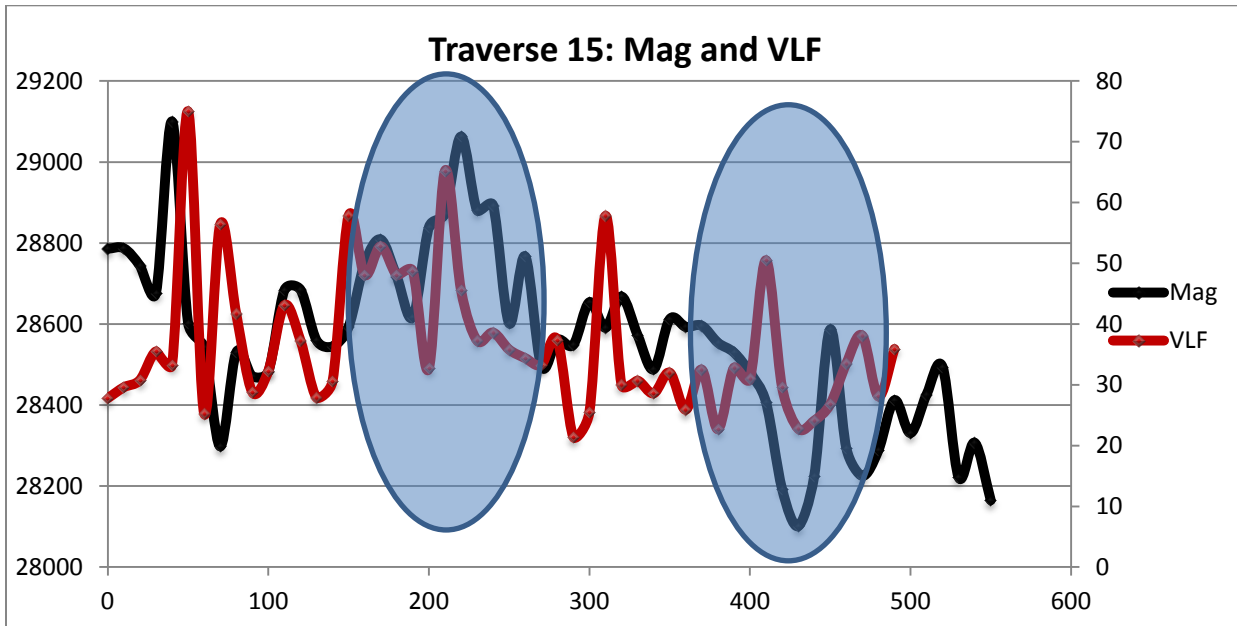


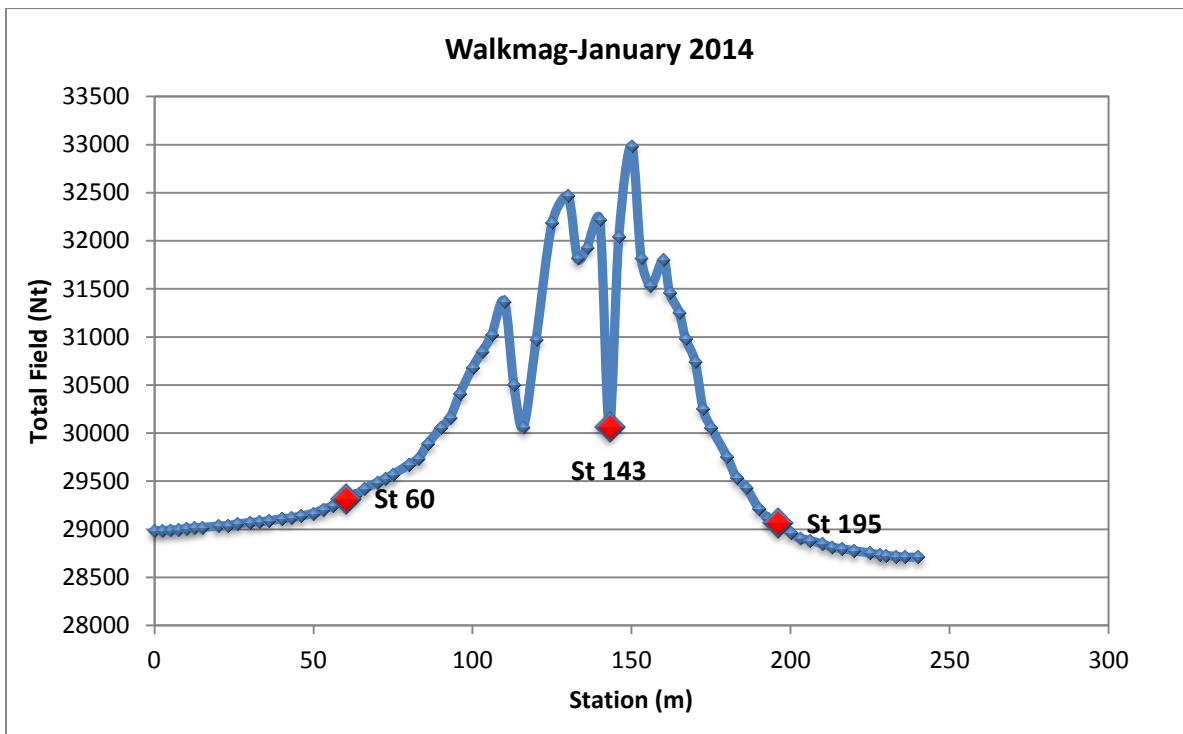
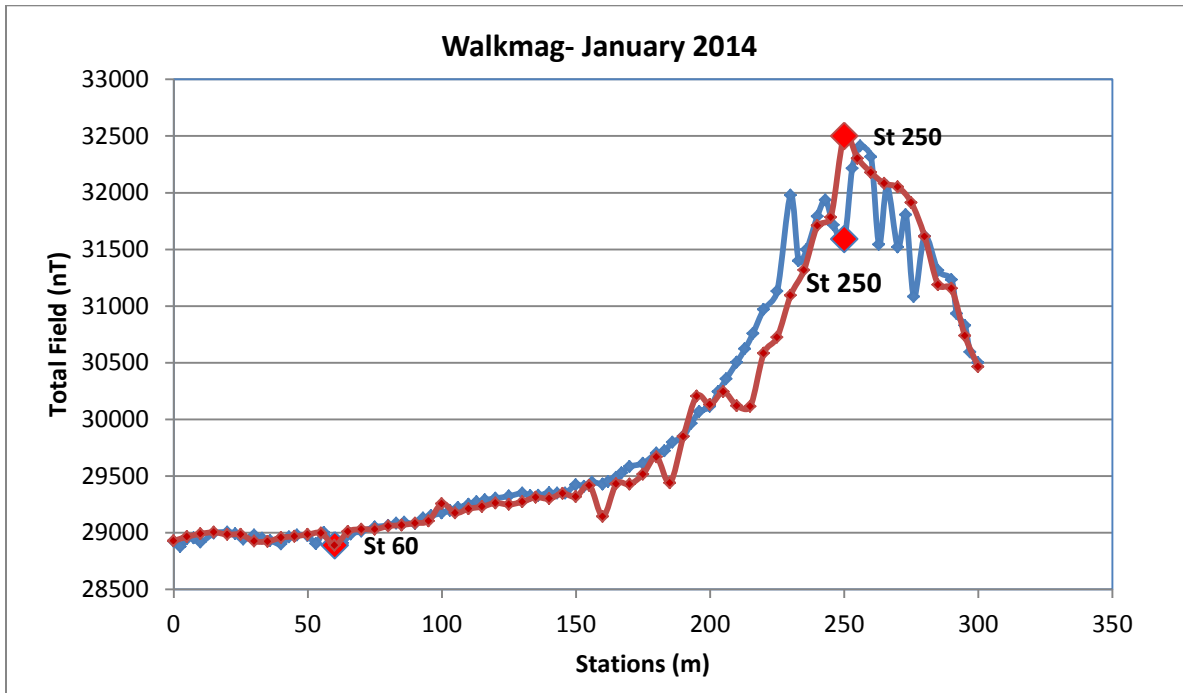


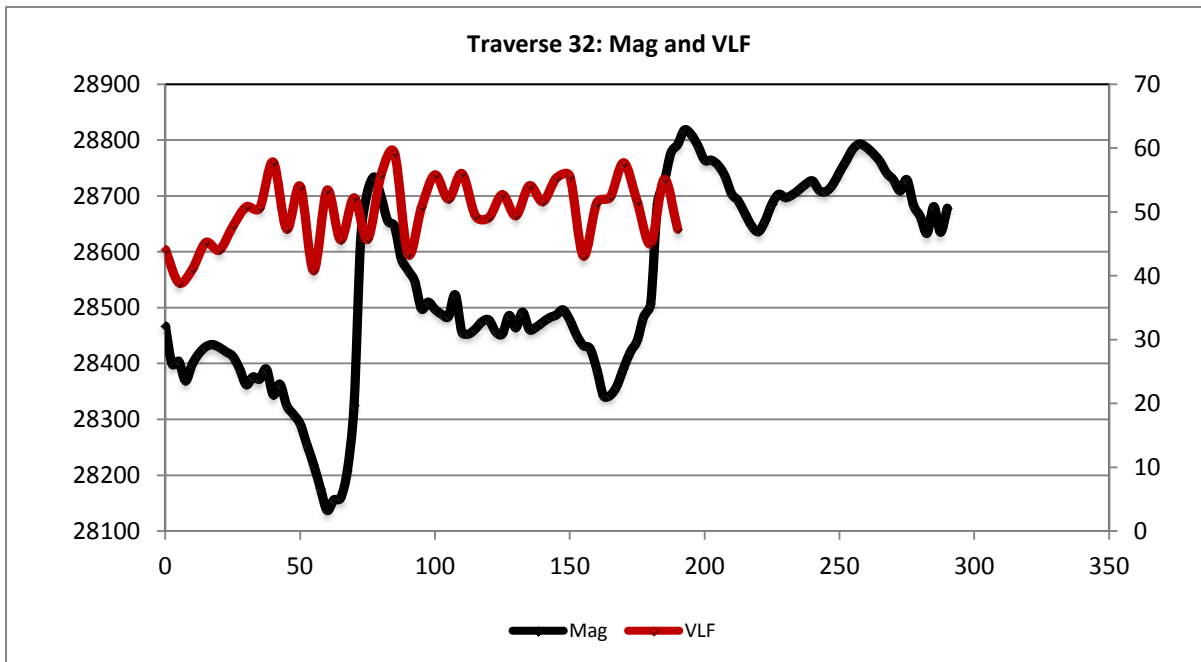
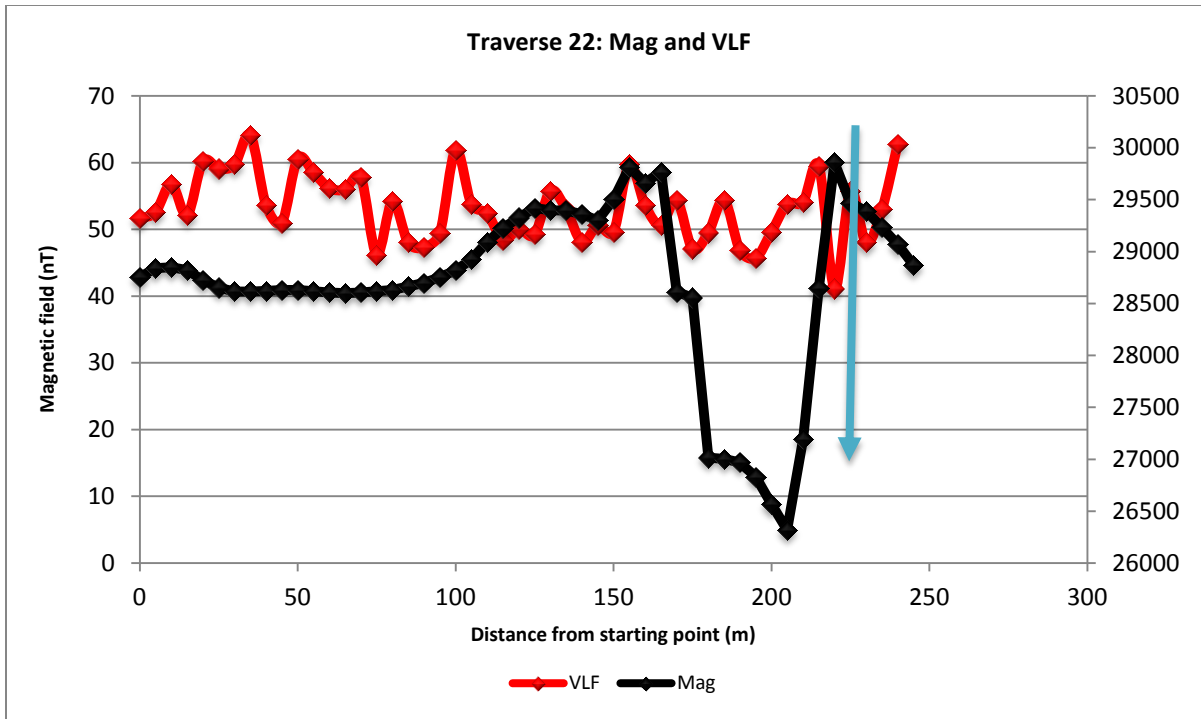


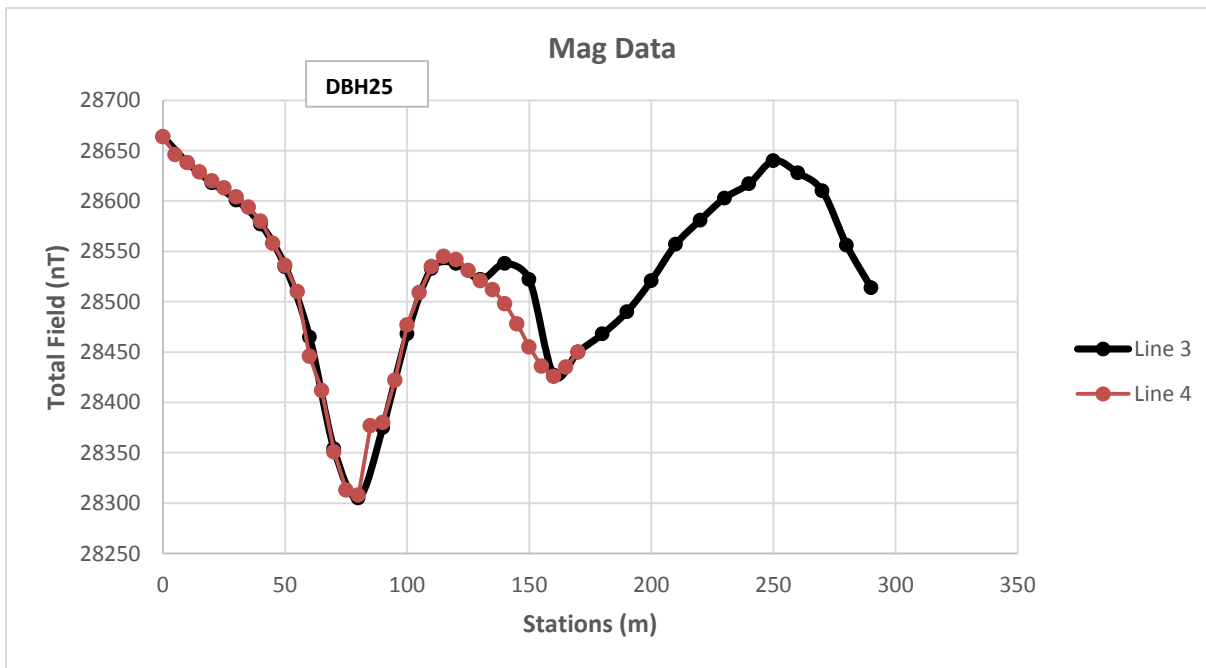
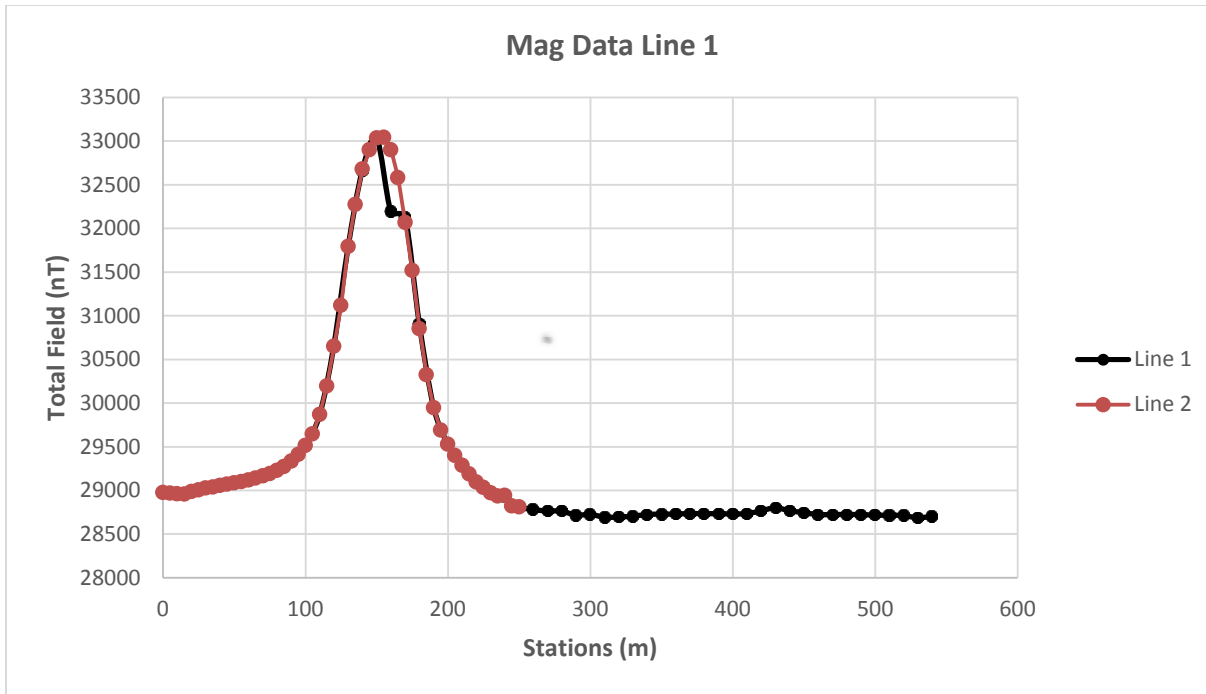


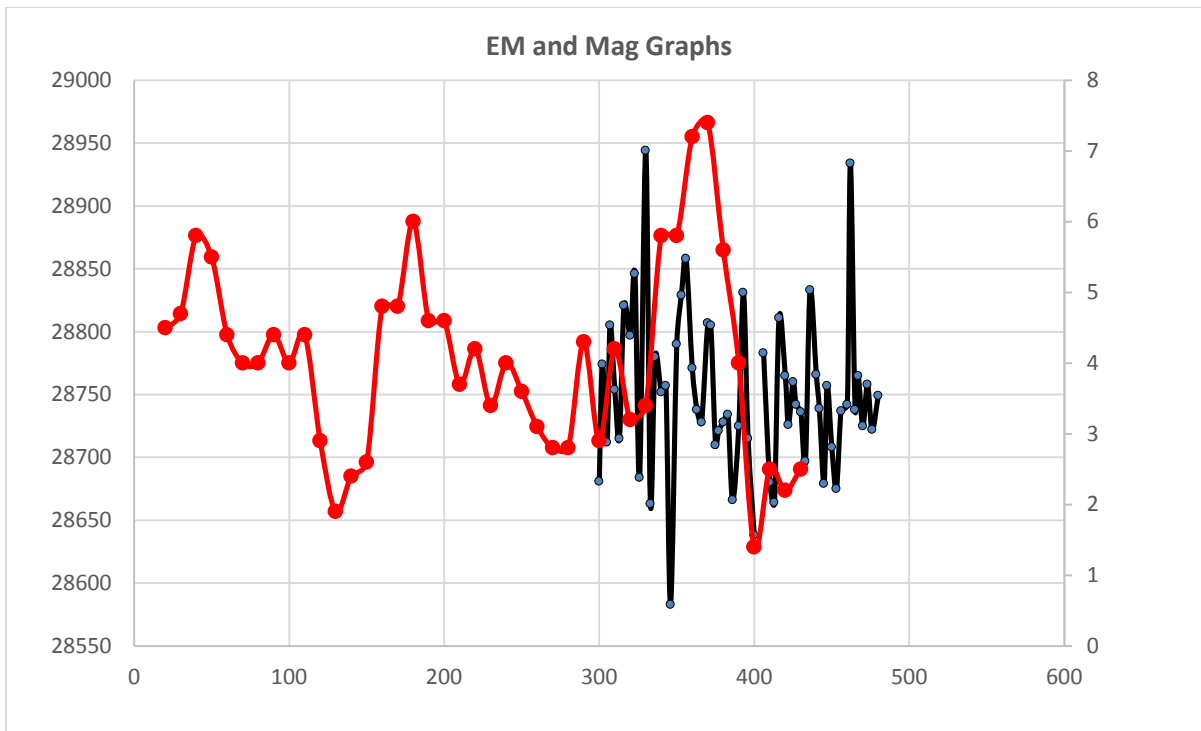
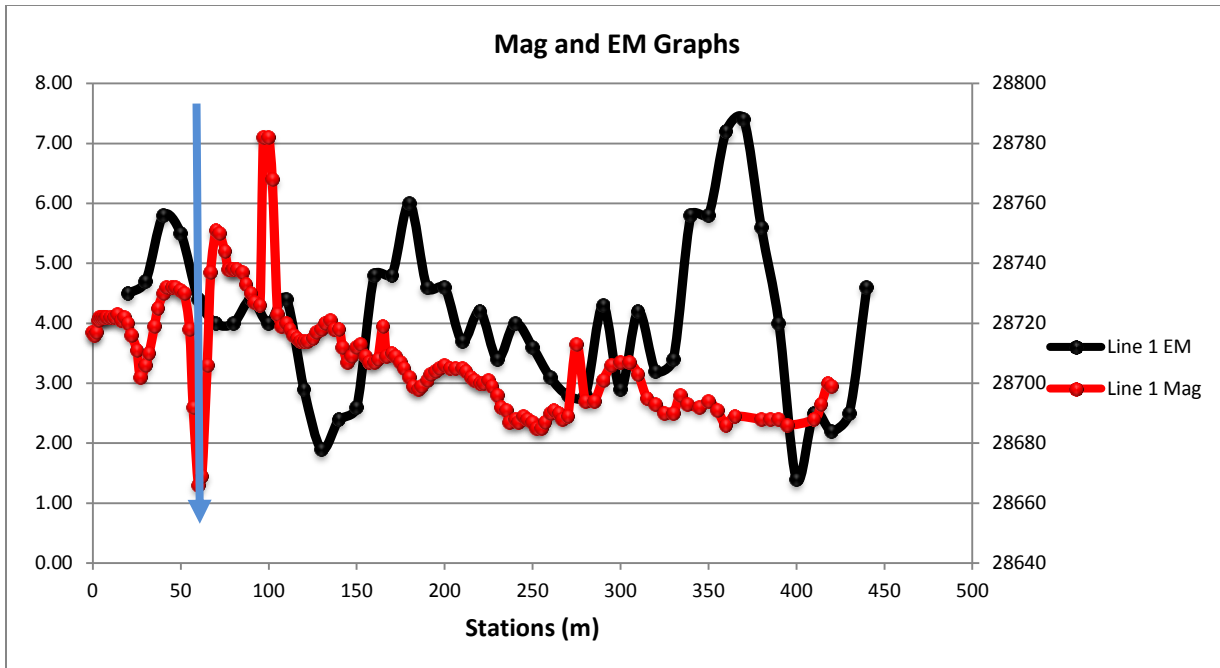












10.2 Appendix B: Summary of percussion drillings results

Borehole Number	Co-ordinates		Depth	Steel Casing (∅ mm)			Water level	Blow Yield	Water Strike	Comments
	Geographic WGS84			152 (Plain)	177 (Plain)	177 (Slotted)				
	Latitude	Longitude								
			(mbgl)	(m)	(m)	(m)	(mbgl)	(l/s)	(mbgl)	
DPC 1A	- 23.9613	28.8886	14	-	-	-	-	Dry	-	Backfilled
DPC 1B	- 23.9613	28.8886	16	-	-	-	-	Dry	-	Backfilled
DPC1	- 23.9616	28.8887	102	18	-	-	19.47	0.01	22	Mined/Destroyed
DPC2	- 23.9617	28.8887	104		-	12	19.60	0.20	24	Mined/Destroyed
DPC3	- 23.9620	28.8889	69	18	-	-	19.19	Dry	-	Mined/Destroyed
DPC4	- 23.9623	28.8891	117	-	-	-	19.55	Seepage	50	Mined/Destroyed
DPC5	- 23.9575	28.8739	83	-	-	5	3.39	Seepage	36	Available
DPC6A	-	28.8743	34	-	-	-	-	Seepage	3	Backfilled

	23.9578									
DPC6	- 23.9578	28.8743	77	-	-	13	3.18	0.90	-	Available
DPC7	- 23.9522	28.8703	126	-	12	12	5.96	6.00	10-15, 26	Available
DPC8	- 23.9498	28.8687	54	-	6	8	4.94	2.00	14 - 15	Available
DPC9A	- 23.9580	28.8743	12	-	-	-	-	Dry	-	Backfilled
DPC9	- 23.9580	28.8743	85	-	-	6	2.95	2.00	21, 29	Available
DPC10	- 23.9458	28.8867	74	24	-	-	-	Dry	-	Available
DPC11	- 23.9365	28.8732	105	14	-	-	14.91	0.10	24, 76	Available
DPC12	- 23.9588	28.8941	89	23	-	-	21.60	Seepage	23	Available
DPC13	- 23.9590	28.8943	57	17	-	-	21.50	Seepage	-	Available
DPC14	- 23.9667	28.8798	92	-	6	6	2.56	6.00	13, 17, 23	Available
DPC15	-	28.8802	97	-	-	6	2.97	8.00	18, 23,	Available

	23.9671								27	
DPC16	- 23.9696	28.8798	121	-	-	6	3.32	Dry	-	Available
DPC17	-23.969	28.8806	113	-	-	12	3.59	0.10		Available
DPC18	- 23.9692	28.8803	86	-	-	6	2.03	2.80	10, 23, 32	Available
DPC19	- 23.9663	28.8793	90	-	6	10	3.17	0.60	4;13	Available
DPC20	- 23.9320	28.8912	90	-	-	9	73.78	Dry	-	Available
DPC21	- 23.9641	28.8842	70	-	12	8	7.99	Dry	-	Available
DPC22	- 23.9646	28.8847	37	-	9	6	8.95	Dry	-	Available
DPC23	-23.965	28.8851	96	-	12	6	9.00	Dry	-	Available
DPC24A	- 23.9644	28.8844	20	-	-	-	-	Dry	-	Available
DPC24	- 23.9644	28.8844	50	-	18	4	8.28	Dry	-	Available
DPC25	- 23.9352	28.8771	110	-	18	6	17.45	0.40	33, 55, 81	Available
DPC26	-	28.8936	80	-	6	6	3.27	4.70	20, 27	Available

	23.9751									
DPC27	- 23.9727	28.8937	60	-	6	6	9.32	1.70	21	Available
DPC28	- 23.9834	28.90457	50	-	-	9	8.47	seepage	20	Available
DPC29	-23.933	28.8904	100	-	3	12	-	Dry	-	Available
DPC30	- 23.9476	28.8896	80	-	9	12	-	Dry	-	Available
DPC31A	- 23.9481	28.8895	41	-	6	12	-	Dry	-	Available
DPC31B	- 23.9482	28.8896	31	-	6	12	-	Dry	-	Available
DPC31C	- 23.9486	28.8894	102	-	3	12	-	Dry	-	Available
DPC32	- 23.9516	28.8909	80	-	3	12	-	Dry	-	Available
DPC33	- 23.9583	28.8946	177	-	3	6	-	0.02	39	Available
DPC34	- 23.9586	28.8948	30	-	3	9	-	Dry	-	Available
DPC35	- 23.9581	28.8945	81	-	0	21	-	Dry	-	Available

VPC1	- 23.9628	28.8961	180	-	6	6	-	Seepage	42	Available for Vibrating wire line piezometers
VPC2	- 23.9660	28.8969	180	-	3	17	-	Seepage	41	Available for Vibrating wire line piezometers

10.3 Appendix C: Recharge rates calculation

Borehole Name	y	x	Cl (mg/L)	Recharge (%)	Recharge (mm)
Hse 10118	- 24.00016	28.94046	999.7	0.10003	0.642193
RPC16	- 23.96147	28.92402	959.8	0.104188	0.668889
Hse 10319	- 23.99536	28.94462	836.4	0.11956	0.767575
RPC7	- 23.99306	28.92954	495.95	0.201633	1.294485
RPC8	- 23.99292	28.92557	478.95	0.20879	1.340432
Hse 10321	- 23.99494	28.94444	476	0.210084	1.348739
Hse 10364	- 23.99648	28.93901	416.2	0.240269	1.542528
RPC18D	- 23.96801	28.93237	416	0.240385	1.543269
Hse 10302	- 23.96548	28.81705	360.5	0.277393	1.78086
Thage Tavern	- 23.95398	28.84563	354.9	0.28177	1.80896
Leleso Exploration Hole	- 24.03218	28.92365	350.3	0.28547	1.832715
Hse 10108	- 24.00059	28.94186	343.5	0.291121	1.868996
Hse 60277	- 23.95517	28.86656	341.9	0.292483	1.877742
Hse 10709	- 23.98518	28.93658	311.7	0.320821	2.059673
RPC5	- 23.98529	28.91497	308.75	0.323887	2.079352
RPC15	- 23.99291	28.91557	300.2	0.333111	2.138574
Makgenene School	- 23.91656	28.87739	298.7	0.334784	2.149314
Hse 3001-Clinic	- 23.91641	28.87619	296.7	0.337041	2.163802
Makhafalo J.M.	- 23.95993	28.85644	287.9	0.347343	2.229941
Molekane Rooms	- 23.98472	28.93976	274.9	0.363769	2.335395
Limberg BH1	-	28.91556	271.9	0.367782	2.361162

Borehole Name	y	x	Cl (mg/L)	Recharge (%)	Recharge (mm)
	23.86244				
RPC11	- 23.98309	28.93619	269.85	0.370576	2.379099
Hse 60167	- 23.95877	28.86543	254.9	0.392311	2.518635
Hse 20234	- 23.99314	28.93811	248.9	0.401768	2.579349
Hse 10327	- 23.99410	28.94317	244.9	0.40833	2.621478
Hse 10362	- 24.02090	28.84790	240	0.416667	2.675
Hse 10714	- 23.98540	28.93742	229	0.436681	2.803493
RPC2	- 23.98901	28.91503	228.95	0.436777	2.804106
P44	- 23.99082	28.88189	218.9	0.45683	2.932846
Mmagope Crech	- 23.97392	28.84801	216.9	0.461042	2.959889
Hse 20128	- 23.88987	28.90529	216.1	0.462749	2.970847
RPC24	- 23.99125	28.93314	213.15	0.469153	3.011963
Hse 20061	- 23.91608	28.87178	212.9	0.469704	3.0155
Hse 10521	- 24.03875	28.90059	212.8	0.469925	3.016917
RPC1	- 23.98970	28.91511	211.2	0.473485	3.039773
Hse 20169	- 23.98411	28.93951	209.9	0.476417	3.058599
Hse 10033	- 23.90995	28.88189	208.1	0.480538	3.085055
RPC13	- 23.97250	28.92993	203.45	0.491521	3.155566
RPC13S	- 23.97252	28.92989	194.55	0.514007	3.299923
Mapela Clinic	- 23.95671	28.84741	191.9	0.521105	3.345492
P114S	- 23.99099	28.91230	180.5	0.554017	3.556787
RPC3	- 23.99051	28.91531	179.55	0.556948	3.575606

Borehole Name	y	x	Cl (mg/L)	Recharge (%)	Recharge (mm)
Hse 30147	- 23.88650	28.90801	177.4	0.563698	3.61894
Hse 20072	- 23.91461	28.87374	175	0.571429	3.668571
P118	- 23.98429	28.89937	173.7	0.575705	3.696028
Hse 20244	- 23.91086	28.87258	172	0.581395	3.732558
P127	- 23.98059	28.90854	171.4	0.583431	3.745624
P125	- 23.96009	28.88052	171.35	0.583601	3.746717
Hse 10089	- 23.90983	28.87836	157	0.636943	4.089172
Hse 10082	- 23.91063	28.87736	156.3	0.639795	4.107486
Hse 10572	- 23.98867	28.94426	155.5	0.643087	4.128617
SKM 10339	- 24.00443	28.87193	155	0.645161	4.141935
A Makafula	- 23.94433	28.83848	154.5	0.647249	4.15534
Hse 30074	- 23.89186	28.90946	154	0.649351	4.168831
P115D	- 24.00049	28.92373	152.95	0.653808	4.19745
Hse 10406	- 23.99473	28.93839	149.4	0.669344	4.297189
Leballo Hse 50138	- 23.96276	28.85507	148	0.675676	4.337838
Hse 10247	- 23.86465	28.84925	145	0.689655	4.427586
Dipela	- 23.93927	28.85684	142	0.704225	4.521127
Hse 10899	- 23.98537	28.95254	140.3	0.712758	4.575909
SKM 14B	- 24.00080	28.87271	140	0.714286	4.585714
Hse 43B	- 23.91108	28.87288	139.4	0.71736	4.605452
RPC18S	- 23.96798	28.93240	138.3	0.723066	4.642082
Somo	-	28.85712	137	0.729927	4.686131

Borehole Name	y	x	Cl (mg/L)	Recharge (%)	Recharge (mm)
	23.93597				
Tribal Office BH	- 23.96150	28.84847	136.5	0.732601	4.703297
Hse 23B	- 23.91569	28.87256	136	0.735294	4.720588
Hse 10081	- 23.91106	28.87677	136	0.735294	4.720588
Hse 20574	- 24.05725	28.88963	134.5	0.743494	4.773234
Hse 10281	- 24.04585	28.89349	133.9	0.746826	4.794623
SKM 10380	- 24.00180	28.87263	131.3	0.761615	4.889566
Hse 10259	- 24.00666	28.87394	125.8	0.794913	5.103339
Mohagane	- 23.95245	28.84267	123.5	0.809717	5.198381
Hse 10292	- 24.04773	28.89148	119.4	0.837521	5.376884
Kgoadiaka Crech	- 24.05321	28.88963	119	0.840336	5.394958
Hse 10307	- 24.05010	28.88870	118.4	0.844595	5.422297
P117	- 23.98068	28.90548	113.8	0.878735	5.641476
Hse 09	- 24.01249	28.87471	110.5	0.904977	5.809955
Hse 10136	- 24.01944	28.87265	108.5	0.921659	5.917051
Hse 123	- 24.02174	28.95729	106	0.943396	6.056604
Hse 10092	- 23.90939	28.87894	106	0.943396	6.056604
Hse 10662	- 23.98804	28.93728	104.6	0.956023	6.137667
Hse 10540	- 24.04274	28.88693	101.4	0.986193	6.331361
Hse 10074	- 23.91183	28.87569	101	0.990099	6.356436
Rooiwal School	- 23.86563	28.84855	100	1	6.42
Hse 10209	- 24.01290	28.87473	98.1	1.019368	6.544343

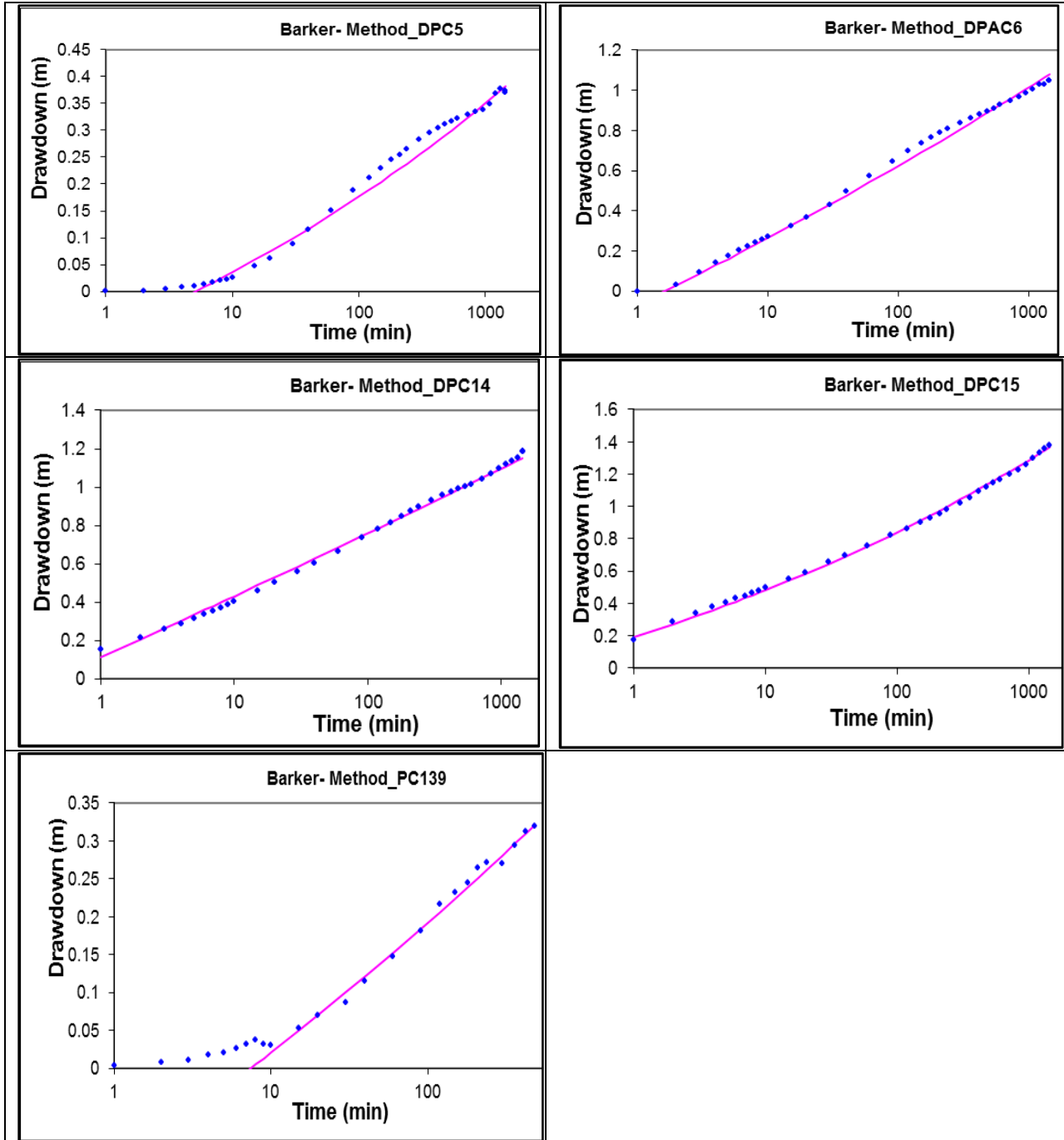
Borehole Name	y	x	Cl (mg/L)	Recharge (%)	Recharge (mm)
DWA 3055	- 23.98173	28.98017	97.5	1.025641	6.584615
Mapela Day Care Centre	- 23.93554	28.85774	95.5	1.04712	6.722513
RPC12	- 23.97481	28.93333	95.4	1.048218	6.72956
Hse 10531	- 24.03927	28.89888	94.4	1.059322	6.800847
RPC23	- 23.95616	28.92401	94	1.06383	6.829787
SKM 10221	- 23.99850	28.88500	92.6	1.079914	6.933045
SKM10511	- 23.99477	28.87233	90.5	1.104972	7.093923
SKM 344	- 23.98620	28.88600	89.6	1.116071	7.165179
A0021A	- 24.05323	28.95635	88.9	1.124859	7.221597
Hse 10297	- 24.04833	28.89103	88.3	1.132503	7.270668
Hse 10554	- 24.04132	28.89676	87.3	1.145475	7.353952
SKM NO2	- 23.98560	28.89090	87.3	1.145475	7.353952
SKM 10497	- 23.99660	28.87180	85.7	1.166861	7.491249
Hse 10207	- 24.01210	28.87457	85	1.176471	7.552941
Hse 41B	- 23.98761	28.93747	79.7	1.254705	8.055207
SKM10446	- 23.99277	28.86977	76	1.315789	8.447368
H03-1696	- 24.05321	28.94563	74.4	1.344086	8.629032
A0063	- 24.05093	28.93927	73.4	1.362398	8.746594
SEK Hse 17	- 23.94213	28.94463	72	1.388889	8.916667
Hse 10225	- 23.86118	28.84928	72	1.388889	8.916667
SEK- Hse 688	- 23.93686	28.94564	70.5	1.41844	9.106383
Hse 118B	-	28.90406	69.3	1.443001	9.264069

Borehole Name	y	x	Cl (mg/L)	Recharge (%)	Recharge (mm)
	24.03240				
Mmanoko Day Care	- 23.99259	28.93620	68.9	1.451379	9.317852
Moshibudi Pri School	- 24.05137	28.94311	68.4	1.461988	9.385965
Hse 108	- 23.91706	28.86674	65.7	1.52207	9.771689
SKM 020	- 23.98156	28.88433	63.2	1.582278	10.15823
SKM 240	- 23.98503	28.89022	63.1	1.584786	10.17433
RPC19	- 23.96585	28.94017	61	1.639344	10.52459
Hse 142	- 24.04740	28.89123	60.5	1.652893	10.61157
P122D	- 23.96821	28.92305	60.25	1.659751	10.6556
Hse 2171	- 23.91192	28.87274	58	1.724138	11.06897
Anglo Agric BH	- 24.02207	28.80631	57.7	1.733102	11.12652
P120D	- 23.96931	28.92427	57.4	1.74216	11.18467
Maleya High School	- 23.94094	28.94454	55.5	1.801802	11.56757
RBK 402	- 23.94165	28.99562	53.2	1.879699	12.06767
P120S	- 23.96932	28.92424	53	1.886792	12.11321
P116S	- 23.99788	28.92360	52.85	1.892148	12.14759
SEK-Hse 80	- 23.94151	28.94730	52	1.923077	12.34615
Hse 10633	- 24.04342	28.88630	48.6	2.057613	13.20988
P122S	- 23.96818	28.92304	47.95	2.085506	13.38895
Hse 10373	- 24.04714	28.88457	46.6	2.145923	13.77682
P128	- 24.02409	28.90493	46	2.173913	13.95652
P121D	- 23.96937	28.92301	44.95	2.224694	14.28254

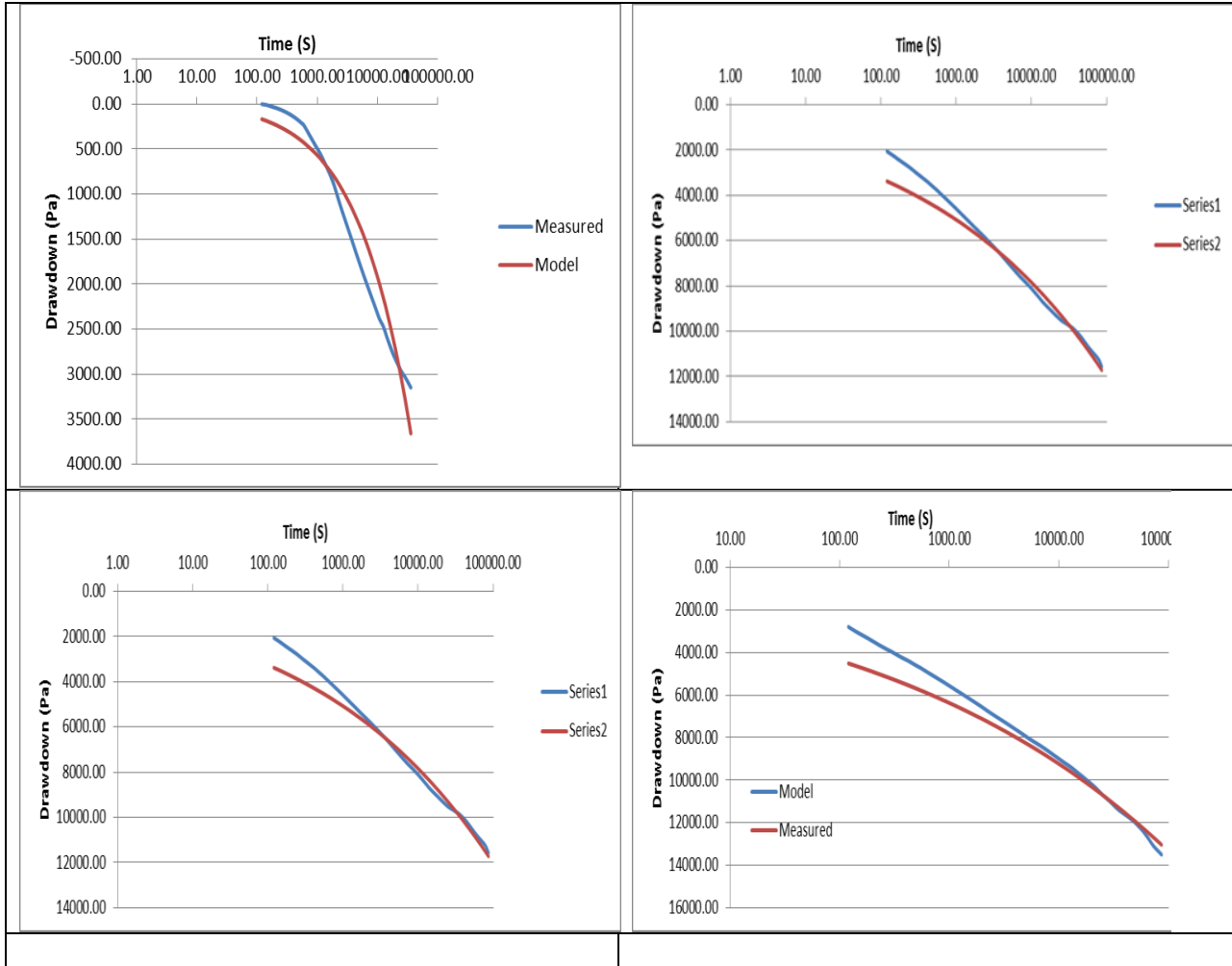
Borehole Name	y	x	Cl (mg/L)	Recharge (%)	Recharge (mm)
Hse 10134	- 24.02224	28.95666	42.3	2.364066	15.1773
P124	- 23.97469	28.89182	39.15	2.554278	16.39847
Hse 1614	- 24.04568	28.88414	35.9	2.785515	17.88301
SRK5S	- 23.94824	28.93908	34.8	2.873563	18.44828
RPC22	- 23.94701	28.93819	29.8	3.355705	21.54362
Hse 10627	- 24.04272	28.88693	27.8	3.597122	23.09353
A0319	- 24.04660	28.94040	27.4	3.649635	23.43066
Hse 10057	- 24.01968	28.95338	27.3	3.663004	23.51648
RPC17D	- 23.96742	28.92729	26.95	3.710575	23.82189
Nkokone Pri School	- 24.03020	28.91083	24.8	4.032258	25.8871
Mmolawa Sec School	- 24.05327	28.95206	22.8	4.385965	28.15789
Matsogela Secondary School	- 23.85576	28.84947	21.5	4.651163	29.86047
Hse 10579	- 23.99206	28.93509	19.3	5.181347	33.26425
Mapanolla Sec School	- 24.04522	28.93970	18	5.555556	35.66667
RPC10	- 23.98740	28.93389	13.35	7.490637	48.08989
K.I.C	- 24.04886	28.83076	12.8	7.8125	50.15625
RPC21	- 23.95573	28.94058	8.25	12.12121	77.81818
RPC17S	- 23.96743	28.92734	8.1	12.34568	79.25926
P121S	- 23.96934	28.92300	6.55	15.26718	98.01527
Hse 10221	- 24.01925	28.85849	6.4	15.625	100.3125
RPC20	- 23.95964	28.94301	3.7	27.02703	173.5135

10.4 Appendix B: Drawdown fitting curves for hydraulic parameters from observation boreholes

10.4.1 Barker model



10.4.2 Logarithmic approximation of fractured fractal model



10.4.3 Fractured Fractal Flow solution with fractional differentiation via Mittag-Leffler law

